Combined current, wave and turbulent flows and their effects on tidal energy devices.

Buckland, Hannah

Combined Current, Wave and Turbulent Flows and their effects on Tidal Energy Devices: Volume 1

Swansea University
Prifysgol Abertawe

Hannah Buckland

College of Engineering

Swansea University

A thesis submitted for the degree of

Doctor of Philosophy

June 2014

Acknowledgements

Above all, I would like to thank my supervisors;

Dr Ian Masters, for his continuous support and direction from day one and his insightful advice and patience with my unforgivable spelling mistakes. Certainly without his expert guidance and undoubtable commitment and friendship this PhD would not have been possible.

Dr James Orme. His infectious enthusiasm and drive has permanently changed my attitude to work for the better.

I would like to acknowledge the Knowledge Economy Skills Scholarships (KESS) project and the tidal turbine developer Swanturbines Ltd. for providing the financial support for my degree and also Dawn Morgan, Cassy Froment and Jane Kelly for their help and patience with the never-ending timesheets and quarterly reports.

I would especially like to acknowledge the Low Carbon Research Institute Marine Energy Research Group for all their support and help; it was a privilege and a pleasure to work with them. In particular, thank you to Tracy Tunstall and Alex Ellis, Professor Dominic Reeve, Dr John Chapman, Dr Miles Willis, Enayat Zangiabadi, Dr Michael Togneri, Mérin Broudic, Dr Alison Williams, Dr Rami Malki and Dr Iain Fairley. I would also like to acknowledge Dr Tim Baker for sharing his technical expertise. Thank you also to the College of Engineering, in particular Professor Oubay Hassan for his guidence.

I would like to acknowledge the many friends I have made in Swansea, beginning with George Pettifor, Hillary Davies and Rich Pettifor. Their unbounded generosity, kindness, sense of adventure and humour has greatly enriched my quality of life in Swansea. My housemates, Kev and Barbs, for their generosity and kindness. To Sean, my breakfast buddy, thank you for listening. To the biker gang, thank you for the adventures Mike. To my close friends Elliot and Alex, for always being there, even if I did let myself in again. To Patrick and Bruce for all the fun and games and heated arguments over lunch. To Dan I, my office neighbour, for all the film nights and interesting distractions. To Andy, Tom, Rachel, Carwyn, to all the office, thank you.

Thank you to my role models, Grandma Joan and Grandad Fred. Your hard work and commitment to life and family inspires me to be the best I can be. I would like to thank Emily and Matt for their continued support. I would like to thank Aunt Col for her support.

I would like to thank Grandma Jean for her endless giving and overwhelming kindness as well as her unconditional support and loving help with any problem. I would also like to thank her for her love of life and cheerful strength in the face of adversity. I would like to thank Fred for his kindness and commitment to me and my family. I would like to thank my friend Nicky for her patience with me over the past three years and for listening to all my problems.

To Ömer, nothing written here can thank you enough.

Abstract

This thesis considers the effect of disruptive waves and turbulence on a horizontal axis tidal stream turbine (TST), in terms of performance and survivability. The TST reaction to transient fluid flow is modelled analytically using Blade Element Momentum Theory (BEMT). Standard BEMT corrections are evaluated for the TST application and an alternative optimisation method is proposed for the steady state BEMT, improving compatibility with transient and depth dependent inflow, as well as the non-dimensionalisation constant needed to calculate the performance coefficients. Also, an alternative BEMT tip and hub loss implementation has led to a significant improvement of the turbine axial force prediction and in the high induction region.

Validation studies are presented for BEMT coupled with regular, nonlinear wave theory and good agreement is found with published experimental data. A novel method to simulate irregular sea states is developed to couple with BEMT and a combined reactive coupling of waves and current is implemented. The TST performance in an irregular sea state is considered against turbine performance with real ADCP data and a good agreement is found. This work evaluates the BEMT implementation for the specific application of modelling TST's and significantly improves the fundamental theory, applicability and quality of results in this case.

Contents

Nomenclature

Roman Symbols

$\eta(x)$	Free surface elevation, m
γ	Azimuth angle of blade element, radians
$\hat{h_\omega}$	Mean wave height, m
Ω	Rotational velocity ms^{-1}
ϕ	Incident flow angle on the aerofoil section, ^{o}
Ψ	Wave stream function
ρ	Fluid density, kgm^{-3}
σ	Cavitation number
σ_{crit}	Critical cavitation number
θ	Angle of blade element from axial plane, radians
θ_w	Angle of tidal flow from wave propagation direction, *radians*
a	Axial induction factor
A_α	Blade element aerofoil cross-sectional area, m^2
A_x	The cross-sectional area of the fixed body parallel to the oscillatory flow for the inertia term of the Morison equation for force, m^2
b	Tangential induction factor

NOMENCLATURE

C Wave celerity, ms^{-1}

c Chord length m

$C(k)$ Theodorsen's complex function (lift deficiency function)

C_D Drag coefficient

C_L Lift coefficient

C_m The added mass coefficient

C_{press} Minimum pressure coefficient

C_p Turbine power coefficient

d Depth of the blade element (distance from base of cavitation tunnel) m

F Loss correction for tip and hub losses in momentum theory

f Wave frequency

F_{Ain} The inertia force term in the axial direction, N

F_A The axial force including added mass term, N

f_a Apparent wave frequency, Hz

f_c Combined wave and tide frequency, Hz

F_{dr} The drag term of the Morison equation for force, N

F_{in} The inertia (added mass) term of the Morison equation for force, N

F_{me} The Morison equation force, N

F_{Tin} The inertia force term in the tangential direction, N

F_T The tangential force including added mass term, N

Fa Axial force N

g Optimisation function

g_1	Squared difference in torque per element
g_2	Squared difference in axial force per element
H	Total water height, m
h	Height of the boundary layer, m
h	Height of the water column above the blade element m
h_b	Limiting breaker wave height, m
H_S	Average water height, m
h_w	Wave height, m
$H_{1/3}$	Significant wave height of sea specturm, m
H_{Hub}	Hub height of the turbine in the water column, m
L	Wave length, m
l	The length of the section of structure considered in the acceleration loading calculations, m
L_s	Lift per unit span, N, for Theodorsen's theory
M_A	Added mass, kg
Mx	Out of plane bending moment, Nm
My	In-plane bending moment around a blade root,Nm
N	Number of waves considered in sea specturm
N_B	The number of blades
p_0	Static pressure, Pa
p_∞	Undisturbed far upstream pressure Pa
p_h	Static pressure head, Pa
p_L	Blade element local pressure Pa

NOMENCLATURE

p_V	Sea water vapour pressure 1200Pa
Q	Total head, m
R	Range of depth spanned by swept area of the turbine, m
r	Radial position m
R_T	Range of axial velocity change swept by the blade tips as a percentage of the total velocity change,
$S(f)$	Wave frequency spectral density
T	Torque Nm
T_w	Wave period, s
$T_{1/3}$	Significant wave period for a sea specturm, s
T_p	Peak wave period, s
TG	Constant torque (Generator torque), Nm
U	Free stream velocity, ms^{-1}
U	Upstream undisturbed flow velocity for momentum theory ms^{-1}
u	Upstream inflow velocity in the tidal stream flow direction, ms^{-1}
u_B	Boundary flow velocity, ms^{-1}
u_B	Free stream velocty in the boundary layer, ms^{-1}
U_w	Wave propagation velocity, ms^{-1}
U_c	Total wave and tidal velocity in the wave propagation direction, ms^{-1}
u_s	Stoke's drift velocity, ms^{-1}, Goda [2010]
v	Upstream inflow velocity in the cross-stream direction, ms^{-1}
V_∞	Aerofoil incident flow velocity for blade element theory ms^{-1}
v_r	Rotational inflow velocity, ms^{-1}

V_{tip} Aerofoil incident flow velocity for blade element theory at the blade tip ms^{-1}

W The facing width of a fixed body in oscillatory flow, m

x Power-law factor

Chapter 1

Literature Review and Introduction

1.1 Introduction

On a global scale, energy demand is growing at the steady rate of $1-2\%$ per annum. In The World Offshore Renewable Energy Report by Department of Trade and Industry's Renewables 2010 Target Team [2009], it is speculated that renewable energy, all forms considered, has the potential to satisfy this demand many times over. The annual UK industry review document, prepared for government in 2007 and 2010 by Future Energy Solutions [2007] and The UK HM Government [2010] respectively, both indicate that in the past 20 years, interest and investment into renewable energy has increased exponentially on a global scale, however the large majority of energy needs are currently met by non-renewable resources. Department of Trade and Industry's Renewables 2010 Target Team [2009] label Europe as leading the world; with a rapidly expanding renewable energy market and with many European countries committed to renewable energy targets.

Although wind and, to a lesser extent, solar energy are somewhat established industries; support for UK renewables, in particular marine and off-shore wind, has increased over recent years. Public support and informed, realistic investment in UK renewable energy is vitally important, mainly for long term global security and also national security. Globally, it is environmentally important to invest in renewables

as a conscious effort to minimise the effects of climate change. On a political level, it is of national importance for the UK to secure energy production in the turbulent political climate of today.

Tidal energy exploits the natural ebb and flow of the tides and has an estimated global potential of 3TW, Department of Trade and Industry's Renewables 2010 Target Team [2009]. Considering feasible extraction locations, it is estimated by Department of Trade and Industry's Renewables 2010 Target Team [2009] that, globally, only 3% (90GW) is suitably situated for capture. The UK is favouably situated, between the North Atlantic Ocean and North Sea, and is considered by Renewables Advisory Board [2008] to experience half of the European, techically extractable, tidal resource. In addtion, the UK is the site of the second largest tidal range in the world, with a 12.3m spring tide Avonmouth range in the Bristol Channel as measured by South Wales Ports [2012].

The NationalGrid [2012] and Parlimentary Office of Science and Technology [2007] claim the UK electricity demand has remained a constant 40GW since 2006, and it is roughly estimated by The Carbon Trust [2010] that tidal energy has the potential to provide 5% of this electricity demand. As a rough quantitative example, by considering an unrealistic 100% capacity factor, this equates to installing 2000 1MW turbines in UK waters. In the report by Department of Trade and Industry's Renewables 2010 Target Team [2009], later the Department for Energy and Climate Change (DECC), the energy provided by renwables target is set to 15% of the UK energy demand by 2015, which has since been extended to 2020, after considering only a 3% contribution from all renewables in 2009.

There are four main tidal energy converter classes, the most common being horizontal axis turbines; which account for over half of the developing technologies identified by The European Marine Energy Centre Ltd [2012]. In 2008, the tidal energy industry was in its infancy and, in the UK, existed as small groups of researchers and developers operating and testing prototype tidal turbines, such as Hammerfest Strom Ltd. [2010]; Marine Current Turbines Ltd. [2013]; Renewables Advisory Board [2008]; Swanturbines Ltd. Tidal Technology [2013] and The European Marine Energy Centre Ltd [2012]. Since then, proven tidal energy converter technologies have built confidence in the industry and it has grown with large investments from the private sector led by government incentive schemes such as the feed-in tariffs and, more re-

cently, the Renewable Energy Certificates (ROCs). However, due to the device and site specific nature of tidal energy extraction deployment, it is essential that funding and investment is adequate as unrealistic financial ultimatums may negatively effect a deployment plan.

To exist as a successful renewable energy, tidal energy must be shown to be competitive and advantageous when compared to other renewable sources, in particular the most successful renewable, wind energy.

For example, the tidal turbine developer Marine Current Turbines claims to confidently provide energy at £200 per MWh. They aim to provide energy competitavely priced against off-shore wind at $£140 - 150$ per MWh by 2020. This is an ambitious target, regardless of the fact that the cost of offshore wind will also reduce with industry experience by 2020.

However, on a comparable timescale of one tidal cycle, off-shore wind produces unpredictable power output; a common disadvantage of general renewable energy sources. The power source magnitude at a tidal energy extractor site can be accurately calculated with time and the high and low power yield, as well as period, can be anticipated.

As water is more dense than air, tidal energy is more concentrated than wind energy. Therefore small tidal turbines will have the same power rating as much larger wind turbines. Tidal turbines produce less wake interference, Malki *et al.* [2011], and can therefore be spaced closer than wind turbines therefore computational analysis of turbine array wake interaction is an active area of research; for example the simulations by Malki *et al.* [2011] and McCombes [2013]. The increase in fluid density does however produce an unwanted increase in loadings on the turbine blades, which increases the risk in the technology and justifies another active research area; turbine simulation and experiment analysis to assess long term durability and survivability.

Many of the disadvantages of tidal energy are due to a general lack of experience, such as the cost of installation and maintenance, the largely unknown interaction of the device with local wildlife and the unpredictable reaction of the device to the wave climate. These unknowns introduce risk but can be expected to reduce with increasing collective industry experience. It is suggested by The UK HM Government [2010] that as the industry evolves from small scale developers to commercialisation, one aim of the collective marine enery industry is to minimise the risk posed by the

uncertainties, in order to accelerate industry growth in the UK.

To address these issues, the complementary approaches of turbine computer simulation, scale experimentation and device developer tests are all active areas of research. At Edinburgh University an all sea test, 1/20th scale basin, the Flowave Tank, FlowaveTT [2012], is due to open in 2013 and can create sea states with multi directional waves, together with tidal schemes. The The European Marine Energy Centre Ltd [2012] provides a real sea test facility for prototype turbines. The Low Carbon Research Istitute, Marine Energy Research Group working at Swansea University utilise numerous computational simulation methods to study the effect of tidal turbines on local wildlife, such as noise pollution and collisions with fish, as well as turbine performance and interaction with other devices and the flow regime.

Computational Fluid Dynamics (CFD) models are developed alongside the BEMT analytical modelling presented here to analyse tidal turbine performance.

This study aims to extend the analytical method of BEMT to simulate loading of tidal turbines in time-varying wave motion. This is achieved by considering the implications of steady state BEMT with varying inflow as well as simulating realistic sea states, wave motions and tidal flows and the interaction between waves and tides. This combines to produce a simple and realtively quick way to determine survivability, and performance of tidal turbines in realistic flows.

1.2 The Tidal Energy Industry

1.2.1 History

The potential energy of the oceans has been known for centuries. Ross [1995] claims that the first marine energy absorber patent was issued in 1799, but was deemed obsolete as the industrial revolution began. Since then, due to the seemingly unlimited abundance of oil and coal, renewable energy was not seriously considered in the UK until the winter of 1973-74, when the oil crisis combined with miners' strikes saw a drastic rise in energy costs. This dramatically highlighted the unsustainable dependency of the UK on non-renewable energy resources.

The first government funded research in renewable energy began in 1976. It did

not include tidal energy, and lasted only 6 years for wave energy. Later that year a collaborative wind energy association was realised. This was the beginnings of the British Wind Energy Association (BWEA).

Although wind energy was accepted as a realistic renewable energy source, interest in marine energy rapidly reduced after the Government presented costings for the technology, that were based on the initially high installation costs of wave energy absorbers. This initial setback, along with pressure from oil companies and many unpredictable and expensive problems, has contributed to major delays for the marine energy industry, which is considered by Renewables Advisory Board [2008] to be 10-15 years behind that of wind energy.

By the 90's, it was clear that wind energy would become the major renewable energy industry and the majority of the government funding for the DTI New and Renewable Energy Programme was consolidated in wind energy research, The Energy Programme [1999].

The programme was fully funded by the government whereas today it is partly funded by industry as the Department of Energy and Climate Change (DECC). Since the re-launch of the government wave energy R&D Programme in 1999, and the launch of the first ever tidal energy R&D Programme in 2000, Ross [1995] states that interest in marine energy greatly increased as many organisations began to support wave and tidal energy. The most noticeable being the BWEA, which was renamed in 2010 as RenewableUK, and now covers a wide range of renewable sources, including marine energy.

From 1999 to 2007 Renewables Advisory Board [2008] states that approximately £160M of public funds was specifically designated to marine renewable energy. This highlights the huge increase of interest when compared to the government expenditure of the 90's and is mainly due to the obvious success of the wind energy industry and greater awareness of the environment and climate change. Of these funds, £35M was set aside to kick start nearly 60 company projects covering 27 device types, Renewables Advisory Board [2008]; Swanturbines Ltd. Tidal Technology [2013]; The UK HM Government [2010]; Wallace [2009].

This investment did not compliment the state of the industry and, interestingly, only about £15.5M of this fund was used. The combination of initial optimism and the uncertain nature of the research has greatly delayed development. To bridge the

gap between R&D and prototype testing, many device testing centres have been built since then, such as NaREC, the The European Marine Energy Centre Ltd [2012] and Wave Hub.

As confidence and interest in the industry grows, so does the number of funding bodies for R&D marine energy projects. Before 1999, the only funding source was the small amount invested by the government, documented in the report by The Energy Programme [1999]. In the UK there are now numerous sources such as the Engineering and Physical Sciences Research Council (EPSRC), The Carbon Trust [2010], the Marine Renewables Deployment Fund (MRDF) and European funding, such as KESS, the funding body for this work.

1.2.2 Present State

The marine energy industry has evolved through adversity to arrive at a critical and exciting state of development today. In January 2010, the majority of devices were at the R&D stage, with the most advanced devices prototyped.

The Hammerfest Strom Ltd. [2010] HS300 was the first tidal turbine to provide energy to a national grid. The 300kW prototype was installed in Norway in 2003 and decommissioned in 2007. Under the new name of ANDRITZ HYDRO Hammerfest, the pre-commercial HS1000 1MW turbine was installed at The European Marine Energy Centre Ltd [2012] in December of 2011 and delivered to the UK grid in February 2012. ScottishPower Renewables are planning to install a 10MW HS1000 array in the sound of Islay and the more ambitious project of a 95MW array at Duncansby Head.

Marine Current Turbines Ltd. [2013] (MCT) is leading the industry with the largest and most powerful twin tidal turbine, the 1.2MW SeaGen, installed in 2008 in Northern Ireland. Early performance analysis of this turbine showed an impressive average power output of 60% of it's rating (double that expected for wind turbines), and in March 2012 Siemens took full ownership of MCT. In September 2012, a milestone was reached; 5GWh of energy produced since installation in 2008 and performance has been continuously optimised to an operational output of 2.5GW today, in effect sufficient power for 750 British homes, Marine Current Turbines Ltd. [2013].

Andrew Tyler, the CEO of MCT since 2010, emphasised the challenge of tidal tur-

Figure 1.1: The SeaGen turbine installed in Northern Ireland. Image Copyright Kenneth Allen. This work is licensed under the Creative Commons Attribution-Share Alike 2.0 Generic License.

bine mechanics by stating that the primary engineering lesson learned from Strangford Lough is the persistent challenge of turbulence-induced vibration. These vibrations manifest themselves by the tidal device's mechanics into the structure: the power-train, the gearbox and the stresses placed on the blades. Subject to a force of over 100 tonnes of weight, SeaGen's blades have suffered a number of fatigue cracks and even a break, forcing a redesign, as stated at Marine Current Turbines Ltd. [2013].

A larger 2MW device is planned for 2013 with the prospect of installation in two tidal turbine farms; 8MW at Kyle Rhea in Scotland and 10MW at the Skerries in Anglesey. Planning is in the advanced development stages, with deployment after 2015. To take advantage of deep water currents, MCT is investing in SeaGenU research and testing at the bay of Fundy, Canada, a non-piercing device, which is sub surface and relies on a pivoting system to raise the turbines for maintenance, Marine Current Turbines Ltd. [2013].

There are many other active tidal turbine developers in the UK and world wide, developing innovative, site specific energy converters. Swanturbines Ltd. Tidal Technology [2013] is the only Swansea based tidal turbine developer and have developed a tidal turbine suitable for tidal estuary bathymetry and flow, the SwanTurbines

Cygnus Inshore Tidal Turbine, to be installed as an array. This turbine will take advantage of the natural flow funneling and blockage effects that occur in tidal inlets.

Other potential site surveys and case studies are being conducted independently by academic institutions such as the Bristol Channel study in 2010, published by Willis *et al.* [2010] and the unique site survey of Ramsey Sound conducted by the Marine Energy Research Group in 2011. This is the only existing survey of the background, natural state of a tidal turbine site as it was conducted in anticipation of the installation of the Tidal Energy Ltd [2012] turbine. The bathymetry and flow regime of the area were extensively recorded to calibrate future surveys against, which will take place during and after operation of the turbine.

Apart from the previously described industrial and academic activity, the growth in the industry is evident in the number of members in relevant on-line forums, such as the Marine Energy Pembrokeshire Coastal Forum, MEP, and the International Network on Offshore Renewable Energy, INORE. The MEP Annual Conference connects academics, companies and communities within South Wales with an interest in marine energy. It has grown from an interested few, in 2010, to a nationally significant event in 2012. Similarly, INORE brings together young researchers from 63 countries and since its creation has grown rapidly, reaching 1000 members in 2013, not only from Europe, but also from America and Asia. The annual INORE Symposium 2013 was held in Pembrokeshire, Wales, further highlighting the global significance of the region for marine energy.

The wider UK marine energy industry is world leading due to the rich marine resource around Britain and the strong marine engineering knowledge as well as government and public support in recent years. However, it is currently at a crucial stage of advancement and continued support is essential as the majority of companies are at the delicate transition stage between prototype testing and pre-commercialisation.

Denmark maintains a world leading wind energy industry. The success in Denmark is based upon strong infrastructure and manufacturing communities and a similar support structure for marine energy should be developed in the UK.

1.3 Modelling Tidal Stream Turbines

Accurate and conservative performance prediction at the R&D stage, as well as continuous performance assessment, is vital to maximise performance whilst minimising costly prototype fault and failure. In addition, a prototype device will attract much scrutiny. It is therefore important to assess the accuracy and applicability of the performance prediction tools. Blade Element Momentum Theory, BEMT, is a quick and robust method of predicting the power output of a tidal turbine. The results presented in this document are a continuation of the work outlined by Orme [2006] and Chapman [2009] and Masters *et al.* [January 2011].

1.3.1 Blade Element Momentum Theory

BEMT theory was originally developed for ship propeller design. Glauert [1934] adapts and applies BEMT to aeroplane propellers and details the theoretical complications of doing so. Lanzafame and Messina [2007] is an example of BEMT applied to wind turbines.

Momentum theory, or actuator disc theory, was used to complement blade element theory, by W.J.M. Rankine, A. G. Greenhill and R. E. Froude. It is now a well established method to determine rotor dynamics, as outlined in Batten *et al.* [2008] and Lanzafame and Messina [2007].

In 1974, Griffiths [1974] made some fundamental changes to BEMT propeller theory in order to correctly apply it to wind turbines. Griffiths [1974] discusses an upper limit on the power output of a turbine due to the geometrical constraints of the problem alone. For this model with ideal assumptions, Griffiths [1974] concludes only 59.3% of the energy available can possibly be harnessed, although the power output will be significantly less than the ideal model predictions.

The paper shows that for maximum power coefficient C_p, the thickness to chord ratio must be kept as small as possible without compromising overall structural stability. Compared to wind turbines, this stability is more important for tidal turbines, as the increased medium density produces larger loadings on the blades. Considering tip and hub losses, Griffiths [1974] finds that a maximum attainable efficiency of 50% is a reasonable reduction on the actuator disc value of 59.3%.

Batten *et al.* [2008] is a modern use of BEMT to model wind turbines, and can be easily and successfully adapted to model tidal turbines by considering a denser fluid. This change has a fundamental effect; such as altering Reynolds number value, cavitation characteristics and turbine stall region characteristics. However, an abundance of knowledge exists, as these factors are well understood for marine propellers.

The ebb and flow of the tides is predictable but, as most turbines will be situated in shallow water, the small blockage effects of the free surface boundary on the water coloumn itself may change with weather conditions and wave climate. This introduces uncertainty into the power supply as the inflow will be spatially and time varying, in an unpredicable way. This may translate into uncertinty in the power supply.

Griffiths and Woolard [1978] highlights the importance of understanding the amount of output power at a range of different rotational speeds in order to correctly couple the turbine with an electrical generator in all situations.

To do this, the relative incident velocity of a fluid at a turbine site, including the blockage effects of the free surface must be determined. In Griffiths and Woolard [1978], the velocity of the fluid, the rotational velocity of the turbine and the complex, three dimensional effects of trailing vortex velocities are considered.

Griffiths and Woolard [1978] also considers variable turbine blade pitch effects on the power output against tip speed ratio curve. It is shown that, by aligining the pitch parallel to the axial flow direction, the torque and power generated are generally greatly increased at low tip speed ratios and greatly reduced at high tip speed ratios. At high TSR, electrical generators operate most efficiently, therefore turbines may be purposely designed to operate at high TSR; with blades aligned perpendicular to the axial flow direction. However, this will greatly reduce the torque and may cause it to be negative at low rotational speeds. Also, the turbine cannot start by itself and would require variable pitch blades. This increases the complexity of the turbine design and can increase maintenance and running costs as well as the probability of faults.

During development of the BEMT tidal turbine simulation model used in this thesis by Orme [2006], Chapman [2009] and Masters *et al.* [January 2011], Hassan and Ltd [2008] published a similar BEMT based design tool for the specific application of tidal turbines, GH Tidal Bladed, with the support of the UK DTI New and Renewable Energy Programme. They also conducted a survey, of commercial and academic

researchers both in the UK and overseas, to identify specifications and requirements for a tidal turbine design tool, Hassan and Ltd [2008]. This survey highlighted cavitation occurrence and blockage as important areas of investigation. The inclusion of wave effects, turbulence, shear and the interaction between wave motion and tidal motion in the flow field were also identified. It is desirable that the model is easily adaptable to different sites and dimensional device specifications. Other considerations identified by Hassan and Ltd [2008] include representation of support structures and buoyancy forces. It is also vitally important to retain a robust and generic code that is easy to use. These findings are also directly relevant to the BEMT model used in this work.

1.3.1.1 Tip and Hub loss

Momentum theory considers the swept area of the turbine as an actuator disc. BEMT corrections must be applied to account for the 'tip loss' and 'hub loss' which reduce turbine power output. These corrections cause the ideal actuator disc theory to become more physically correct as actuator disc theory considers only an azimuthally and radially averaged effect of the turbine presence on the flow. For this idealistic approach, a discontinuity at the turbine wake boundary exists, outside which the turbine holds no effect on the flow regime.

As early as 1930's these losses were being investigated for propellers. The common tip loss representation by Prandtl is presented by Glauert [1934] and results are shown to compare well to exact solutions. In Griffiths and Woolard [1978], the Prandtl and alternative Goldstein tip loss methods are discussed. The rigorous Goldstein analysis is only applicable for high tip speed ratio operation. The Prandtl tip loss is subsequently the most preferred tip loss as it's simplicity deems it a flexible approach. Although alternative tip and hub loss corrections exist, summarised by Shen *et al.* [2005], the Prandtl approximation is the most common approach and assumed to also extend to hub losses by Burton *et al.* [2001]. Masters *et al.* [January 2011] outlines the implementation of a Prandtl approximation loss.

In the literature there is further speculation over the implementation of the tip loss; Glauert [1934] corrects the Prandtl loss correction to the order of approximation and therefore only corrects the induced velocity and not the mass flow through the rotor disc. Willson and Lissaman [1974] later suggested that the mass flux should

be corrected in a similar manner to the induced velocity. In Shen *et al.* [2005], it is suggested that the orthogonality between the induced and relative velocity at the blade element is violated by this formulation. To resolve this, further refinements are suggested, for example, DeVires [1979].

1.3.1.2 High-Induction Correction

During start up or shut down of a turbine, and also at very high TSR, the wake flow can become turbulent. The axial induction factor becomes greater than 0.5 and classical momentum theory is invalid. This inconsistency is highlighted by Glauert [1934] for propellers using experimental data from Lock *et al.* [1926], which compares the axial force coefficient C_{Fa} with the axial induction factor, a. A large spread of data is found, which correctly suggests that the dependency of the axial force coefficient on the axial induction factor is complex in this region. This high-induction state is unusual when the turbine is in normal operation and so it will have little effect on the effective power curve. However, Buhl [2005] suggests the region is very important when determining the durability of the turbine as, by modelling this state, fault conditions and fault loadings can be studied as well as the crucial turbine start up mechanism.

An empirical relationship is proposed by Glauert [1934] to fit the Lock *et al.* [1926] data curve in the high-induction state and to also agree with momentum theory at the high-induction limit. The correction is outlined in Burton *et al.* [2001]. It is shown by Buhl [2005] that this solution could create a discontinuity at the high-induction limit, as it does not consider the tip and hub loss corrected, classical momentum theory. Previous solutions are discussed in Buhl [2005] as inadequate and a correction is proposed that accounts for tip and hub losses, thus eliminating the numerical discontinuity of Glauert [1934].

1.3.1.3 The Boundary Layer

The BEMT model assumes a spatially infinite flow domain. For tidal stream turbines this is usually not the case as the turbine diameter is generally on the same scale as the water depth. This is therefore an unrealistic assumption and needs to be corrected to account for the boundary effect of the sea bed on the current flow.

The boundary layer confines the viscous effects to a relatively thin area. Within this layer, the local stream flow speed drops from the free stream speed to zero at the sea bed. The effect of the sea bed outside this boundary is considered by Mehaute [1927] to be below 1% and so negligible and the tidal flow in this region is considered the free stream flow.

The widely accepted form for the tidal velocity profile within a boundary layer is a power-law model of Equation 1.1, as used by Chapman [2009] in this model and also Mehaute [1927] and Schlichting [7th ed. 1979].

$$u_B = U\left(\frac{h}{H}\right)^{\frac{1}{x}} \tag{1.1}$$

where U is the free stream speed, h is the height above the sea bed and H is the boundary layer height. The power-law exponent, x, dictates the rate of the change in velocity, i.e. how quickly the velocity drops to zero. The value to give this is specific to the location of the turbine and Batten *et al.* [2008] uses $x \approx 7$. However in Orme [2006] it is postulated that $x \approx 10$ for tidal flows. A higher x value means that the boundary is less effective on the tidal flow near the surface and decreases more quickly close to the sea bed whereas a lower x means that the decrease in flow speed is more gradual. Considering the effect on Reynold's number, it is more probable that x is dependent on tidal velocity, where intuitively high x is suitable for fast tidal flows and a lower x for relatively slow flow rates, however this assumption would need to be proven.

In a similar endevour, Chapman [2009] discusses a variable boundary layer height. It is widely accepted, as in Mehaute [1927], that the boundary layer may be ignored as the effect becomes negligible; less than 1%. As the flow rate increases the effective region of the boundary layer decreases. Therefore for slow flow rates, at high and low tide, the boundary layer effects of the sea bed are more significant. It is suggested by Chapman [2009] that the bottom half of the water height should be treated as a boundary layer. However, a further improvement would be to determine the complex relationships between boundary layer height, x and flow speed. The sea bed roughness is also effective on the boundary layer representation and this is further considered in volume 2 of this thesis.

The literature does not, however, consider the suitability of a depth and time

dependent inflow for BEMT.

1.3.2 Coupled Blade Element Momentum-Computational Fluid Dynamics

BEMT is a fast and robust way to determine the performance of a tidal stream turbine. However, in Chapter 2, the wake effect in this theory is shown to be implicit, implying that detailed wake flow cannot be directly studied. A wake representation is vital to analyse arrays and the effect of the turbine on the environment. Malki *et al.* [2011] details a combined Blade Element Momentum-Computational Fluid Dynamics (BEM-CFD) code to determine device interactions. The outer domain around the turbine is most commonly represented by the Reynolds Averaged Navier Stokes model, not only by Malki *et al.* [2011] but also Turnock *et al.* [2011] for example, to calculate the Reynolds stresses and other turbulence characteristics in the turbine wake.

For the BEM based method of Malki *et al.* [2011], the Navier Stokes equations are solved on a time averaged mesh with the addition of a momentum source/sink term to couple to the specific turbine. Blade element theory is used to determine the value of this term directly from the lift and drag values of the aerofoil sections of the blades. The utilisation of BEM to represent the turbine within the CFD model does not only decrease run time, comapred to a blade resolved model, it also allows for better quality meshes as a consequence of the physical blade dimensions built into the source blade element rather than the mesh. However because of the time average principle of the approach, transient flow features due to blade position are not modelled.

The turbulent diffusion in the outer RANS domain model is commonly characterised by an eddy viscosity term. In Masters *et al.* [2012], the most commonly used validations for this term are discussed and it is found that this term effects the hydrodynamics of the wake structure, producing very different results in a BEM-CFD simulation.

In McNaughton *et al.* [2012] a CFD model with a k-ω eddy viscosity term is compared to an alternative, Large Eddy Simulation (LES) to characterise turbulence in the turbine far wake. The turbine blade geometry is directly input as a solid object in the domain, unlike BEM based models, the lift and drag curves for the cross-sectional

aerofoils are not needed. LES eliminates small scales of the solution by low-pass filtering on the Navier-Stokes equations. As opposed to direct numerical simulation, the small scales are modelled. This simulation has higher fidelity and higher computational cost than the RANS model but significantly lower computational costs than a direct numerical simulation. The LES result is found to maintain tip vorticies and wake structure better than the k-ω model. It is also found that the RANS model under predicts pressure forces on the blades. This highlights the need for high fidelity CFD techniques to qualitatively study the flow domain around a tidal stream turbine. However, the computational expense of this approach limits its use for evaluating alternative designs or a wide range of flow conditions. At the tidal turbine design stage of development, BEMT or a BEMT-RANS models are more common turbine simulation approaches. As the demand for array effects research increases and computational time decreases, the use of LES to study the turbulent wake of TST arrays may become more prevalent.

1.4 Waves- Engineering Models

The motion and evolution of wave climate has been studied since the 19^{th} century. It was initially of interest to naval engineers to predict the wave forces on ship hulls. The wave climate can seem sporadic in nature, with an infinite number of possibilities, and could only be predicted by the most experienced sailors. Since then, the motion of waves has been described in various ways, from single, linear wave theory to statistical spreads of the wave energy probability. The interest in wave motion spans many industries, from atmospheric forecasters and theoretical physicists to oil rig companies. In the marine energy industry, the importance of understanding multi-directional current and wave interaction, and the effect on devices, is highlighted by the commission of an all-waters combined current and wave test facility, FlowaveTT [2012].

To take advantage of higher rates of water flow, it is desirable to locate turbines as close as possible to the free surface where wave effects are much more significant. Therefore it is important to determine the coupled effect the presence of waves has on a stream of flow, in order to predict the device limitations and operations as realistically as possible. Wave effects are more significant when the wave velocities

are larger than, or comparable to, the free stream velocity. This is most significant in extreme weather conditions and when the tide is changing. For horizontal axis turbines, the low levels of turbulence minimise stochastic structural loads however velocity shear and yaw effects may cause large cyclic loadings.

To study the turbine performance response in waves, the effect of wave motion must be included in the inflow representation. There are multiple ways to account for wave motion in a BEMT code, and studies are presented here in the time domain or wave frequency domain.

These methods either describe regular or irregular waves. The correct approach is dependent on site specific sea states; regular wave theories are more applicable if the turbine sits in deep water and in the presence of a dominant incoming wave plane. This will occur in sea swell sites where most of the wave effects are due to the large wavelength swell. The simplest regular theory is linear wave theory, as used with BEMT by Barltrop *et al.* [2006]. The wave equation is used to describe a propagating wave and if there is more than one dominant wave front, waves can simply be superimposed. However, it is likely there are many incoming waves, therefore this method becomes computationally costly and complex.

The non-linear, regular wave theory coupled with BEMT by Chapman [2009] is extended in this work to produce irregular sea states, described by Goda [2010]. The non-linear effect on irregular seas is discussed as well as the compatibility with BEMT. This thesis also presents a number of validation studies; comparing simulated results with data from tidal turbine experiments considering wave effects. A complex wave and tidal coupling method is outlined and implemented in the model and an in depth study on the compatibility of transient flows, such as waves and turbulence with BEMT, is presented.

The engineering wave models described as part of this work are suitable for quick and robust simulations of turbine performace and are shown in this thesis to produce meaningful results when coupled with BEMT, compared to experimental tidal turbine test data.

Refined flow modelling, detailed in the following chapters for completeness, is a common approach for studying the wave field itself. However, they are computationally expensive. Considering the needs of the industry as detailed in the previous chapters; refined flow modelling to include wave effects is not used in this work.

1.4.1 Linear Waves

Linear theory is appropriate for small waves and infinite depth conditions and is presented in Goda [2010] and considered by Barltrop *et al.* [2006] as suitable for wave representation with BEMT. However, linear wave theory is limited by its inability to describe specific non-linear effects such as steep and breaking waves in shallow water. If the water is shallow, or the wave amplitude is large, wave crests are pointed, troughs become flat as non-linear effects grow. In the foreseeable future, turbines are likely to be situated close to shore where non-linear effects are more prevalent, therefore it is important to describe breaking waves with a non-linear wave theory.

The velocity of flow induced by the waves must be combined with the tide velocity, for the incident flow used in BEMT. The tide will induce non-linear wave effects and the coupling between the two motions is extremely complex. Aside from this, a simple Doppler effect is observed when waves and tides exist for either linear or non-linear waves. This effect is commonly included in many codes by altering the dispersion relation given in Equation 1.2, as used in GL Garrad Hassan Tidal Bladed [2013] and Barltrop *et al.* [2006],

$$f_c = f + \frac{U}{L}\cos\theta_\omega \tag{1.2}$$

where U is the current velocity and f_c is the combined frequency. This coupling finds the 'frequency' of the current as if it were traveling as a wave with the same wavelength of the coupling wave. Therefore, if the current is moving with the wave, the wave frequency is amplified. In the same way, if the current is opposing the wave the frequency is reduced. If the wave is traveling perpendicular to the current there is no effect on the frequency of the wave. Tidal Bladed, as described by Hassan and Ltd [2008], also incorporates diffraction effects by using MacCamy-Fuchs theory.

Barltrop *et al.* [2006] couples waves and tides in this very simple way and claims it is sufficient for modeling the effects of waves on tidal turbines. However, it is suggested in Roland *et al.* [2009] and Umgiesser and Zampato [2001] that a more complex coupling between waves and tides to replace Equation 1.2 is needed.

1.4.2 Non-Linear Waves

1.4.2.1 The Stream Function

An alternative regular wave theory is the stream function theory by Chaplin [1979] which describes a singular, non-linear wave front. It presents a solution for breaking waves, which is applicable in any water depth. However, Chaplin [1979] presents an assessment of the errors which shows that the particle velocities may be under estimated by as much as 25%, in particular for steep waves.

Chaplin [1979] states that Cokelet has presented an exact solution for a periodic wave, but then questions the practicality of this solution for problems. The Dean stream function formulation, on which Chaplin's function is based, is easily applicable to all depths and easily extended to higher orders.

Stream function theory to represent waves was implemented in the Swansea University BEMT code used in this thesis by Chapman [2009]. The formulation is similar to linear wave theory and is described in detail by Chaplin [1979].

Although the methodology is more complex than that of Dean's solution, the results are not interpolated but directly obtained for a particular wave height. It is also found that the crest velocity increases rapidly with wave height near limiting conditions. The stream function method gives accurate results for steep waves as long as the wave height is an independent parameter and a sufficiently high order is taken.

1.4.3 Irregular Waves

Both linear wave theory and non-linear, stream function theory describe regular waves and can include more than one dominant wave front by superposition only. Therefore, these regular wave theories are applicable to swell waves which are naturally regular in shape. Irregular wave theory is more applicable when there is no dominant wave, as in wind wave dominated seas. In this case the body of water around the turbine will be homogeneous and it is more correct to describe the state of the sea.

1.4.3.1 Sea State Spectrum

Ross [1995] states that sea states were first formally introduced by oil companies in the 1980's and they represent the statistical probability curve for wavelength in a particular sea. They are used extensively for maritime structural design such as oil platforms and wind-power plants. This thesis extends the theory to represent irregular seas in BEMT for modelling the dynamic response and long term fatigue of tidal stream turbines.

In the absence of a dominant regular wave swell, it is obvious from observations of the water surface, that the motion is somewhat irregular. The movement at a certain time comes from the superposition of the multiple waves that coexist at that instant. These waves can, and do, differ in period, amplitude, wavelength and direction. The sea surface can be modelled by assuming an infinite number of differing waves with randomly distributed phases.

The total wave climate can consist of more than one sea swell caused by wind generated sea surface disturbance, creating swell frequency energy peaks on the wind wave sea spectrum. Swells and wind wave spectra can differ in origin, direction and intensity. They are formed in the presence of a consistent wind force and the shape of the sea spectrum peak will change and evolve from a limited fetch sea state to a fully developed sea state.

The limiting factor for the evolution of the sea state spectrum is the wave phase speed equal to the wind speed, after which the sea spectrum is stable and no longer dependent on fetch length. If a sea state develops and the wind decreases, the sea state begins to decay. The sea state at the turbine location is dependent on the physical distance and direction from the sea state source, the local wind climate, the local bathymetry and water depth and the local instantaneous current velocity.

The sea spectrum is the instantaneous 'spectral density' of the energy in the body of water and represents the energy distribution of the waves with respect to wave frequency. Past analysis of large amounts of wave data, taken from around the globe, has established well defined sea spectra characteristics. The significant wave height can be determined, as:

$$H_{1/3} = 4\sqrt{m_0} = 4\sqrt{\int_0^\infty S(\omega)d\omega} \tag{1.3}$$

The ordinate of the $S(\omega)$ curve is not consistently defined in literature. In this thesis, as in Michel [1999], it is defined as the most common ordinate of $1/2A^2$, which has the units $m^2/(rads^1)$, where A is wave amplitude so that the area under the curve is equal to the variance, m_0.

The sea state can be unique and can contain multiple peaks, however some common sea state types have been defined. For example the Pierson-Moskowitz $(P-M)$ spectrum was developed in 1964 for a fully developed sea, Crapper [1984]. A constant wind is assumed for a significantly long time and over a large area. In general, all wave frequency spectral densities can be defined as,

$$S(f) = Af^{-5}e^{-Bf^{-4}} \tag{1.4}$$

where A and B are constants.

1.4.4 Pierson-Moskowitz Spectra

This model is most suited to a fully developed sea, meaning the state of a sea when the winds have been blowing sufficiently long, about 10,000 wave periods, over a large stretch of water, about 5,000 wavelengths squared. For a typical wave of period 9 seconds and wavelength 50m, the wind must have been blowing for more than 20 hours over 6000km. Such vast stretches of unbroken water is only found in the largest oceans. In this case, the maximum amount of energy from the wind blowing has been transferred to the waves and therefore, if the winds do not increase, the waves will not gain any more energy. This causes the high frequency waves into equilibrium and is a typical state of the sea in the North Atlantic Ocean. Considering the P-M spectrum, A and B are derived as dependent on the wind speed 19.5m above the surface only, Crapper [1984], and are given in Equations 1.5 and 1.6.

$$A = C1_{\mathrm{PM}} H_{1/3}^2 T_p^{-4} \tag{1.5}$$

$$B = C2_{\mathrm{PM}} T_p^{-4} \tag{1.6}$$

For the P-M spectrum, the value of $C1_{PM}$ is 0.219 and the value of $C2_{PM}$ is set to 1.250. With this relation, the peak wave period, T_p, can be expressed in terms of $H_{1/3}$ as in Equation 1.7, and the sea state is determined by one parameter only, U_{wind}.

$$T_p = 2.76 H_{1/3}^{1/2} \tag{1.7}$$

$H_{1/3}$ is defined in Equation 1.8 in terms of the wind speed 19.5m above the surface U_{wind}.

$$H_{1/3} = 0.2092 \frac{U_{wind}^2}{g} \tag{1.8}$$

As the one parameter P-M spectrum is determined by wind speed only, it is less suited to wind waves and tidal turbine applications.

For more enclosed areas, such as the North Sea, the wave spectrum does not fully develop and the JONSWAP spectral density is more appropriate as outlined in section 3.3.2. This model is similar to PM but assumes the waves continue to grow with distance and, due to less equilibrium, the peak of the energy spectrum vs wave frequency curve is more pronounced. Therefore the band of frequencies of waves with high energy is narrower but the peak energy is higher resulting in larger wave heights.

The site specific nature of sea states challenges tidal turbine design. For example, a turbine situated in the North Atlantic needs to function well in a wide range of incident wave frequencies whereas, in the North Sea it is only required to function at the peak wave energy but must be able to cope with high energy waves at that frequency.

1.5 Waves- Refined Flow Modelling

Although the wave simulations outlined in this work are based on engineering models, this section presents a literature review and summary of refined flow modelling CFD techniques. These meshed methods are commonly used to solve wave potential flow theory and, as well as the turbine performance, they can accurately simulate the wave field around the tidal turbine.

Groeneweg and Battjes [2003] present more advanced wave models. However the focus of their research is the behaviour of waves over a non-uniform sea bed rather than the complexities of wave and tidal interactions. Commercial software such as FLOW-3D Flow Science [2010], WAMIT INC. MIT and ANSYS [2012] and has been successfully employed in the past to model waves on solid structures. Compared to engineering models, these are more accurate but also more complex and less robust. A fluid structure interaction solver is needed to apply to dynamic structures. A dynamic and complex tidal turbine structure has been used with open source wave mesh models successfully, as by Umgiesser and Zampato [2001] and Versteeg and Malalasekera [2007], and some mesh approaches are presented here.

The difference in the density of air and water means that the surface of the sea can be assumed to move independently of the air and is modelled as a free surface. A moving boundary that has limited constraints creates complications for accurate numerical analysis of the situation Versteeg and Malalasekera [2007]. Special methods are needed to predict the movement, position and coupling with current flow of the free surface.

There are many variations of these methods however they all have a common approach to the free surface problem. Firstly, a routine is used to set the initial input shape and location of the surface. Then the progression of the surface with respect to time is employed by an algorithm while the sea surface consistently satisfies the free surface boundary conditions.

Some finite element methods use a Lagrangian grid that moves with the fluid, as in FLOW-3D Flow Science [2010]. Intuitively, this is the simplest approach, because as the grid moves with the free surface it will automatically track the motion. To accurately simulate the free surface the approximating equations must be modified to include the boundary and the fact that fluid does not exist beyond it.

The limits of this approach are identified in FLOW-3D Flow Science [2010], as the inability to simulate free surfaces that intersect or break apart. Even coarse, large amplitude motion can only be effectively tracked by the use of complex regridding techniques, such as th Arbitrary-Lagrangian-Eulerian method.

Improved, Incompressible, Smoothed Particle Hydrodynamics (SPH) is presented in Khayyer and Gotoh [2009] as a method for predicting the wave impact pressure on a coastal structure. It is described as initially developed for modelling astrophysical

phenomena. Since then, it has been adapted for modelling many varied engineering problems.

The Navier-Stokes equations describe the motion of an incompressible, viscous fluid and form the basis of wave impact numerical models as in FLOW-3D Flow Science [2010] and Versteeg and Malalasekera [2007]. When using grid-based Eulerian solvers the free surface must be described mathematically. To do this, Volume Of Fluid (VOF) methods can be used.

The advantages of SPH are outlined in Khayyer and Gotoh [2009]. Particle methods analyse problems without numerical diffusion because of their Lagrangian nature. As they are also gridless, they are useful in simulating many varied situations, such as the moving discontinuities and large deformations found in free surface hydrodynamic flow. Incompressible, free surface fluid flow may be modelled as weakly compressible SPH with the addition of a suitable equation of state or alternatively solving Poisson Pressure equation using incompressible SPH.

To account for more complex surface movements, the following methods all use an alternative, fixed, Eulerian grid as the basis for computations. This is the more popular choice of grid.

When the amplitude of the free surface motion is small, this amplitude, $\eta(x, z, t)$, above some mean, y, can be used to track the surface. For example, this can be used to simulate low amplitude sloshing and shallow water waves. By considering the function, $F(\overline{x}, t) = y - \eta(x, z, t)$, the surface boundary is at the position $F(\overline{x}, t) = 0$. As with linear wave theory, the kinematic condition is applicible at the boundary and governs the time evolution of the surface height. It says that a particle on the free surface stays on the free surface while this free surface moves with the fluid. Therefore, if the velocity vector of the fluid at the surface is $\overline{u} = (u, v, w)$,

$$\frac{DF}{Dt} = \frac{\partial F}{\partial t} + (\overline{u}.\nabla) F = 0 \qquad \forall\, \overline{x}, t \qquad (1.9)$$

By substitution of $F(\overline{x}, t) = y - \eta(x, z, t)$,

$$-\frac{\partial \eta}{\partial t} - u\frac{\partial \eta}{\partial x} - v\frac{\partial \eta}{\partial z} + \frac{\partial y}{\partial t} = 0 \qquad on\ y = \eta(x, y, t), \qquad (1.10)$$

$$\frac{\partial \eta}{\partial t} + u\frac{\partial \eta}{\partial x} + v\frac{\partial \eta}{\partial z} = w \qquad on\ y = \eta(x, y, t) \tag{1.11}$$

Although this is a three-dimensional simulation, the memory requirements are low as the input consists only of the surface height at a set of horizontal locations FLOW-3D Flow Science [2010]. It is now easy to implement finite difference approximations to this equation. The boundary conditions on the free surface are also simplified by the assumption that the amplitude of the motion is small.

Marker And Cell (MAC) method is the earliest method used to simulate time dependent, free surface flow and is based on a Eulerian grid of control volumes. MAC is used by FLOW-3D Flow Science [2010]. A set of marker particles, with no mass or properties of their own, are used to flag the fluid within the grid. If a grid cell contains a full set of marker particles, it is assumed to be filled with fluid and if none, it is assumed completely empty. If a grid cell is filled but has a neighbouring void cell it contains a free surface. A more exact location of this surface, however, was not originally considered. To simulate the evolution of the fluid with time, a marker is moved if it has locally interpolated fluid velocities. Then adaptations are needed to detect newly filled or emptied cells.

In this method, free surface boundary conditions are considered by applying the air pressure to cells on the surface and by also assigning velocity vectors to locations near or on the free surface. In this way, a state of incompressibility and zero-surface shear stress can be imposed.

As the markers track fluid volumes and not the free surface directly the surface is simply defined by the edges of the volume elements. Therefore complex flow, such as intersection or diffusion of free surfaces is easily represented by merging or parting volume elements, respectively.

This method has been extensively modified for increased accuracy and applicability. For example, the surface location can be interpolated to fall within a cell or surface tension forces can be included.

The disadvantages of this method are also outlined in FLOW-3D Flow Science [2010]. For accurate three-dimensional simulations many marker particles are needed and this requires a lot of memory and CPU time. For accurate simulations of large motions a typical number of marker particles per cell is about 16. Another disad-

vantage is that marker particles may create unphysical voids in the flow. This can occur in areas of converging or diverging flow. The markers can be interpreted as the centres of small fluid elements. In these regions, the fluid elements are pulled into convoluted strands and voids occur if they are deformed more than the width of a cell in any direction.

A way of reducing the high CPU and memory needs of the MAC method is to limit the markers to the free surface, the surface marker method, again described in FLOW-3D Flow Science [2010]. To simplify the computations, the marker particles are arranged in a linear order along the surface with uniform spacing. When applying the boundary conditions, they also represent the position of the free surface more accurately.

However, this approach removes the volume tracking property of the MAC method and it becomes complicated to model combinations and separations of free surfaces. Also, when considering a three-dimensional problem, there is no obvious way of ordering the markers effectively on the free surface. For example, in a region where the free surface is expanding, due to no markers below the surface, new markers cannot be added and the surface is completely unknown.

Volume of Fluid (VoF) was first formally presented by Hirt and Nichols in 1981 and is simple and robust but computationally expensive and described in FLOW-3D Flow Science [2010] and Weymouth and Yue [2010]. This method combines the low CPU and memory of having one tracking variable, as in the surface height method, with the powerful volume tracking of the MAC method. This is the most popular free surface modelling technique and is used in many applications, Aulisa *et al.* [2003]; Lv *et al.* [2010]; Weymouth and Yue [2010].

As with the MAC scheme, it is also based on a Eulerian grid of control volumes. By implementing physical boundaries on such a grid, these methods are able to simulate more energetic flow, such as breaking waves and fragmentation. In each grid cell, one value for each flow property of velocity, pressure and temperature is found, resulting in low CPU.

This approach tracks the free surface using the single quantity of fluid volume fraction for each cell which is consistent with the resolution of the existing flow values. The fluid volume fraction determines the amount of fluid in the cell and the free surface is found in partially filled cells or between full and empty cells as described

in FLOW-3D Flow Science [2010].

However, due to the complexity of the model, many fundamental problems with the VOF method exist and are outlined in Weymouth and Yue [2010], such as interface reconstruction and conservative advection of the volume fraction field.

In Christensen *et al.* [2007], the wave loads on an offshore wind turbine mono-pile are calculated using traditional engineering methods, such as stream function theory and Morison's equation, and again using VOF CFD method. The two are compared and it is found that, for small, linear waves, the loadings given by the two methods are very similar. As non-linear effects grow, the differences between the loadings given by the two methods increase. In general, VOF predicts larger wave loadings than the traditional theories for steep or breaking waves. Morison equation is found to significantly underestimate the loadings from waves and the largest differences, 96% difference compared with CFD, are found with large loadings.

There are two different classes of surface boundary capture method, the volume of fluid method and the level set method. Both methods are well established and vibrant research areas. Recent extensions of level set methods produce sharp free surface characteristics by direct application to numerical simulations of turbulent breaking waves FLOW-3D Flow Science [2010]; Lv *et al.* [2010].

It is also common to use hybrid models. These span two or more of the set methods outlined above and, in this way, the programmer can tailor the method to the application, as shown in Aulisa *et al.* [2003] and Lv *et al.* [2010]. Williams *et al.* [2010] is an example of successful coupling between BEM theory and finite volumes (FV) and the underlying code has been used previously to track surfaces using VOF.

1.6 Experimental Investigations for Benchmark Validation

1.6.1 The Bahaj Turbine

It is important to validate any simulation with experimental data but, as tidal turbine simulation is a relatively new application, there are only a few suitable investigations considering TST's in experimental tanks and flumes, such as in de Jesus Henriques

et al. [2013], Afgan *et al.* [2012].

The Bahaj *et al.* [2007] paper details a tidal turbine, the experimental set up and presents two turbine performance result sets; conducted in a towing tank and in a cavitation tunnel. This investigation has become a useful validation benchmark for simulation routines of marine current turbines.

A test turbine with a 0.8m diameter, 0.16m diameter hub, is fully described by Bahaj *et al.* [2007] as well as the flow conditions and the dimensions of the experiment tank.

1.6.1.1 Pitch Angle Selection

For the first investigation in the towing tank, the blades are fixed-twist and variable-pitch, and five hub pitch angles are investigated. $\phi_{root} = 15^o$, $\phi_{root} = 20^o$ and $\phi_{root} = 25^o$ are considered, where ϕ_{root} is ϕ, as defined in Figure 2.1, for the blade root.

In these investigations, excessive tunnel blockage correction is avoided and the Reynolds number is kept high. Reynolds number affects the lift and drag coefficients and the cavitation characteristics of the rotor. A low Reynolds number can cause discrepancies when comparing the experimental data with simulations, as it degrades the dynamical properties of the rotor. The second investigation of the turbine in Bahaj *et al.* [2007] determines cavitation inception conditions.

The investigations were carried out in a tank or tunnel, therefore the wall boundaries will increase the power output of the turbine due to blockage effects. Bahaj *et al.* [2007] corrects for this by using a tidal turbine version of Glauert's blockage correction equations for a propeller. It was found that this correction decreases the power results by as much as 18% and the axial force results by 11%. By implementing the correction, the data is suitable to validate against unbounded, free stream flow turbine performance simulations, as in Chapter 2.

As well as a useful validation study, the first Bahaj *et al.* [2007] blade pitch investigation concludes that, for maximum energy absorption, TSR values between 5 and 7 and hub pitch angles of 20° are more suitable. As would be expected, where the incoming fluid flow is at an yaw angle to the rotor plane the power production is reduced. This is also the case if the turbine is moved closer to the surface of the water. When two turbines were placed close together no significant effect was seen, which

validates the proposition that turbines can sit in close proximity without reducing power production. The final finding of this investigation was that cavitation can be suppressed by carefully designing the blade angles and tip speeds.

The second investigation, detailed in Batten *et al.* [2008], is a continuation of the previously discussed paper, both are by the Sustainable Energy Research Group at the University of Southampton. A BEMT code is presented to model tidal turbines and to specifically investigate cavitation inception, the influence of the tidal velocity profile and the influence of blade drag which may develop over time due to roughness and fouling.

BEMT predicts the span-wise loadings but does not predict loadings in the chord-wise direction. Batten *et al.* [2008] uses the 2D panel method by XFOIL Subsonic Airfoil Development System to predict the chord-wise pressure. XFOIL Subsonic Airfoil Development System is a linear vorticity stream function panel method with a viscous solution that interacts with incompressible potential flows using a surface transpiration model. The lift and drag forces and pressure distribution predicted by this method were in good agreement with experiment, however the most noticeable difference being that the drag force is under estimated when approaching the stall angle. Beyond this angle, post stall predictions were made in Batten *et al.* [2008] using methodology by Viterna and Corrigan [1981].

The most significant result by Batten *et al.* [2008], is that cavitation is apparent on both sides of the blade. Therefore, when using turbine and aerofoil design to avoid cavitation, all areas of the turbine need to be considered as cavitation is found to occur on all surfaces. The same result has been found in other, similar studies.

Blade fouling was also simulated in Batten *et al.* [2008] by increasing the drag coefficient by up to 50%. This has little effect on the lift slope but does alter the stall angle. The power output is unaffected for $TSR < 4$ but at higher TSR values a $6 - 8\%$ decrease in power is seen. The effect of the tidal velocity profile shows that fluctuations in blade loadings are not insignificant and must be included in blade fatigue studies. It is suggested that a similar study is needed for nonlinear flows, such as waves, as presented some what in this thesis. This paper also suggests further studies into tidal turbine array interaction, as presented by Malki *et al.* [2011].

1.6.1.2 Pitch Control

Although the turbines described in Bahaj *et al.* [2007] and Batten *et al.* [2008] are fixed pitch, many devices utilise continuous pitch control to counteract variation in inflow angle due to operation in a shear profile or unsteady flow. Although this is a viable option for test devices, it is a more challenging solution for full scale, due to the increased complexity and inherent risk in the device design.

1.6.2 The Barltrop Turbine

An earlier study by Barltrop *et al.* [2006], details experimental data for a turbine operational in a wave/towing tank. This is the first example of experiment to describe tidal turbine response in a wave climate. The turbine is towed to simulate current flow at two different speeds in a prescribed wave climate of a single, regular incident wave. The bending moments around one blade root is recorded against time. The moment acting in the plane of the turbine swept area is referred to as the in-plane bending moment, M_y, and is mainly due to torque on the blade. The bending moment acting perpendicular to the turbine swept area is the out of plane bending moment, M_x, and is the axial force moment about the blade root. Due to the blockage effects of the tank, the regular wave can be considered non-linear and these results are the basis for validation of the non-linear, regular wave simulation, as presented in Section 4.15.

The turbine is towed at speeds between 0.3ms^{-1} and 1ms^{-1} into a single incident wavefront set at a consistent wave height of 150mm. The wave frequency is either set to 0.5Hz for long waves, or 1.0Hz for steep waves. The turbine rotational velocity is set to about 200rpm. Although the chord is dependent on blade position, the blade cross-sectional area shape is always the S814 aerofoil. The lift and drag coefficients for this aerofoil against fluid inflow angle is given in Figure 1.6.2. Further details of the experimental set up can be found in Barltrop *et al.* [2006].

The torque and axial force for the turbine, is used for different flow velocity investigations by Barltrop *et al.* [2006]. A good agreement is found between experimental results and a simulated BEMT based scheme with linear wave theory coupled with Equation 1.2, particularly for torque. The simulation is found to slightly underpredicts axial force however this difference is under 10% of experimental data.

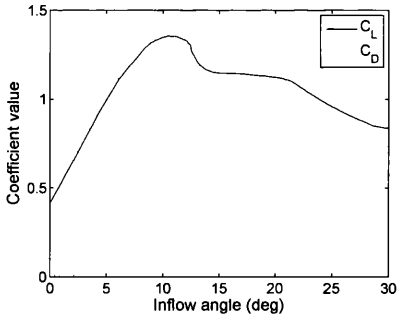

Figure 1.2: The lift and drag coefficients against incident angle of attack, relative to aerofoil, as used for S814 aerofoil shape. This data was sourced from wind tunnel tests, Barltrop *et al.* [2006].

This is a commonly found inaccuracy of BEMT based schemes in the high-induction are and can therefore be seen as an innate problem with BEMT.

By changing both incoming flow speed and rpm of the turbine, a further investigation is carried out by Barltrop *et al.* [2006] at a lower constant TSR of 2.34. In this instance, torque is reduced by the presence of waves. A sudden fluctuation in torque and axial force leads the author to suggest that the presence of waves has induced a stall of the turbine. If the incident flow velocity becomes very high, a stall control turbine will induce a stall to reduce the lift effect of the blades on the turbine. This keeps the power output at a maximum. However, from the cyclic nature of the fluctuation around the torque curve, it is more likely that the presence of waves is altering the incoming flow rate and the TSR is not constant in this investigation. This would give the exact effect that is presented of a cyclic deviation from the still water results. Therefore, the correct calculation of TSR is an important research area.

In Barltrop *et al.* [2006] the averaged axial force and torque are also plotted against wave height and it is shown that at lower frequencies the torque is particularly sensitive to wave height changes, especially between 0.02m and 0.115m. Changes in wave height are less effective at higher wave frequencies. It is shown, however, that at a high wave frequency, as wave height increases there is a steady increase in torque. Wave height seems to have little effect on mean axial force. These conclusions are true from the plotted results, however more simulated data points would give a complete understanding.

The investigations by Barltrop *et al.* [2006] consider the average axial force and torque acting on the rotor. By plotting the axial force and torque against time for different wave heights it is shown that they vary periodically with time, as expected in the presence of waves. Although the average axial force is unchanged by wave height, it is seen in Barltrop *et al.* [2006] that the peak axial force and torque increase with wave height. Doubling the wave height is shown, in some cases, to also double the axial force and is also capable of doubling the torque. This shows that wave effects are extremely significant when considering the maximum loadings sustained by a marine turbine.

The second paper by Barltrop *et al.* [2007] investigates the axial force and torque for a larger 0.4m diameter tidal turbine in the presence of controlled tide and wave. In a wave tank ($77 \times 4.6 \times 2.4$m deep) the wave height is prescribed and, to simulate tide, the turbine is towed close to the free surface at a constant velocity.

The results were calibrated by the amount of axial force and torque produced when a lump of mass with the weight of the rotor rotates at 7.5rpm. The lift and drag curves are based on wind tunnel tests at Reynolds number of 3×10^6, however for the Barltrop *et al.* [2007] investigations, Reynolds number ranges from 4.05×10^4 to 1.43×10^5. The full details of the experiment, including turbine measurements and aerofoil lift and drag curves and the definition of Reynolds number, are presented in Barltrop *et al.* [2007].

In Barltrop *et al.* [2007] it is shown that although the average axial force increases by only 2N from a 35mm to 126mm wave height, the maximum peak axial force is greatly increased. For example, increasing wave height from 84mm to 126mm nearly doubles peak axial force on the turbine. Similarly, increasing wave height from 35mm to 126mm increases the average torque by less than 0.1Nm, however the peak torque is greatly increased.

1.7 Literature Review Summary

This literature review has shown that the wave and turbulent effect on a device is a significant and active area or research as it has the potential to impact the power output and survivability of a tidal marine turbine. The marine energy industry in

the UK is at a crucial stage of prototype development and testing and there is a need for a simple and robust tidal performance simulation tool, such as BEMT to model turbine performance in site specific sea states and tides.

The current most popular BEMT based models are discussed as well as relevant papers and validations with experimental data. Two sets of recent experimental investigations of tidal turbines in wave flow are outlined in this chapter and are used in this thesis to validate the effective results from BEMT coupled with stream function wave theory.

BEMT gives a full simulation of the turbine performance within a fraction of the computational time needed for an alternative fully three-dimensional models, as summarised in this chapter.

As an alternative approach, more traditional CFD methods are presented. These methods have the disadvantage of being computationally time intensive and less robust but are widely used and accurately capture the complex movement of a free surface. Of these methods, VOF is the most popular for modelling ocean waves. However, literature has shown agreement between stream function wave theory and a VOF method for shallow water, small waves. As the wave amplitude increases and non-linear effects grow, there is less agreement between the two approaches.

Wave effects are a high-priority research area for many UK academics and companies. To progress the technology of tidal turbines, there is a need for the study of three-dimensional wave effects and turbulence. Also the complex interaction between waves and tidal flow must be well defined.

It is shown that the prediction of wave motion for a real sea surface is extremely complex and there are many different approaches to this problem for many varied applications. The seemingly random movement of the sea surface is site specific but typical wave patterns can be categorised into linear theory, non-linear stream function theory or irregular sea state spectra. It is advantageous for the wave implementation to be flexible and all such states are considered in this thesis. There are infinite possibilities for the wave climate and this must be reflected in a generic code whilst retaining the robust features of BEMT.

The objective of this research is to explore the applicability of a simple, analytical and widely used turbine design and simulation tool to TST's in time and spatially

varying inflow fields. Radially dependent aerofoil shape is considered. Blade root aerofoils typically have increased camber to make the root aerofoils able to restart the turbine after stall, as part of a stall control mechanism. The work also considers various BEMT compatible wave representations for both regular, non-linear and irregular wave states. The quality of the turbine performance results are analysed and it is found that the effect of waves on turbine power, torque and axial force can be successfully simulated. This allows developers to adapt and use the method with suggested wave and turbulent inflow and have a level of confidence in the results and their meaning.

The extension of a steady state theory to be used in time and spatially varying inflow is a key knowledge gap, as well as the compatible wave representations and BEMT high induction region representation.

Chapter 2 considers the theoretical basis of BEMT, in particular the high-induction region and the Prandtl BEMT correction for turbine blade tip loss is analysed.

Published experimental data are compared to the BEMT scheme to illustrate the effect of tip and hub losses on the simulated result as well as hub shadow and the high-induction correction. The experiment is also used to consider the change to the results, when a novel tip and hub loss expression is implemented and shown to agree well with experimental data.

This thesis extends the Swansea BEMT simulation model to include cavitation inception and high induction factor corrections for modelling of a tidal stream turbine. The cavitation results from the published experimental data are used to validate a cavitation prediction tool. Support structures are considered as well as turbine self weight buoyancy forces. Published experimental data is used to validate the self-weight buoyancy representation in the simulation.

However,the main theme of this work develops the incident flow field, beginning in Chapter 3. The incompatibilities between BEMT and time-varying inflow are identified and discussed. The theoretical implications of a time and spatially varying inflow field suggest an alternative approach to solve the BEMT simultaneous equations, presented in Chapter 4, which are shown to agree well with previous simulation results and experimental data.

Morison's equation is utilised in both models by Hassan and Ltd [2008] and by

Chapman [2009] to represent the force of the flow acceleration in BEMT. The Strouhal number is suggested by Hassan and Ltd [2008] as important in predicting excitation of the structure. The Keulegan-Carpenter number is adapted to measure the importance of wave disturbance in the flow in the axial direction parallel to the current and perpendicular to the current.

The results are analysed against the usual BEMT solution method. The difference between the two approaches is expected to increase as BEMT is more commonly employed to simulate tidal turbines in waves and turbulent flows.

Non-linear wave theory, Chaplin's stream function wave theory, has been previously coupled with a BEMT model. This wave theory is able to describe non-linear and linear, regular waves. This thesis presents the compatibility of transient inflow with the steady-state BEMT model and this work is also relevant to non-linear wave theory with BEMT. This thesis also considers complex wave and tide coupling to more accurately simulate the effects of tide on waves, and to a lesser extent, waves on tides.

Finally, this thesis describes these sea states and more flexible models and extends the use of sea states in BEMT based tidal turbine simulation tools. The compatibility is discussed and some results are presented in terms of turbine performance and compatibility with BEMT.

The effects of changing device design parameters, such as aerofoil, cross-sectional blade shape, blade pitch, blade twist, chord length and blade length are explored in this work and the main resource is characterised in axial direction, stream flow in m/s. Care must be taken when defining frane of reference, in particular when comparing different studies, as the magnitudes of these values is dependent on value frame of reference and units, which is inconsistent within literature. Blade pitch control is widely used for wind turbines to improve turbine efficiency over a range of flow speeds, however it is not common for tidal turbine to have variable pitch and this is therefore not considered in this thesis. Tower shadow acts to increase flow speed around the tower and decrease flow speed behind the tower, the reaction of the blade performance is heavily dependent on the design parameters and so is device specific.

Chapter 2

Blade Element Momentum Theory for Uniform Flow

2.1 Introduction

Blade Element Momentum Theory (BEMT) is a well-understood and popular method of modelling the performance of turbines and propellers. It is used extensively in the wind energy industry and can be adapted for tidal energy turbines, with some vital considerations. It consists of two complamenting theories, one-dimensional momentum theory with rotational momentum and blade element theory. It provides a steady-state and analytical derivation of the turbine performance characteristics. The robustness and flexibility of the analytical scheme together with the fast computational advancement, deem it suitable and computationally inexpensive to run on a single processor. These qualities support BEMT as a useful industry tool that will predict the power output and loadings of an existing turbine. Alternatively, BEMT can be used at the turbine design stage to positively influence the design performance for a relatively low cost, compared to traditional experimental testing.

In Section 2.2 to Section 2.6, the theory of BEMT as well as the theoretical derivation and implementation are discussed from first principles. The primary assumptions of momentum theory and the most prevalent methods used to correct for these assumptions are presented. For each method, the validity is investigated, particularly for the tidal turbine case. The significance of the corrections on the turbine perfor-

mance result is also explored in Section 2.7 by comparison with published turbine data.

The tip loss correction as derived by Prandtl is presented in Section 2.4 and shown to be compatible with BEMT as well as the derivation and implementation. This correction is usually adapted to also represent root losses, however the theoretical implications of this adaptation are challenged, particularly for the case of tidal turbines and propellers. A hub shadow theory is presented in Section 2.5.1 as an alternative explanation of performance deterioration at the blade root. It is compared against the root loss method for turbine performance, by comparison of the results with the published turbine data set in Section 2.7.

Section 2.6 considers the validity of the momentum theory in the high-induction region. A cubic high-induction dependence of the axial force coefficient, C_{fa}, on the axial induction factor, a, is presented as an alternative to the quadratic dependency of C_{fa} on a. The differences are highlighted by comparison with the published data set in Section 2.7.

A further comparison study is presented in Section 2.7. The final BEMT scheme used within this document is considered against another BEMT based scheme and also against an unverified alternate loss implementation scheme, as presented in Section 2.9. Although the final BEMT scheme used in further chapters is as presented, the BEMT scheme in Section 2.9 gives and improved result and verification of this scheme is suggested as further work.

BEMT is steady state, therefore the relative velocity at each blade on a set radial annulus is the same in both space and time. This limits the BEMT method to flow that is uniform over the rotor plane nd quasi-steady in time. For realistic flows, this onset velocity will vary spatially over the rotor plane and may vary rapidly with time.

2.2 Blade Element Theory

Blade element theory was initially proposed to model the propellers of ships but has since been adapted to model wind turbines, helicopters and, more recently, marine turbines. It is now a well established method to determine rotor fluid dynamics. The turbine blades are partitioned along their lengths into elements. In Burton *et al.*

[2001] each element is assumed to be a two-dimensional aerofoil which suggests that the lift and drag characteristics of each aerofoil can be summed in such a way to give the loadings on the whole blade and therefore the whole rotor. The lift and drag coefficients are defined in the usual way, as in Griffiths and Woolard [1978],

$$C_L = \frac{dL}{N\frac{1}{2}\rho|\vec{V}|^2 cdr}, \qquad C_D = \frac{dD}{N\frac{1}{2}\rho|\vec{V}|^2 cdr} \tag{2.1}$$

with $\vec{V}$ as the incident velocity in the blade element frame of reference, shown in Figure 2.1. The axial component is always considered perpendicular to the swept area of the blades. The tangential component is always considered parallel to the swept area of the blades and perpendicular to the blade length. Therefore, when observing squarely the swept area of the blades, a blade positioned vertically above the hub will impose a tangential component of opposite sign to a blade positioned directly below the hub. The axial velocity component will have the same direction for the two locations. The physical rotation of the blades will create a tangential velocity in the aerofoil section frame of reference of $r\Omega$, considering a turbine rotational velocity of $-\Omega$.

Glauert [1934] states that the element behaves as a two dimensional aerofoil only if $\vec{V}$ also accounts for the induced velocity, $\vec{W}$, which forms the system of trailing vortices in the wake. The presence of a turbine creates a helical vortex system. The trailing vortices propagate in the form of a multi-start helix as described in Section 2.4. This causes a drop in circulation around the blade at the hub and tip. Griffiths and Woolard [1978] takes the usual BEMT approach of complementing momentum theory with blade element theory to specify two sets of axial force and torque simultaneous equations. A simple iterative search loop method is suggested to satisfy these simultaneous equations. Chapman [2009] and Masters *et al.* [January 2011] discuss the main difficulties with this approach.

Also, in Griffiths and Woolard [1978], the high-induction, BEMT breakdown region is not considered therefore a solution cannot be found in this region. $\vec{V}$ must therefore comprise of $\vec{W}$, and the innate axial and tangential velocities, $\vec{U}$.

$$\vec{V} = \vec{U} + \vec{W} = \begin{Bmatrix} U \\ r\Omega \end{Bmatrix} + \begin{Bmatrix} -Ua \\ r\Omega b \end{Bmatrix} \tag{2.2}$$

$$|\vec{V}| = \left((U(1-a))^2 + (\Omega r(1+b))^2\right)^{1/2} \tag{2.3}$$

where a and b are defined as the axial and tangential induction factors and are a measure of the change in axial velocity and the tangential velocity of the flow due to the presence of the turbine. The values of these factors prescribe the wake flow regime. Substituting $\vec{V}$ into Equation (2.1), axial thrust and resultant torque for a particular element can be deduced from the lift and drag coefficients, C_L and C_D respectively. The axial and tangential direction respectively, C_n and C_t are defined as the resolved lift and drag forces in the axial direction and tangential directions.

The total axial force of the turbine is then the elemental axial force integrated along an individual blade and one full revolution. In a similar manner, the total torque, which is the product of the torque force and the radial position of the foil, is integrated over the blade length and one revolution. These formulations are also outlined in Griffiths and Woolard [1978]; Masters *et al.* [January 2011] and reproduced here for completeness.

$$dF_{a1} = N\frac{1}{2}\rho|\vec{V}|^2 c C_n dr = N\frac{1}{2}\rho|\vec{V}|^2 c(C_L(\varphi)sin\phi + C_D(\varphi)cos\phi)dr \tag{2.4}$$

$$dT_1 = N\frac{1}{2}\rho|\vec{V}|^2 r C_t dr = N\frac{1}{2}\rho|\vec{V}|^2 cr(C_L(\varphi)cos\phi - C_D(\varphi)sin\phi)dr \tag{2.5}$$

Considering a specific blade element, the chosen aerofoil contour will dictate the lift and the drag coefficient, C_L and C_D respectively, dependency on the incident velocity angle of attack, φ. This angle is deduced from $\vec{V}$ and the specific C_L and C_D for the instantaneous flow regime are interpolated from lookup tables. Reynolds number does effect C_L and C_D and this effect is considered in the look up table selection. Turbulence will also affect C_L and C_D. This effect is significant and is considered by Togneri *et al.* [2011].

This section considers transient in flow for BEMT without turbulent effects. When defining inflow velocity angle there are two frame of references to consider in BEMT that are not to be confused. φ is the inflow angle incident on the aerofoil section with respect to the chord, as used in the look up tables. For example, if φ is zero, the incident velocity is parallel to the chord length moving towards the aerofoil tip.

The second definition of inflow angle, ϕ, is defined with respect to the turbine axial direction, as in Figure 2.1. ϕ is the angle used in Equation (2.4) and (2.5) to resolve the forces into the axial and tangential directions. The static twist of a blade for a TST is the angle between the horizontal axial direction and the pitch of the root blade element and is therefore equal to $\varphi + \phi$ in this figure.

This method alone cannot describe the performance of a turbine with any accuracy as there are two equations with four unknowns, namely dF_a, dT, a and b. In the following section, a and b are alternatively derived using momentum theory. Therefore, the effective velocity of the blade element theory is found and so the forces on the turbine can be determined.

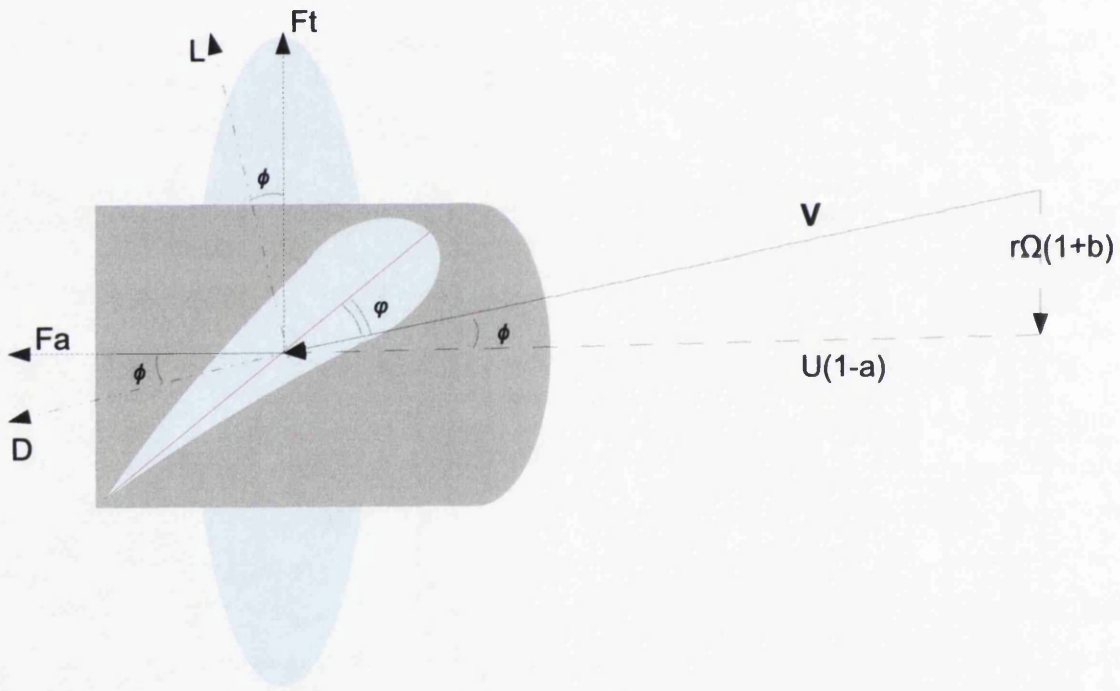

Figure 2.1: Blade orientation with incident flow direction right to left. Axial force $dF_a = dL\sin\phi + dD\cos\phi$ and torque force $dT = dL\cos\phi - dD\sin\phi$ directions shown.

2.3 Momentum Theory

One-dimensional momentum theory with rotational momentum is employed to model the turbine as a frictionless, permeable, actuator disc in a control flow stream bounded by a stream tube and can also be found in Masters *et al.* [January 2011] and Griffiths 1974]. It was first derived as a way of calculating $\vec{V}$, needed in blade element theory, as discussed in Section 2.2. However, unlike blade element momentum theory, it considers the rotor as a whole and uses the azimuthally and radially averaged $\overline{a}$ and $\overline{b}$. This creates theoretical inconsistency which significantly affects the results of the scheme, corrections to which are discussed in Sections 2.4 and 2.6 and analysed in Section 2.7.

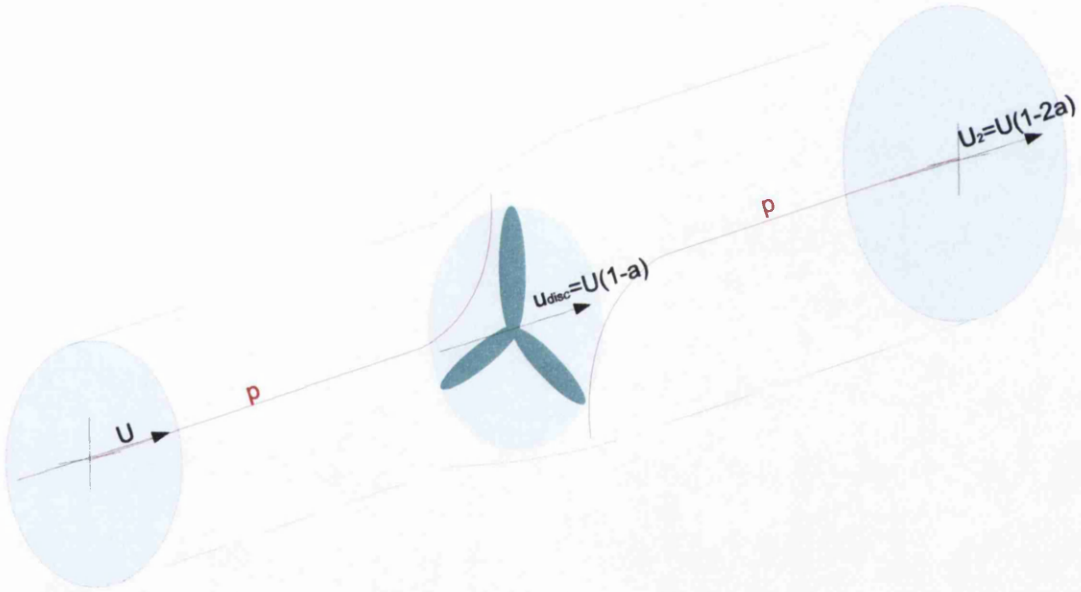

Figure 2.2: Momentum theory illustration. Qualitative pressure gradient(illustrated in red) and velocity values far upstream, at the rotor and far downstream, as given by Burton *et al.* [2001].

Figure 2.2 gives a qualitative illustration of the pressure profile through the stream tube of the swept area of the turbine, which is now considered an actuator disc. This disc exerts a drag on the flow and the axial force, F_a, is the reaction force to this drag. It is found by assuming the disc does not create a rotation of the flow and using Bernoulli's Equation to compare the pressure profile in the areas before and after the rotor separately, Equations (2.6) and (2.7).

Considering Figure 2.2, there is an area of high pressure directly before the disc, which also affects an expansion of the stream tube, and there is an area of low pressure directly after the disc. Considering the axial velocity and the pressure at the disc (upstream and downstream) as u_{disc} and p_{Udisc}, p_{Ddisc} respectively, and setting the far upstream axial velocity to U and the far downstream axial velocity to U_2, then Bernoulli's Equation gives,

$$p_\infty + \frac{1}{2}\rho U^2 = p_{Udisc} + \frac{1}{2}\rho u_{disc}^2 \tag{2.6}$$

$$p_\infty + \frac{1}{2}\rho U_2^2 = p_{Ddisc} + \frac{1}{2}\rho u_{disc}^2 \tag{2.7}$$

The axial force is related to the pressure difference over the disc and so Equations (2.6) and (2.7) can be combined to give,

$$F_a = A_{disc}\triangle p = A_{disc}\frac{1}{2}\rho(U^2 - U_2^2) \tag{2.8}$$

Also noting that F_a represents the change in momentum flux,

$$A_{disc}\frac{1}{2}\rho\left(U^2 - U_2^2\right) = \dot{m}(U - U_2) \tag{2.9}$$

where $\dot{m}$ is conserved as the mass flow rate. Considering this value at the disc, gives u_{disc} as the average of the upstream and downstream speeds. By setting the averaged axial induction factor as $\overline{a} = \frac{U - u_{disc}}{U}$,

$$F_a = A_{disc}\frac{1}{2}\rho U^2 4\overline{a}(1 - \overline{a}) \tag{2.10}$$

The turbine power is therefore found as,

$$P = F_a u_{disc} = A_{disc}\frac{1}{2}\rho U^3 4\overline{a}(1-\overline{a})^2 \tag{2.11}$$

Some energy loss from the axial flow is converted into a small rotation of the stream tube, not yet considered by momentum theory. To introduce rotational effects, the stream tube is divided into annular sections. In this way the elemental flux is the product of the pressure difference over the turbine and the area of the annulus.

$$dT = dA_{disc}\rho U_1 \omega r^2 \tag{2.12}$$

where ω is the rotational velocity of the flow in the wake and is assumed a constant. By substituting for U_1 and dA_{disc} and setting $\overline{b} = \omega/2\Omega$ where $-\Omega$ is the corresponding rotational velocity of the rotor,

$$dT = \left(4bU(1-\overline{a})\rho\Omega\right)\pi r^3 dr \tag{2.13}$$

Converting Equation (2.10) to the annular form, the rotational torque and also the axial force produced by an annulus of a rotor can be written in terms of $\overline{a}$ and $\overline{b}$.

$$dF_{a2} = 4\pi r\rho U^2\overline{a}(1-\overline{a})dr \tag{2.14}$$

$$dT_2 = 4\overline{b}\left(1-\overline{a}\right)\rho \mathrm{U}\Omega r^3\pi dr \tag{2.15}$$

Physically, this theory says that considering a non-rotational, constant, far upstream, axial inflow velocity of U, a respective constant, far downstream, axial velocity of $U(1-2\overline{a})$ is created in the wake. It is assumed that half of the total loss of energy occurs before the turbine, and the other half occurs after suggesting that $u_{disc} = U(1-\overline{a})$, as shown in Figure 2.2. The wake rotational velocity of $r\omega = r\Omega 2\overline{b}$ is also considered constant and has the opposite sign convention to the rotation of the blades. Unlike the axial velocity, all the rotational velocity is imparted on the flow regime instantaneously at the actuator disc.

Alternatively, considering the actuator disc does have a small width, it is assumed that the rotational velocity is imparted on the flow equally across this width. This way, the rotational velocity at the actuator disc can be taken as the mid-width value of $r\Omega\bar{b}$. In addition, the physical blade rotation with angular velocity $-\Omega$ will induce an equally and opposite rotation in the flow of velocity $r\Omega$, giving the total rotational velocity at the actuator disc as $r\Omega(1+b)$.

By no coincidence, these velocity values draw parallels with $\vec{V}$ of Section 2.2 with a slight difference in the definition of a or $\bar{a}$ and b or $\bar{b}$. By considering these complementing theories of blade element theory and momentum theory together, there are now two sets of equations; (2.4),(2.5) and (2.15),(2.14) and four unknowns, a (or $\bar{a}$), b (or $\bar{b}$), dF_a and dT. Complete BEMT therefore provides a sufficient number of equations for a closed system and the axial force and torque of the turbine can be deduced after solving for the values of a and b.

2.4 Tip and Root Corrections

Before momentum theory can be combined with blade element theory effectively, the inconsistency between the two theories of a, b and $\bar{a}$, $\bar{b}$ must be resolved. the $\bar{a}$ and $\bar{b}$ of momentum theory does not account for circulation of flow around the aerofoil contours and therefore is solving for an infinite number of infinitely long blades that meet at a singularity at the centre of rotation. This inaccurate assumption leads to a significant overprediction in turbine power output, illustrated in Figure 2.7(a), suggesting a need for tip and root corrections.

The subsequent loss of aerodynamic efficiency gives a more physical result and reduces power production. As water is denser than air, tidal stream turbines are subjected to more load per unit blade length when compared to wind turbines. The increased loading dictates shorter blades and therefore tidal stream turbines less resemble the infinite length blades assumed by momentum theory thus loss correction is a vital consideration for a tidal stream turbine BEMT method.

Considering the turbine blade cross-section as a 2D aerofoil, as in blade element theory, Glauert [1934] states that the lift is directly dependent on the circulation of flow around the aerofoil contours. This circulation creates a vortex line along the

whole blade length and bound to the blade surface. Vortex theory states that the vortex line cannot appear or disappear, assuming a frictionless fluid. At the blade extremities, the vortex line separates from the blade surface and therefore a free vortex is shed into the wake at the blade tip.

If the effective blade root does not connect directly to the hub, as for a common horizontal axis wind turbine, then a helical vortex system propagates into the wake from the root in a similar way to the tip, this is the case considered in Burton *et al.* [2001].

If the effective root connects directly to the hub, as for propellers and common tidal turbines, the vortex line continues onto the nacelle and separates from the nacelle. In this case, a straight line vortex is shed from the hub as described by Glauert [1934]. The vortex lines will propagate with the local flow velocity, $\vec{V}$, as already defined in Section 2.2, and will trace a helix in the wake.

The exact solution of the effect of tip and hub vortices on turbine power can be calculated and is considered in Glauert [1934] but is complex and not compatible with BEMT. Therefore a simple approximation is suggested by Prandtl in Glauert [1934].

It is postulated that, as the vortex system prescribes the wake it is a component of the effect of the turbines presence on the innate flow regime. This effect is the basis of momentum theory therefore the shape and intensity of the vortex system can be used to approximately describe the losses of momentum theory due to the radial flow created by the trailing vortex lines at the tip and the root. This approximation is BEMT compatible and commonly employed to represent the effect of tip and hub vortices. In Glauert [1934] it is shown that this approximation compares well to the exact solution.

2.4.1 The Prandtl Tip Loss Function

The local axial induction factor used in blade element theory, a, is not radially uniform and will be high at the tip due to the significant effect of the tip vortex. Momentum theory utilises the averaged axial and tangential induction factors, $\overline{a}, \overline{b}$, which remain constant over the radius. To use blade element and momentum theory consistently, $\overline{a}$ and $\overline{b}$ must be substituted in the momentum equation by the functions F_a and F_b, which are the local axial and tangential induction factors affected by the vortex

system radial flow that creates tip and hub losses.

The previous description of the vortex formation assumes a constant circulation along the blade length. This is physically unlikely therefore Glauert [1934] considers a radially dependent circulation, which implies a vortex is shed from the whole length of the trailing edge of each blade. Due to the rotational path of the blades, a helical wake vortex is shed and, instead of vortex lines, vortex sheets propagate into the wake in the form of a screw surface. The wake is now considered to consist of these surfaces and the fluid in between them, as in Figure 2.3.

Prandtl suggests that the shed vortex sheets are impermeable and can therefore be considered as material sheets moving axially with the speed of the fully developed wake far downstream, $U(1-2\overline{a})$, and no radial flow occurs on the sheet surfaces in the wake. The sheet propagation velocity at the turbine location is therefore $U(1-\overline{a})$, and so no losses are needed on the sheet surfaces. The sheets are assumed to be separated by the normal distance between vortex sheets, $d = \frac{2\pi R_w cos\phi}{N}$, derived in Section 2.4.4.

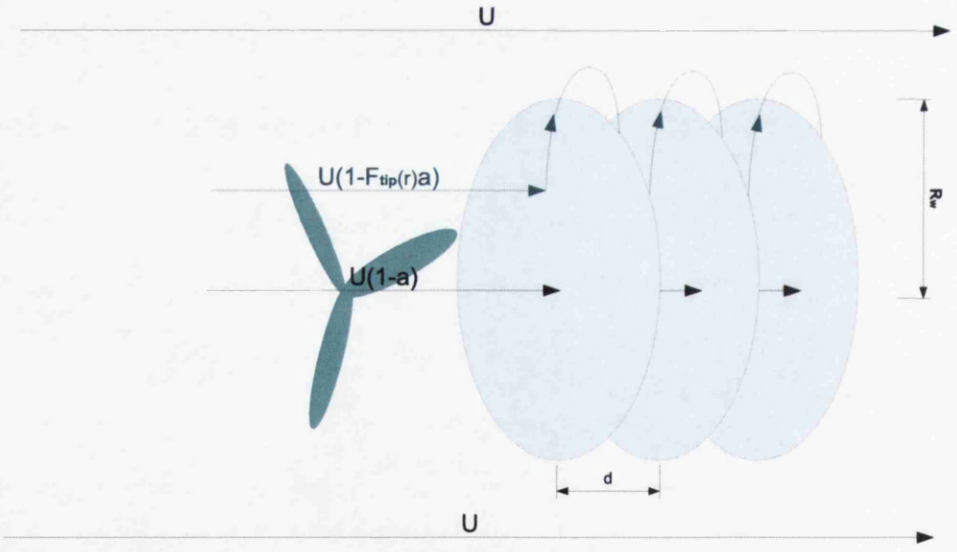

Figure 2.3: Qualitative schematic of Prandtl theoretical formulation of tip losses.

2. BLADE ELEMENT MOMENTUM THEORY

Momentum theory assumes that no flow mixing occurs between the stream tube and the outside flow. However, Prandtl suggests the presence of the vortex sheets with circulation around the edge causes the outside flow to weave radially in-between the vortex sheets in the wake, which will cause some wake flow to also propagate radially. This loss in wake flow increases the local axial velocity to a value between $U(1-\overline{a})$ and U. The relatively quick moving axial flow at a distance r from the centre cannot permeate the vortex sheets in the wake. Therefore the flow can be thought of as weaving in and out of the gaps between discs. The sheet propagation velocity of $U(1-\overline{a})$ is now a minimum value and the velocity of the flow at a distance r from the centre can be expressed as $U(1-F_{tip}(r)a)$. The effect of $F_{tip}(r)$ diminishes as r decreases and is unity at the centre of the rotor where no tip loss effects are felt and $a=\overline{a}$.

At the blade element, the total decrease in axial velocity due to the turbine presence of $U-U(1-2a)=2aU$ is only true on the vortex sheets and is considered the maximum decrease in axial velocity. The average decrease in axial velocity is now a fraction of this velocity $2FaU=2\overline{a}U$. As a result, Burton *et al.* [2001] directly replaces $\overline{a}$ with Fa in the momentum theory equations. It is postulated by Burton *et al.* [2001] that the tangential induction factor is corrected in the same manner, $\overline{b}=Fb$. The tip loss factor is defined by Prandtl as,

$$F_{Tip}=\frac{2}{\pi}\cos^{-1}[\exp-\left\{\frac{(N/2)[(R-r)]}{R\cos\phi_{Tip}}\right\}] \tag{2.16}$$

where ϕ_{Tip} is the inflow angle relative to the axial direction, Figure 2.1, at the tip. Theoretical derivation of this equation is given in more detail in Section 2.4.4. Glauert [1934] considers $R\cos\phi_{Tip}\simeq r\cos\phi_r$ as a simplification to Equation (2.16) and this is commonly implemented in modern BEMT schemes. However, this correction is now redundant as, by solving for the tip element first, the original expression of $R\cos\phi$ can be directly used in F_{Tip} for all elements thereafter.

2.4.2 Blade Element Momentum Theory Loss Implementation

The $\overline{a}$ and $\overline{b}$ of momentum theory are thus corrected for vortex losses to the order of approximation, as given in Equations (2.19) and (2.20). Therefore the complementing theories of blade element theory and momentum theory can now be combined together, using the least squares method, into the optimisation function g with the local a and b as the independent variables.

For a steady-state, fixed-flow condition, g is determined for each individual blade element and if $g = 0$ blade element theory and momentum theory produce the same axial force and torque and it is assumed they have converged on a solution.

For each blade element, the error indicator, g, is minimised and a low-value upper limit for g is set, above which an element is assumed not converged. By summing all the blade elements on the turbine the whole axial force and torque is deduced and therefore the steady-state performance of the turbine is successfully calculated. Masters *et al.* [January 2011] shows how this method only works well for small incident aerofoil angles, ϕ, onto the blade element and appropriate estimate starting values of a and b to input into the optimisation function.

The optimisation function employs sequential quadratic programming in the MatLab `fmincon` function to minimise g in the non-linear optimisation problem to obtain the blade element value for axial force and torque. Chapman [2009] shows how this improves the robustness of the routine, compared to a simple line search. It is also shown by Chapman [2009] that the routine has a low computational demand but has difficulties converging, particularly in cases with high tangential induction or multiple local minima of the error indicator, g.

The introduction of a Monte-Carlo Method, to increase the quality of the initial values of a and b improves the number of converged blade elements and therefore the validity of the solution. The Monte-Carlo Method begins with a large number of random solutions for a and b and the best result from this set is chosen as a starting pair of values for the iterative procedure, thus reducing the chance of convergence on a local minimum only. The overall rise in computational time is minimal as it subsequently reduces the convergence time penalty. This Monte-Carlo scheme is run for the very first iteration step, or for any elements not converged.

2. BLADE ELEMENT MOMENTUM THEORY

Consider the solution values of the axial and rotational induction factors as $a_{i,e}$ and $b_{i,e}$ for an individual blade element, e. Now consider a small change in the steady-state, as would occur when iterating, for example, a set increasing time, tip speed ratio or rotation position. It is assumed that the solution values for this new steady-state, $a_{i+1,e}$ and $b_{i+1,e}$, for blade element e will also change by a small amount. In this manner, the Monte-Carlo starting value scheme is not needed beyond the first iterative step, as $a_{i,:}$ and $b_{i,:}$ are used as the starting values in the transient iteration loop $i+1$. If a solution is not found then the scheme reverts back to Monte-Carlo or the change that occurs on the iterative step is reduced.

The iterative scheme continues and therefore the steady-state BEMT method can be used to solve dynamic inflow problems using small time iterations. Using TSR iterations gives the power and axial force profile with TSR which is the usual way to consider the performance of a turbine. Steady-state, iterative TSR, study results are presented in the figures of Section 2.7 to compare with the experimental data of Bahaj *et al.* [2007] and to illustrate the effect of the BEMT corrections. Further dynamic inflow, time iterative results are presented to illustrate wave effects.

$$dF_{a1} = N\frac{1}{2}\rho|\vec{V}|^2 c(C_L(\varphi)sin\phi + C_D(\varphi)cos\phi)dr \tag{2.17}$$

$$dT_1 = N\frac{1}{2}\rho|\vec{V}|^2 cr(C_L(\varphi)cos\phi - C_D(\varphi)sin\phi)dr \tag{2.18}$$

$$dF_{a2} = 4\pi r\rho U^2 a(1-a)F_{Tip}dr \tag{2.19}$$

$$dT_2 = 4b\,(1-a)\,F_{Tip}\rho \mathrm{U}\Omega r^3\pi dr \tag{2.20}$$

$$\begin{aligned} g &= (dF_{a1} - dF_{a2})^2 + (dT_1 - dT_2)^2 \\ g &= \left(N\tfrac{1}{2}|\vec{V}|^2 c(C_L sin\phi + C_D cos\phi) - 4\pi r U^2 a F_{Tip}(1-a)\right)^2 \\ &\quad + \left(N\tfrac{1}{2}\rho|\vec{V}|^2 c(C_L cos\phi - C_D sin\phi) - 4(F_{Tip}b(1-a)\rho U\Omega r^2\pi\right)^2 \end{aligned} \tag{2.21}$$

This method of including F_{Tip} in Equations (2.19) and (2.20) is commonly applied,

as in Bahaj *et al.* [2007], and is used in this research. In Shen *et al.* [2005] it is stated that this approach creates an inconsistency at the wake boundary; $r = R$ and $F_{Tip} = 0$, forcing $\vec{V} \to 0$ at the blade tip. As the vortex lines at the tip propagate into the wake, $\vec{V}$ cannot be 0 at the tip. In Shen *et al.* [2005] further corrections to F_{Tip} to counteract this inconsistency are evaluated. However, this inconsistency is a consequence of a simplification by Glauert [1934] and so provides no representation of the physical situation.

Now that the variables a and b are determined, by minimising g, for each blade element; the torque and axial force, T and F_a are found for the whole turbine by summing over the radius, r, and number of blades, n. The turbine performance coefficients are determined from these values in the usual way, the equations in (2.22). The values of these coefficients are determined at each iterative TSR step and plotted against TSR to produce the figures in Section 2.7.

$$\begin{aligned} C_p &= \frac{\Omega \sum_{n=1}^{n=N} \sum_{r=1}^{r=R} (T(n,r))}{\frac{1}{2}\rho\pi R^2 {u_{hub}}^3} \\ C_t &= \frac{\sum_{n=1}^{n=N} \sum_{r=1}^{r=R} (T(n,r))}{\frac{1}{2}\rho\pi R^3 {u_{hub}}^2} \\ C_{fa} &= \frac{F_a}{\frac{1}{2}\rho\pi R^2 {u_{hub}}^2} \end{aligned} \tag{2.22}$$

When using this theory for turbine losses the original application of propeller blades must be considered. The wake of a turbine is propagating more slowly than the surrounding flow, whereas the wake of the propeller, as outlined by Glauert [1934], is considered to be moving more quickly. The flow circulation around the 2D aerofoil blade sections is the same for propellers and tidal turbines. Therefore, for propellers, the circulation of flow around the edges of the vortex sheets has the same axial direction as the surrounding flow, in the wake frame of reference. For turbines the axial flow is now in the opposite direction and so opposes the circulating flow. This effect has not been quantified and will act to decrease the losses. The Prandtl approximation is still applicable to tidal stream turbines but must be considered as a conservative correction.

2.4.3 Adaptation to Hub Losses

Depending on the blade design a vortex is also shed either from the hub of the rotor or from the blade root itself and both are defined here as F_{Hub} for ease. It is common to adapt the tip loss factor of Prandtl to account for these losses in a similar manner.

In Burton *et al.* [2001] the effective aerofoil at the blade root is assumed to be detached from the hub nacelle, a reasonable assumption for wind turbines. The flow velocity between the hub and the blade root is considered to be the free stream velocity, although it may be larger than the free stream velocity due to blockage effects. As the blade root is not attached to the nacelle, a root vortex is shed from each blade. The root loss is characterised by the movement of the free stream flow in-between the wake vortex sheets, which are now considered the wake vortex annuli. However, in this case, the effect of $F_{Hub}(r)$ is greatest at the lowest radius of effective blade, i.e. the blade root $r = R_{Root}$, and must decrease towards wake edge. The point at which $F_{Hub}(r)$ reaches unity is arbitrarily chosen as $r = 2R_{Root}$. The remaining formulation of F_{Hub} is similar to F_{Tip} and these losses are easily combined into one correction F which replaces F_{Tip} in the optimiser objective function of Equation (2.21). However, the effective root aerofoil of a tidal stream turbine is commonly attached to the hub nacelle and the vortex line remains attached to the surface of the nacelle and combines with the other blade root vortices into a line vortex, shed from the hub, Burton *et al.* [2001].

$$F_{Hub} = \frac{2}{\pi} cos^{-1}[exp - \left\{ \frac{(N/2)[r - R_{Root}]}{(R_{Root})sin\varphi} \right\}] \tag{2.23}$$

$$F = F_{Hub} F_{Tip} \tag{2.24}$$

2.4.4 Theoretical Derivation

Tip loss was derived by Prandtl by considering the radial mixing of flow in the wake created by the vortex sheets. The wake vortex sheets are assumed to be impermeable discs and the flow velocity outside the wake stream tube is assumed the free stream velocity. Figure 2.4 illustrates the unfurled wake stream tube surface with the blue lines representing the vortex sheet positions. The wake stream tube radius is assumed

to be the turbine radius and the known local wake flow angle θ_w is $\theta_w = pi/2 - \phi_{Tip}$. This leads to the expression given in Equation (2.25) for the distance between vortex sheets, d, shown in Figure 2.4.

If d is large, the sheets are wide apart and the free stream flow can weave in-between reducing performance and increasing tip losses which implies $F_{Tip} < 1$. If d reduces, the sheets are closer to each other, the free stream flow radial permeation reduces and tip losses are less which increases F towards 1. It follows that F_{Tip} increases with $1/d$.

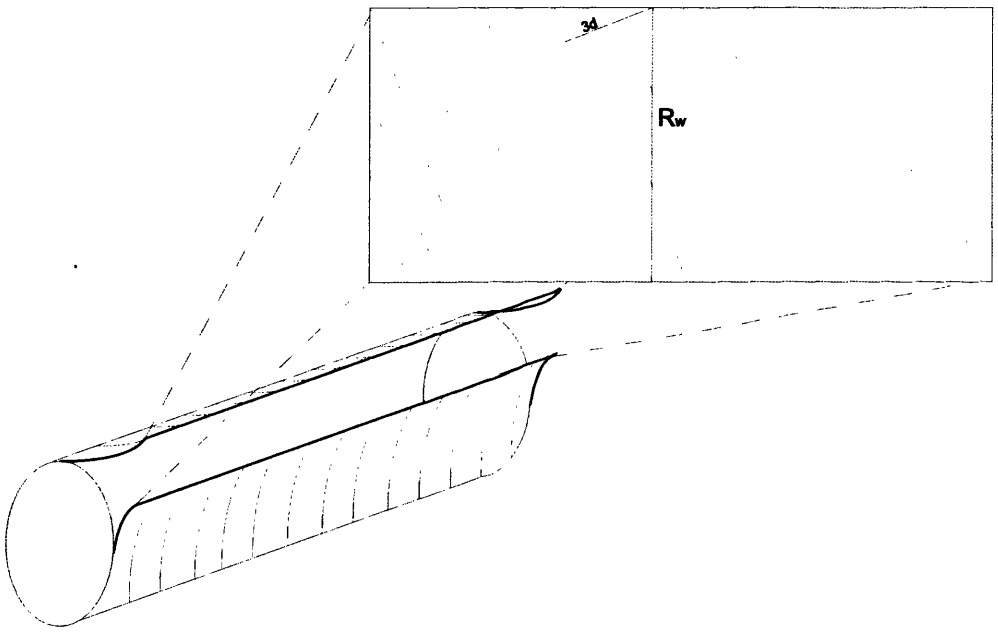

Figure 2.4: Wake vortex sheet edge marking on unfurled stream tube for a 3 bladed turbine.

$$d = \frac{2\pi R}{N} \sin\theta_w \tag{2.25}$$

where,

$$\sin\theta_w = \cos\phi_{Tip} = \cos\left(\arctan\left(\frac{r\Omega(1+b)}{U_\infty(1-a)}\right)\right) \tag{2.26}$$

At low TSR, the local inflow direction is similar to the axial direction, θ_w is large and tip losses are high as the distance between vortex sheets is large. As TSR increases θ_w is small, reducing the distance between the vortex sheets and also tip loss. Equation (2.27) shows that the formulation by Prandtl satisfies the relationship $F_{Tip} \propto 1/d$ and causes $F_{Tip} = 1$ at $r = 0$ and $F_{Tip} = 0$ at $r = R$.

$$F_{Tip} = \frac{2}{\pi}\cos^{-1}[\exp - \left\{\frac{\pi[(R-r)]}{d}\right\}] \tag{2.27}$$

2.5 The Problem with a Prandtl Root Loss Function

In Section 2.4.3, this formulation is extended to also represent root loss; as a vortex line is present at the blade root as well as the blade tip. Prandtl assumes a similar process occurs, and that between the blade root and the axis of rotation the flow velocity is U; the same as the flow velocity outside the stream tube. Therefore, instead of a wake vortex stream tube with a circular cross-section, a stream tube of annular cross section is considered. In a similar manner to tip loss, the hub loss is due to radial flow created in the stream tube due to the mixing of the central flow U in-between the annular vortex sheets.

This formulation can only be applicable when the innate free stream flow is present at $r < R_{root}$, that is, the effective blade root of the turbine is not connected to the hub nacelle, such as on a common wind turbine.

However, the effective blade root of a tidal stream turbine is usually designed to connect directly to the hub. Therefore the vortex line may remain on the surface of the hub nacelle. This will create a single shed vortex from the hub in a similar way to propellers, as described in Glauert [1934]. Therefore the Prandtl formulation for hub loss can no longer be valid as the radius of the centre of the annular stream tube reduces to 0 and so no radial flow is induced as no mixing will occur.

However, the close proximity of the blades to the hub nacelle suggests that the flow regime at the blade elements may be affected by the hub, which also will cause a reduced performance at the root blade elements. In Section 2.5.1, an alternative hub shadow is presented and in Section 2.7, it is shown to produce a similar turbine

performance result to the Prandtl hub loss formulation on tidal stream turbines. Due to the proximity of the blade root to the hub, this effect may be a more suitable correction to consider rather than the Prandtl hub loss formulation in the case of fixed pitch tidal stream turbines. However, when the effective blade root does not connect directly with the hub nacelle, as with common wind turbine design and some variable pitch tidal stream turbines, the Prandtl hub loss is a more theoretically suitable.

2.5.1 Hub Shadow

The root loss described in Section 2.4.3 physically accounts for the radial flow created in the wake at low r, as the flow occupying the centre, but not a part, of the annulus stream tube mixes with the flow in the annulus stream tube. It is suggested that this is unphysical for tidal stream turbines and propellers as it is common for the blade root to be in close proximity, or attached, to the hub structure. This section outlines a hub shadow correction to the surrounding inflow velocity vectors and, in Section 2.7, this approach is shown to result in a similar effect on the performance of the turbine.

The effect of the tower structure on the surrounding velocity flow field has already been successfully implemented in the BEMT scheme by Chapman [2009] and a working example of the results is given in the studies in Volume 2 of this thesis. Parallels can be drawn between the tower structure and the hub structure considering only a change in geometrical shape. The tower effect on BEMT is therefore analysed and adapted to represent a hub structure instead of a tower structure.

The method combines a near field solution from potential flow theory with a far field solution for the wake effect and is based on the AeroDyn manual and work by, where it is validated against CFD results, Moriarty and Hansen [January 2005]. When considering the tower, a base flow field solution around a cylinder is combined with the downstream wake solution which is dependent on a tower drag coefficient, C_{Tower}. The model also considers the blockage effect of an increase in axial and cross-stream flow velocity around the sides of the tower.

If x is the horizontal flow direction, y is the horizontal cross-stream direction and z is the vertical direction (all normalised by the tower radius) then the effected stream

flow and cross-stream velocities U_{Tower}, V_{Tower}, are given as,

$$U_{Tower} = uU_\infty = \left(1 - \frac{x^2 - y^2}{(x^2+y^2)^2} + \frac{C_{Tower}}{2\pi}\frac{x}{x^2+y^2}\right)U_\infty \tag{2.28}$$

$$V_{Tower} = vV_\infty = \left(2\frac{xy}{(x^2+y^2)^2} + \frac{C_{Tower}}{2\pi}\frac{y}{x^2+y^2}\right)V_\infty \tag{2.29}$$

To extend this result to hub structure, the change in geometry is considered. The dependency of the tower effect in the y direction, the horizontal direction perpendicular to the flow, is replaced by a radial dependency. This reduces the effect to the effect of a sphere on the velocity profile. By setting $x = X$ where X is the constant, half the axial distance between the upstream hub tip and the blade plane, the geometric profile will be similar to a hub nacelle with a spherical tip.

$$U_{Hub} = uU_\infty = \left(1 - \frac{X^2 - r^2}{(X^2+r^2)^2} + \frac{C_{Hub}}{2\pi}\frac{X}{X^2+r^2}\right)U_\infty \tag{2.30}$$

$$V_{Hub} = vV_\infty = \left(2\frac{Xr}{(X^2+r^2)^2} + \frac{C_{Hub}}{2\pi}\frac{r}{X^2+r^2}\right)V_\infty \tag{2.31}$$

In addition there is the added wake shadow effect, the domain of which increases with downstream distance from the hub tip. If the boundary of the hub shadow is at radius b and the fraction of velocity reduction at the nacelle surface is f,

$$f_{Wake} = f\cos\left(\pi/2(r-1)/b\right)^2 \tag{2.32}$$

f_{Wake} is a measure of the reduction in velocity. At the nacelle surface, $r = 1$, $f_{Wake} = (1 - f)$. For these investigations, f is set to 1 to reduce the velocity to zero at the nacelle surface. The radius of the wake shadow, b, will increase with distance from the hub tip.

Using this formulation, the whole wake can be deduced with minimal input information. Considering the reference location, x_{ref}, where the wake width is known to be b_{ref}, as b increases with the $\sqrt{x}$, the wake width at any distance in the horizontal axial direction from the hub can be found. In this way, BEMT can be used to simulate turbines operating downstream of the nacelle tower position. Distance is normalised

with respect to the hub tip radius.

$$b = b_{ref}\sqrt{\frac{x}{x_{ref}}} \tag{2.33}$$

This is then used in Equation (2.32) to calculate the wake effect f_{wake} when $r < b$. In this case, the effect of the potential theory and wake around a hub on the velocity flow field is given by Equation (2.34) which replaces Equation (2.28) when $r < b$.

$$U_{Hub} = u(1 - f_{Wake})U_{\infty} \tag{2.34}$$

At a fixed downstream distance x_{ref}, b_{ref} will be dependent on free stream flow velocity. At high velocity free stream flow b_{ref} will reduce and at low velocities b_{ref} will increase. For the Bahaj *et al.* [2007] turbine used in this comparison, these values are set to $x_{ref} = 2$, $b_{ref} = 3.7$ and the velocity field in the blade plane is visualised in Figure 2.5. The values are taken from a CFD result of the experimental set up for this case. The aim of this work is to illustrate the methodology and theory. The wake effect is dictated by the values of x_{ref} and b_{ref} and the sensitivity considerations and additional comparisons is an area of further work.

The effect of the hub is clearly shown with a reduction of velocity close to the hub surrounded by an acceleration of velocity at a larger radius 2 hub radii away from the hub tip centre the wake radius is 3.7 times the hub radius, measured from the rotational axis. The undisturbed free stream flow is $U_{\infty} = 1.73\text{ms}^{-1}$ and the effective turbine blade spans from radius, r to $r = 0.08$ and $r = 0.4$. Accounting for hub shadow, the incident axial velocity at the turbine root becomes $U \simeq 0.5\text{ms}^{-1}$, similarly to the Prandtl representation of hub loss, at $r \simeq 2R_{root} = 0.16$, the effect of the hub is small, i.e. $U \simeq 1.73\text{ms}^{-1}$. However, above $r = 2R_{root}$, the blockage effect causes $U > U_{\infty}$.

Unlike the Prandtl formulation, this hub shadow is independent of turbine rotational velocity. The result of this hub shadow formulation is compared to the Prandtl root loss correction and the Bahaj *et al.* [2007] data set in Section 2.7.2.

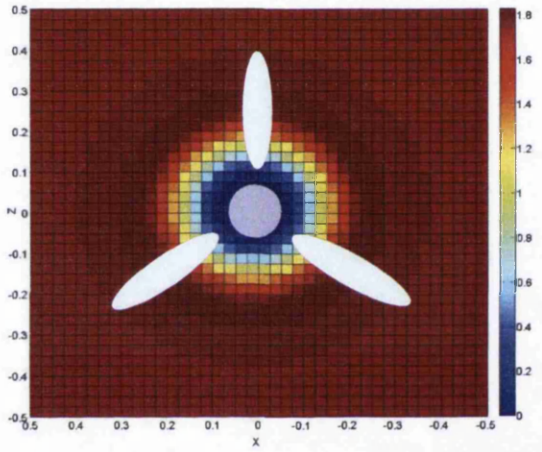

Figure 2.5: The cross-stream velocity field around a 0.05 radius hub in a free stream flow of 1.73ms^{-1}.

2.6 Momentum Theory Breakdown

By considering the stream flow speeds in Figure 2.2, when $\overline{a} > 0.5$ the wake flow is theoretically reversed, while the flow across the turbine is still in the positive direction. This is the case for a heavily loaded turbine during forced start up and shut down, at low TSR. If the tip loss in Section 2.4.1 is implemented, high-induction occurs at the tip in normal operating conditions. The tip section of the blades is most significant at maximum power operating conditions therefore it is important to consider high-induction when determining the power production of the turbine in normal operation. It is also important to model the stalled state, to determine durability. By modelling this state, fault conditions and fault loadings can be studied at low TSR conditions.

When the averaged axial induction value, $\overline{a}$, is larger than 0.5, the wake flow does not physically reverse. Instead the reduced velocity flow in the wake becomes turbulent and begins to mix with the relatively fast, free stream flow outside the stream tube. No interaction between adjacent stream tubes is a fundamental assumption of momentum theory, therefore this theory cannot describe the high-induction state.

Considering the whole turbine in the high-induction state, the momentum theory actuator disc become less permeable to the flow and, if $\overline{a} = 1$, the turbine is effectively a solid plate. This occurs at very high TSR.

For a solid plate, perpendicular to a constant velocity field, the flow must propagate in a radial direction at the disc due to the low permeability. At the flow reaches the disc edge, much of the kinetic energy has been lost to viscosity. Burton *et al.* [2001] states that the boundary layer will continue onto the trailing surface of the disc and accelerate, which implies a drop in static pressure on the trailing disc side. For the flow to remain with the boundary layer, it needs to also accelerate, however there is insufficient static pressure. Therefore the flow past a solid disc separates at the disc edge and propagates in the general stream flow direction.

This creates an area of extremely low pressure directly behind the disc where the flow is stagnant. A stagnation point is also produced directly before the centre of the disc, however the pressure here is extremely high. This results in a large pressure drag force on the solid disc.

Burton *et al.* [2001] suggests that the majority of the flow past a spinning rotor, with a high TSR, behaves as flow past a solid disc. A small amount of flow, however,

will propagate through the rotor. It emerges, with low velocity, into a low pressure region. There is insufficient kinetic energy in the flow to raise the pressure to the atmospheric pressure of the far wake and so turbulent wake mixing must occur in order to propagate the wake. The unstable boundary layer between the free flow and the wake collapses to allow mixing. The large difference in pressure either side of the turbine causes a large axial force that increases with a until flat plate theory is reached at $a \simeq 1$. As momentum theory assumes there is no exchange of flow between stream tubes, alternative schemes are explored in Section 2.6.1. The momentum theory expression for torque is unaffected by high-induction but alternative formulations of the axial force coefficient, C_{fa}, are presented.

2.6.1 Buhl High-Induction Correction

As classical momentum theory breaks down when $a > 0.5$, unphysical instabilities are created in the iterative BEMT routine. Momentum theory gives the dependence of the axial force coefficient, C_{fa}, on a as,

$$C_{fa} = 4aF(1-a) \tag{2.35}$$

In Glauert [1934], the result of this relationship is compared to the experimental data of Lock *et al.* [1926], reproduced here in Figure 2.6.

Figure 2.6 shows how, in the high-induction region, Equation (2.35) underestimates axial force coefficient and predicts that C_{fa} will decrease with increasing a, whereas the experimental data shows increasing C_{fa} with increasing a. The experimental data agrees well with the flat plate, high-induction theory of Section 2.6 and flat plate theory is reached when $C_{fa} = 2$.

Lock *et al.* [1926] reports a large spread of data in the region $a > 0.5$, suggesting that the dependency of the C_{fa} on a is difficult to quantify in high-induction due to the turbulent wake mixing. An empirical relationship is proposed by Glauert [1934] to fit the Lock data curve in the high-induction state. The quadratic function is derived to purposely agree with flat plate theory at $a = 1$ and momentum theory at $a \simeq 0.5$.

The paper by Buhl [2005] shows how this correction does not account for the BEMT tip and hub corrections, as described in Section 2.4. To account for these

corrections, a line fit is suggested by Burton *et al.* [2001], parallel to the parabola from Glauert [1934], with a high-induction start value of $a = 0.326$. Willson and Lissaman [1974] suggest that high-induction should be implemented after $a = 0.368$, which affects the slope and fit of the curve. It is noted by Buhl [2005] that these corrections create a discontinuity at the transition point between momentum theory and high-induction.

Buhl [2005] continues in a similar manner to Glauert [1934], by assuming that the relationship between the axial induction factor and the axial force coefficient is quadratic in nature after $a = 0.4$, in high-induction. At $a = 0.4$ the quadratic and its derivative are equal to the momentum theory result and at $a = 1$ flat plate state is reached, therefore $C_{fa} = 2$.

However, unlike Glauert [1934], Buhl [2005] considers the classical momentum theory expression for C_{fa} with the inclusion of the loss factor F, as given by Equation (2.36). Using the conditions and the momentum theory expression, all the coefficients of the quadratic can be found and this equation is dependent on the tip and hub losses thus eliminating the gap where the curves meet. The resultant relationship between C_{fa} and a is shown in Equation (2.36) in the momentum theory region and the high-induction region.

$$C_{fa} = \begin{cases} 4aF\left(1-a\right) & \text{for} a < 0.4 \\ \frac{8}{9} + \left(4F - \frac{40}{9}\right)a + \left(\frac{50}{9} - 4F\right)a^2 & \text{for} a > 0.4 \end{cases} \tag{2.36}$$

This formulation of C_{fa} is also compared in Figure 2.6 and, even though most turbine operating speeds give $a \simeq 0.3$, the addition increases the accuracy and suitability of the momentum theory at low TSR and in the vitally important tip region at operating conditions. From the graph it is obvious that this formulation cannot describe exactly the axial coefficient found in experiments, it is, however, a vast improvement on the momentum theory predictions. Only the momentum theory breaks down and this correction is applied to the momentum axial force coefficient in Equation (2.19). Section 2.6.2 outlines an alternative cubic high-induction correction scheme and in Section 2.9.1 this quadratic formulation is re-evaluated for an alternative tip and hub loss implementation.

2.6.2 Cubic High-Induction Correction

The correction for high-induction proposed by Buhl was formulated by assuming it agreed with classical momentum theory at $a \simeq 0.5$ and is quadratic in nature. A quadratic dependence of C_{fa} on a in the high-induction state causes a mirrored C_{fa} result, considering $a = 0.5$ as the mirror line. For example, assuming $F = 1$, at $a = 0.6$ the incorrect, momentum theory result gives $C_{fa} = C_{fa}(0.5) - 0.4$ and the quadratic high-induction result gives $C_{Fa} = C_{Fa}(0.5) + 0.4$. As classical momentum theory is invalid in high-induction, the C_{fa}/a curve shape is completely independent from momentum theory. Therefore, a cubic high-induction relationship between C_{fa} and the a coefficient could be equally considered, as long as the momentum theory solution is met at $a \simeq 0.4$ and flat plate theory is reached at $a \simeq 1$. Indeed, other alternative formulations of the high-induction state C_{fa} dependency on a would also be valid research areas.

Consider the cubic high-induction C_{fa} dependence on a,

$$C_{fa} = c_1 + c_2 a + c_3 a^2 + c_4 a^3 \tag{2.37}$$

where c_i, $i = 1, 2, 3$ are constant coefficients. At $a = 1$, flat plate theory is reached and $C_{fa} = 2$ which suggests,

$$2 = c_1 + c_2 + c_3 + c_4 \tag{2.38}$$

At $a = 0.4$ the momentum theory solution of $C_{fa} = 4Fa(1 - a)$ is valid. By equating C_{fa}, $\frac{dC_{fa}}{da}$ and $\frac{d^2C_{fa}}{da^2}$ for the momentum theory and the cubic solution, and by substitution with Equation (2.38):

$$c_3 = -2/(a^3 - 3a^2 + 3a - 1) \tag{2.39}$$

$$c_2 = -3c_3 a - 4F \tag{2.40}$$

$$c_1 = 3c_3 a^2 + 4F \tag{2.41}$$

These expressions are substituted into Equation (2.37), which can then replace C_{fa} in the momentum theory axial force solution in a similar manner to Section 2.6.1.

In theory the flat plate state solution is reached when $a \simeq 1$. However, this assumption is purely theoretical and it may be the case that the flat plate theory is not reached when $a \simeq 1$. The cubic high-induction solution of Equation (2.38) can be generalised so that $C_{fa} = C_{MAX}$ at $a = 1$ as given in Equation (2.42). The transition between the classical and high-induction states occurs at $a \simeq 0.5$. As a further generalisation, the value used for the upper limit of momentum theory in the scheme can be considered a_{limit}.

$$C_{MAX} = c_1 + c_2 + c_3 + c_4 \qquad \text{for} \quad a = 1 \tag{2.42}$$

$$c_3 = -C_{MAX}/(a_{\text{limit}}^3 - 3a_{\text{limit}}^2 + 3a_{\text{limit}} - 1) \tag{2.43}$$

$$c_2 = -3c_3 a_{\text{limit}} - 4F \tag{2.44}$$

$$c_1 = 3c_3 a_{\text{limit}}^2 + 4F \tag{2.45}$$

$$C_{fa} = \begin{cases} 4aF\,(1-a) & \text{for} a < 0.4 \\ c_0 + c_1 + c_2 a^2 + c_3 a^3 & \text{for} a > a_{\text{limit}} \end{cases} \tag{2.46}$$

This generalised formulation is now compared to the experimental data of Lock *et al.* [1926]. Figure 2.6 compares the theoretical solution of $C_{MAX} = 2$ against $C_{MAX} = 1.5$, both with a_{limit} set to 0.4 and also the experimental data set from Lock *et al.* [1926]. The spread of the data may be due to blockage effects or turbulent flow, both of which are more apparent at high water velocities where high-induction may occur. It can be seen in Figure 2.6 that a value of $Cfa \simeq 1.2$ is found at $a \simeq 0.95$ and $a \simeq 0.75$ and also at $a \simeq 0.55$ and the general tend increases with less slope than the quadratic correction slope provides. Figure 2.6 shows how the cubic solution reduces the slope at lower a compared to the quadratic solution whilst still satisfying the $Cfa \simeq 2$ condition at $a = 1$. Although the high-induction solutions presented so far do somewhat describe the high-induction region, they do not account for the spread

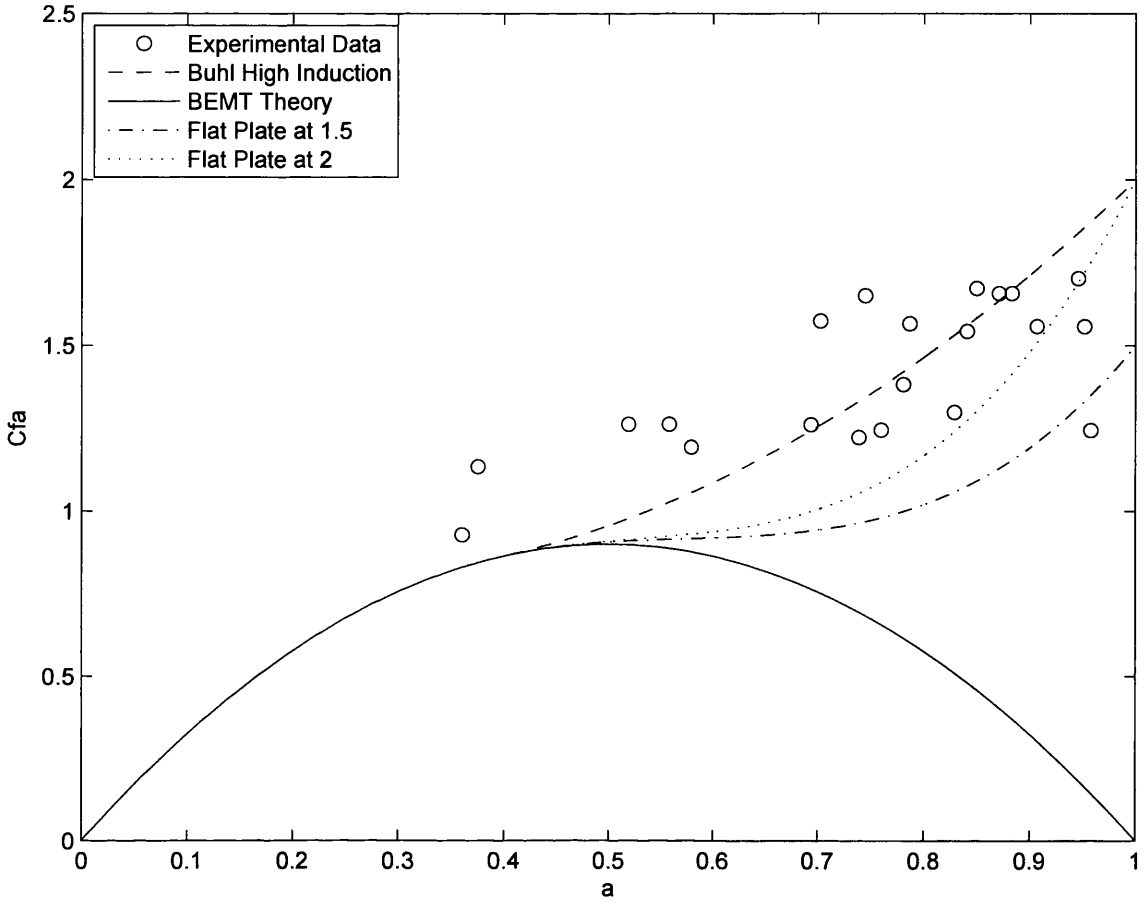

Figure 2.6: The variation of the axial force coefficient, C_{fa}, with axial induction factor, a, according to classical momentum theory (solid curve), high-induction correction (dashed curve), two proposed induction relations and experimental data as given in Lock *et al.* [1926]

of the data. A further alternative formulation is considered in Section 2.9, which does provide the first solution producing large spread in the high-induction region.

2.7 Results

The Bahaj *et al.* [2007] paper is evaluated in Section 1.6.1 and describes a turbine with a 0.8m diameter, 0.16m diameter hub, which is used for comparison against the results presented in this section. The three hub pitch angles with the most data points are compared to the BEMT scheme and presented here. $\phi_{root} = 15^o$, $\phi_{root} = 20^o$ and

$\phi_{root} = 25^o$ are considered, where ϕ_{root} is ϕ as defined in Figure 2.1 for the blade root.

The axial force coefficient C_{fa} and the power coefficient C_p, as defined in the equations of (2.22), are corrected for blockage effects by Bahaj *et al.* [2007] and then plotted against TSR. The result is compared to a BEMT scheme by Bahaj *et al.* [2007] which utilises an alternative to the Prandtl tip loss, the Goldstein averaging factor, as described in Bahaj *et al.* [2007]. In Bahaj *et al.* [2007] hub loss is not considered and the Glauert [1934] tip loss implementation is used. Of the discrete pitch settings and incoming flow rates investigated by Bahaj, the most data points are published with a pitch of 20^o and incoming constant velocity $U = 1.73\text{ms}^{-1}$. As the incident flow velocity is varied for each pitch setting, the turbine rotational speed is different for the same TSR position. In Bahaj *et al.* [2007] the measuring equipment resolution for a typical run is considered (flow speed of 1.5ms^{-1}, $C_p = 0.4$, $C_{fa} = 0.8$) leading to an accuracy for power of 71.3% and for axial force of 71.1% of the measured data against real power and axial force. A further description of this error can be found in Bahaj *et al.* [2007].

2.7.1 BEMT Tip and Hub Loss Results

Considering the 20^o root pitch investigation, Figures 2.7(a) and 2.7(b) show how the Prandtl tip loss and hub loss affects the BEMT scheme result in terms of C_p and C_{fa} respectively. As would be expected, it is shown that the power production is highest when no losses are accounted for. Comparing the tip loss with tip and hub losses, it is clear that tip loss has a greater effect than hub loss, which is also expected, as the extent of the tip loss is dependent on the large blade radius whereas the extent of hub loss is dependent on the double the smaller blade root radius. These results utilise the Buhl [2005] high-induction correction as this dramatically improves convergence in the high-induction region.

In Chapman [2009] it is shown that BEMT consistently predicts higher values than the Sharpe lifting line theory as it does not account for all three dimensional flow effects; most importantly, vortices induced on the rotor disc or radial flow created by blade rotation. The Prandtl tip and hub loss corrections are shown to improve the model compared with lifting line theory and implementing them incurs only a small computational cost.

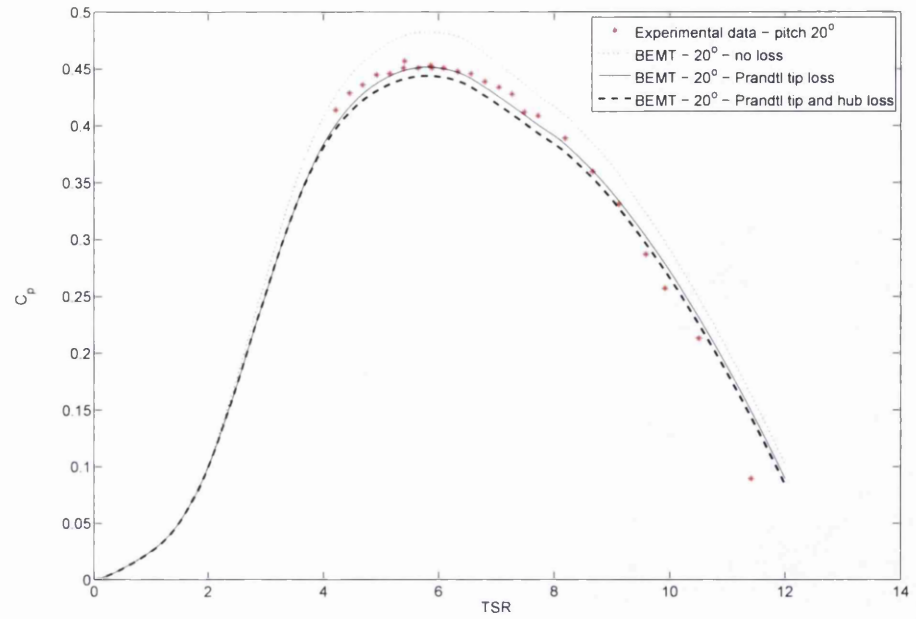

(a)

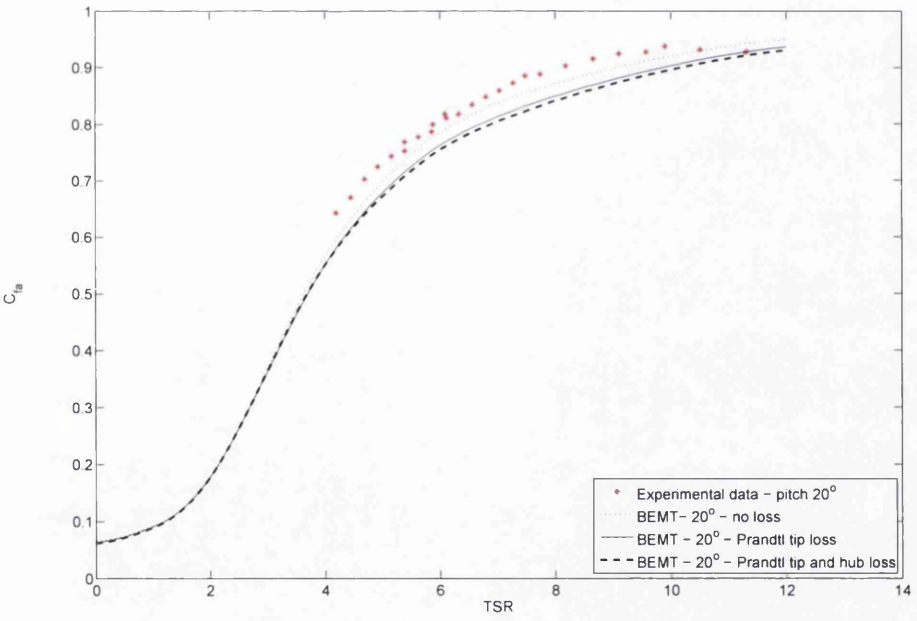

(b)

Figure 2.7: Experimental data, 20° pitch set, from Bahaj *et al.* [2007] compared to BEMT prediction, considering tip and hub loss effects on (a) the power coefficient C_p and (b) the axial force coefficient, C_{fa}, both against TSR.

Figures 2.8(a) and 2.8(b) give the three Bahaj *et al.* [2007] data sets considered and the simulated BEMT results with Prandtl tip and hub loss implemented. For $TSR > 6$, the simulated results are all effected by the quadratic Buhl [2005] high-induction correction as described in Section 2.6.1. Good agreement is shown between the results and the experimental data. However, at high TSR the BEMT scheme is shown to overpredict the power and axial force. This is particularly evident for the low pitch case of 15^o above a TSR of 6. In this region and for this pitch setting, many of the blade elements are operating in high-induction. In addition, for the 25^o pitch case, this inaccuracy at high TSR does not occur and no blade elements are operating in high-induction. Due to these observations, Section 2.7.3 explores alternate high-induction formulations.

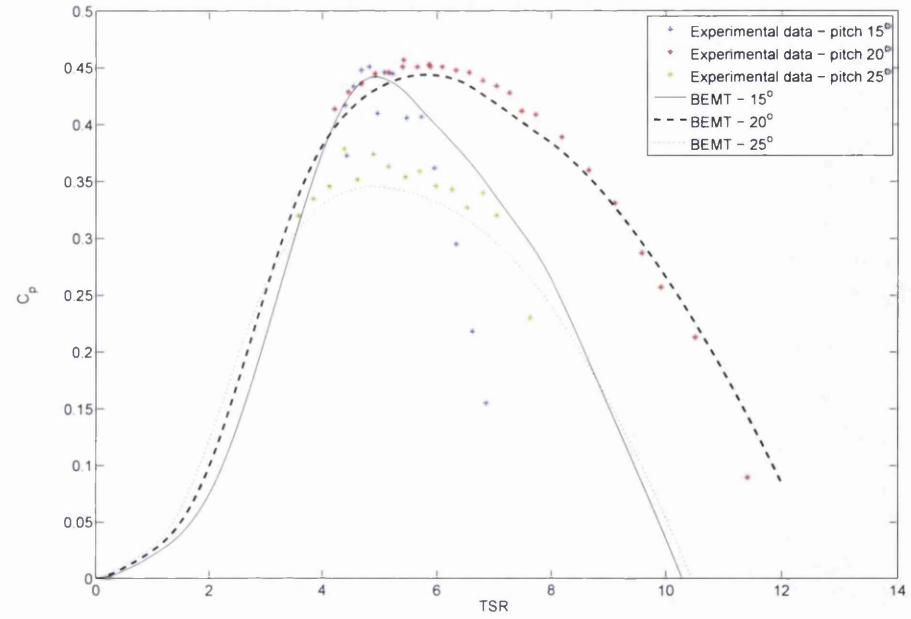

(a)

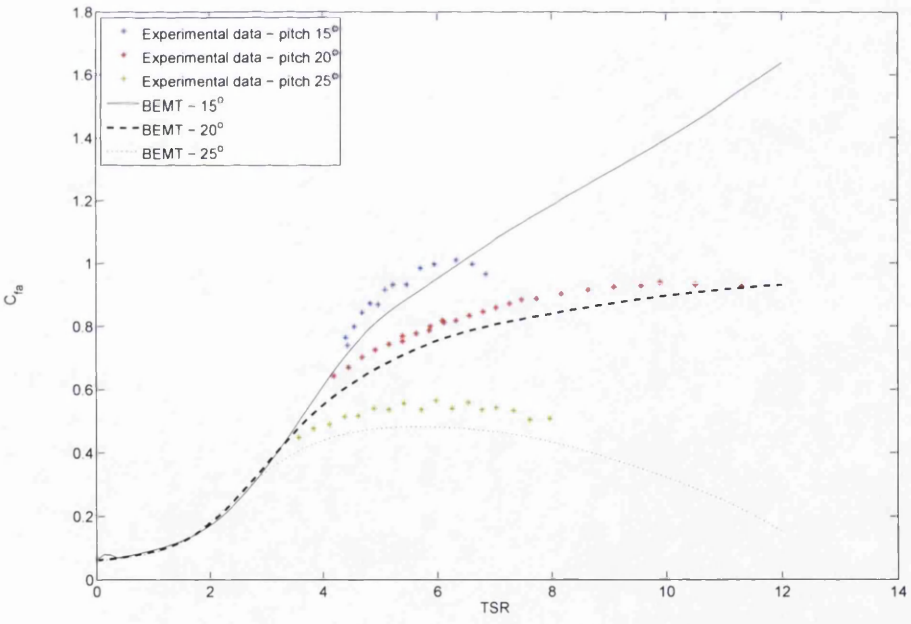

(b)

Figure 2.8: All experimental (a) power coefficient, C_p, and (b) axial force coefficient, C_{fa}, data sets against TSR from Bahaj *et al.* [2007] compared to BEMT prediction.

2.7.2 Hub Shadow Results

The effect of the turbine hub on the root incident flow is considered as an alternative to the Prandtl hub loss in Section 2.5.1. The main effect of this change is that hub performance reduction is no longer dependent on the rotational velocity of the turbine. Using the Prandtl root loss formulation, if the free stream velocity is held and rotational velocity increases, root losses decrease. BEMT can overpredict power performance of the turbine at high TSR and the reason for this could be that the root losses are dependent on rotational velocity. The effect of a hub on the surrounding velocity field is independent of turbine rotational velocity and in this case, at high TSR the reduction in root performance remains the same. The wake width is however dependent on free stream flow velocity. This dependence is unknown and could be researched to further develop the model.

Figures 2.9(a) and 2.9(b) show power and axial force coefficients respectively. Experimental data is given against the BEMT scheme with Prandtl tip and hub loss and also against the BEMT scheme with Prandtl tip loss only with hub shadowing on the local velocities, as in Figure 2.5. Figure 2.9(b) shows how hub shadow gives a constant and significant reduction in C_{fa} of $\simeq 0.04$.

Considering Figure 2.9(a), the effect on C_p is a change in curve shape. Directly before maximum C_p the hub shadow case results in less power and the peak itself is shifted from $TSR \simeq 5.5$ to a slightly higher value of $TSR \simeq 6$. It is also noted that at very high TSR, less power is predicted using hub shadow. This was expected as, at high TSR, the rotational velocity is large and therefore Prandtl root losses become zero. This leads to an unphysical root performance recovery at high TSR that is not present in hub shadow. The peak C_p value is similar, however, and the maximum difference in C_p is 0.01 at $TSR \simeq 5$. Also, by altering x_{ref} and b_{ref} in Section 2.5.1 the result can be drastically altered. A method of deducing these values is an area of further research.

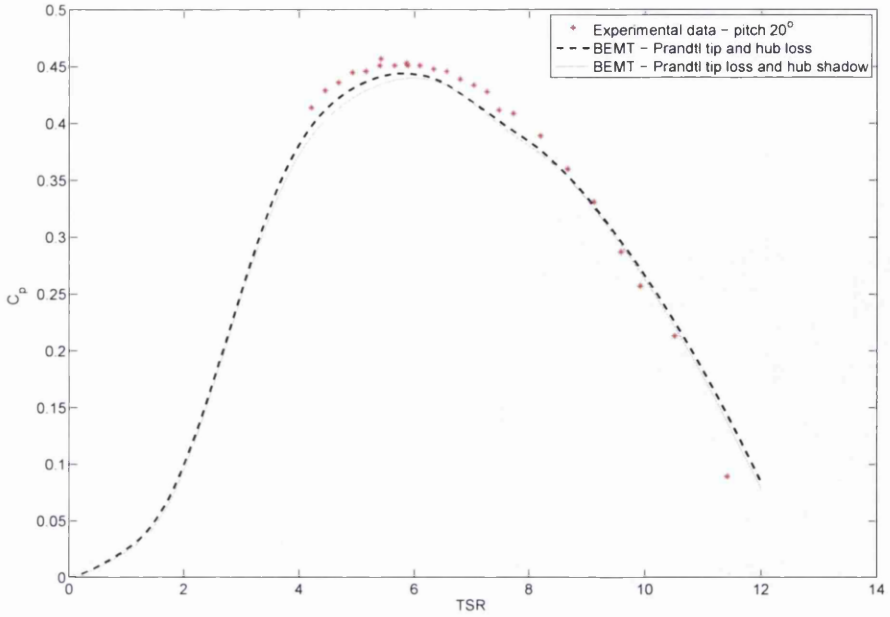

(a)

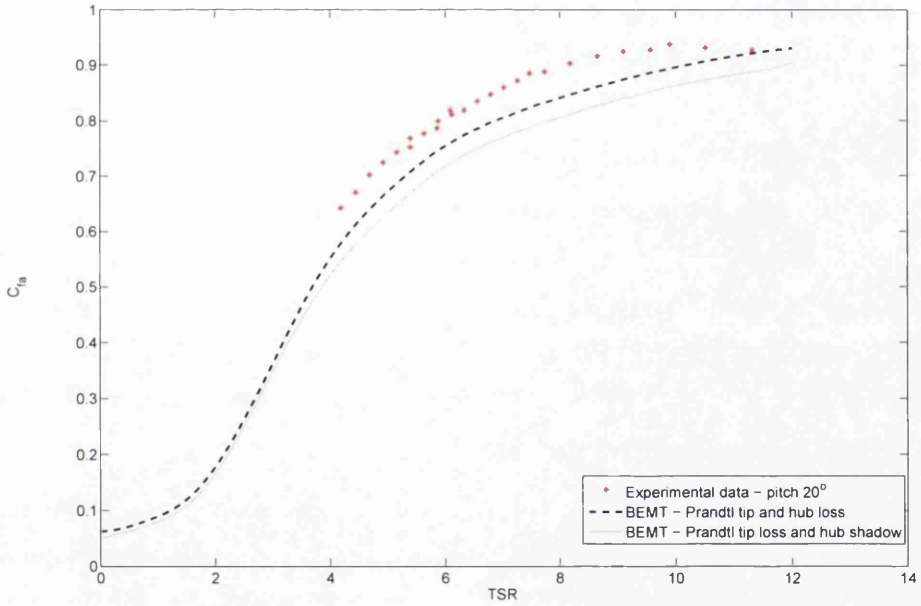

(b)

Figure 2.9: Experimental 20^O data set from Bahaj *et al.* [2007] compared to BEMT prediction with a Prandtl based tip and hub loss and a BEMT prediction with tip loss only and hub shadow, (a) power coefficient, C_p, and (b) axial force coefficient, C_{fa}.

2.7.3 High-Induction Correction Results

Both Sections 2.6.1 and 2.6.2 utilise a method for determining the dependency of C_{fa} on a in the high-induction region. In Section 2.6.1 the commonly used, quadratic dependency is outlined. In Section 2.6.2, an alternative cubic dependency is presented and the results of this suggestion are analysed here, compared to the experimental results of Bahaj *et al.* [2007]. C_p and C_{fa} for the usual root pitch settings of 15^o, 20^o and 25^o, are compared in Figures 2.10, 2.11 and 2.12 respectively.

The largest effect on the results is shown with the 15^o blade root pitch at high TSR. This is expected, as it is the area with the most blade elements operating in high-induction. A cubic dependency of C_{fa} on a acts to decrease C_p and C_{fa} with the maximum difference occurring at $TSR \simeq 8$, where both C_p and C_{fa} reduce by $\simeq 0.15$. This acts to improve the agreement with the experimental data points in Figures 2.10(a) and 2.10(b).

Figures 2.11(a) and 2.11(b) show less effect on the 20^o hub pitch result as, with this hub pitch setting, less blade elements operate in the high-induction state. However, the differences that are shown in C_p and C_{fa} are most significant above $TSR \simeq 10$ and, as with the 15^o hub pitch setting, act to greatly improve agreement with the experimental data in this region.

In Figures 2.12(a) and 2.12(b), the same result is found for the two high-induction cases. This unchanged turbine performance result, suggests that no blade elements reach high-induction for the 25^o hub pitch case in the TSR region considered. Now, considering the initial case of Figure 2.8, it is clear that this pitch setting shows the most agreement with experimental data only because the blade elements do not experience high-induction at high TSR, which highlights the need for an alternative high-induction correction, as presented here and in Section 2.9.

Considering Figure 2.6, the cubic relationship reduces the axial force coefficient at high axial induction compared to the quadratic relation, which increases faster with a. There is a better correlation with experimental data when using the cubic relationship, suggesting the Buhl correction increases too rapidly with a in this region.

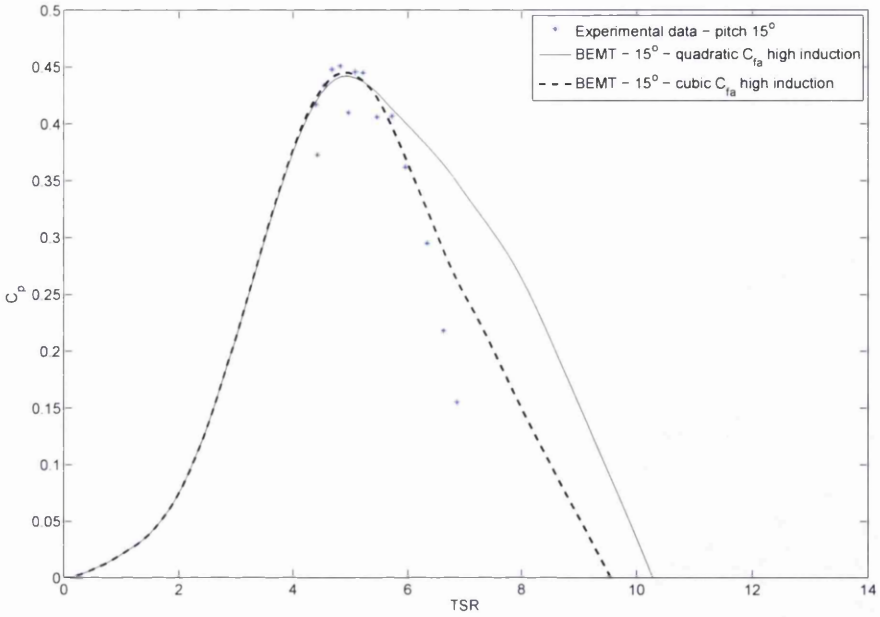

(a)

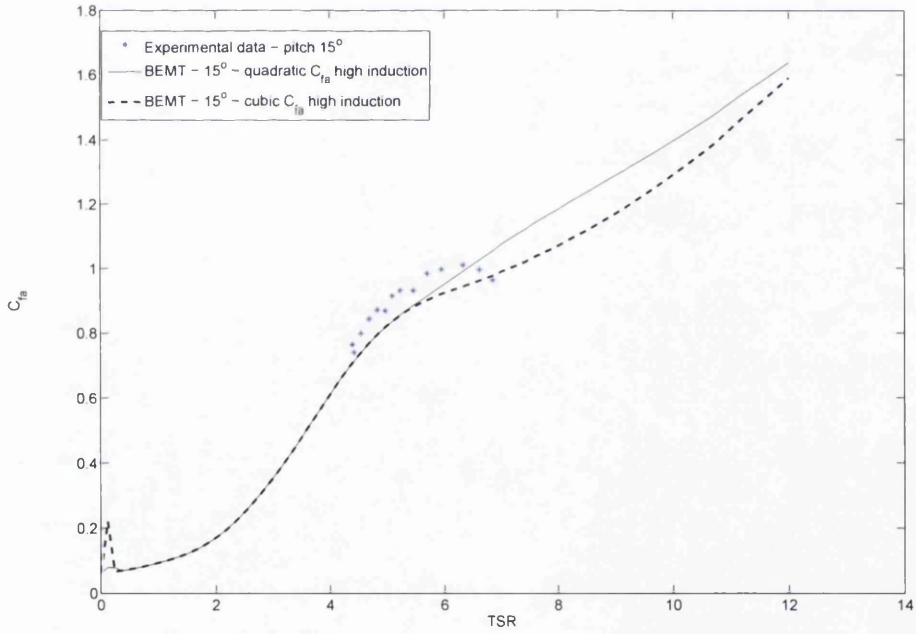

(b)

Figure 2.10: Experimental 15^O data set from Bahaj *et al.* [2007] compared to BEMT prediction with a quadratic high-induction dependency of C_{fa} on a and a BEMT prediction with a cubic C_{fa} dependency on a for (a) power coefficient, C_p, and (b) axial force coefficient, C_{fa}.

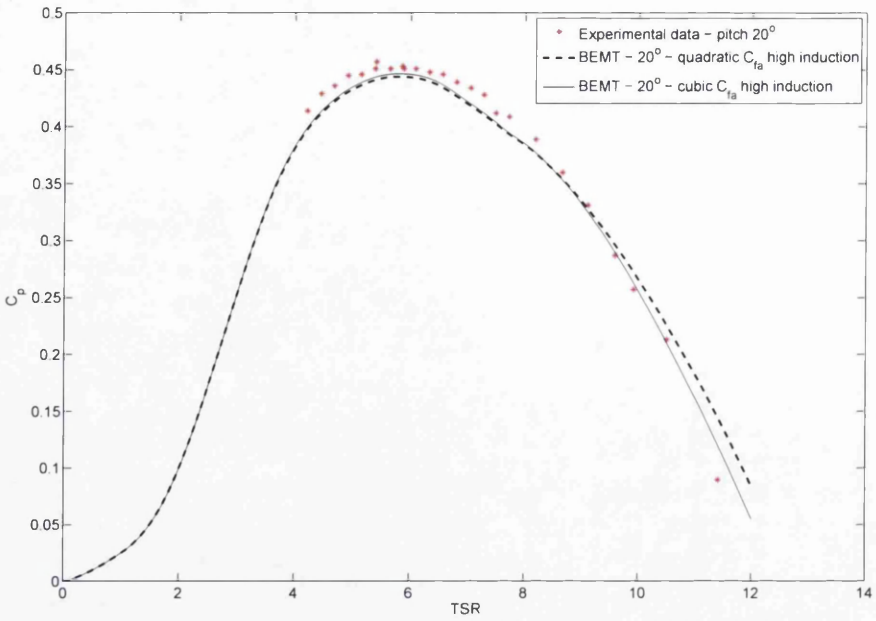

(a)

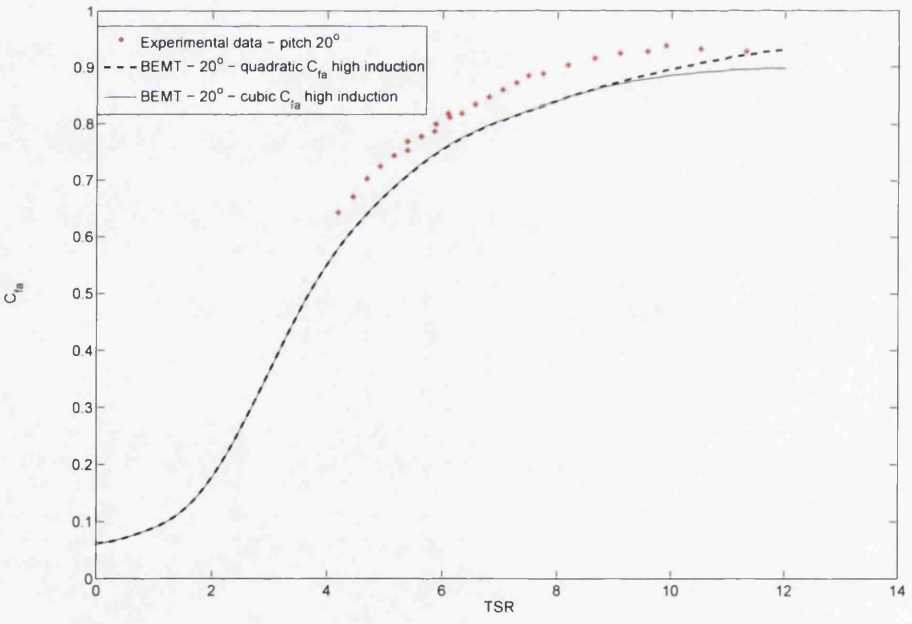

(b)

Figure 2.11: Experimental 20^O data set from Bahaj *et al.* [2007] compared to BEMT prediction with a quadratic high-induction dependency of C_{fa} on a and a BEMT prediction with a cubic C_{fa} dependency on a for (a) power coefficient, C_p, and (b) axial force coefficient, C_{fa}.

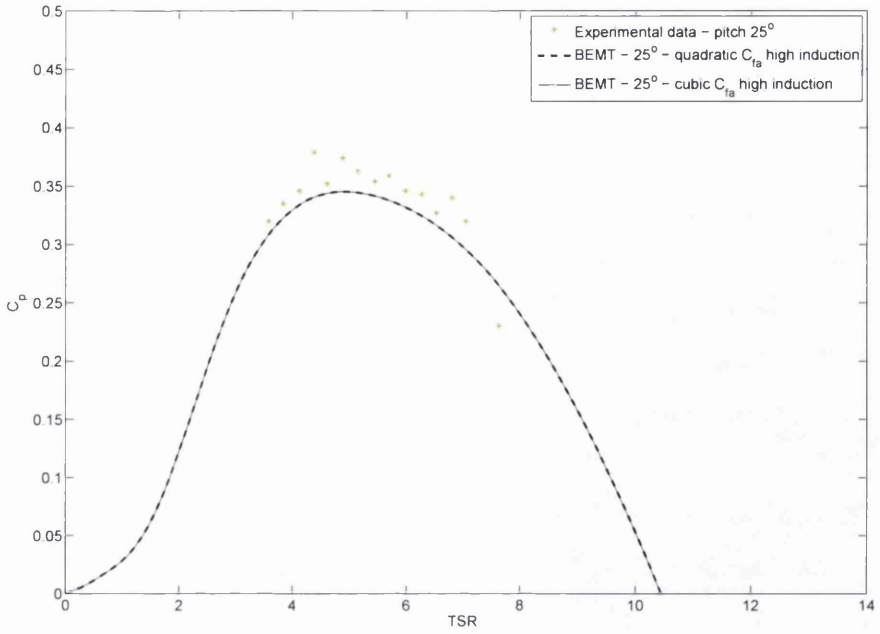

(a)

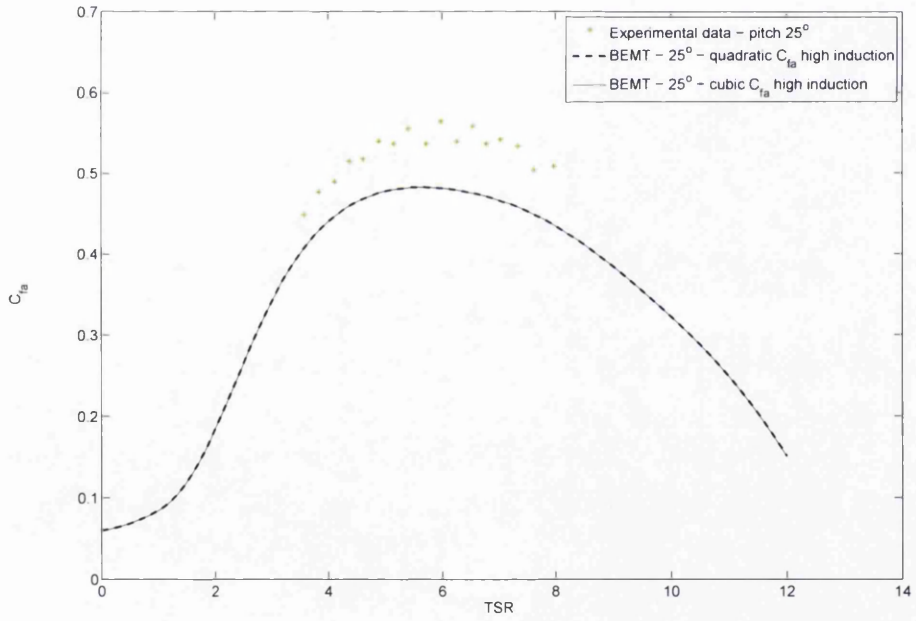

(b)

Figure 2.12: Experimental 25^O data set from Bahaj *et al.* [2007] compared to BEMT prediction with a quadratic high-induction dependency of C_{fa} on a and a BEMT prediction with a cubic C_{fa} dependency on a for (a) power coefficient, C_p, and (b) axial force coefficient, C_{fa}.

2.8 Discussion

In this section, the usual BEMT corrections for tip and hub loss effects and high-induction effects are analysed. Figures 2.7(a) and 2.7(b) clearly show the expected loss of C_P and C_{fa} due to the Prandtl tip and hub loss formulation. The extension of Prandtl's tip loss to hub loss is evaluated for the application of tidal stream turbines. This results in the development of an alternative hub shadow correction which is compared against the Prandtl hub loss in Figures 2.9(a) and 2.9(b). A similar solution is found for C_p and C_{fa}. C_{fa} is undersapredicted by the hub shadow method and agrees less with the experimental data.

In Figures 2.8(a) and 2.8(b), at high TSR the quadratic Buhl high-induction scheme is shown to overpredict the turbine power and axial force result. The theory of the quadratic high-induction correction is considered and an alternative cubic high-induction correction is developed. The two approaches are compared for all blade pitch variations for C_p and C_{fa}. By pitching the blades to 15^o, high-induction is most effective therefore this case is the most significant for comparing the corrections. In particular, by using a cubic high-induction, there is much improved agreement between simulation and experiment in the high-induction region for C_p.

2.9 Alternative Loss Implementation

Section 2.4 discusses the theoretical derivation of tip and root corrections and, although the Glauert [1934] and Burton *et al.* [2001] proposals are discussed, the theoretical basis of the loss implementation in BEMT is still unclear. The difference between the axial velocity far downstream and far upstream of the turbine is corrected by F in Section 2.4.1 and Glauert [1934] proposes an approximate solution for the momentum equations that are shown in Equations (2.20) and (2.19) and subsequently used to solve for C_p and C_{fa} in BEMT. This approximate solution is unnecessary and so it is now suggested that the average axial induction factor, $\overline{a}$, can be directly replaced with Fa in the momentum equations, as in Burton *et al.* [2001] and in agreement with Figure 2.3.

It is also common, as in Burton *et al.* [2001] and Bahaj *et al.* [2007], to replace the tangential induction factor, $\overline{b}$ with Fb. The material sheets of the wake helical

structure form the basis of the Prandtl loss function theory of Section 2.4.4. The angle ϕ from Figure 2.1 is used to calculate the normal difference between the sheets in the wake. Therefore it is suggested here that the tip loss factor F is applicable to the difference between the undisturbed far upstream flow, $\vec{U_0}$, and the incident aerofoil velocity vector $\vec{V}$ to convert from the average factors, $\overline{a}, \overline{b}$ and the local factors a, b.

$$\vec{U_0} - \vec{V} = \begin{pmatrix} U \\ 0 \end{pmatrix} - \begin{pmatrix} U(1-\overline{a}) \\ r\Omega(1+\overline{b}) \end{pmatrix} = \begin{pmatrix} U\overline{a} \\ -r\Omega(1+\overline{b}) \end{pmatrix} \tag{2.47}$$

Applying F,

$$\begin{pmatrix} \overline{a} \\ (1+\overline{b}) \end{pmatrix} = \begin{pmatrix} Fa \\ F(1+b) \end{pmatrix} \tag{2.48}$$

As before, $\overline{a}, \overline{b}$ are substituted in the momentum equations. This gives an alternative closed system of equations to be solved in BEMT.

$$dF_{a1} = N\frac{1}{2}\rho|\vec{V}|^2 c(C_L sin\phi + C_D cos\phi)dr \tag{2.49}$$

$$dT_1 = N\frac{1}{2}\rho|\vec{V}|^2 cr(C_L cos\phi - C_D sin\phi)dr \tag{2.50}$$

$$dF_{a2} = 4\pi r\rho U^2 aF(1-aF)dr \tag{2.51}$$

$$dT_2 = 4(F(1+b)-1)(1-aF)\rho U\Omega r^3\pi dr \tag{2.52}$$

Therefore, the least squares method, optimisation function, g, becomes,

$$\begin{aligned} g &= (dF_{a1} - dF_{a2})^2 + (dT_1 - dT_2)^2 \\ g &= \left(N\tfrac{1}{2}|\vec{V}|^2 c(C_L sin\phi + C_D cos\phi) - 4\pi r U^2 aF(1-aF)\right)^2 \\ &\quad + \left(N\tfrac{1}{2}\rho|\vec{V}|^2 c(C_L cos\phi - C_D sin\phi) - 4(F(1+b)-1)(1-aF)\rho U\Omega r^2\pi\right)^2 \end{aligned} \tag{2.53}$$

Considering this implementation of tip and hub loss, at the wake boundary as

$F \to 0$, $\vec{V} \to \binom{U}{0}$, and therefore there are no inconsistencies. The formulation also has an important effect on the high-induction region which is discussed in Section 2.9.1. The effect is deduced in Section 2.10 using the Bahaj *et al.* [2007] data sets.

2.9.1 The effect on High-Induction

As the high-induction correction, described in Section 2.6.1, is dependent on the momentum theory expression for the axial force coefficient, this must also be revised to account for the new implementation of F. Considering Equation (2.51), the axial force coefficient C_{fa} is now,

$$C_{Fa} = 4aF(1 - aF) \tag{2.54}$$

By including tip and hub loss, F, in this way, not only is the magnitude of the maximum turning point of C_{Fa} dependent on the value of F, the a value where this maximum occurs also depends on F as shown in Figure 2.13. With the Glauert [1934] implementation of F, the a value at maximum C_{Fa} is a constant 0.5. In Section 2.6.1 the upper limit of momentum theory is set to $a_{limit} = 0.4$. Considering this, the revised momentum theory upper limit is $Fa_{limit} = 0.4$ and so the transition value between momentum theory and the high-induction state is now a variable dependent on F. As the high-induction C_{Fa} against a expression is now largely dependent on F, more variation is introduced which produces results with a large spread. A large spread of data in the high-induction region is consistent with the findings of Lock *et al.* [1926].

As the cubic high-induction results of Section 2.6.2 improved the simulation in the high-induction region, the relationship between a and C_{Fa} is assumed cubic in nature in high-induction. As before, at $a = a_{\text{limit}}$, the high-induction curve, and its derivative are equal to the low induction curve and at $a = 1$ flat plate state is reached and $C_{Fa} = 2$. Using these conditions, all the coefficients of the polynomial from Section 2.6.2 are recalculated to account for the new momentum theory solution for C_{Fa}, as shown in Equation (2.54). As in Section 2.6.2,

$$C_{Fa} = c_1 + c_2 a + c_3 a^2 + c_4 a^3 \tag{2.55}$$

where c_i, $i = 1, 2, 3$ are coefficients to be found. Maximum a in Section 2.6.2 occurs when flat plate theory is reached and takes the value $a_{max} = 1$. However, with the revised tip and hub loss implementation, the flat plate theory value of a is $1/F$. This suggests,

$$2 = c_1 + c_2/F + c_3/(F^2) + c_4/(F^3) \tag{2.56}$$

Also, when $a_{\text{limit}} = 0.4/F$, the momentum theory solution of $C_{Fa} = 4Fa(1 - Fa)$ is valid. By equating $C_F a$, $\frac{dC_{fa}}{da}$ and $\frac{d^2 C_{Fa}}{da^2}$ at $Fa_{limit} = 0.4$ for the momentum theory and the cubic solution, and be substitution with Equation (2.56):

$$c_3 = 2/(1/(F^3) - 3/(F^2)a_{\text{limit}} + 3/(F)a_{\text{limit}}^2 - 3a_{\text{limit}}^3) \tag{2.57}$$

$$c_2 = -3c_3 a_{\text{limit}} - 4F^2 \tag{2.58}$$

$$c_1 = 3c_3 a_{\text{limit}}^2 + 4F \tag{2.59}$$

As before, these expressions are substituted into Equation (2.55), which can then replace C_{Fa} in the momentum theory axial force solution in a similar manner to Section 2.6.2.

$$C_{fa} = \begin{cases} 4aF\,(1-a) & \text{for} a < a_{\text{limit}} \\ c_0 + c_1 + c_2 a^2 + c_3 a^3 & \text{for} a > a_{\text{limit}} \end{cases} \tag{2.60}$$

The revised formulation of C_{fa} is compared in Figure 2.13 to the Lock *et al.* [1926] data set. This can also be compared to Figure 2.6 which shows the cubic and quadratic high-induction expressions for the common Glauert [1934] implementation. Figure 2.13 illustrates how, as F varies, the high-induction results now vary for the same a value which produces a large spread of results in this region. It also shows how at $a = 1$ the flat plate state C_{fa} value of 2 is not necessarily reached. Flat plate state now occurs at $a = 1/F$. It is also shown how the upper limit of classical momentum theory is no longer constant but dependent on F. The two cases considered by Figure 2.13 represent the upper and lower limit of a high-induction range and the value of F

varied along the blade length which will produce the spread of data as seen in Figure 2.13.

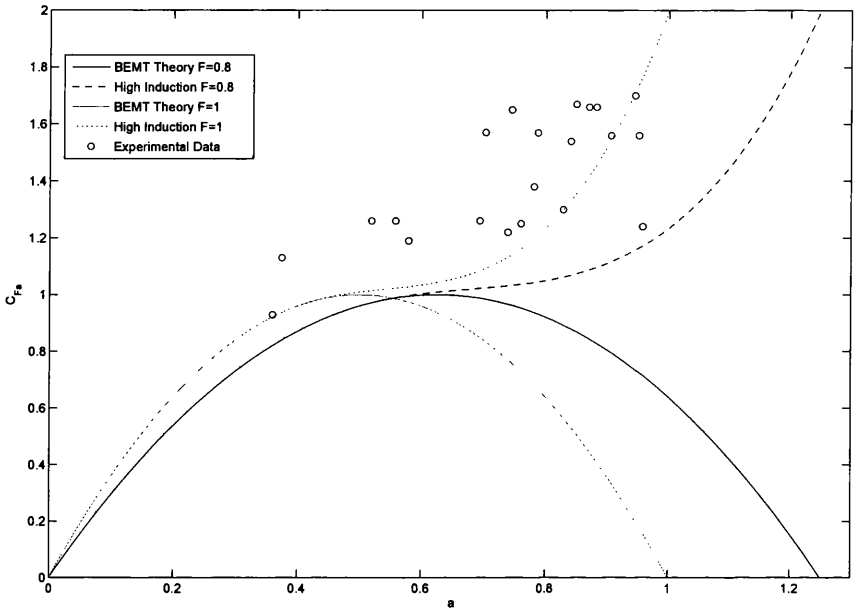

Figure 2.13: The variation of the axial force coefficient,C_{Fa}, with axial induction factor, a, for an arbitrary low value of $F = 0.8$ and the no loss case upper limit of $F = 1$. Compared with experimental data as given in Lock *et al.* [1926]

2.10 Results

The axial force and power coefficients are plotted in Figures 2.14(a) and 2.14(b) for the 20^o hub pitch results respectively. In Figure 2.14(a) the revised formulation is shown to have a small effect on the C_pTSR curve which improves the agreement with the experimental data. However, the largest improvement is with the C_{fa}/TSR simulation result in Figure 2.14(b), which now agrees well with the experimental data.

In Bahaj *et al.* [2007] a BEMT scheme is proposed using the Glauert [1934] implementation of tip loss and the result is also plotted in Figures 2.14(a) and 2.14(b) for comparison. The form of the high-induction correction is not published. However, the results suggest that the high-induction used is quadratic in nature, this gives the noticeable difference in C_{fa} at high TSR between the Bahaj *et al.* [2007] result and the BEMT scheme proposed here with the Glauert [1934] implementation, reminiscent of Figure 2.11(b).

The revised implementation result provides an improved result compared to our BEMT scheme with the Glauert [1934] loss implementation and also the Bahaj *et al.* [2007] result, which employs the Glauert [1934] implementation of F as well. This is further evidence for the validity of the new implementation presented here. However, further validation is needed, in particular, an experiment to obtain quality high-induction region data, similar to the Lock *et al.* [1926] data, is vital in understanding the high-induction region.

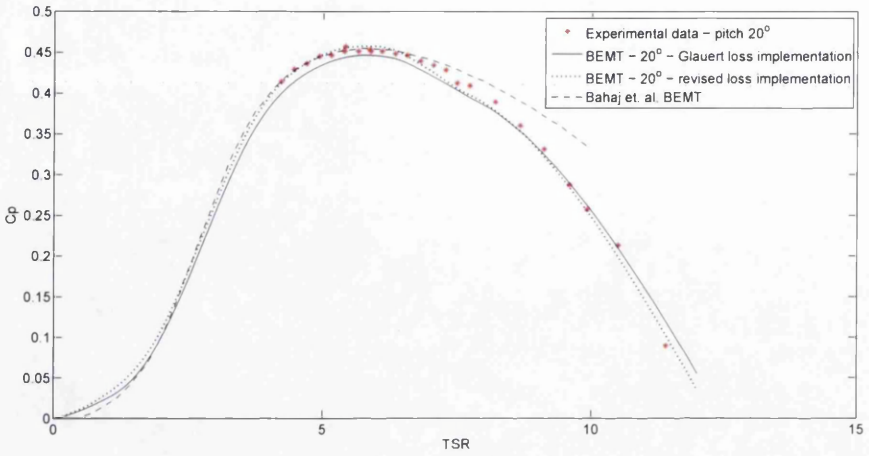

(a)

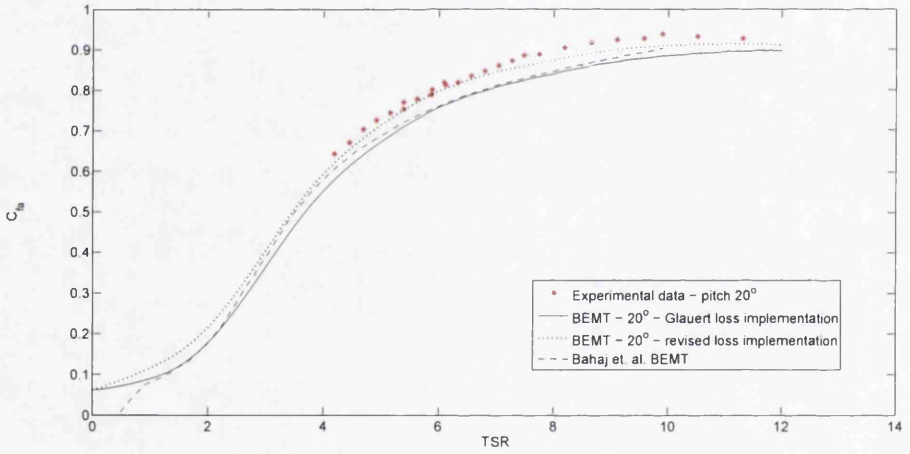

(b)

Figure 2.14: Experimental 20^O data set from Bahaj *et al.* [2007] compared to BEMT with Glauert and Burton loss implementation and BEMT with revised loss implementation for (a) power coefficient C_p and (b) axial force coefficient, C_{fa}.

2.11 Discussion

The theoretical derivation of the Prandtl tip loss is considered. An approximation is identified and this section considered the tip, and consequently hub, loss without the approximation and the implications for the high-induction formulation. A cubic high-induction is still used, however Figure 2.13 illustrates that the value of a in high-induction is dependent on the loss factor F and so occupies a range of values. This is consistent with the spread of data in the high-induction region found in experiments.

Figures 2.14(a) and 2.14(b) show the effect of the new loss factor formulation on the turbine performance results. For C_p, a similar result is found and the new simulation shows better agreement with the experimental data. The effect on C_{fa} is most significant. BEMT theory has been shown to consistently underpredict C_{fa} in this work and the work by Bahaj *et al.* [2007]. The loss factor formulation, presented here in Figure 2.14(b), does not underpredict C_{fa} and therefore shows a much better agreement with the experimental data.

2.12 Conclusion and Recommendations

This chapter outlines a computationally efficient scheme based on BEMT and considers the validity of extending the method to tidal turbines within the marine renewable energy sector. The common approach to tip and hub loss is outlined in detail. The theoretical problems with using the Prandtl hub loss are highlighted, particularly for tidal turbine simulation. An alternative explanation for hub performance deterioration is hub shadowing. As an extension to the tower shadow model, the hub shadow can affect the local inflow velocity used in BEMT. The Prandtl tip and hub loss is then evaluated and analysed against published experimental data and compared to an alternative hub shadow scheme, adapted from an existing tower shadow model.

The extent of this effect is controlled by four variables, C_{hub}, b_{ref}, x_{ref} and f. C_{hub} is the hub drag coefficient. b_{ref} is the reference hub wake width at the reference position x_{ref}. f is the maximum fractional reduction in axial velocity at the nacelle radius, if $f = 1$ then the axial velocity reduces to zero at the nacelle radius. Considering a CFD study of a cylinder in constant flow, values of $x_{ref} = 2$, $b_{ref} = 3.7$ and $C_{hub} = C_{tower} = 0.6$ are used.

This work illustrates how the hub shadowing scheme can give similar turbine performance results as the Prandtl hub loss factor and therefore it may be that hub shadow is mainly responsible for the blade hub performance deterioration. Particularly, hub shadowing removes the unphysical dependency of hub loss on the rotational velocity of the turbine. However the four hub shadow variables mentioned above are unknown and further work can be done to validate these variables. They also may not be constant but may have an unknown dependency on free stream velocity.

Further work is needed on the hub shadow effect and hub loss remains an active area of interest in the tidal turbine industry and the turbine simulation research community. It is concluded that the Prandtl formulation of tip and hub loss gives good agreement with the experimental data and is currently sufficient for this work.

It is found that, for power coefficient against TSR, the simulated results generally agree well with the experimental data, particularly at peak power output. In the high TSR region the proposed BEMT scheme overpredicts the power and axial force of the turbine, particularly for the hub pitch settings of 15^o and 20^o. This tendency to overpredict power output at high TSR is a common attribute of BEMT simulation and in this chapter it is found that the reason for this is the dependency of C_{fa} on a in the high-induction state.

A cubic dependency of C_{fa} on a in the high-induction region is suggested and compared to the quadratic dependency postulated by Buhl [2005]. Using the published experimental data for evaluation, this improves the power and axial force predictions in the high-induction region. Due to the improvement in the agreement with experimental data, a cubic high-induction C_{fa} dependency on a is used in this work.

An alternative implementation to the Glauert [1934] implementation of losses used in this work is proposed in Section 2.9. In a similar way to the Burton *et al.* [2001] implementation, it does not simplify the final momentum theory equations to the order of approximation and therefore avoids this inconsistency at the wake boundary. In addition, a new rotational induction factor correction is proposed that deviates from the Burton *et al.* [2001] correction of $F_{Tip}b$. This formulation is not used in the subsequent analyses due to the lack of validation, however it has a more elegant theoretical basis and this is discussed in Section 2.9. Validation of the loss implementation in Section 2.9 is highlighted as an area of future research. The new loss implementation causes a spread of data in the high-induction region depending

on the loss factor F. This agrees with the findings of Lock *et al.* [1926] in high-induction and a similar present day experiment is of vital importance to simulating the effect and validating these simulations. This formulation gives an improvement in both C_p and C_{fa} and, in particular, eliminates the constant underprediction of C_{fa} when compared to experimental data. This formulation is unvalidated and is an area of further work.

Chapter 3

Onset Flow: Depth Profile and Waves

3.1 Introduction

In Chapter 2 an analytical blade element momentum theory, BEMT, scheme is outlined and the suitable corrections to the unrealistic assumptions of momentum theory are discussed. A further assumption of momentum theory is that the innate, undisturbed flow far upstream, at the turbine and far downstream are equal, i.e. the turbine is operating in steady state. A time independent but depth dependent velocity profile create unsteady state, as the streamwise velocity incident to the blade changes as the blade rotates. As a consequence the relative velocity and inflow angle of the flow incident to the blade are both time-varing. Therefore the local blade element flow velocity, previously defined as V, changes with time when considering a rotating turbine in depth dependent flow, however the axial inflow velocity, defined as U, is time independent.

BEMT can be progressed in an iterative scheme with a discrete change in state between iterations; such as a change in time or Ω. Consider an arbitrary change in the innate flow velocity. Steady state is not reached instantaneously, as there is a reaction time associated with the wake. This creates an instant when the velocity far upstream is produced by the new flow regime and the wake after the turbine represents the old flow regime. Since the blade element velocity is shown in Chapter

2 to be dependent on the helical wake and the far up-steam velocity, the result is not steady state.

The discrete time step size is made conservatively small so that the turbine performance is sensitive to dynamic inflow changes only. However, the wake reaction time makes the turbine resistive to change where the limiting factor is the wake reaction time. Freeman *et al.* [2009] gives a model for the response of a tidal turbine under the influence of waves as oscillatory motion. Dynamic inflow was implemented in the form of the Sears function. The results show that the specific turbine modelled was insensitive to low frequency oscillations of 0.01Hz but was more sensitive to higher frequencies, around 1Hz. BEMT simulation of the two cases would give no difference in the sensitivity of the turbine; as steady state is assumed at each iterative step the turbine is completely responsive to all dynamic inflow changes, irrespective of timespan or amplitude.

When investigating dynamic inflow, the wind industry has focused experimental efforts on pitch changes in the air flow rather than speed changes. Dynamic inflow theory is discussed in Whelan [2010]. It originates from two phenomena. Firstly, the circulation contained within the helical wake of the turbine and, secondly, the vorticity of the shed wake. This second effect comes from changes of the circulation at the blade section. Both these effects contribute to the time history of the induced velocity at the rotor plane. In Whelan [2010] it is stated that the relationship between these effects is complex and a full three dimensional investigation is needed to uncouple them. However, at low turbine rotational speeds the trailing vorticity dominates the wake as the vorticity of the shed wake from the blades is low. In this case the trailing vorticity dictates the time lag of dynamic inflow. In Whelan [2010] the reaction time lag in the trailing vorticity is implemented as a pseudo added mass correction.

In Snel [2004], dynamic inflow is alternatively derived from the time varying load on a wind turbine and a characteristic time scale of the effect is suggested as the order of the diameter of the rotor over upstream flow speed. A typical tidal turbine, of diameter 10m, in a flow speed of $4ms^{-1}$ gives the time lag a typical length scale of 2.5 rotor revolutions. Considering a 10m diameter rotor in these conditions, the optimum TSR value will be around 4.5, which gives the rotations per second as 0.25. Therefore it will take at least 10 seconds for steady state to be recovered. Throughout this time, BEMT predictions will be strictly incorrect. Waves continuously alter the

speed of the incoming flow therefore it is important to consider dynamic inflow in turbine models that include waves. In the wind industry, semi-empirical corrections to quasi-steady blade element methods are used.

Considering the non-varying investigations presented in 2.7, the TSR step was set to a constant, and conservative value of 0.12 to avoid the low convergence present when the iterative change is too large. To give the CPU usage order of magnitude, considering a standard desktop PC in 2013, the first TSR step requires $\simeq 120s$ of CPU time to calculate, due to the first iteration Monte-Carlo selection scheme, described in more detain by Chapman [2009], and all TSR steps thereafter only require $\simeq 2.5s$ of CPU time. The maximum TSR= 12 is reached in $< 370s$.

The simplicity of BEMT, results in fast computations, however the size of the iterative step must be conservative to give meaningful results from the steady state momentum theory. Dynamic inflow is considered by this scheme by reducing Δt to linearise the BEMT equations to solve in time in a similar way to the TSR iterative steps. Therefore direct simulation of dynamic inflow is avoided by setting conservative iteration steps. It is noted that this is a limitation of BEMT and iteration step size is a particularly important consideration for turbulent dynamic inflow simulations. For a regular wave the scheme is shown to converge well and gives meaningful turbine performance results as presented in chapter 4.

3.2 Regular, Non-Linear Wave Theory

Although BEMT assumes steady state, a time stepping sequence has been implemented by Chapman [2009] in this model to consider varying inflow in the form of Chaplin's stream function wave theory. In Chapter 3, a theoretically compatible BEMT and varying inflow scheme is developed.

This section introduces Chaplin's stream function wave theory as a BEMT compatible representation of regular, non-linear waves. In Appendix A, the stream function theory is introduced. The coupling method with BEMT is discussed in following chapters as well as the effect on the acceleration forces on the turbine. A method of simulating the effect of the tidal flow on the wave non-linearity, using Chaplin's stream function wave theory is outlined.

The stream function wave theory describes a 2D periodic wave of permanent form, in non-rotational and incompressible flow. The frame of reference moves with wave speed C, reducing the problem to one of constant flow. Consider a wave that is periodic in x with wavelength L and is symmetric about a vertical plane through the crest. A stream function through the fluid is defined below as $\Psi(x, y)$. In a similar way to linear wave theory $\frac{\partial \Psi}{\partial y} = v$ but, due to the moving frame of reference, $\frac{\partial \Psi}{\partial x} = u - C$. The problem is defined in the same way as finite-depth, linear wave theory and similar boundary and flow conditions apply. Appendix A describes this approach in more detail.

3.3 Irregular Wave Theory

Tidal turbines can be designed to minimise wave load. If the site specific, extreme wave variables are known, regular wave theory can be effectively used to investigate the turbine loadings and response for an incident extreme wave. However, to investigate turbine operating dynamics and long term fatigue, the incident wave climate must be considered irregular. The operating cyclic loadings created by waves are determined by simulating a realistic wave climate.

The instantaneous wave climate over a body of water is quantified by a combination of many regular waves of differing wave height, frequency and period. The transient wave front over a fixed point in the body of water is therefore unsteady and contains a degree of randomness in both shape and direction. To correctly simulate a real sea, the combination and direction of regular waves to create a sea state can be considered a stochastic process.

Probability theory can be applied to both the wave frequency, in the form of sea spectra, and wave height using the Rayleigh distribution. A sea state spectrum is the energy density spectrum against wave frequency and shows the total energy contained in the wave climate is distributed between the component wave frequencies. Sea spectrum used in literature to describe the irregular wave theory of wind wave states is introduced in Chapter 1. This chapter considers the relevance of these sea spectra as statistical representations of multiple waves for the application of tidal stream turbine modelling, in particular blade element momentum theory.

The spectra can be used to describe linear, fully developed sea swells as well as developing, limited fetch seas and also non-linear, shallow water wave states. The dependency of the spectra on variables such as significant wave height, $H_{1/3}$, significant wave period, $T_{1/3}$ and wind speed are analysed. The relation between $H_{1/3}$ and the Rayleigh statistical distribution of wave heights is used to determine discrete wave heights.

The method of simultaneously discretising the sea spectra and Rayleigh wave height distribution to create a set number of incident waves is presented in Section 3.6. This section also recovers the frequency domain result from the simulation inflow and compares this to the sampled wave spectrum as a validation of the method.

Figure 3.9, considers the frequency domain comparison of this time series and a good agreement is found between the sampled sea spectrum and the resultant time series, particularly when considering the moving average result for the same data as in Figure 3.10. However, is clear that, when the crests of superimposed waves combine, unrealistic wave heights are produced. In reality, when wave crests combine, the wave is likely to become unstable and break causing a reduction in wave height as specified in Goda [2010]. For wind wave sea states, wave breaking is not spatially regular. Wave breaking is found far offshore and far inshore, however other unbroken wave trains can propagate close to the shore. The hydrodynamics of this wave breaking zone is discussed by Goda [2010] for regular waves. This effect is significant, therefore this section introduces a wave breaking model to simulate this effect for irregular waves.

3.3.1 Bretschneider-Mitsuyasu Spectra

The Bretschneider-Mitsuyasu Spectrum was proposed by Bretschneider [1968] by adjusting the Mitsuyasu coefficients and can be found in Goda [2010]. Many variations of this spectrum exist, the most popular being the P-M spectrum defined in Chapter 1. The B-M spectrum is more suitable to this application, as the spectrum is derived dependent on the wave variables, $H_{1/3}$ and $T_{1/3}$ instead of the wind properties. The B-M spectrum definitions of A and B, given by Equations 3.1 and 3.2, are substituted

into Equation 1.4 in this model.

$$A = C1_{\mathrm{BM}} H_{1/3}^2 T_{1/3}^{-4} \tag{3.1}$$

$$B = C2_{\mathrm{BM}} T_{1/3}^{-4} \tag{3.2}$$

$C1_{BM}$ and $C2_{BM}$ are the B-M spectrum constants, originally defined from observations as 0.257 and 1.03 respectively, as shown in figure 3.1. These original values assume the relation $T_p \simeq 1.05 T_{1/3}$ for wind waves. However it is stated in Goda [2010] that later measurements by Mitsuyasu suggest $T_p \simeq 1.1 T_{1/3}$, which leads to the modified values for $C1_{BM}$ and $C2_{BM}$ of 0.205 and 0.75.

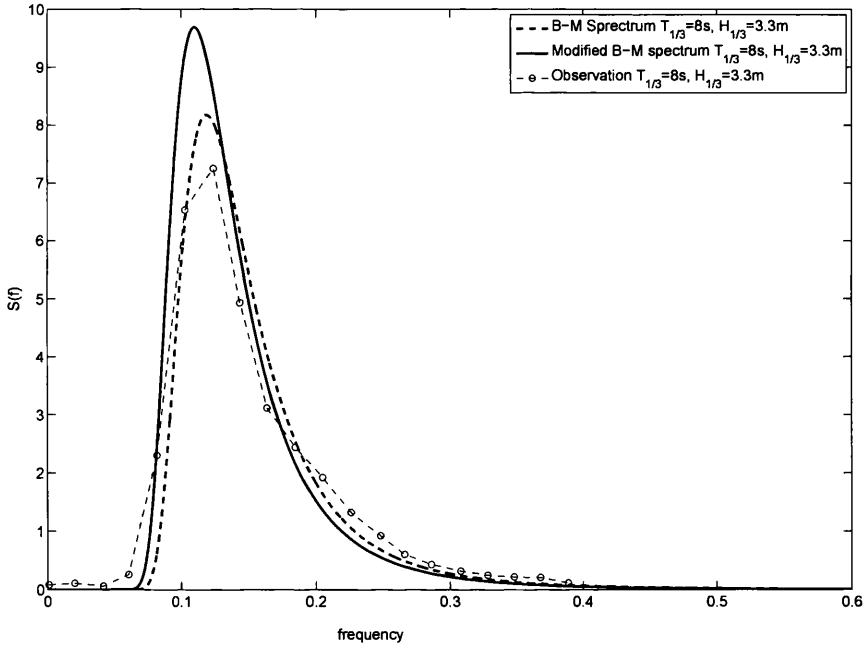

Figure 3.1: The Bretschneider-Mitsuyasu wave frequency, energy density spectrum, $S(\omega)$, units $\mathrm{m}^2/(\mathrm{rad}s^{-1})$, for $H_{1/3} = 3.3\mathrm{m}$ and $T_{1/3} = 8\mathrm{s}$. Compared to the observations, from Goda [2010] and the refined modified B-M spectrum.

Both the original and modified versions can be specified in this model, however the modified B-M spectrum is considered by Goda [2010] as a better representation for a fully developed wind wave sea state. Bretschneider [1968] proposed omission of

the dependency in Equation 1.7, to produce the more flexible two parameter spectra described here which depends on both wave height and frequency. One parameter spectra, dependent on $H_{1/3}$ are suitable for a swell dominated sea and two parameter spectra are more suited to wind waves dominated seas. Figure 3.1 shows good agreement between the wave record and the B-M spectrum. The wave record was taken in 11m depth water. The shallow water effect on sea spectra is to increase the spectral density at frequencies above peak frequency and this can bee seen for $f > 0.2$Hz.

3.3.2 JONSWAP Spectra

Fully developed seas require a large fetch and are found in large bodies of water, such as the Atlantic Ocean. However strong winds are unsustainable for long periods of time, therefore developing seas are more common and more widely found. They are sensitive to any change in the wind direction or intensity. For a developing sea, the spread of energy density over the wave frequencies is different to that of a developed sea. The energy spectrum peak will have a smaller standard deviation and this is not captured by the two parameter B-M spectrum, despite having $T_{1/3}$ as an input variable. In 1973 Hasselmann *et al.* [1973] devised the JONSWAP spectrum as part of the Joint North Sea Wave Project as a suitable sea spectrum for a developing sea state by multiplying the modified B-M spectrum by a peak enhancement factor function, $G_p(f,\gamma)$, given in Equation 3.4. The variable γ is the peak enhancement factor.

$$S(f)_{\text{JONSWAP}} = S(f)_{\text{MODIFIED B-M}} G_p(f) \tag{3.3}$$

with,

$$G_p(f) = \gamma \left(\exp \left[-\frac{1}{2} \left(\frac{f - f_p}{\sigma(f) f_p} \right)^2 \right] \right) \tag{3.4}$$

The standard deviation of $G_p(f)$ either side of the peak is considered non-symmetric,

$$\sigma = \begin{bmatrix} \sigma_a & \text{for } f < f_p \\ \sigma_b & \text{for } f > f_p \end{bmatrix} \tag{3.5}$$

This gives maximum flexibility in sea state representation. Large scatter was found for the values of γ, σ_a and σ_b and so the constant average values are commonly used.

$\gamma = 3.30$
$\sigma_a = 0.07$
$\sigma_b = 0.09$

The B-M values for A and B in $S(f)$ are given in Equations 3.1 and 3.2 respectively. However, in Goda [2010], the relationship between T_p and $T_{1/3}$ is considered non-linear for the JONSWAP sea spectrum and dependent on the the value of the peak enhancement factor, γ, as shown in Equation 3.6. Therefore, the A and B are now given in Equations 3.7 and 3.8.

$$T_p \simeq T_{1/3} / \left[1 - 0.132\left(\gamma + 0.2\right)^{-} 0.559\right] \tag{3.6}$$

$$A = C1_{JONSWAP} H_{1/3}^2 T_p^{-4} \tag{3.7}$$

$$B = C2_{JONSWAP} T_p^{-4} \tag{3.8}$$

$C2_{JONSWAP}$ is simply the constant 1.25. However,

$$C1_{JONSWAP} = \frac{0.0624}{0.23 + 0.0336\gamma - 0.185\left(1.9 + \gamma\right)^{-1}} \left[1.094 - 0.01915 \ln \gamma\right] \tag{3.9}$$

With the peak enhancement factor set to 1, the B-M spectrum is recovered from the JONSWAP spectrum, as in figure 3.2. In the Joint North Sea Wave Project the value for γ was found from wave records to be between 1 and 7 and so the mean value of 3.3 is used for limited fetch wave spectra. Figure 3.2 also compares the JONSWAP sea spectra with these maximum and minimum of $\gamma = 1$ and $\gamma = 7$ to the mean value of $\gamma = 3.3$.Increasing the peak enhancement factor, γ, is shown to indeed enhance the $S(f)$ values around peak f.

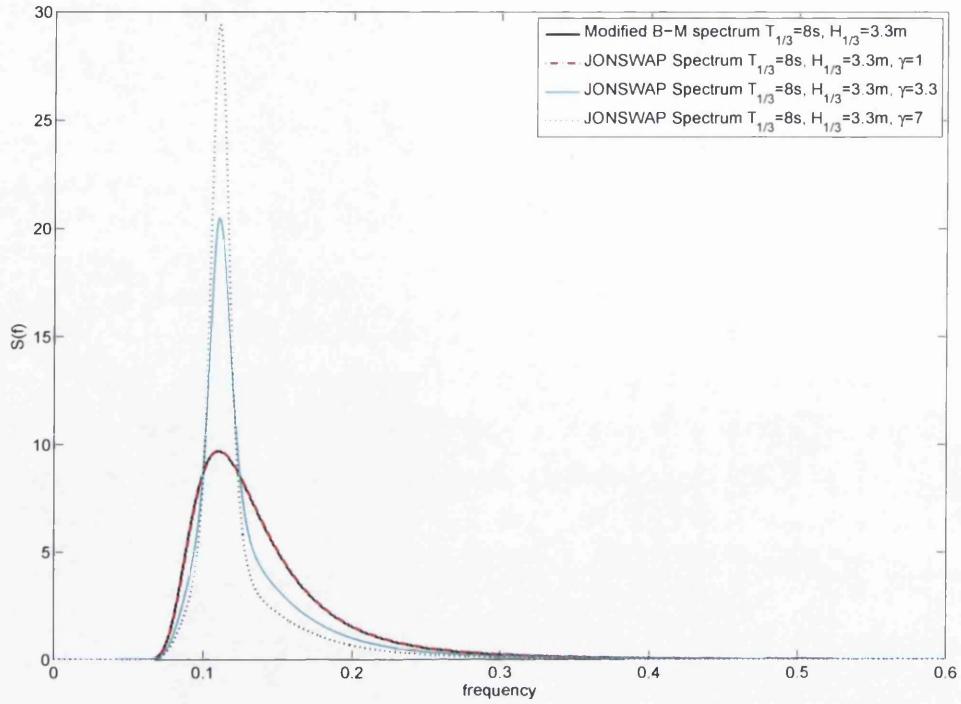

Figure 3.2: The JONSWAP wave frequency, energy density spectrum, $S(\omega)$, units $\mathrm{m}^2/(\mathrm{rads}^{-1})$ suitable for the limited fetch North Sea with peak enhancement factor, $\gamma = 3.3$. Compared to minimum $\gamma = 1$ and maximum $\gamma = 7$ as found in the North Sea Goda [2010]. Also compared to the modified Bretschneider-Mitsuyasu wave frequency, energy density spectrum, $S(\omega)$, units $m^2/(\mathrm{rads}^{-1})$. In all cases, $H_{1/3} = 3.3\mathrm{m}$ and $T_{1/3} = 8\mathrm{s}$.

Figure 3.3(a) uses the modified B-M spectrum to show that increasing significant wave height, $H_{1/3}$, increases the spectral density, i.e. there is more energy in the waves at all wave frequencies, but does not effect the peak frequency. However, in figure 3.3(b) the effect of significant wave period on sea spectra is considered and it shows how increasing $T_{1/3}$ decreases peak wave frequency, as expected, but also increases the spectral density. To compare with JONSWAP spectra, figures 3.4(a) and 3.4(b) consider the same change in $H_{1/3}$ and $T_{1/3}$ respectively. A similar result is found, therefore for both spectrum representations $H_{1/3}$ dictates the area under the $S(f)$ curve and therefore the total energy in the wave climate and $T_{1/3}$ determines the peak frequency.

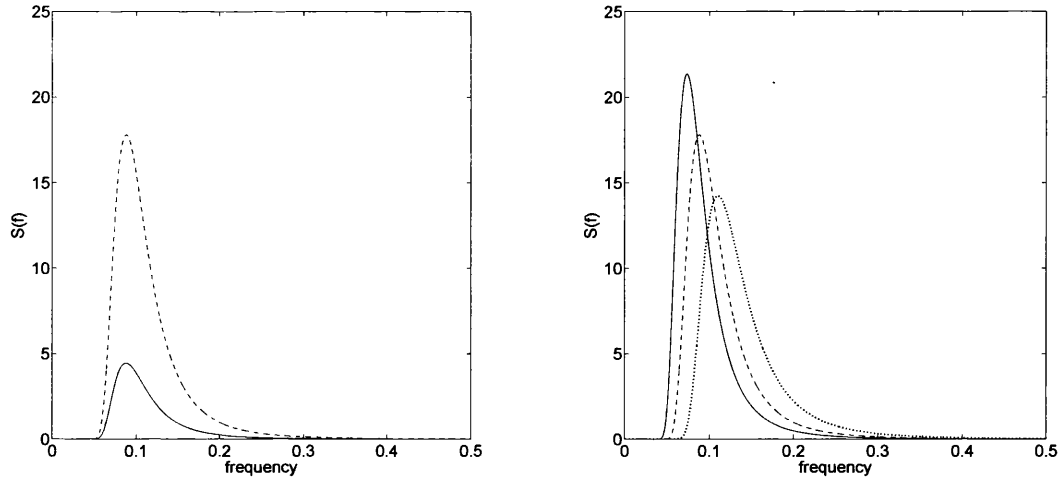

(a) (b)

Figure 3.3: Modified B-M energy density spectrum, $S(\omega)$ m^2/(rads^{-1}). (a) $H_{1/3} = 2$m compared to $H_{1/3} = 4$m with a fixed $T_{1/3}$ of 10s. (b) Fixed $H_{1/3} = 4$m with $T_{1/3}$ of 10s, $T_{1/3} = 12$s and $T_{1/3} = 8$s.

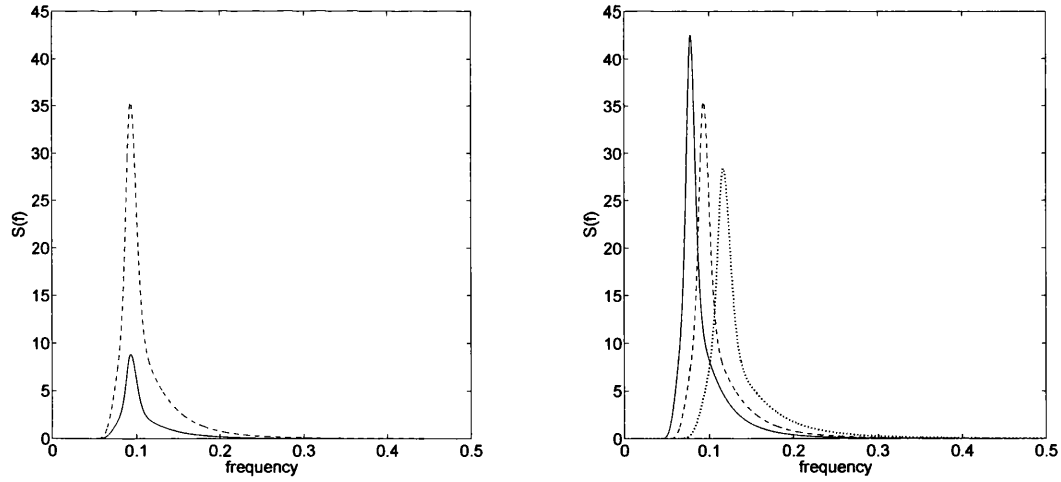

(a) (b)

Figure 3.4: JONSWAP energy density spectrum, $S(\omega)$, m^2/(rads^{-1}), $\gamma = 3.3$. (a) $H_{1/3} = 2$m compared to $H_{1/3} = 4$m with a fixed $T_{1/3}$ of 10s. (b) Fixed $H_{1/3} = 4$m with $T_{1/3}$ of 10s, $T_{1/3} = 12$s and $T_{1/3} = 8$s.

3.3.3 TMA Spectra

The B-M and JONSWAP spectra describe fully developed and developing wave climates in deep water. Considering the application in this work, the turbine site may be shallow where non-linear effects become significant. The sea spectrum derived from data in figure 3.1 is effected by shallow water non-linearity and $S(f)$ at high frequencies is higher that predicted by the modified B-M spectrum. The TMA spectrum, proposed by Tucker [1995], extends the JONSWAP spectrum to consider a finite depth sea state by implementing the non-linear wave effect onto the sea spectrum, Goda [2010]. The non-linearity of the sea spectrum is implemented onto $S(f)_{\text{JONSWAP}}$ by multiplication with a depth-dependent function $M(h_r)$, where h_r is the water height, H_s, relative to mean wave height, $\hat{h_\omega}$.

$$M(h_r) = \frac{H_s}{\hat{h_\omega}} \tag{3.10}$$

$$S(f)_{TMA} = S(f)_{\text{JONSWAP}} M(h_r) \tag{3.11}$$

where,

$$M(h_r) = \frac{\tanh^2 h_r}{1 + 2h_r / \sinh 2h_r} \tag{3.12}$$

Figure 3.5 shows the effect of h_r on the sea spectrum against frequency. With $h_r \simeq 5$ the deep water JONSWAP result is recovered and the non-linear wave effects are insignificant. Figure 3.6 considers the TMA spectrum to describe the wave record sea spectrum data, plotted in 3.1. By setting h_r to 2.45, the TMA spectrum gives a better fit to the data compared with the B-M spectrum. This is due to a water depth of 11m with a significant wave height of 3.3m. However, considering h_r as specified by Tucker [1995], $h_r = 5.32$. Figure 3.5 shows how this value would have little effect on the sea spectra and it is suggested that $h_r/2$ is used instead.

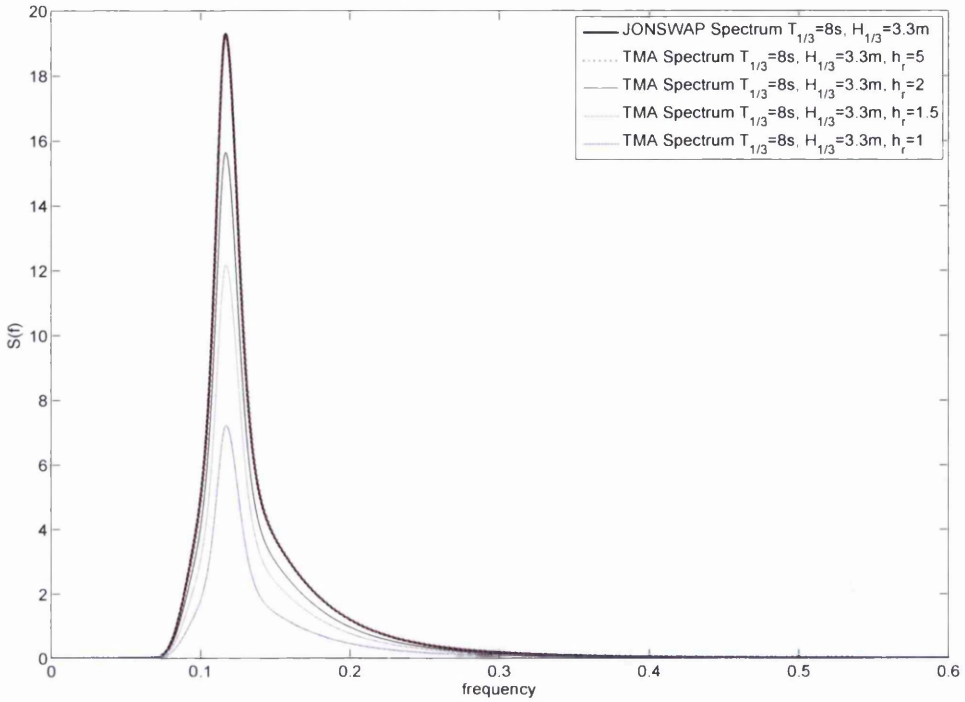

Figure 3.5: The shallow water TMA wave frequency, energy density spectrum, $S(\omega)$, units $m^2/(rads^{-1})$ compared to the JONSWAP spectrum. Fixed $H_{1/3} = 3.3$m with a $T_{1/3}$ value of 8s. Relative water height is consider by comparing $h_r = 5$, $h_r = 2$, $h_r = 1.5$ and $h_r = 1$.

3.4 2D Wave Frequency Spectra

By observing a wind wave sea state for any length of time, it is clear that the discrete waves do not travel in the same direction. A directional 2D wave spectrum, $S(\theta_f, f)$ is presented in Goda [2010] by introducing a directional spreading function term, $G(\theta_f, f)$. A correlation is found between wave frequency and G therefore G is also found dependent on f. Any sea 1D wave spectrum, $S(f)$, can now be written as the 2D wave spectrum given in Equation 3.13 as found in Goda [2010].

$$S(\theta_f, f) = S(f)G(\theta_f, f) \tag{3.13}$$

$G(\theta_f, f)$ is a scaling function that represents the relative magnitude of the direc-

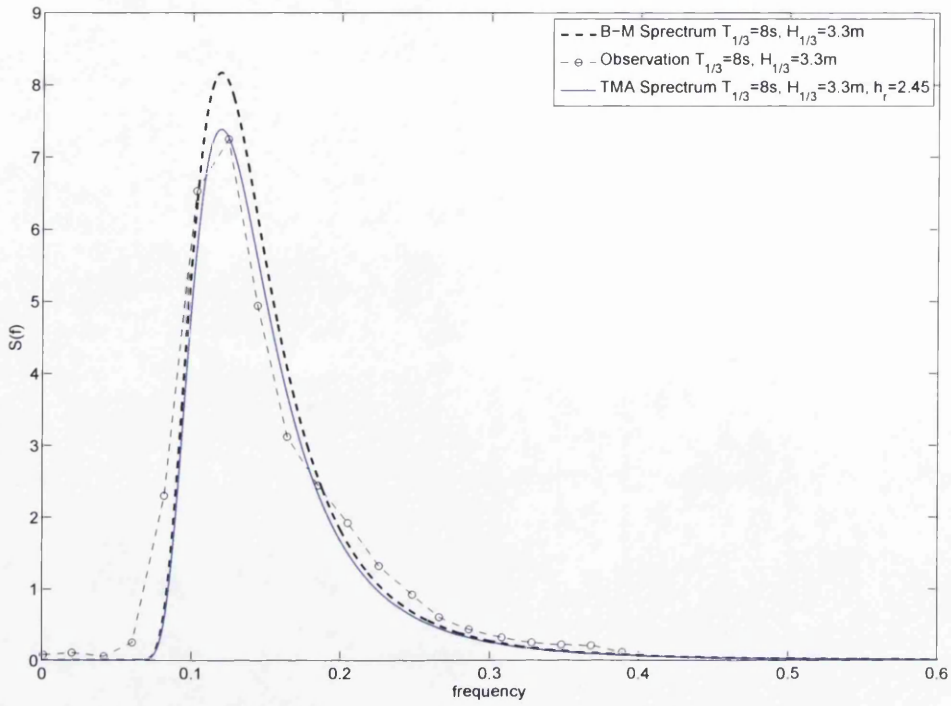

Figure 3.6: Figure 3.1 with the addition of the shallow water TMA wave frequency, energy density spectrum, $S(\omega)$, units $\mathrm{m}^2/(\mathrm{rad}s^{-1})$, with $h_r = 2.45$.

tional spreading of the sea state energy whereas $S(f)$ is the absolute value of the wave energy density. Although the directional spreading function is an important consideration for accurate wave energy density simulation, it must be considered in the context of the application. As BEMT determines the turbine performance from the inflow properties in the plane of the turbine rotation only, the wave density field does not need to be accurately simulated over a larger domain. Therefore the effect of $G(\theta_f, f)$ on the turbine performance results will be minimal.

3.5 Irregular Wave Heights

3.5.1 The Rayleigh Distribution

The sea spectrum is purposely defined so that the area under the curve is the variance of the wave time history and is equal to the mean amount of total energy in the instantaneous sea. The significant wave height, $H_{1/3}$, is solely dependent on the time series variance and can therefore be set by the sea spectrum and wind speed. The Rayleigh distribution is widely used as the statistical probability of the occurrence of various wave heights in any sea state. Therefore using $H_{1/3}$ from the sea spectrum, the component wave heights are determined. The probability that a wave height is between H and $H + dH$ is,

$$p(H)dH = \frac{2H}{\bar{H}^2} e^{-\frac{H^2}{\bar{H}^2}} dH \tag{3.14}$$

p(H) is the probability percentage of wave height H and $\bar{H}^2$ is the average of the square of the wave heights in the spectrum, Michel [1999]. Considering the spectrum contains N waves,

$$\bar{H}^2 = 1/N \sum_{i=1}^{N} H_i^2 \tag{3.15}$$

From the definition of the wave frequency spectral energy density, $S(\omega)$, as $1/2A^2$ and remembering that the area under the curve, m_0, is the total energy of the irregular wave front,

$$H_{1/3} = 4\sqrt{m_0} = 4\sqrt{\frac{1}{N} \sum_{i=1}^{N} 1/2A_i^2} \tag{3.16}$$

$$H_{1/3}^2 = \frac{16}{N} \sum_{i=1}^{N} 1/2A_i^2 = \frac{8}{N} \sum_{i=1}^{N} A_i^2 = \frac{2}{N} \sum_{i=1}^{N} H_i^2 \tag{3.17}$$

Therefore,

$$H_{1/3} = 2\bar{H}^2 \tag{3.18}$$

This can be directly substituted into the Rayleigh distribution to give the probability in terms of $H_{1/3}$ as in Michel [1999].

$$p(H)dH = \frac{4H}{H_{1/3}^2} e^{-2\frac{H^2}{H_{1/3}^2}} dH \tag{3.19}$$

The probability that a wave height exceeds the wave height H_e is given by the integral,

$$p(H > H_e) = \int_{\frac{2H_e^2}{H_{1/3}^2}}^{\infty} e^{-2\frac{H^2}{H_{1/3}^2}} d\left(\frac{2H^2}{H_{1/3}^2}\right) \tag{3.20}$$

The average wave height, H_a, of the component waves in the sea state can now be determined as the sum of each wave height multiplied by its probability.

$$\frac{H_a}{H_{1/3}} = \frac{1}{\sqrt{2}} \int_0^{\infty} \left(\frac{2H^2}{H_{1/3}^2}\right)^{\frac{1}{2}} e^{-\frac{2H^2}{H_{1/3}^2}} d\left(\frac{2H^2}{H_{1/3}^2}\right) \tag{3.21}$$

The integral is in fact a definite integral and therefore can be easily solved as,

$$\frac{H_a}{H_{1/3}} = \frac{1}{\sqrt{2}} \Gamma\left(\frac{3}{2}\right) \tag{3.22}$$

$$H_a = \frac{1}{2}\sqrt{\frac{\pi}{2}} H_{1/3} \tag{3.23}$$

For example, Figure 3.7 shows the Rayleigh distribution for $U_{wind} = 20\text{ms}^{-1}$. The significant wave height and mean wave height are shown.

Considering the relationship between the wave height and sea state energy density spectra, Section 3.6 discusses further the discretisation and implementation method. This combines the sampling of sea spectrum with the Rayleigh distribution into one inflow wave model to determine a set of discrete wave heights and wave periods. These

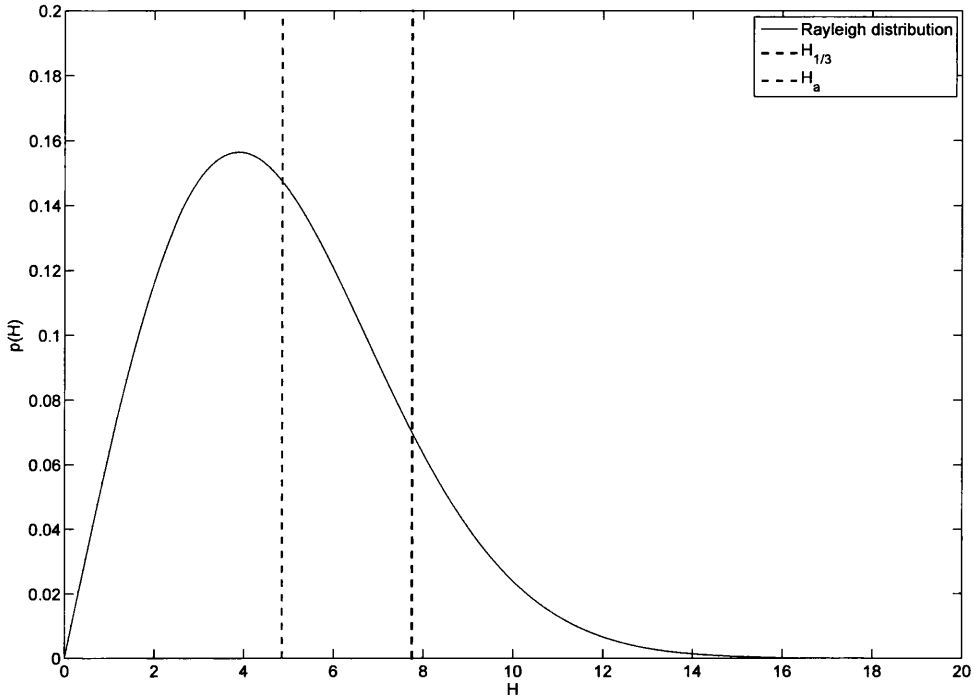

Figure 3.7: The Rayleigh distribution for wave height probability against wave height with significant wave height and mean wave height. Wind speed=20ms^{-1}.

waves are superimposed using a random element and Figure 3.8 gives an example resultant water surface elevation.

3.5.2 Breaker Model

A wave breaking height, h_b, is defined for a specific wave spectrum to simulate the instability cause by large irregular wave elevations after superimposition of the discrete regular waves. Incident breaking of random waves is introduced by Kamphius in Goda [2010] and Equation 3.25 is derived from the breaker index formula. The breaker index formula is applicable to regular waves and gives a breaking height, dependent on wave height and frequency therefore, for a regular wave, h_b is a constant.

For this simulation the wave train of figure 3.8 is irregular. To extend the breaker index formula to irregular waves, the usually constant value of wavelength L is replaced with L_{temp}, the temporary wave period. This value is the distance between

the local zero crossing point and turning point of the surface elevation and a variable for irregular waves.

$$L_{\text{temp}} = 4(x_{\text{turning}} - x_0) \tag{3.24}$$

where x_{turning} is the horizo$L_{\text{temp}} = 4(x_{\text{turning}} - x_0)$cal turning point in m and x_0 is the horizontal location of the local zero crossing point. Both of these values are temporary and vary with x position.

h_b is now dependent on the local wavelength, L_{temp}, and therefore h_b is real time dependent.

$$h_b = \frac{\log(1 + (H_s/(0.12L_{\text{temp}})))L_{\text{temp}}}{3\pi} \tag{3.25}$$

Figure 3.11 compares the simulated water elevation with and without the limiting wave height, h_b, for a single case. Further investigation of the wave breaker simulation could include other case studies. However, as a preliminary study, this case considers the wave height, H_s, as limited by a water depth of 45m. Figure 3.12 shows that the irregular breaker index formula acts to decrease large amplitude and, as before, the moving average result is considered in Figure 3.13. $S(f)_{MAX}$ decreases from about 22 to 12 and the majority of lower $S(f)$ values agreeing with the sampled sea state are maintained. However, Sf_{MAX} is still over double the sampled sea state and some $S(f)$ values below the sampled sea state are effected. This is due to random, small L_{temp} values.

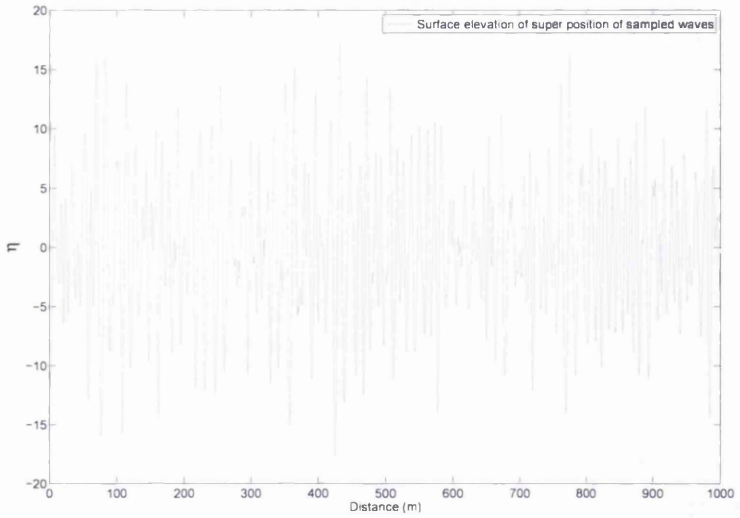

Figure 3.8: Surface elevation for a simulated B-M spectrum wave climate with $H_{1/3} =$ 2m and $T_{1/3} = 7$s without breaking limit.

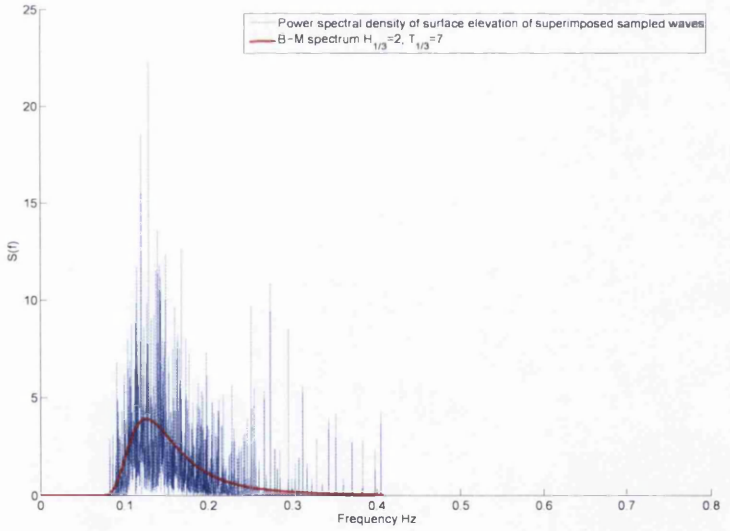

Figure 3.9: The B-M wave spectrum, with $H_{1/3} = 2$m and $T_{1/3} = 7$s, compared to the recovered energy density spectrum of the simulated wave climate, as plotted against time in figure 3.8.

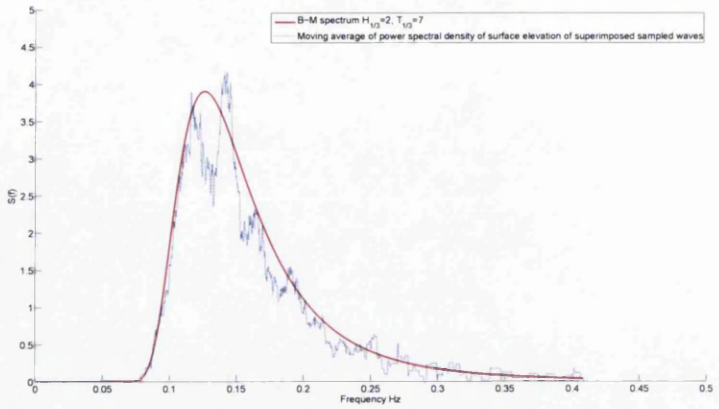

Figure 3.10: The B-M wave spectrum, with $H_{1/3} = 2$m and $T_{1/3} = 7$s, compared to the moving average of the recovered energy density spectrum of the simulated wave climate, as plotted against time in figure 3.8.

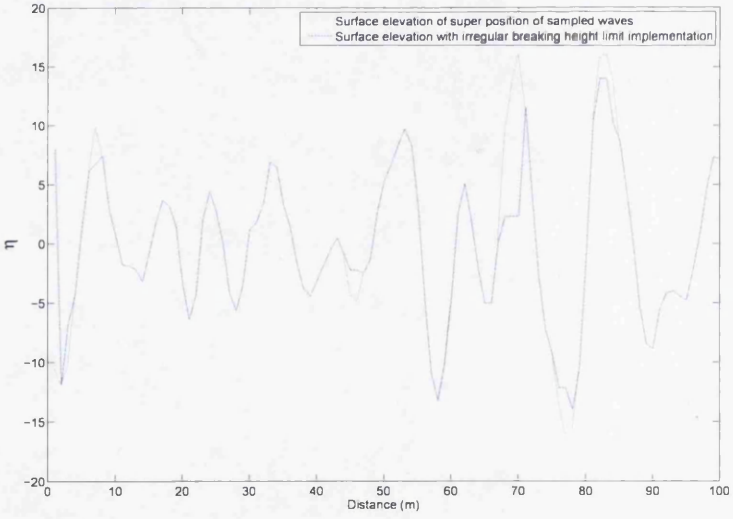

Figure 3.11: Surface elevation for a simulated B-M spectrum wave climate with $H_{1/3} = 2$m and $T_{1/3} = 7$s compared to the surface elevation with the proposed time varying breaker limit, h_b, as defined in Equation 3.25, with water depth, H_s, set to 45m.

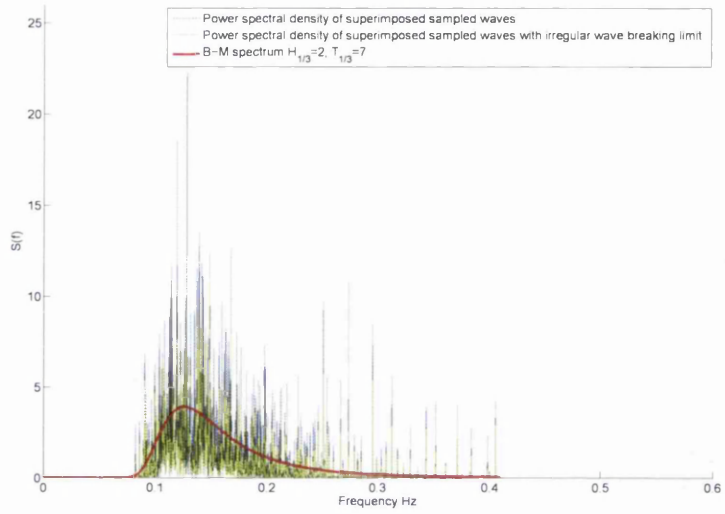

Figure 3.12: The B-M wave spectrum, with $H_{1/3} = 2$m and $T_{1/3} = 7$s, compared to the recovered energy density spectrum of the simulated wave climate with the wave breaker limit h_b, as plotted against time in figure 3.11.

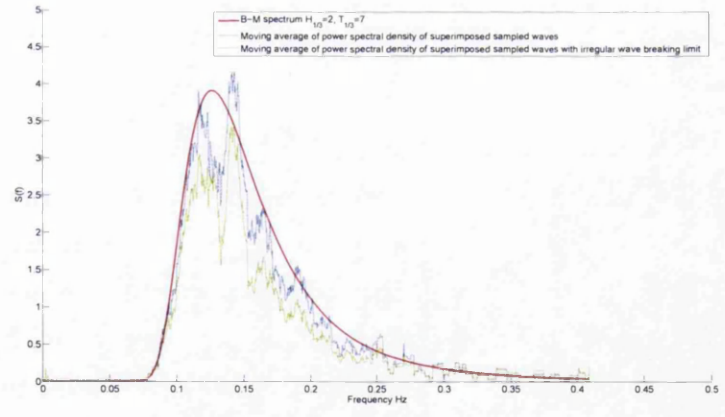

Figure 3.13: The B-M wave spectrum, with $H_{1/3} = 2$m and $T_{1/3} = 7$s, compared to the moving average of the recovered energy density spectrum of the simulated wave climate with the wave breaker limit h_b, as plotted against time in figure 3.11.

3.6 Irregular Wave Implementation

The sea state spectrum and the Rayleigh distribution are continuous probability spectra and give details about the surface waves as a whole sea state. They do not consider the effect of depth on the waves through the water column. Chaplin stream function wave theory has been used to create the velocity and acceleration profiles of regular non-linear waves on the free surface and through the water column. Therefore the Rayleigh distribution is used together with the sea spectrum to discretise wave height and period into a set of regular waves present in the irregular sea state.

The regular wave values are then superimposed with a random phase shift factor. This creates an irregular incident wave front, the characteristics of which originate from the sea spectrum definition. All waves are assumed to propagate in the same direction.

The scheme can be used to determine the effect of tidal velocity on the sea spectra. The simple coupling between waves and tides is considered with 0ms^{-1} tidal velocity, $+2.1\text{ms}^{-1}$ tidal velocity and -2.1ms^{-1} tidal velocity. Figure 3.14 presents the effect of the tidal velocity on the wave frequencies by comparing the reconstructed sea spectra. It is shown that, with tidal flow in the wave propagation direction the apparent wave frequencies over the turbine site is increased. In a similar way, tidal flow opposing the wave propagation direction decreases the wave frequencies. For the increased wave frequency, the high energy peak at 0.77Hz is a unphysical numerical result and neglected in th time series result.

The computational method randomly samples N wave heights from the Rayleigh distribution. Now that the wave heights are set, the definition of sea spectra can be used to find the wave frequencies. As the area under the sea state curve is representative of the average energy in the sea state, there are two common ways to deduce these frequencies, USFOS Theory Manual [1993]. The first is to assume that each wave occupies an equal amount of area under the curve, i.e. all waves have the same amount of energy and therefore the same amplitude. The second approach is to have equal spacing between the wave frequencies. This way, the corresponding area under the curve varies which leads to variable wave amplitudes, USFOS Theory Manual [1993].

Alternatively, this approach considers the amount of energy contributed by a single

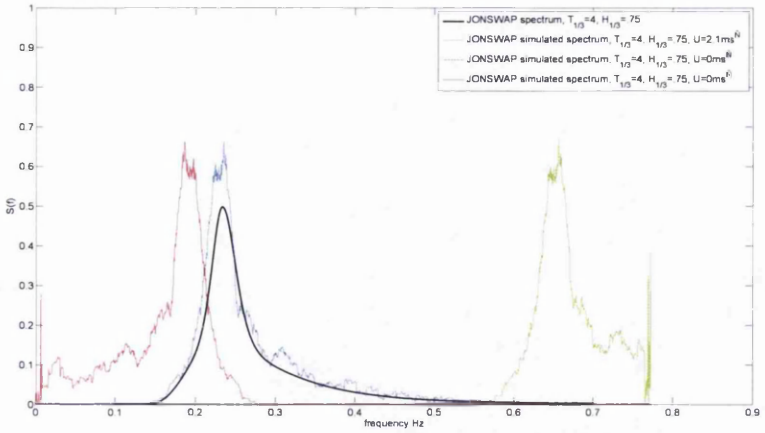

Figure 3.14: The prescribed sea spectrum, $S(f)$, against the wave frequency f and also compared to the moving average of the power spectral density of the water elevation produced by the simulation, with no tidal flow, tidal flow in the wave propagation direction, 2.1ms^{-1}, and tidal flow velocity -2.1ms^{-1}, i.e. against the wave propagation.

wave, i.e. the area occupied under the sea spectrum, is calculated from the Rayleigh distribution wave heights. It is first assumed that highest waves occupy the low frequency part of the spectrum and the wave heights are sorted in descending order. Then the area under the curve can be written as a sum of the component discrete wave areas,

$$\int_0^\infty S(\omega)d\omega = \sum_{i=1}^{N} \int_{\omega_i}^{\omega_{i+1}} S(\omega)d\omega \tag{3.26}$$

where the area for wave i lies between ω_i and ω_{i+1}. As i increases from 1 to N, wave height decreases. If the lower limit of the first area is set to $\omega_1 = 0$ and the upper limit of the last area is set to $\omega_{N+1} = \infty$ then these areas can become unreasonably large. Alternatively, the standard deviation for proportion of the curve before the peak, σ_L, is calculated and ω_1 is set to the corresponding ω value at $S(\omega_P) - 1\sigma_L$. In a similar way, the standard deviation for the proportion of the curve after peak, σ_U, is used to calculate ω_N as $S(\omega_P) + 1\sigma_U$. Equating the sum of the integrals to the

average,

$$\frac{1}{N}\sum_{i=1}^{N} 1/2A_i^2 = \sum_{i=1}^{N}\int_{\omega_i}^{\omega_{i+1}} S(\omega)d\omega \tag{3.27}$$

This equality can be considered for a single wave as,

$$\frac{1}{8N}H_i^2 = \int_{\omega_i}^{\omega_{i+1}} S(\omega)d\omega \tag{3.28}$$

Considering a sea state, for example as defined in Equation 1.4, and solving for the integral,

$$\frac{1}{8N}H_i^2 = \frac{A}{4B}\left[e^{-B\omega_{i+1}^{1/4}} - e^{-B\omega_i^{1/4}}\right] \tag{3.29}$$

For $i = 1$, ω_i has been previously set. Also H_i is the highest wave in the Rayleigh distribution. The unknown is $\omega_{i+1} = \omega_2$.

$$\omega_{i+1} = \left(-B\left(\ln\left[\frac{4B}{A8N}H_i^2 + e^{-B\omega_i^{1/4}}\right]\right)^{-1}\right)^{1/4} \tag{3.30}$$

In this way, the area under the energy density curve is dependent on the height. This area decreases with decreasing H, as i increases from 1 to N. This process iterates, increasing i, and at each step ω_{i+1} is found and used as ω_i for the next iteration.

The wave angular frequency, ω, is found for each wave as,

$$\omega = \omega_i + \frac{(\omega_{i+1} - \omega_i)}{2} \tag{3.31}$$

The discrete wave variables are now used as input variables in turn for the stream function wave theory which produces velocity and acceleration grids through the water column for each regular, non-linear, single wave. As waves of different frequencies do not combine in any way other than super position, these 2D velocity and acceleration grids are summed to give a representational sea state through the water column. As the component waves contain a random phase factor, this summation causes construc-

tive and destructive interference and the resultant wave front is irregular, morphing with time. The flow chart in Figure 3.19 summmarises the sampling process.

It is possible to reconstruct the wave spectrum by taking the resultant, irregular wave surface elevation and applying a Fourier transformation. This is then squared and multiplied by $1/(2\pi)$ to produce the energy density spectrum $S(f)$. Figure 3.15 below is a further example of a reconstructed sea spectrum result against the original sea spectrum with significant wave height, $H_{1/3} = 5$m and significant wave period $T_{1/3} = 7$s.

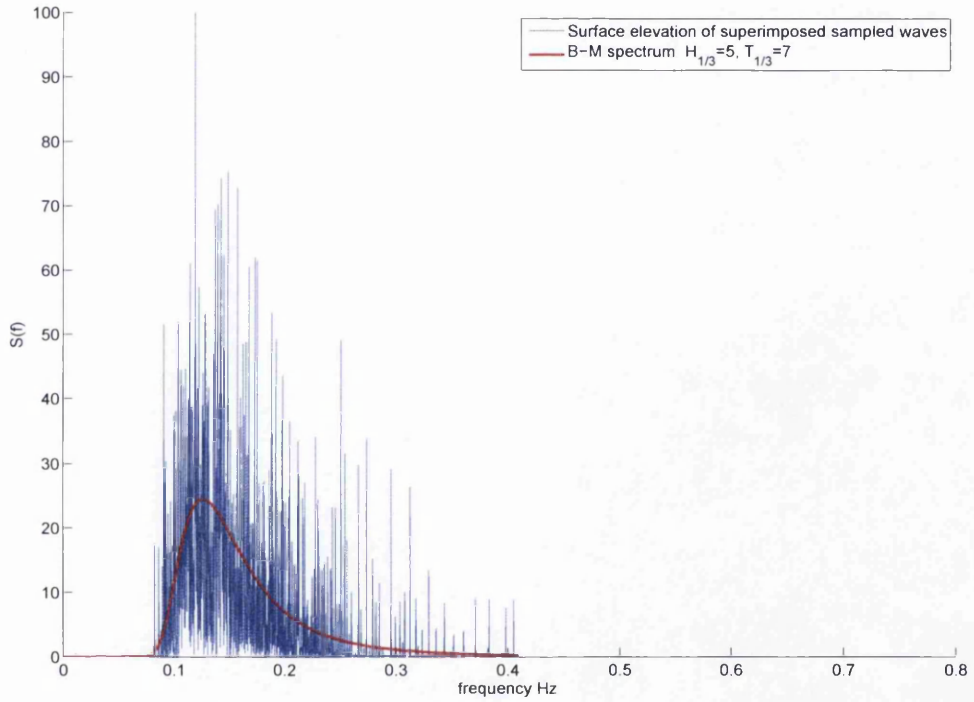

Figure 3.15: The B-M sea spectrum with $H_{1/3} = 5$m and $T_{1/3} = 7$s. A comparison of the reconstructed and originally sampled sea states. $N = 500$

The number of discrete waves is a user defined input and as N increases so does the accuracy and computational run time of the model. 500 frequency increments have been used in these studies. In order to directly compare the presented reconstructed results, the random element of the sampling method is fixed. Figure 3.16 also presents a B-M sea spectrum against the discretised reconstructed sea spectrum with alternative significant wave height and significant wave period values for com-

pleteness. Good agreement is found between the sea spectrum for sampling and the reconstructed sea spectrum. This validates the method as a technique of creating irregular sea state inflow with velocity and acceleration profiles throughout the water column. Similarly, figures 3.17 and 3.18 show good agreement between the sampled sea spectrum and the moving averaged result of the reconstructed sea spectrum for a JONSWAP and a limited depth TMA sea state respectively.

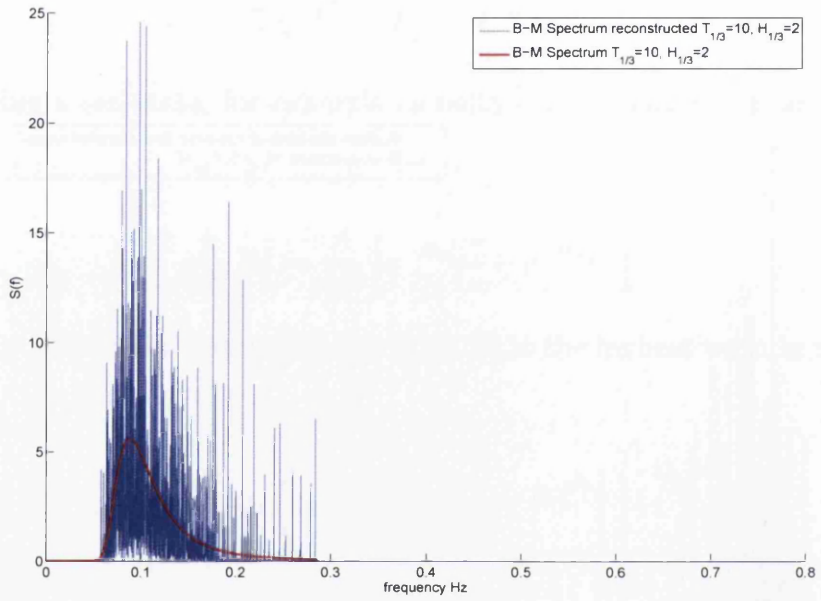

Figure 3.16: The B-M sea spectrum with $H_{1/3} = 2$m and $T_{1/3} = 10$s. A comparison of the reconstructed and originally sampled sea states. $N = 500$

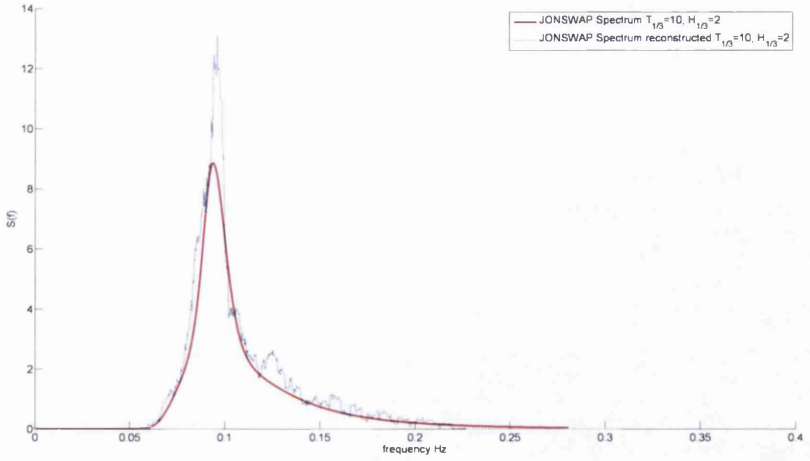

Figure 3.17: The JONSWAP sea spectrum with $H_{1/3} = 2$m and $T_{1/3} = 10$s. A comparison of the reconstructed moving averaged sea state and originally sampled sea state. $N = 500$

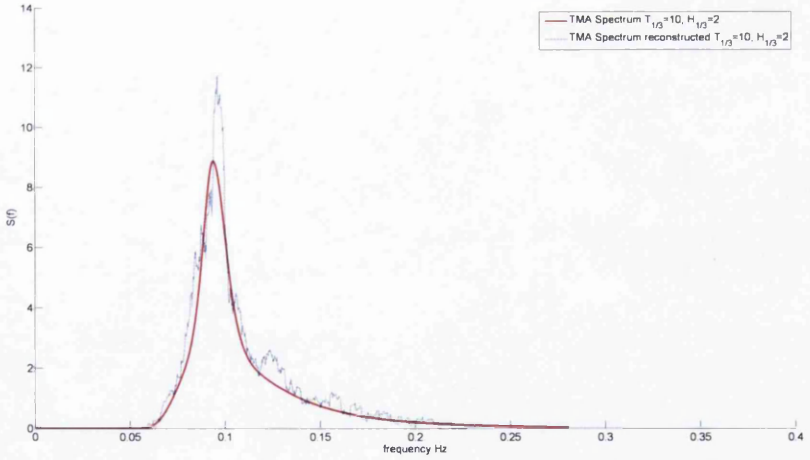

Figure 3.18: The TMA sea spectrum with $H_{1/3} = 2$m and $T_{1/3} = 10$s. A comparison of the reconstructed moving averaged sea state and originally sampled sea state. $N = 500$

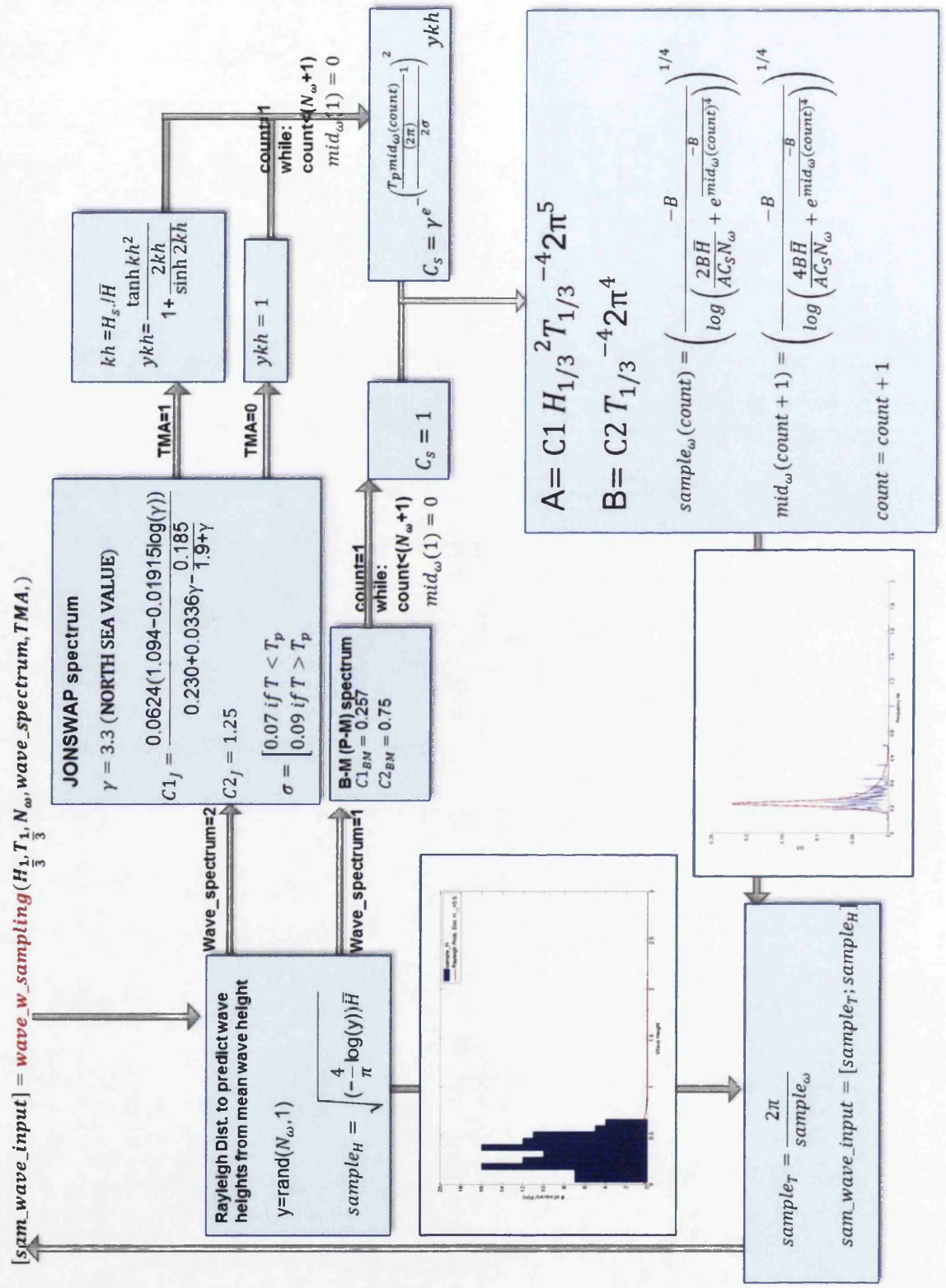

Figure 3.19: A computational flow chart to accompany Section 3.6, detailing sampling method to create an irregular sea state. Beginning with a Rayleigh distribution random sampling of set number N waves. Sea spectrum generated considering the energy assigned to each wave. Finally combining N wave heights from Rayleigh distribution with N wave frequencies from sea state representation and superimposing all N waves for irregular inflow velocities.

3.7 Reactive Wave and Current Coupling

Simple coupling between waves and tide has been considered in this thesis as well the effect on non-linear regular wave fronts and irregular sea states. Stream function wave theory represents a non-linear, regular wave as a discrete 2-D grid of input velocities and accelerations. A simple coupling theory is used where the tide flow direction and magnitude effects the speed of wave propagation only and does not alter the wave shape.

In reality, the tidal flow and wave climate have a complex and reactive relationship as they co-exist in the same environment. This chapter outlines a reactive coupling between wave and tide. As well as effecting the turbine frame of reference propagation speed of the wave, tidal flow also effects the wave non-linearity in the stream function wave theory. Therefore the tidal flow direction and magnitude effects the wave shape. Similarly, the wave climate has an effect on the near surface and this is represented by the Stokes drift model, however this effect is expected to be less significant.

By implementing these effects within an iterative loop, the wave and tidal flow react to each other and converge onto a steady couping solution. The computational flow chart in Figure 3.24 summarises the complete scheme.

Although the reactive wave and tidal coupling scheme does increase running time, it is a novel technique to simulate the complex wave and tide interactions and considers the wave and tide system as a whole. The resultant flow field is compatible with BEMT and has been successfully implemented in the previous chapter to simulate a turbine in simulated irregular waves and tidal flow compared to real ADCP data results.

3.7.1 The tide effect on the wave

This section considers the most significant effect of tidal flow on the wave non-linearity, which determines wave shape. Stream function wave theory considers finite depth, linear wave theory in the wave frame of reference, therefore at the sea bed there is no net fluid movement. The non-linearity of the waves causes an average fluid net transport in the wave propagation direction which decreases with depth. This is illustrated by the particle paths in the velocity vector field with no tidal velocity in

Figure 3.20.

Figure 3.21 shows the resultant velocity vector field of the wave with a constant current flow in the wave propagation direction and in the opposite direction for Figure 3.22. In both cases, there is a net transport of fluid through the whole water column and the equal and opposite effect of waves on fluid flow is clearly seen near the free surface. In Figure 3.22, the dependence of fluid transport on depth is illustrated by considering the particle paths at three different depths. The fluid velocity at each blade element changes with blade position in space and time.

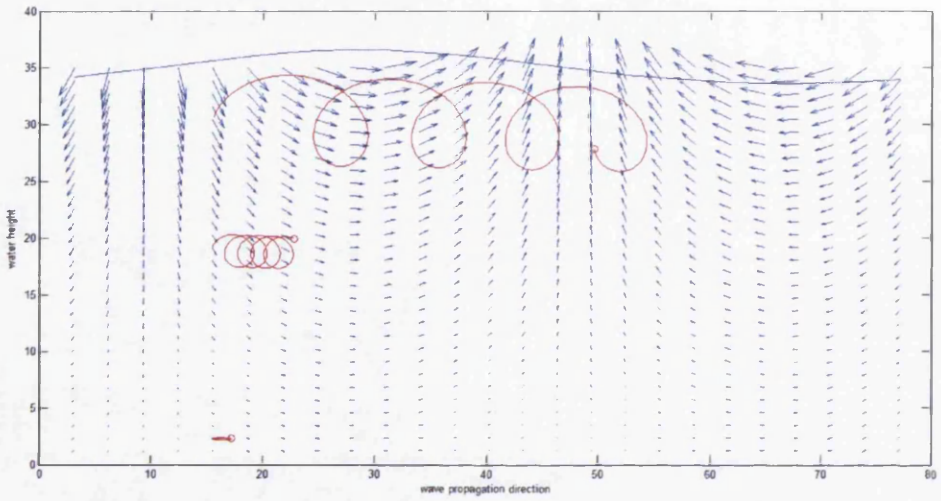

Figure 3.20: Depth profile cross-section for stream function velocity vectors with no tidal flow. Free surface elevation shown as well as three particle paths through the water column.

Figures 3.21 and 3.22 consider the simple coupling method of the wave and tide velocities as the wave non-linearity is not dependent on tidal flow direction. The wavelength is assumed constant and it is suggested that tidal flow will affect the wave frequency, giving a coupled wave frequency f_c and therefore a resultant total coupled velocity, U_c. However by considering the current flow $U \to \infty$, following this theory, $f_c \to \infty$. Physically, this suggests that in infinitely strong current flow the wave physical sizes remain and many more pass over the turbine in a given length of time. This result is clearly incorrect as a direct result of neglecting the effect of tidal flow on the non-linearity of the wave.

Considering the stream function wave theory, the wave velocities are found by

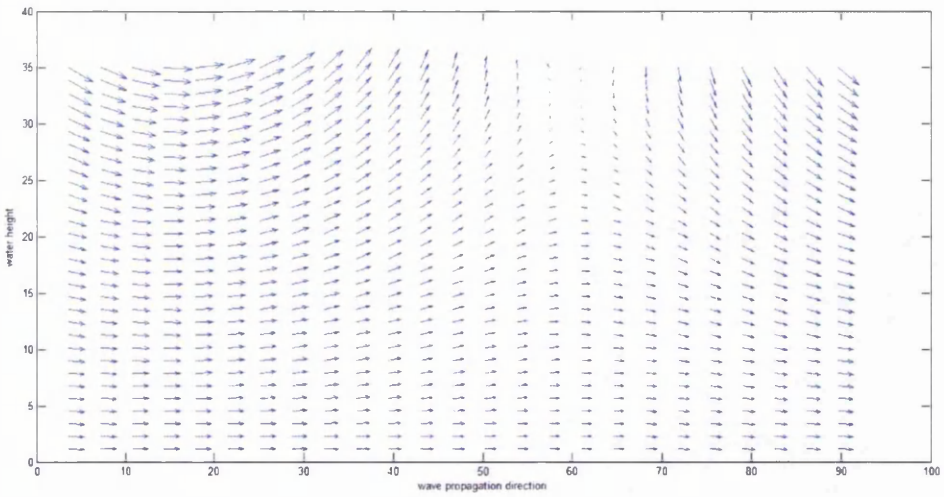

Figure 3.21: Depth profile cross-section for stream function velocity vectors with a constant 1ms^{-1} tidal flow.

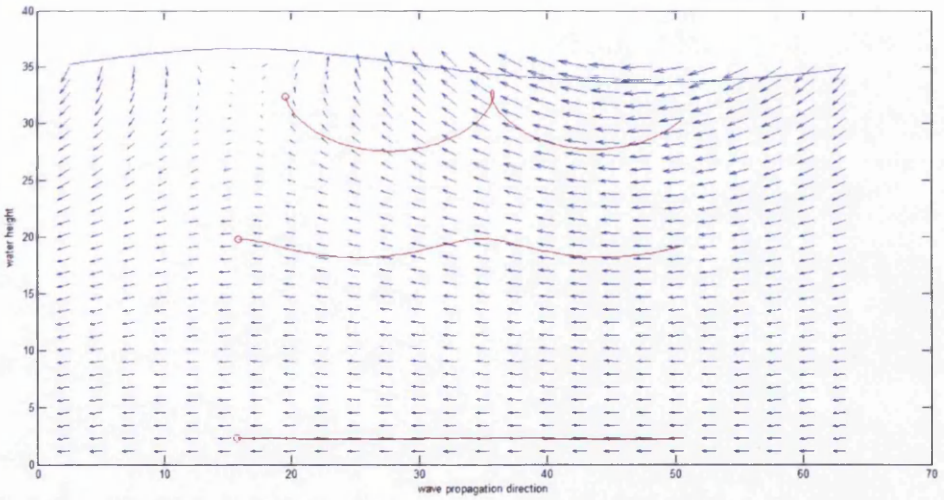

Figure 3.22: Stream function velocity vectors with a constant -1ms^{-1} tidal flow. Free surface elevation shown as well as three particle paths through the water column.

assuming the frame of reference moves with the wave, with speed C, which simplifies the problem to one of constant stream flow. To derive an alternative tidal and wave coupling theory, consider moving with the wave frame of reference where a constant tidal flow is included in C, as in Figure 3.7.1. In Chapman [2009], this theory is

rejected as a depth-dependent C is considered incompatible input for Chaplin's stream function wave theory. However, as the waves act close to the free surface, the free surface tidal flow will be more effective on the wave shape. Therefore, the alternative coupling model presented here uses the surface tidal velocity in the frame of reference of the wave to effect the wave non-linearity and the depth-dependent tidal velocity in the frame of reference of the turbine to affect the wave propagation velocity.

The flow chart in Figure 3.24 outlines the computational coupling scheme and the reactive coupling is considered. Using this novel technique, not only does tidal flow effect the speed of the wave, it also effect the wave velocity and acceleration profile shape. In this way, constant tide flow alters the wave velocity profile by affecting wavelength instead of wave frequency. Now again considering $U \to \infty$, this produces $L \to \infty$, implying that in strong current flow, the wave period remains the same and the wave profile physically deforms into a less peaked wave. The difference in flow velocity due to waves between two spacial positions is therefore reduced and tidal flow is dominant. This is a physically correct result.

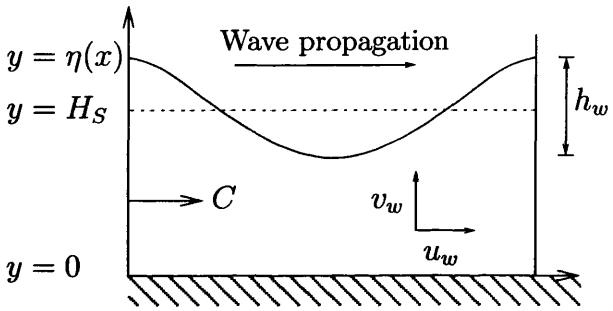

Figure 3.23 considers a current flow of 5ms^{-1} and -2ms^{-1}. The difference between the addition of Equation (4.14) and the Chaplin result with current flow highlights the inaccuracies in the velocity addition method. Although the surface elevations are similar, the velocity profiles are significantly different. In the case considered here, the plots show an elevation maximum difference of 10%, velocity maximum difference of 10% and acceleration maximum error of 25% between uncoupled and coupled tide and wave. These differences will influence the loads predicted. A tidal flow in the same direction does produce a velocity increase, however this increase is not a constant 5ms^{-1} as suggested by (4.14). In the wave trough the increase is more than 5ms^{-1} and reduces to below 5ms^{-1} near the crest. For both a positive and negative tidal flow, the effect on the wave profile is more significant in the wave trough and less significant towards the wave crest. This effect is also reflected in significant changes in acceleration profile which is used in Morison's equation to calculate inertia forces

on the turbine. This highlights the importance of coupling tidal and wave motion.

3.7.2 The wave effect on the tide

Considering non-linear waves, the effect on tide velocity is assumed localised at the free surface and will be most significant at slack tide with large waves. As well as the tidal effect on wave velocity and non-linearity in Chaplin's stream function wave theory, the non-linear wave disturbance at the free surface will have a small effect on the tidal velocity and direction.

Stokes drift is an effect of non-linear waves where a fluid particle will experience an average fluid transport velocity over one wavelength, as shown by the particle paths in Figure 3.20. This Stokes drift velocity is defined as, u_s and is summed with the tidal flow to give a combined tidal flow velocity. In this way, the wave motion will effect the tide.

$$u_s = 4\pi^2 h_\omega^2 \lambda T_\omega \tag{3.32}$$

3.7.3 A combined, reactive wave and current coupling

To represent a completely reactive wave and tide coupling, the effect of the tide on the wave non-linearity is considered and the wave shape is revised. After this, the effect of wave non-linearity on the tide is implemented by calculating Stokes drift velocity from the revised wavelength, λ. A new tidal velocity is found and used to calculate a second revised wave shape. This process continues until the revised Stokes drift velocity agrees with the previous Stokes drift velocity, considering a specified tolerance. The fully coupled tide and wave inflow is accepted as the BEMT input. The flow chart of the computation is outlined in Figure 3.24 including the expression used for stokes drift.

3.8 Conclusions and Recommendations

Regular wave theory is introduced and irregular waves are represented by frequency domain spectral energy densities. From this, the significant wave height and the Rayleigh distribution are used to create a discrete set of N waves present, in the irregular sea state. The wave heights are used to calculate the amount of energy for each discrete wave. In this way, the wave frequencies are calculated as the mid frequency of the discrete wave bins on the energy density spectrum curve.

This method is a hybrid of the methods employed in industry to sample sea state spectra. It eliminates the inaccuracies of assuming a constant amplitude for each wave or assuming a constant frequency bin size. The only reasonable assumption is that low frequency waves have larger wave heights. Therefore the area of the frequency bins will decrease with increasing frequency.

It is shown that the sea state can be recovered from the surface elevation of the superimposed discrete waves. Chaplin's stream function wave theory is used to produce an inflow grid of velocities and accelerations through the water column for the irregular sea state. The depth-dependent sea state velocity is an important input for sea state fluid structure interactions and is used in this work as an input to BEMT for tidal turbine modelling.

The model is further developed by including a breaking limit model. This model extends the regular wave breaking limit formula to consider an irregular sea state. The breaker model is found to reduce the unphysiclly large wave heights and therefore, when recovering the sea state, a greater resemblance of the sampled sea state is found. Future work will include the introduction of a further probability spectrum for wave direction. This will be particularly important for double peaked sea spectra, indicating two separate sea swells, that form in different locations.

The result of this sampling scheme is a set of N wave values of wave height H and wave angular frequency ω. The wave heights satisfy the Rayleigh probability distribution and the significant wave height of the sea spectrum, $H_{1/3}$ and a breaking limit is considered. The energy contribution of each single regular wave to the irregular sea state wave front is calculated from the height and affects the angular frequency ω of the single, component wave. This sampling does not account for a wave directional probability spectrum and assumes all waves travel in the same direction. If this was

implemented, this work could be further extended to represent double peaked wave energy density spectra where the two sea spectra originate in different places. This sampling scheme is for a steady sea state. Variations in the sea state with time are not considered. For example, considering a site situated at some distance from the sea state origin, the quickly propagating waves will reach the site before the more slowly propagating waves. If a time variable, dependent on distance from the sea state origin, is introduced to each wave then they can be introduced depending on propagation speed. However, the resultant model can be used to study the effect of tidal flow on the sea spectrum and is investigated further in Chapter 5.

This section also describes wave and tidal flow regimes with a complex and reactive coupling. Wave motion is described using regular linear or non-linear wave theory or the irregular sea state wave theory model. The tidal flow effects the wave apparent frequency over the turbine and, using the reactive coupling method, also the wave velocity and acceleration profile shape by effecting wave non-linearity.

The BEMT inflow model is now able to simulate the physical phenomena of increased wave peakedness in opposed tidal flow and a relax of the wave peakedness with tidal flow in the wave propagation direction. As well as considering the tidal effect on waves, the less significant effect of the waves on the current flow is considered. At mid tide, the tidal flow will strongly effect the wave profile. The waves will only have a significant effect on the tide near the free surface and at slack tide or strong storm conditions. This coupling is utilised instead of the usual wave and tide coupling, outlined in Section 4.11. Using the Stokes drift velocity, for a non-linear wave representation the tidal flow velocity on the free surface is effected by the mass transport velocity of the wave field.

Chapter 5 presents a preliminary study using uncoupled, irregular waves simulation to represent loadings on a turbine compared to measured kinematics from both waves and turbulence. However, validation of this scheme is limited by the availability of published experiments on wave and current interactions.

This method creates realistic inflow for BEMT with a novel, coupled wave and tidal flow scheme where waves effect tides and tides effect waves until a steady coupling solution is reached. The model has been integrated into the BEMT code and used to model a full scale tidal stream turbine in Chapter5.

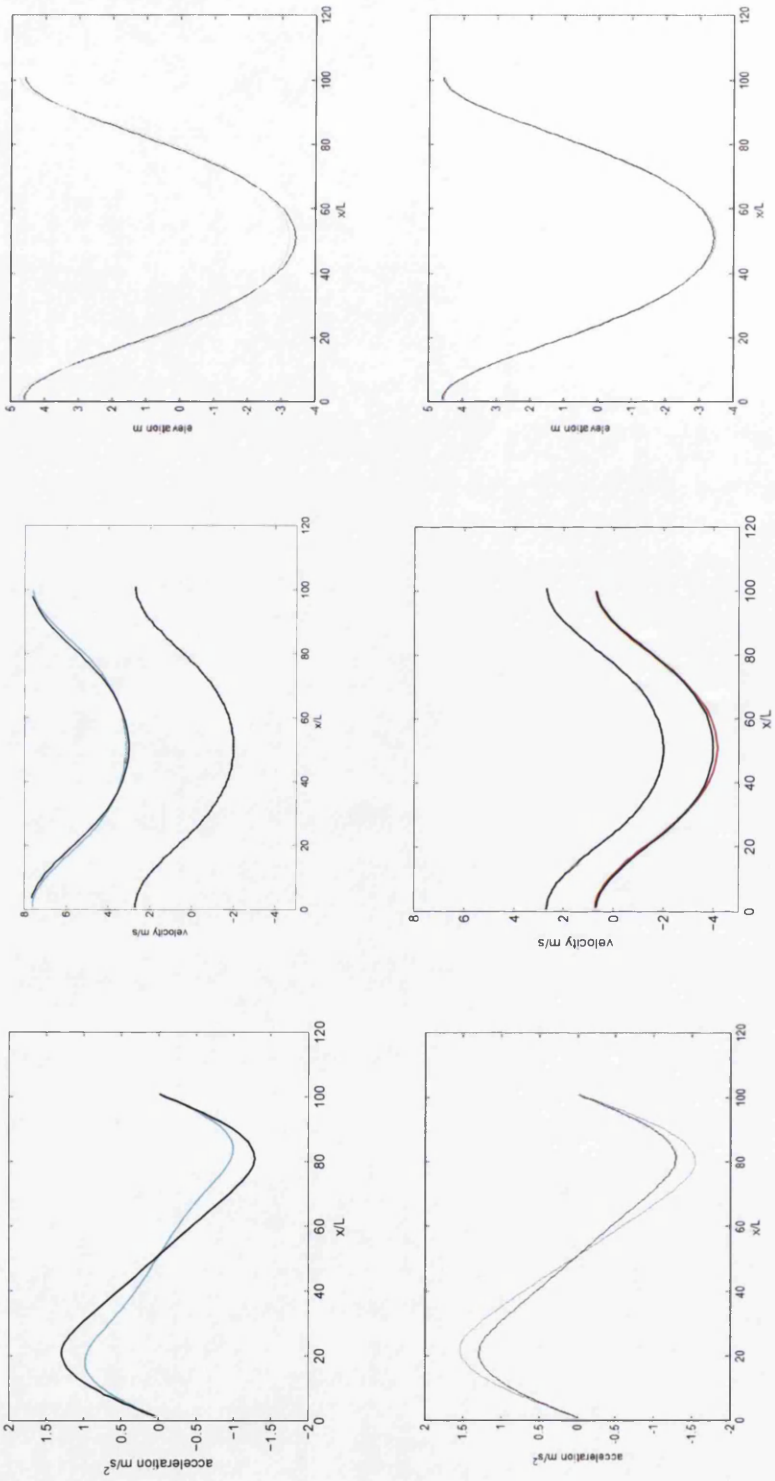

Figure 3.23: The effect of tidal flow on the Chaplin wave on elevation, velocity and acceleration profile when the tidal flow is in the same direction as the wave propagation and of magnitude 5ms^{-1}, blue, and opposite direction to wave propagation with magnitude 2m^s, red. dotted black line is with no tidal flow and solid black line is summed with tidal flow.

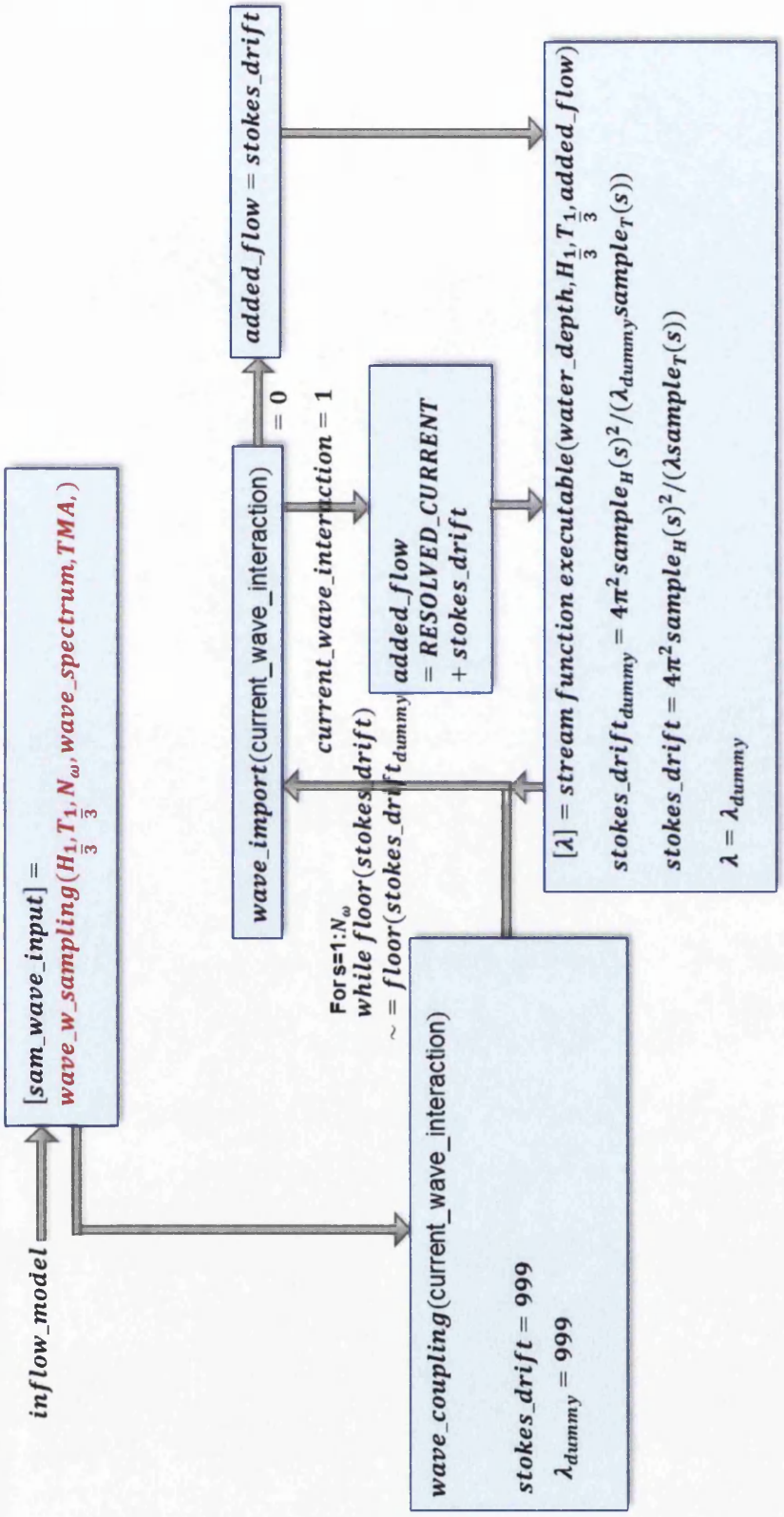

Figure 3.24: A computational flow chart to describe the numerical coupling of wave and tide. An iterative procedure is shown in the 'while' loop, which includes Stoke's drift from the wave in the surface tidal flow. This is then used to re-evaluate the non-linear effect of the tide on the wave and a new Stoke's drift is calculated until the error is below a set error criterion.

Chapter 4

BEMT for Time-Varying Flow

4.1 Introduction

The non-linear and three-dimensional effects of a regular wave and tidal dynamic inflow on a tidal stream turbine are important to optimise performance and determine survivability. BEMT is a method of modelling the performance of a wind or marine turbine by combining one-dimensional momentum theory with rotational momentum and blade element theory and is discussed in Chapter 2. To provide an incident wave front, BEMT is combined with stream function wave theory, which is derived by considering linear wave theory in a moving frame of reference. The result is a BEMT compatible, regular, non-linear wave theory. This scheme can successfully simulate tidal turbine performance, with low computational time when compared to a more traditional CFD approach.

Also in Chapter 2, the scheme is considered against time independent inflow experimental results of Bahaj *et al.* [2007], without wave effects. The Bahaj 0.8m diameter rotor was successfully simulated using this scheme. The data is used to compare against the results of several BEMT based studies such as tip and hub losses, cavitation, high induction and also a depth-dependent velocity profile in Chapter 3.

These initial investigations provide a foundation that transient inflow profiles, such as waves, can now be built upon. This thesis extends the simulation scheme to include non-linear wave effects using stream function wave theory and the simulation results are compared to the steady state Bahaj *et al.* [2007] experimental results.

This section provides validation of the scheme with incident waves; as the published Barltrop *et al.* [2007] experimental set up is simulated and the results compared to the experimental results. The first validation, in Section 4.14, considers the Barltrop *et al.* [2007] investigation results of the axial force and torque for a 0.4m diameter tidal turbine in the presence of controlled tide and wave.

In a wave tank ($77 \times 4.6 \times 2.4$m deep) the wave height is prescribed and the turbine is towed close to the free surface at a constant velocity to simulate tide. The full details of the experiment, including turbine measurements and aerofoil lift and drag curves, are presented in Barltrop *et al.* [2007] and outlined in Section 1.6.2.

For the second validation study, presented in Section 4.15, the self weight and buoyancy term is introduced and the simulation of this torque is compared to the experimental results of Barltrop *et al.* [2006]. This additional torque is dependent on the blade material composition.

Research into blade composition focuses on the overall turbine strength and water resistant properties of tidal turbine blades. The self weight and buoyancy term is shown not to contribute to whole turbine torque but is shown to create an additional azimuthally varying load on each blade root. This loading contributes to fatigue at the blade root and must be considered in the blade composition design stage. It is possible to cancel the buoyancy and self weight torque with neutrally buoyant blades, thus eliminating the additional torque fatigue on the blades.

Comparing to experimental data with incident waves gives a validation of the compatibility of BEMT with transient inflow, in the form of Chaplin's stream function wave theory. After the validation presented in this chapter, further significant regular, non-linear wave and BEMT simulation results are discussed.

4.2 Theory

4.2.1 Tidal Flow Boundary Layer

Many turbine performance coefficient results are published where the turbine is in a confined flow tunnel or tank. The standard value for the non-dimensionalisation constant value, U_{ref}, is U, as used in Equations (2.22). U is the far upstream free

stream flow and is assumed constant in the stream tube. However, the significance of a depth-dependent stream tube velocity should be investigated and, for this case, a suitable standard non-dimensionalisation constant velocity, U_{ref}, is found. This is a crucial consideration for non-dimensional analysis of tidal turbines as U_{ref} is used in the definition of TSR and C_p, C_{fa} and C_t. Any variation of this value has a significant effect on the magnitudes of the performance coefficients and their position on the TSR curve.

The magnitude of tidal velocity will vary through the water column due to boundary friction, as the solid surface of the sea bed creates a boundary layer in the fluid flow. The boundary layer friction from the free surface is negligible in comparison and can be assumed to be zero. The widely-accepted power-law approximation for boundary layers is effective for confined flows, as in Equation (4.1). It is usual that the whole water column is considered a boundary layer of the base.

$$u_B = U(h/H)^{1/x} \tag{4.1}$$

where x gives the steepness of the velocity drop off, and is usually set to 7. Tidal variations can be considered negligible within the time scale of analysis presented and, due to the comparatively small time period of wave effects, the mean free surface height is assumed a constant. Introducing a boundary layer alters the local velocity magnitude and incident angle as a function of height. The local TSR and local velocity incident angle are now dependent on angular position and are therefore not the same for all blades. Both these quantities will affect the individual blade element performance and incident forces.

Considering a time independent study conducted with BEMT, such as the TSR examples in Chapter 2, a depth-dependent inflow causes inconsistency with the momentum theory assumptions and with the definition of TSR.

Momentum theory considers the stream tube as a whole, dictating a constant value for U_{ref}. However, with a depth-dependent inflow, U_{ref} in the stream tube varies with depth.

To compare the non-dimensionalised values of the performance coefficients and TSR, U_{ref} is usually defined as the constant, far upstream, U, defined in BEMT. Considering a depth-dependent inflow axial velocity, as in Chapter 2, the hub velocity,

U_{Hub}, will remain constant for a fixed turbine and is therefore the value usually used instead for U_{ref}.

Nevertheless, the state is still time dependent. For a TSR study, the azimuthal position of the blades is set and the position can significantly effect the performance. For example, two constant blade positions are given in Figure 4.1. The results in Chapter 2 use the default Position 1 and use $U_{ref} = U_{Hub}$. In Figures 4.4 and 4.5 this result is compared to the Position 2 result and Figure 4.6 shows that the difference is physical. It can be seen that the default Position 1 gives a minimum power output result and Position 2 gives a maximum power output result.

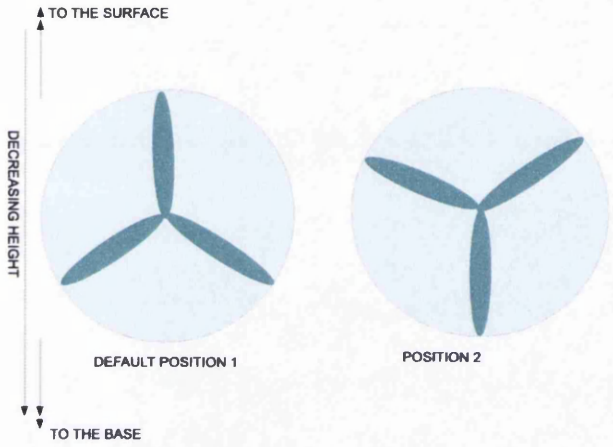

Figure 4.1: The two steady state turbine blade positions investigated in Figures 4.3, 4.4, 4.5 and 4.6.

The validity of U_{Hub} as the constant non-dimensionalisation value is disputed. Alternatively, by adhering to the assumption of momentum theory, Equation (4.1) can be used to find the axial velocity at the hub depth and then this can be assumed the constant axial velocity over the whole stream tube. Position 1 and Position 2 give the same result which is also compared in Figures 4.4 and 4.5. As the problem is independent of blade azimuthal position it is truly steady state. However, by considering the non-dimensionalised power in 4.6, it is clear that some difference in power is a physical result and not a product of non-dimensionalisation.

U_{Hub} is sufficient for U_{ref} if ratio of turbine diameter to total water height is large and the turbine is positioned close to the surface. Therefore the significance of the variable depth velocity effect can be related to the range of the turbine span in the vertical direction, R_T, specified in Equation (4.2). This is the range of axial velocity

change swept by the blade tips as a percentage of the total velocity change.

$$R_T = 100\left(\frac{R + H_{Hub}}{H}^{1/x} - \frac{H_{Hub} - R}{H}^{1/x}\right) \tag{4.2}$$

If the ratio between turbine diameter and total water height is small, U_{Hub} is insufficient and the average tip axial velocity, Equation (4.3), is suggested as an alternative non-dimensionalisation velocity.

$$U_T = \sum_{i=0}^{2}\left[U\frac{R\cos(\Theta + 2i\pi/3) + H_{Hub}}{H}\right]^{1/x} \tag{4.3}$$

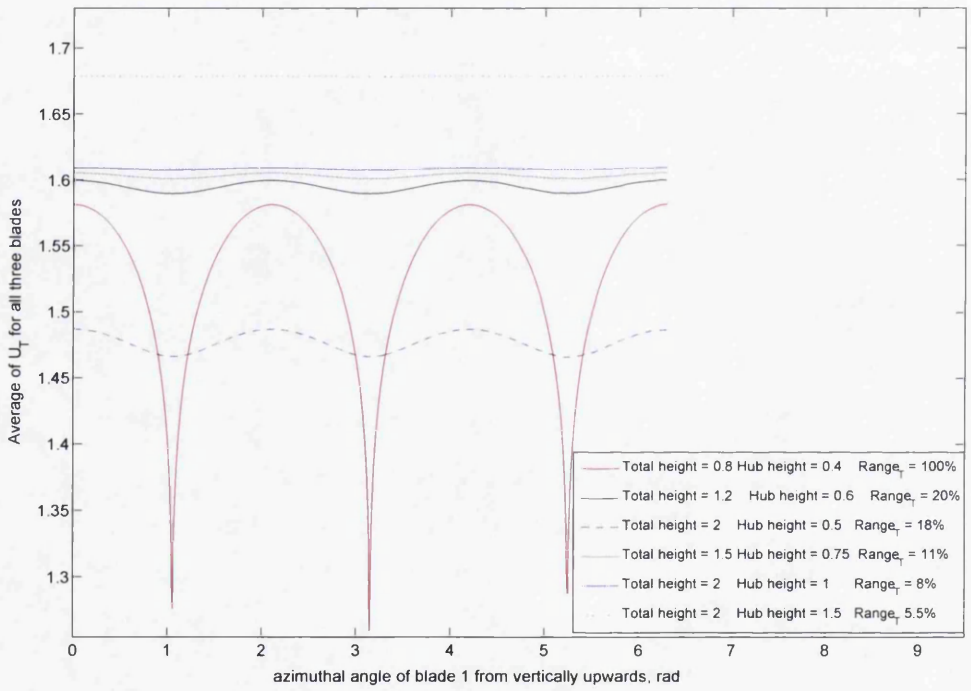

Figure 4.2: The average tip U for one full turbine revolution for different total water column heights and hub location heights.

This value minimises the effect of a depth-dependent axial velocity on the power, torque and axial force non-dimensionalisation, whilst retaining the physical difference in performance between Positions 1 and 2 in Figure 4.1. To illustrate the effectiveness

of R_T as an indicator of the significance of a depth-dependent axial velocity, the average U_T is shown in Figure 4.2 for the $R = 0.4$m Bahaj turbine, as described in Section 1.6.1. Although different total water heights and H_{Hub} positions are compared, the azimuthal dependency of average U_T is shown to be only significant when $R_T >$ 10% for all cases.

A final amendment to the optimiser scheme is proposed to solve for an annulus of the turbine swept area as a whole, rather than each blade element at the annulus radius individually.

4.3 Bed Friction Power-Law

If the boundary layer effect on flow is disabled, comparing a and b for the same blade element but on different blades, the same result is found. This is because a and b are only radially dependent. Therefore if a simulation is run without sea bed boundary effects the computational time can be easily reduced by 1/3 and the same result is found. This is achieved by calculating torque and axial force for all elements on one blade and simply multiplying by the number of blades, as an alternative to calculating for all elements on all blades.

If the boundary layer effect is enabled, slightly different a and b are found for the same blade element on different blades. As a and b come from momentum theory, this is incorrect as they should be dependent on radial position only. The original optimisation function, labeled optimisation configuration 1, is given in Equations (4.4) to (4.6).

For optimiser configuration 1, each blade element is taken in turn. For the blade element equations, dT_1 and dFa_1 are found assuming V, C_L and C_D are azimuthally independent and equal to their values at the particular, local position of the blade element in question. This produces azimuthally dependent a and b which conflicts with momentum theory assumptions.

The suggested optimiser, optimiser configuration 2, is given in Equations (4.7) to (4.9) and introduces a connection between the a and b values on different blades by simultaneous calculations. For optimiser 2, the variables are now blade number dependent, V_{nb}, C_{Lnb}, C_{Dnb} and the dT and dFa values are summed during the optimi-

sation process. For the stream tube annulus averaged, momentum theory expressions for dT_2 and dFa_2, assuming that each blade contributes a third of dT_2 and dFa_2, the equation is divided by three, and calculated for the blade element on each blade and summed. The blade element dependent variables are F_{nb} and U_{nb}.

For uniform flow, the same result is found using either approach. With a non-uniform depth profile, the results are slightly different and are given in Figure 5.2(b). Using the optimiser 2 configuration of g, a and b are now only dependent on radial position and are the same for the same blade element on different blades. Although Figure 5.2(b) shows the optimiser configuration has only a slight effect on the results, the computational time is slightly reduced and the formulation of g is now theoretically in agreement with momentum theory. In addition, as more complex dynamic inflow is considered, such as waves and turbulence, a more significant difference between the two optimiser results is anticipated.

Optimiser configuration 1:

$$\begin{aligned} g_1 &= (dT_1 - dT_2)^2 \\ &= (N_B \frac{1}{2}\rho V^2 cr(C_L \cos\phi - C_D \sin\phi)dr - 4bF\,(1-a)\,\rho U\Omega r^3 \pi dr)^2 \end{aligned} \tag{4.4}$$

$$\begin{aligned} g_2 &= (dFa_1 - dFa_2)^2 \\ &= (N_B \frac{1}{2}\rho V^2 c(C_L \sin\phi + C_D \cos\phi)dr - 4F\pi r\rho U^2 a(1-a)dr)^2 \end{aligned} \tag{4.5}$$

$$g = g_1 + g_2 \tag{4.6}$$

Optimiser configuration 2:

$$\begin{aligned} g_1 &= (dT_1 - dT_2)^2 \\ &= (\sum_{nb=1}^{3}\left[\frac{1}{2}\rho V_{nb}^2 cr(C_{Lnb}\cos\phi - C_{Dnb}\sin\phi)dr\right] - \sum_{nb=1}^{3}\left[\frac{4}{3}bF_{nb}\,(1-a)\,\rho U_{nb}\Omega r^3\pi dr\right])^2 \end{aligned} \tag{4.7}$$

$$g_2 = (dFa_1 - dFa_2)^2$$
$$= (\sum_{nb=1}^{3} \left[\frac{1}{2}\rho V_{nb}^2 c(C_{Lnb}\sin\phi + C_{Dnb}\cos\phi)dr\right] - \sum_{nb=1}^{3} \left[\frac{4}{3}F_{nb}\pi r\rho U_{nb}^2 a(1-a)dr\right])^2 \tag{4.8}$$

$$g = g_1 + g_2 \tag{4.9}$$

4.4 Depth-Dependent Velocity Results

The Bahaj *et al.* [2007] investigations are highly blocked with a 0.4m turbine with hub height of 0.6m in a 1.2m tunnel and $R_T = 20\%$. Figure 4.4 is a closer view of Figure 4.3 and shows the power coefficient curve against TSR. The Position 1 result from Chapter 2 is shown in black and a different result is shown for Position 2. The result with no power-law is shown to be the same as the constant U_{Hub} over the stream tube result. By setting the constant U_{ref} to the average U over all three blades, Figures 4.4 and 4.5 show how the physical difference in power between Position 1 and Position 2 is still captured but the result is comparable to the no power-law result and therefore the non-dimensionalisation does not adversely effect the performance coefficient result. Figure 4.4 highlights the relatively small magnitude of this C_P difference, typically about 0.01. This effect is expected to be subtle as it is dependent only on the power-law gradient across the turbine. However, to consider more significantly varied inflow, such as waves, the value of U_{ref} has the potential to significantly alter the results of the power coefficients and their TSR position.

Wave induced kinematics are also depth-dependent, a correct definition of U_{ref} is vital and it is suggested here that the average U over all three blades is used for this value. The resultant effect on the performance coefficients is presented.

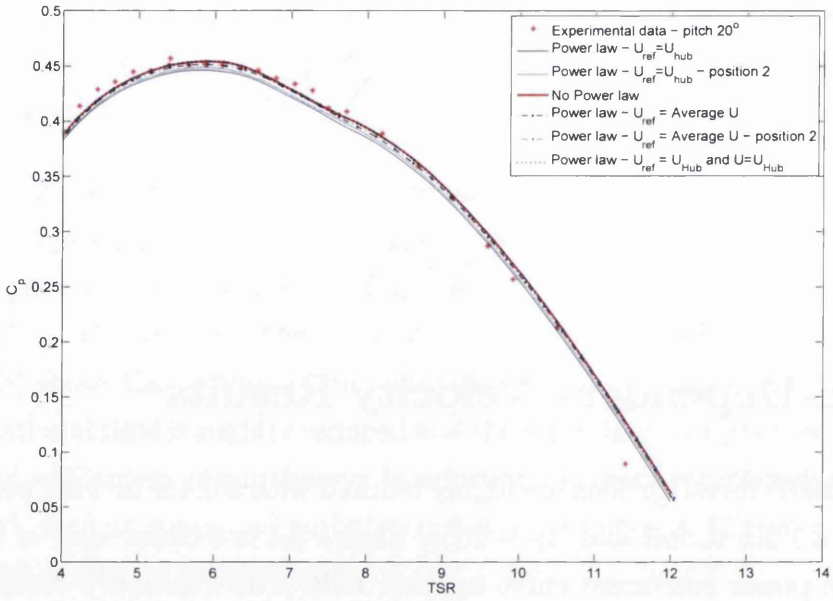

Figure 4.3: A comparison of power coefficient with TSR for different axial flow conditions and non-dimensionalisation velocity constants.

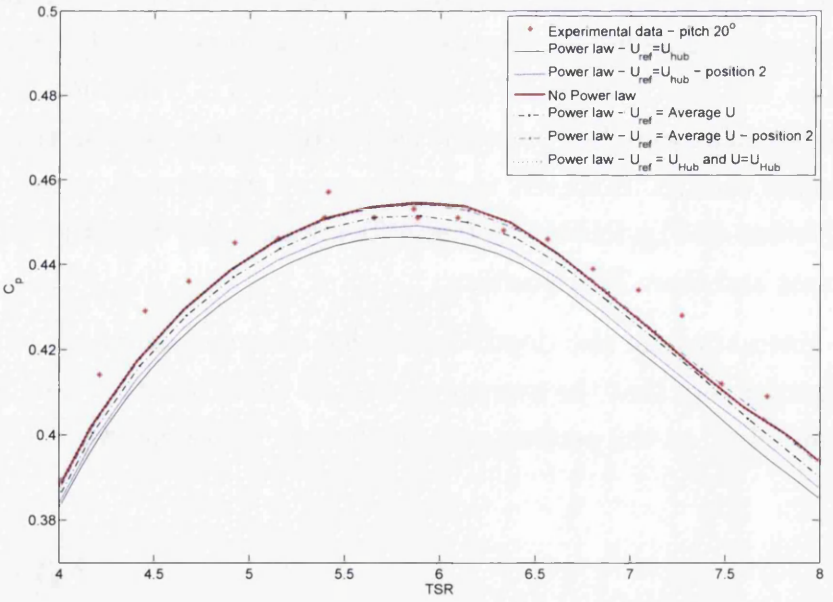

Figure 4.4: A closer view of Figure 4.3, a comparison of power coefficient with TSR for different axial flow conditions and non-dimensionalisation velocity constants.

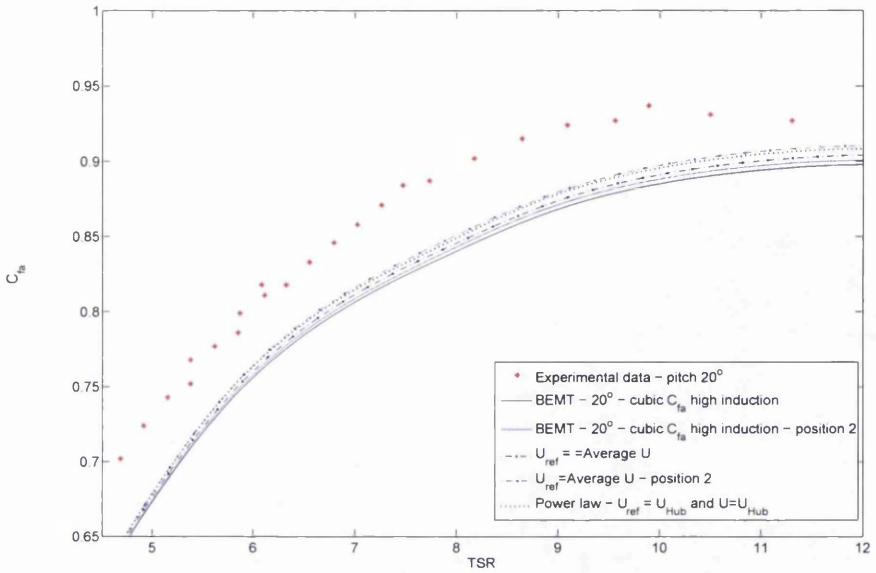

Figure 4.5: A comparison of axial force coefficient with TSR for different axial flow conditions and non-dimensionalisation velocity constants.

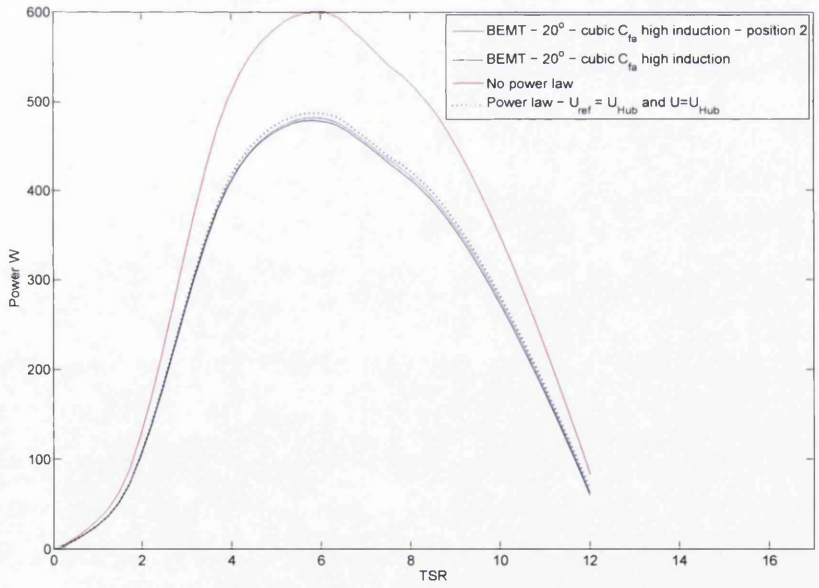

Figure 4.6: A comparison of power with TSR for the different axial flow conditions in figures 4.4 and 4.5.

4.5 New Implementation of Bed Friction Power-Law Results

The original optimiser configuration, as specified in Section 4.3, is the preferred and popular approach to simulate a tidal turbine using BEMT, as found in the literature of Section 1.3.1. Section 4.3 outlines the inconsistencies of this approach with momentum theory. For a steady state inflow simulation the inconsistency is irrelevant, however in this case the new formulation decreases run time. To extend BEMT to simulate a tidal turbine in dynamic inflow, this inconsistency becomes significant and is the cause of the difference in the optimiser configuration 1 and optimiser configuration 2 results compared in Figure 5.2(b). As the aim of this work is to extend BEMT for more complex dynamic inflows, such as waves and turbulence, the inconsistency is a significant consideration. It is suggested that, for dynamic inflow BEMT simulations, optimiser configuration 2 is implemented in place of optimiser configuration 1. In the model, both configurations are implemented and available to the user as input options.

In summary, configuration 1 considers annulus averaged blade forces whereas configuration 2 considers individual blade forces separately summed to give an annulus blade forces.

4.6 Discussion

This chapter introduces the factor R_T which indicates the depth gradient velocity change. When $R_T > 10\%$, the depth-dependent velocity effect is shown to be significant. Figures 4.3 and 4.4 consider various U_{ref} values for a depth-dependent velocity profile. The two azimuthal blade positions, varying by 60^o, are also considered. Figure 4.4 shows clearly that Position 2 produces more power for the same inflow than Position 1. The uniform free stream flow is also shown to produce more power than either Position 1 or Position 2. It is suggested that this is not a physical difference but a consequence of using hub velocity to non-dimensionalise the performance coefficients and find TSR in a depth-dependent flow domain. The presented averaged formulation of U_{ref} is proposed as a more approporiate non-dimensionalisation value for depth-dependent flow. This formulation produced similar results to the uniform

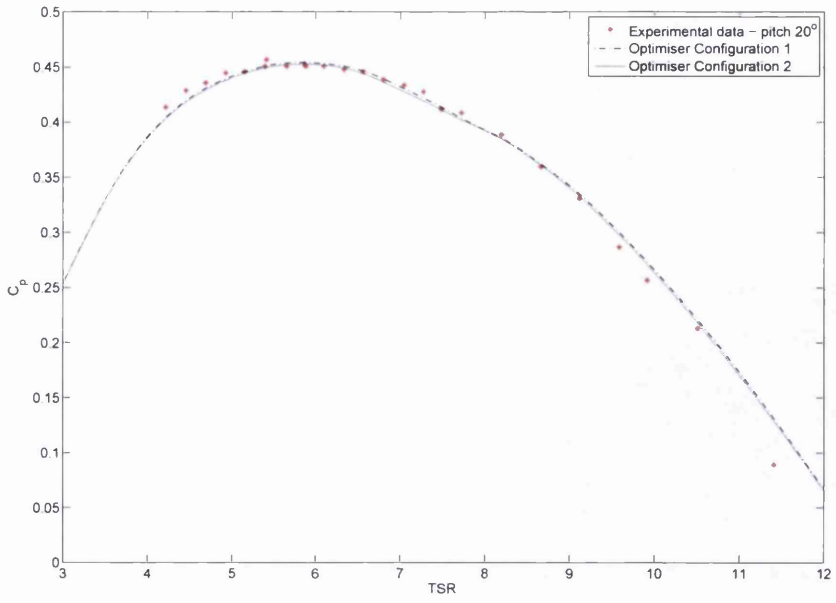

Figure 4.7: A comparison of C_p with TSR for the different optimiser configurations, as specified in Section 4.3.

flow for C_p and C_{fa}, whilst retaining the physical differnce in performance of the turbine in Position 1 compared to Position 2.

By plotting power in Figure 4.5, the large difference between uniform inflow and depth-dependent inflow is shown as a result of the higher average velocity at the turbine height. The difference between Position 1 and Position 2 is shown to be physical and inflow velocity independent as the same depth-dependent velocity profile is used in both these cases. A further result, $U_{ref} = U_{hub}$ is considered, where a depth-dependent velocity is considered constant over the swept area of the turbine.

An alternative optimiser configuration is suggested for BEMT and in Figure 5.2(b) the configuration is shown to be consistent with experimental data and the previous configuration, for C_p against TSR. The proposed configuration considers the instantaneous state of all the turbine blades simultaneously. The results are combined to use in the momentum theory, whole turbine considerations.

In this chapter, spatially and time varying velocity inflow for BEMT is considered. A method of measuring the depth dependency of the inflow velocity is proposed. The effect of the profile on C_p and C_{fa} against TSR is presented with particular

emphasis on the constant non-dimensionalisation velocity used to calculate TSR as well as the turbine performance coefficients. An average velocity value over the three turbine blades is shown to accurately produce physical non-dimensionalised turbine performance results and is proposed as an alternative to the commonly used hub velocity.

Depth-dependent velocity and transient inflow are shown to be compatible with steady state BEMT to produce turbine simulations if the optimiser in BEMT is configured correctly. Steady state BEMT does not consider the turbine blades together which is not compatible with transient inflow. The proposed configuration considers the three turbine blades simultaneously and reduces simulation time for steady state cases. This configuration makes the momentum theory calculation consistent with transient inflow.

Further analysis and validation of this optimiser is suggested as further work. Although the effect of the optimiser configuration is small in the depth-dependent velocity example presented here, the effect is expected to be more significant with wave affected velocity inflow.

4.7 Cavitation Inception with BEMT

4.7.1 Introduction

Blade Element Momentum Theory (BEMT) is an analytical modelling tool that describes the performance of turbines by cross-referencing one dimensional momentum theory with blade element theory. Each blade is discretised along its length and the dynamic properties of torque and axial force are determined as described in the earlier sections of this chapter. A compatible cavitation detection model is now introduced to indicate any cavitating blade elements. Cavitation occurrence is dependent on proximity to the free surface, the incident flow velocity and inflow angle and the blade cross-section aerofoil shape. The shock waves associated with cavitation can significantly damage the blade surface and therefore performance. This model is a useful addition to BEMT and can be used in turbine design to minimise cavitation occurrence. The results are validated using the cavitation experiment observations by Bahaj *et al.* [2007].

To simulate the experiment, it is assumed that the temperature of the water is the room temperature value of 20°c and the velocity of the inflow is constant, apart from a power law reduction near the cavitation tunnel base, as previously described with an x value of 5. Further details of the experiment can be found in Bahaj *et al.* [2007].

4.7.2 Cavitation Inception

Considering a body of fluid with a constant temperature, vaporisation of the fluid will occur if the pressure reduces below the fluid vapour pressure at the specific temperature. Regions of low pressure cause cavities to form in the body of fluid. If a low pressure region is surrounded by high pressure, above the fluid vapour pressure, the cavities implode rapidly creating a jet of fast moving fluid. Low pressure occurs on the downstream side of a tidal turbine blade and this region is surrounded by higher pressure, Munson *et al.* [2006]. Therefore cavitation can occur and, as the cavities implode, the many rapid jets of fluid impact on the blade surface and cause cyclic surface fatigue, Bansal [1998]. In the long term, pitting roughens the blade surface causing an increase in turbulent flow and deterioration in the performance of the aerofoil section. The rough surface also provides nucleation sites for further cavitation. Cavitation inception on a tidal turbine blade will occur if the local pressure on the blade element surface, p_L, is less than the cavitation inception pressure for sea water vapour, $p_V = 1200$Pa is used for this study.

The cavitation number, σ, is the non-dimensionalised difference between p_L and p_V using a reference velocity which is taken as V_∞ from Equations (4.4) and (4.5). σ_{crit} is the critical cavitation inception value, above which cavitation will occur. It is the non-dimensionalised difference between the undisturbed far upstream pressure, p_∞, and p_V.

$$\begin{array}{ll} \text{Cavitation occurs} & \text{if } \sigma \geq \sigma_{\text{crit}} \\ \text{No cavitation} & \text{if } \sigma < \sigma_{\text{crit}} \end{array} \tag{4.10}$$

$$\sigma = \frac{p_\infty - p_L}{\frac{1}{2}\rho V_\infty^2} \tag{4.11}$$

$$\sigma_{\text{crit}} = \frac{p_\infty - p_V}{\frac{1}{2}\rho V_\infty^2} \tag{4.12}$$

The undisturbed free stream pressure is the sum of the static pressure and the gravitational pressure of the body of water above the blade element. During one rotation the proximity of the blade elements from the free surface will vary. Additionally, V_{tip} varies due to the velocity profile. Therefore the cavitation number will take a value in a range depending on vertical position, as seen in the results table, Table 4.1.

4.7.3 Implementation

For any aerofoil and any V_∞, it is possible to estimate the minimum surface pressure using a tool such as XFOIL. This is non-dimensionalised to a pressure coefficient C_{press} with respect to the undisturbed local pressure V_∞. Finally we note that C_{press} and σ are the same non-dimensionalised quantity. Therefore C_{press} can be interpolated from a lookup table of minimum pressure coefficients in the same way as the lift and drag coefficients, C_L and C_D in blade element theory. These pressure coefficients are unique to each aerofoil shape and were taken from XFOIL for incident aerofoil angles $0 \rightarrow 15$ degrees. This is the normal operating region for tidal turbines however after the stall angle (15^o) XFOIL cannot calculate the minimum C_{press} accurately due to flow separation. The XFOIL data is therefore extrapolated logically to give a full 360^o data set for minimum pressure coefficient. It is assumed that the minimum C_{press} increases towards a maximum value at 180^O. This is now compatible with the BEMT scheme.

By interpolating the tabulated C_{press} data from local inflow angle ϕ the limit in (4.10) is implemented by rearranging equations (4.11) and (4.12).

$$\frac{1}{2}\rho {V_\infty}^2 C_{\text{press}}(\phi) + p_\infty \leq p_V \qquad (4.13)$$

p_∞ is the water pressure far upstream and is equal to the sum of static pressure p_0 and static pressure head $p_h = \rho g h$, where h is the height of the water column above the blade element position.

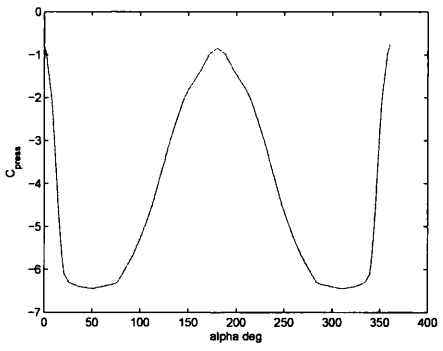

Figure 4.8: Minimum C_{press} extrapolated from XFOIL data.

4.8 Validation Study Results

Bahaj *et al.* [2007] have published a series of investigations of a test turbine in a cavitation tunnel under various operating conditions shown in Figure 4.10. The 0.8m diameter turbine was placed in the centre of the 5mx2.4mx1.2m tunnel, therefore the height of the blade in the water column ranges from 0.2m to 1m. The root pitch of the turbine blades is set to 25^o in 1.4ms^{-1} fluid flow.

BEMT assumes the turbine is in freely flowing fluid. In a cavitation tunnel blockage will occur due to the side walls and increase the flow through the turbine greatly affecting the turbine performance. To account for this, a blockage correction is used by Bahaj *et al.* [2007] on the torque and axial force performance results. However the cavitation observations cannot be corrected and are the result of blocked flow. To compare the BEMT result with the blocked cavitation observations a compatible blockage model is implemented as proposed by Whelan [2010]. The operating conditions set by Bahaj for the five cases in Figure 4.10 are simulated using the proposed model. These blocked simulated cavitation results are summarised in Table 4.1. Visual representation of these results are shown in Figure 4.9 to compare to the experimental observations, 4.10.

Table 4.1: Simulated Results for 25° hub pitch and $U = 1.4\text{ms}^{-}1$

Label	rpm	TSR	Tip σ_{crit}	Number of cavitating elements /64	% of blade length cavitating	% of swept area cavitating
(a)	274	8.2	1.14-1.26	0	0%	0%
(b)	274	8.2	1.04-1.16	1	1.25%	0.30%
(c)	272	8.1	0.61-0.73	11-16	13.75%-20%	31.47%
(d)	240	7.2	0.56-0.70	10-16	12.5%-20%	29.86%
(e)	250	7.5	0.56-0.72	11-17	13.75%-21,25%	37.60%

σ_{crit} at the blade tip is specified by Bahaj *et al.* [2007] and also given is Ω, U and blade pitch. For a stable operating condition, V_∞ at the blade tip, V_{tip}, will be a constant; if a constant upstream undisturbed flow U is assumed. However, a bed boundary power-law inflow model is implemented, therefore V_{tip} will vary with depth. This results in a depth-dependent range for σ_{crit} at the blade tip, illustrated in table 4.1. As cavitation occurrence presents first at the blade tip, Tip σ_{crit} is the limit for any cavitation occurrence on the blade. For blade elements not at the tip, this limit will overpredict cavitation.

Considering cases (a) and (b), the difference is in σ_{crit}; as there is less static pressure in case (b) compared with case (a). The p_∞ for each experiment can be calculated from the cavitation number using Equation (4.11). Figure 4.9 shows the cavitation number, σ, for all blade element positions for one revolution for cases (a) to (e). The critical cavitation factor σ_{crit} is also presented to show the relationship between σ_{crit} and depth. From Equation (4.10) if a blade element cavitation factor is over σ_{crit} then cavitation will occur. These results can be compared to the experimental observations made by Bahaj *et al.* [2007] in Figure 4.10.

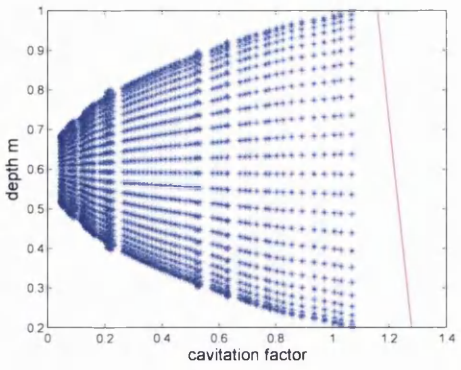

(a)

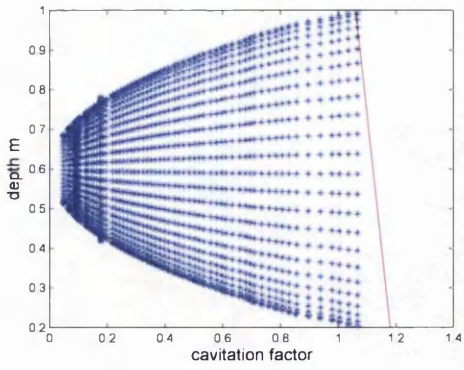

(b)

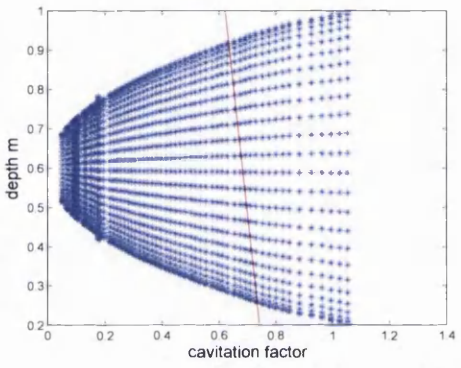

(c)

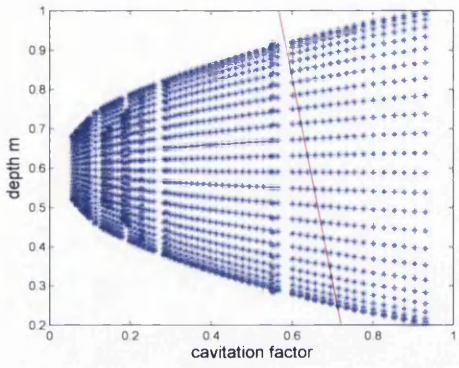

(d)

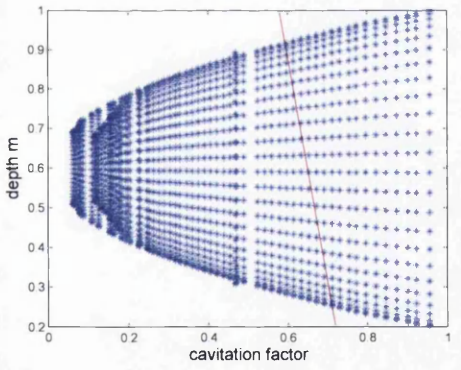

(e)

Figure 4.9: σ against depth (measured from the cavitation tunnel floor) for all blade elements over one revolution with the limit σ_{crit}.

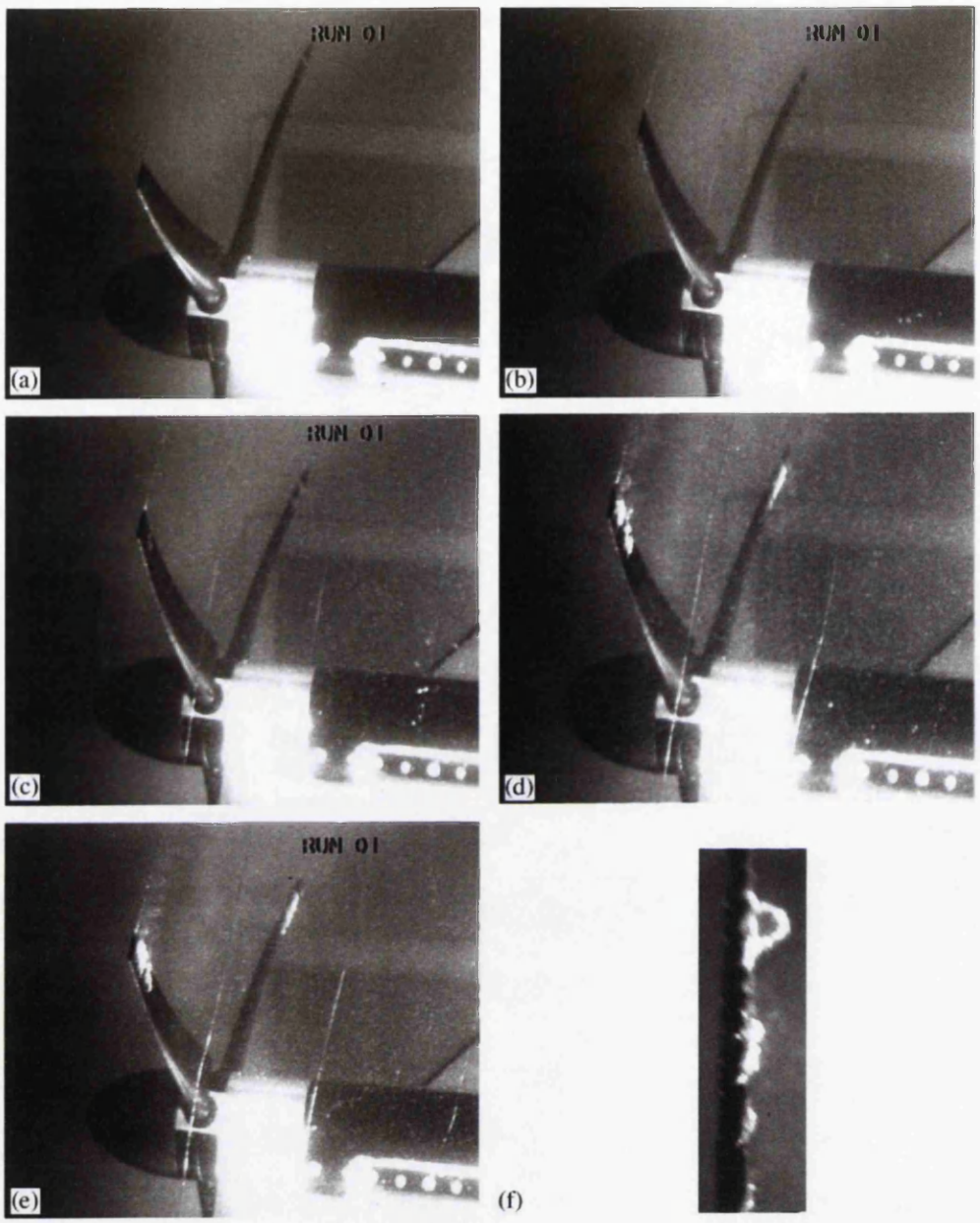

Figure 4.10: Experimental observations by Bahaj *et al.* [2007].

4.9 Discussion

By considering Equation (4.13), cavitation theory suggests that a change in inflow velocity V_∞ is significant when calculating the local pressure on the blade element and therefore the cavitation occurrence. However the inflow velocity is greatly dependent on the lift and drag profile of the turbine aerofoil. The Bahaj investigation lift and drag profiles come from wind tunnel testing at various aerofoil Reynolds numbers and give an approximation to the actual lift and drag of the turbine, therefore the model is an approximation to the occurrence of cavitation. Further details are found in Bahaj *et al.* [2007].

Table 4.1 gives the simulated cavitation results in terms of percentage of blade length cavitating and percentage of swept area cavitating. In Bahaj *et al.* [2007] a conclusion of the experiment is that cavitation first occurs when $\sigma \simeq 0.9$. As this is an average value, we can consider the maximum cavitation factors in each case. These values are between 0.93 and 1.08 which shows agreement with Bahaj *et al.* [2007]. This provides some validation for the cavitation model as it can correctly predict the onset of cavitation in this case.

Figure 4.9 gives σ against depth, as measured from the base of the cavitation tunnel, for all the blade elements during one revolution and compares well with Figure 4.10. Figure 4.9 also illustrates how σ_{crit} is highest close to the cavitation tunnel base and decreases towards the top of the cavitation tunnel. Therefore cavitation inception first occurs at the blade tip and near to the top of the cavitation tunnel.

In addition to this, the percentage of the blade length over which cavitation occurs is also recorded in Table 4.1. The experimental results for this graph are read directly from the images published, as in Figure 4.10. There are limitations to this method and this method will introduce an error as the values are read directly from the images. However, as a preliminary study to determine the suitability of the simulation, this method is sufficient. Figure 4.11 compares the percentage of cavitating elements along the blade length from the experimental observations with the combined BEMT and cavitation model. The results are compared to the solid black line, which represents complete agreement between model and simulation. A percentage range is shown for the simulated results; as the percentage of blade length cavitating is depth-dependent. This is shown in Table 4.1. Figure 4.11 shows that there is agreement between the

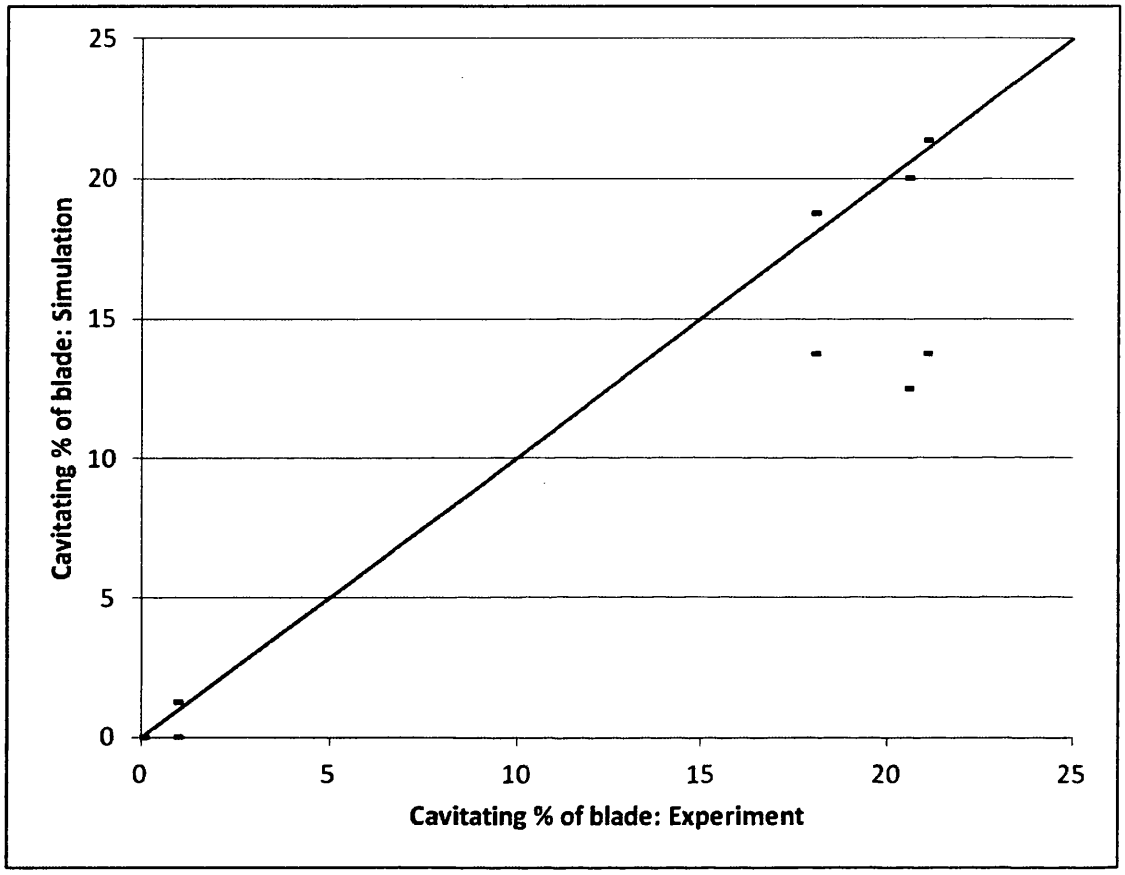

Figure 4.11: The percentage of cavitating blade elements, from experimental observations, against the percentage range of cavitating blade elements, from the cavitation model with the BEMT scheme. Cavitation results along the black line indicates agreement with the experimental observations. The Red dashes are simulation results at the minimum height in the water column; the blade positioned vertically downwards from the hub. The Blue dashes are simulation results at the maximum height in the water column; the blade positioned vertically upwards from the hub. The simulated result lies between these two limits.

experimental observations and the simulated results. The black line agrees well with the maximum cavitation limit given by the BEMT simulation. This suggests that the blade position shown clearly in the experimental observations, Figure 4.10, is near the top of the cavitation tunnel where cavitation occurrence increases.

4.10 Regular, Non-Linear Waves

The Chaplin stream function theory is compatible with BEMT as the wave velocities are coupled to the tidal velocities to give a combined flow velocity for a number of points in the x, y and z directions, stored in a velocity matrix. The results are determined from a minimum number of input variables, consisting of the water depth, d, wave height, h_w and wavelength, λ.

There is one more variable to consider; the speed of the moving frame of reference, a constant C. Chaplin's wave theory cannot theoretically accommodate a non-uniform tidal flow, as the speed at which the moving frame of reference propagates must be spatially independent. Also, if the flow was to be non-uniform, the fluid is no longer irrotational and the Laplace equation is not valid. This complicates the expansion so that the formulation is not easily incorporated into BEMT, where the tidal velocity is dependent on height as described in Section 4.2.1.

Solutions to this complication are also explored in Chapman [2009]. Swan *et al.* [2001] suggests that Chaplin's wave theory be used, purely to produce wave motion components of flow velocity without consideration for current effects. These components can be summed with the tidal flow velocity components, which are calculated independently of the wave motion, as described in Section 4.11. The tidal flow velocity profile can be depth-dependent, therefore the propagation speed of the moving frame of reference varies with depth. Therefore, as in Swan *et al.* [2001], C is set to 0 by Chapman [2009].

This approach is not theoretically rigorous as wave and tidal flows do not act independently of each other. Visually, the wave climate on a flood tide will have very different features to the same wave climate on an ebb tide. Waves and tides do not act independently, but rather the wave profile is highly dependent on the tide flow and, depending on the wave climate and the tide cycle, there may also be an effect of the

waves on the tidal currents near the surface. The approach used by Chapman [2009] and Swan *et al.* [2001] cannot capture the rotation of flow which may occur, nor the effect of the current velocity on the dispersion of the waves, Masters *et al.* [2008]. In Galloway *et al.* [2010] an improved wave and tidal coupling theory is discussed and this is an active research area.

In Section 4.12, the accelerative terms calculated from stream function wave theory are retained as they produce hydrodynamic force on the turbines which is calculated using Morison's equation, as in Orme [2006]. This calculation is further described in Section 4.12.

For the investigations in Chapman [2009] and the results in this chapter, the wave climate is considered over short distances therefore the loss of accuracy is minimal and the user can input the wave climate variables, already affected by tidal flow. Further work into the complex tidal and wave coupling is presented.

In addition to the specific torque and axial force output, the standard non-dimensional power, torque and axial force coefficients are also calculated for comparison between different turbines and flow conditions, as defined in Equation 2.22 in Section 2.4.2.

4.11 Tidal Inflow Velocity with Wave Effects

A common approach to couple the wave effect and tidal velocity profile from Section 4.2.1, within BEMT is to solve for wave and tidal inflow velocities in the same discrete positions independently and then take the sum, as in Equation 4.14. The tidal flow direction may be at an angle θ to the wave propagation and is resolved to the wave direction:

$$U_c = U_w + U\cos\theta_w \tag{4.14}$$

The final result from stream function wave theory with tidal considerations is a set of discretised axial and vertical velocities, u and v respectively, that include wave and tidal effects. The axial velocity replaces the far upstream velocity flow,

U, in the BEMT model. U now varies with blade element position on the rotor plane. This is a significant change in the BEMT theory as the flow in the stream tube is not a constant velocity; also it must now be assumed that the upstream and rotor positions experience the same wave climate. To consider vertical wave effects, the vertical velocity v is now resolved using the azimuth angle γ between the blade element and the rotational plane, to give v_r, and therefore affects the local rotational velocity at each blade element. At a single point in time, the effect of v_r on one side of the turbine, will be the opposite for the other side, as the rotational velocity of the turbine acts in the rotational plane and v in the vertical plane:

$$v_r = v \cos \gamma \tag{4.15}$$

The position of each blade element is now crucial in order to interpolate the correct local velocities for the BEMT calculations, from the three-dimensional discretised non-uniform flow. It is necessary to account for yaw, tilt and rotational position by tracking the blade position in a global co-ordinate system and resolving the flow field velocities relative to the blade element. Using a translational rotation matrix, the new position of a blade element can be found from its starting position, further mapping details can be found in Masters *et al.* [2008].

To illustrate the output for Chaplin's stream function wave theory, a large regular wave is considered in the experimental set up incident on the 0.4m radius turbine of Bahaj *et al.* [2007], with $\lambda = 0.5$m and $f = 0.2$Hz. The magnitude of the velocity and acceleration components, (u, v) and $(du/dt, dv/dt)$, in the moving frame of reference is output; the x ordinate is the distance in the axial flow direction and the y ordinate is height. The result is independent of cross section direction. The far up stream and far down stream velocities are no longer uniform over the stream tube but are interpolated from the blade element position. Momentum theory also dictates that the same wave climate exists far upstream and far downstream.

Figure 4.12 shows the example wave theory outputs for slack tide, 0ms^{-1}, a tidal velocity of 1.73ms^{-1}; traveling in the wave propagation direction, and also a tidal velocity of -1.73ms^{-1}; traveling against the wave. As the wave propagation direction is parallel to the current flow for all these cases the vertical velocity component v and the accelerations $du/dt, dv/dt$ are the same for all cases. This is an effect of the simple

coupling used by Chapman [2009]. These frames also illustrate the propagation of waves below the sea surface and the effects on the flow velocity and acceleration.

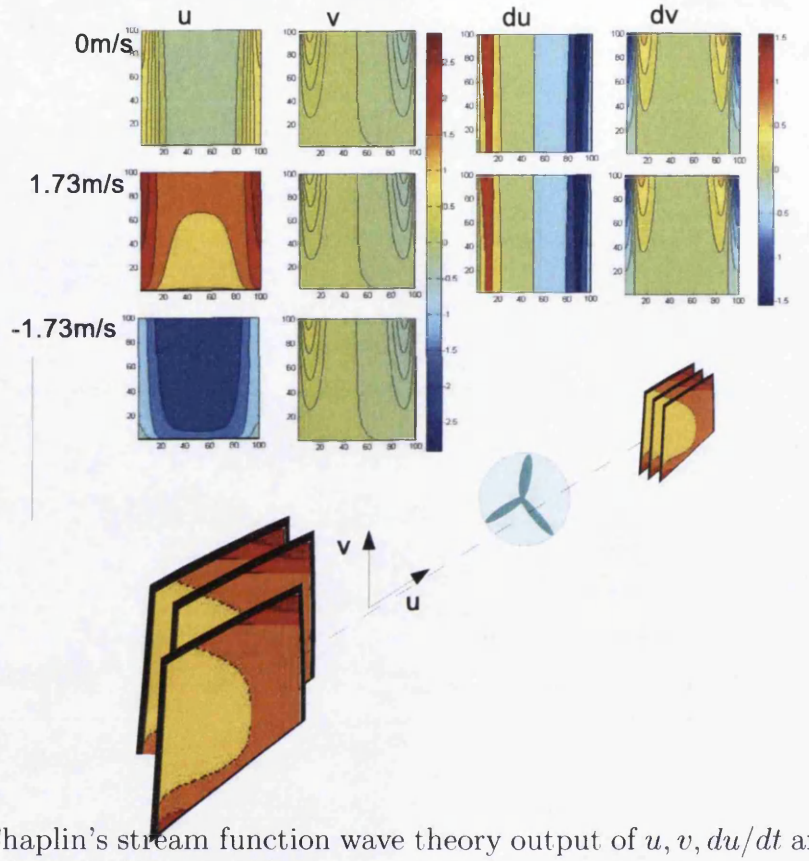

Figure 4.12: Chaplin's stream function wave theory output of $u, v, du/dt$ and dv/dt in tidal velocities of 0ms^{-1}, 1.73ms^{-1} and -1.73ms^{-1}, parallel to the wave propagation direction. u and v use the same reference colour bar in units ms^{-1}. The units for the du/dt and dv/dt reference colour bar is ms^{-2}. The x-ordinate is distance, normalised to one wavelength, and the y-ordinate is height.

4.12 Acceleration Forces

The Morison equation is a semi-empirical function that describes the forces on a fixed body fully submerged in oscillatory fluid flow, Orme [2006]. It has been used extensively to estimate the loadings caused by waves on offshore structures. The Morison equation is the sum of a drag term and an inertia term, $F_{ME} = F_{dr} + F_{in}$.

The drag term is proportional to the square of the local flow velocity, whereas the inertia term depends on the local flow acceleration. This inertia term can be used independently to calculate the torque force, F_{Tin}, and the axial force, F_{Ain}, owing to wave accelerations obtained from stream function wave theory. These loadings are then combined with the BEMT loadings T and F_a as in Equations 4.23 and 4.24. dF_{in} represents the inertia force per unit length in the wave propagation direction, where C_m is the inertia coefficient and A is the cross-section area of the fixed body parallel to the oscillatory flow.

$$dF_{in} = \rho C_m A \frac{du}{dt} dl \tag{4.16}$$

Considering a cylindrical structure placed vertically such as a pile or tower, the value of C_m is 2 and $A = \pi {R_c}^2$ where R_c is the radius of the cylinder and u is the local incident velocity on the aerofoil. Therefore the inertia force in the horizontal direction is equal to twice the displaced mass multiplied by the horizontal fluid acceleration in the absence of a structure.

To extend this formulation to non-cylindrical structures the inertial coefficient is made dependent on an added mass coefficient, C_A. This was first defined by Newman [1977] as the ratio of added mass to the displaced fluid mass. It is later discussed by Orme [2006] and then by Whelan [2010].

$$C_m = 1 + C_A = 1 + \frac{M_A}{\rho A_x dl} \tag{4.17}$$

where A_x is now the cross-section area of the non-cylindrical structure and $M_A$is added mass. By considering a turbine blade as a non-cylindrical submerged structure, the inertia forces on the blade in the axial and tangential directions from wave accelerations can be derived if A_x and M_A are known.

To find added mass of a blade element, Whelan [2010] considers Theodorsen's theory as outlined in Bisplinghoff and Ashley [1975]. This theory describes a thin plate making small amplitude oscillations in both pitch and heave and the lift per unit span is derived from potential flow theory. An aerofoil with oscillating inflow velocity from waves can be compared to Theodorsen's flat plate, oscillating in heave, if the frame of reference moves with the wave inflow. Also the blades are fixed at

an angle, θ, to the oscillating inflow. Therefore the chord length is now replaced by $c\sin\theta$. By adapting Theodorsen's theory, the lift per unit span for a fixed-pitch aerofoil in oscillatory inflow is,

$$L_s = \rho\pi\frac{(c\sin\theta)^2}{4}\ddot{y} + \rho\pi V c C(k)\sin\theta\dot{y} \tag{4.18}$$

$C(k)$ is Theodorsen's complex function (or lift deficiency function), with k as the reduced frequency which is a measure of unsteady flow and not covered in this work, further details can be found in Bisplinghoff and Ashley [1975]. The first term is the non-circulatory, true added mass term. The second term is a circulatory term and represents pseudo added mass owing to the presence of a wake, in this work the second term is not considered. As the added mass term for a fixed-pitch flat plate also equals M_A, this implies that,

$$M_A = \rho\pi(c\sin\theta/2)^2 dl \tag{4.19}$$

Alternatively, comparisons are drawn in Whelan [2010] and in figure 4.13, between an aerofoil, ellipse or flat plate. In all these cases, the added mass is proportional to the square of the facing width to the oscillatory flow, W. This concurs with earlier work, Orme [2006], where an ellipse is used and also agrees with added mass per unit span for an aerofoil in waves as derived from Theodorsen's theory.

Oscillatory inflow:

Figure 4.13: With horizontal oscillating inflow, structures with these cross-section shapes all have the same added mass per unit length equation of $\rho\pi(W/2)^2 dl$ where W is the facing width.

Similarly, for tangential oscillatory flow, the added mass is,

$$M_A = \rho\pi(c\cos\theta/2)^2 dl \tag{4.20}$$

Combining Equations 4.16, 4.17 and 4.19 gives the axial and tangential added inertia forces for a blade element,

$$dF_{Ain} = \rho \left(1 + \frac{\pi (c \sin\theta/2)^2}{A_\alpha}\right) A_\alpha \frac{du}{dt} dr \tag{4.21}$$

$$dF_{Tin} = \rho \left(1 + \frac{\pi (c \cos\theta/2)^2}{A_\alpha}\right) A_\alpha \frac{dv}{dt} dr \tag{4.22}$$

Where, similarly to the axial velocity, v is the tangential local velocity incident on the aerofoil. With incident wave flow, the inertia forces in both axial and tangential directions are calculated for each aerofoil element and are in addition to the BEMT axial and tangential forces.

$$dF_A = dFa + dF_{Ain} \tag{4.23}$$

$$dF_T = dT/r + dF_{Tin} \tag{4.24}$$

4.13 Discussion

In this section the Chaplin's stream function theory of the regular, non-linear waves simulated in this model is presented. A simple way of simulating the non-linear effects of the tide on the wave velocity and acceleration profile is discussed and an example output is considered.

The momentum theory assumption of the same velocity profile far upstream and far downstream in a streamtube without a turbine present is now violated. However, a similar profile is assumed, suggesting a large-scale constant wave climate before or after the turbine location to minimise the significance of this violation. The tide direction and magnitude is shown to have a significant effect on the wave shape. Morison's equation is introduced to simulate the accelerative forces and the Keulegan-Carpenter number is extended to both axial and tangential directions for tidal steam turbines and represents the importance of the wave acceleration force.

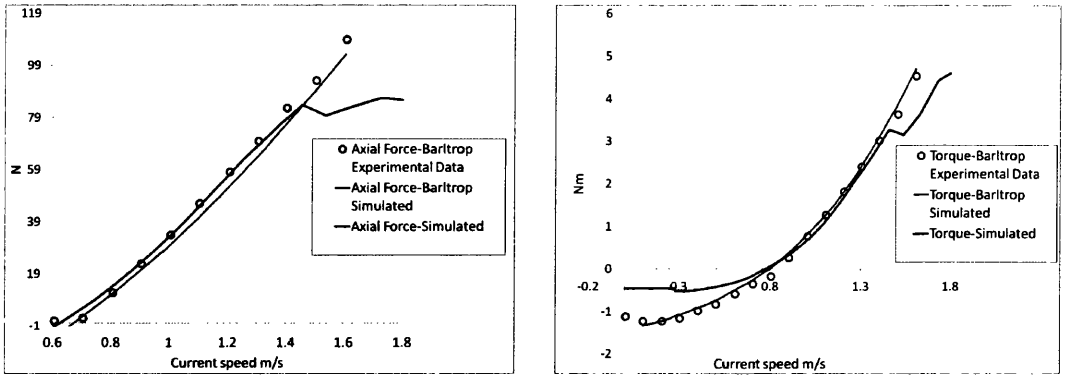

Figure 4.14: Axial force and torque against current speed in the absence of waves for towing tank experiment and simulation by Barltrop *et al.* [2007] with turbine rotational speed 200rpm. Compared with predicted BEMT results.

In Chapter 4, this theory is evaluated against experimental data sets from two tidal turbine, tank, test data sets and some simulation results are discussed for a freely rotating turbine and a fixed rotation turbine. In particular, periodic turbine stall is significant when simulating a turbine response in waves.

4.14 Validation Study 1

4.14.1 Calibration of Simulation Model

The lift and drag curves are based on wind tunnel tests at Reynolds number of 3×10^6 however, for the Barltrop *et al.* [2007] investigations, Reynolds number ranges from 4.05×10^4 to 1.43×10^5. This is significantly lower than the lift and drag coefficients for the S814 airfoil and could be a source of discrepancy between the experiment and the presented simulation data.

The figures 4.14(a) and 4.14(b) show the experimental results with no incident wave as published in Barltrop *et al.* [2007]. These graphs clearly show a good agreement between experimental results, the Barltrop BEMT results and the BEMT scheme as outlined in Chapters 2 and 3, particularly between 0.6ms^{-1} and 1.4ms^{-1} flow velocities. Further details about the experiment are found in Barltrop *et al.* [2007], and Figure 4.14.1 shows the dimensions of the experiment. The sample interval results compared with the simulations in this work are taken only because they

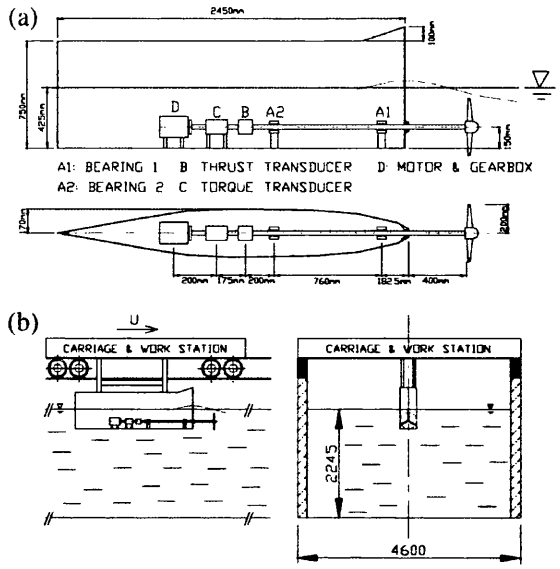

Figure 4.15: Diagram of experimental setup, taken from Barltrop *et al.* [2007]

are the published results from Barltrop *et al.* [2007].

Inflow velocities of 0.6ms^{-1} or less give a high TSR and the BEMT scheme over-predicts axial force and torque in this region. This is a consequence of the high induction correction method, as previously discussed in Section 2.9.1.

At low inflow angles the aerofoil behaves similarly to other aerofoils; C_L increases with inflow angle and the aerofoil stalls at around 12^o characterised by a sudden drop in C_L. However, this aerofoil shape plateaus C_L between 13^o and 20^o and after 20^o continues the stall. This is not a typical aerofoil feature and, by removing it, the discontinuity in the figures 4.14(a) and 4.14(b) is also removed.

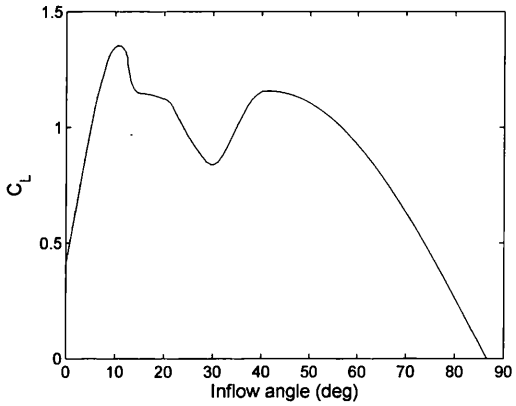

Figure 4.16: Lift coefficient for 0 to 180 degrees aerofoil inflow angle for the S814 aerofoil shape.

The aerofoil lift and drag data was sourced from wind tunnel tests, Barltrop *et al.* [2007], however in this stall region aerofoil data is less reliable than at lower inflow angles. After the stall region, $>$ 45^o, there is the recovery peak and all aerofoils will give similar lift coefficients.

Another possible explanation is that the experimental rotor experienced stall delay. However, this is difficult to quantify and we have reported BEMT results that include the discrepancy caused by the published C_L curve. This will allow other researchers to replicate our results and to explore this discrepancy further.

Figure 4.17 is taken directly from Barltrop *et al.* [2007] and gives the experimental findings when towing a turbine in waves with constant frequency but of various heights.

In Barltrop *et al.* [2007], it is shown that although the average axial force increases by only 2N from a 35mm to 126mm wave height, the maximum peak axial force is greatly increased. For example, increasing wave height from 84mm to 126mm nearly doubles peak axial force on the turbine. Similarly, increasing wave height from 35mm to 126mm increases the average torque by less than 0.1Nm, however the peak torque is greatly increased.

From figure 4.19(a), it is clear that increasing wave height increases the deviation of torque from its mean, both positively and negatively, therefore increasing wave

height has less effect on the average torque compared to the effect on average axial force.

To simulate tidal flow in the experimental towing tank, the turbine was towed along the length towards a prescribed wave which was induced throughout the towing tank. Because of the experimental setup, realistic coupling between tides and waves will not be captured.

To correctly simulate this experiment, Chaplin's wave theory must be implemented independent of tidal flow to create an uncoupled wave inflow acceleration and velocity field as would be present in the experiment.

Although the effect of towing a turbine through an incident wave will not produce realistic wave and tidal coupling, the apparent wave celerity will increase as the wave frequency seen by the turbine increases. This is now the apparent wave frequency and agrees with the previously presented, simple and separate wave and tidal superimposed,

$$f_a = f_w + \frac{(U_w + U\cos\theta)}{L} \tag{4.25}$$

4.14.2 Results

The tidal flow velocities are superimposed onto the wave velocities before the inflow is used in the BEMT equations. It was found that, to produce figures 4.17(a) to 4.20(b), the simulated axial force and torque values were shifted to the datum consistent with the methodology of the experimental paper. Figures 4.17(a) to 4.20(b) compare experimental measurements with simulated results and a good agreement is seen between experimental data and the proposed BEMT and wave model scheme, as described thus far. There is greater agreement between simulation and experiment with larger wave heights.

This may be the result of a flow disturbance creating turbulent inflow, the effect of which is seen in the experimental results for no waves, particularly for torque results as seen in Figure 4.19 ans 4.20. This disturbance is periodic and has a frequency of 9 per rotor revolution. This implies that the 3 blades may be passing structures in

turn.

The blade-pass disturbance becomes less significant with increasing wave height as the wave period begins to dominate the inflow velocities and accelerations. Therefore a more likely explanation of the oscillation is a more effective depth-dependent inflow as described in Section 4.2.1. By increasing x in Equation 4.1 this effect can be amplified.

An interesting feature of these time-step results is that, with waves, the axial force resolved in experimental direction, does not decrease much below the base value with no waves, -however the torque result does.

As well as the performance coefficients, instantaneous TSR is calculated using the instantaneous average of the tip velocities, U_{ref}, as described in Section 4.4. This is found to be an accurate representation when considering a depth-dependent flow field. Therefore, considering the same result on a TSR graph, as in figure 4.21, a wave causes anti-clockwise circulation with time which produces a hysteresis loop on the steady state graph.

As a wave trough passes over the turbine, inflow velocity will decrease which increases TSR. This increases axial force to a point, after which increasing inflow velocity any further has little effect on axial force. Then, as the passing wave moves from trough to crest, U_{ref} increases which decreases TSR and the axial force decreases.

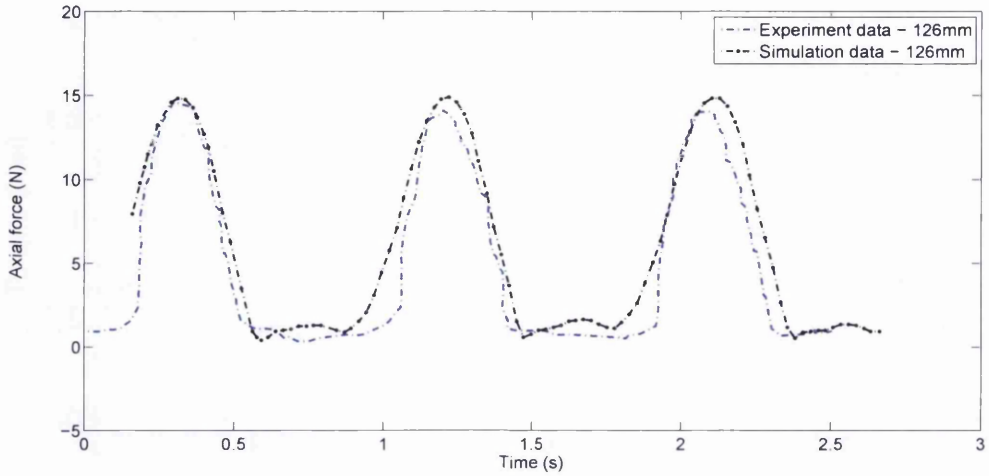

(a)

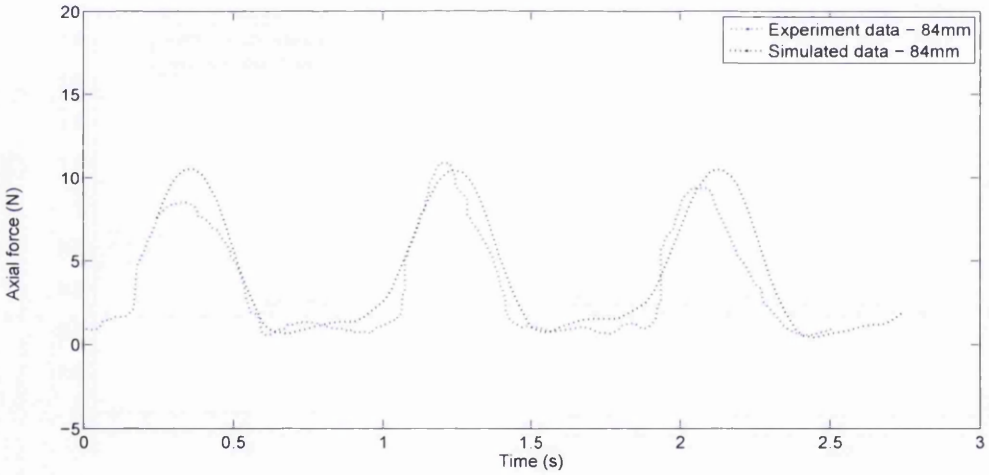

(b)

Figure 4.17: Towing tank experimental results for a turbine rotating at 90rpm compared to simulated results: Time histories of (a)Axial force with 126mm wave height and (b)Axial force with 84mm wave height, 0.7ms^2 current flow, in the presence of waves with frequency 0.833Hz as presented in Barltrop *et al.* [2007].

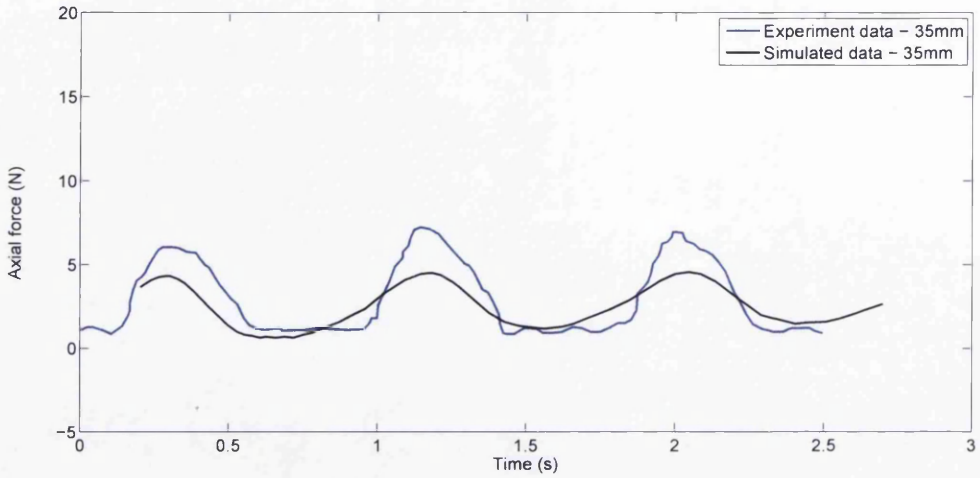

(a)

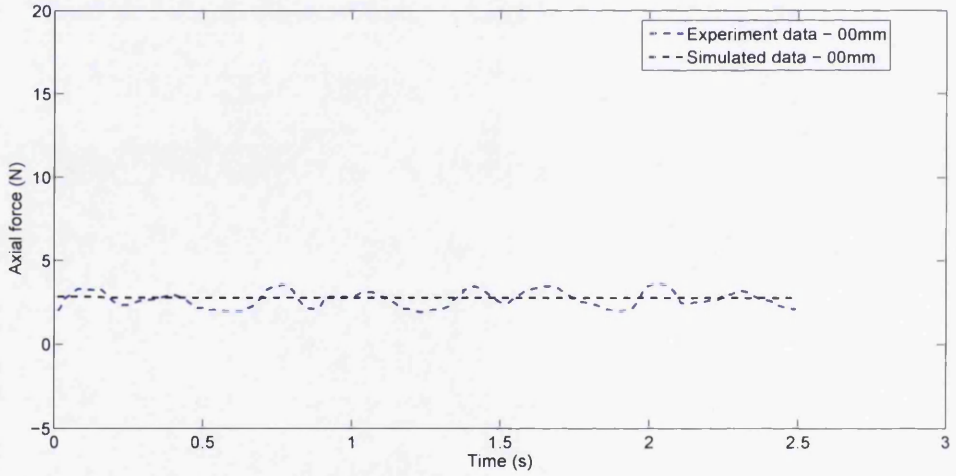

(b)

Figure 4.18: Towing tank experimental results for a turbine rotating at 90rpm compared to simulated results: Time histories of (a)Axial force with 35mm wave height and (b)Axial force with 0mm wave height, 0.7ms^2 current flow, in the presence of waves with frequency 0.833Hz as presented in Barltrop *et al.* [2007].

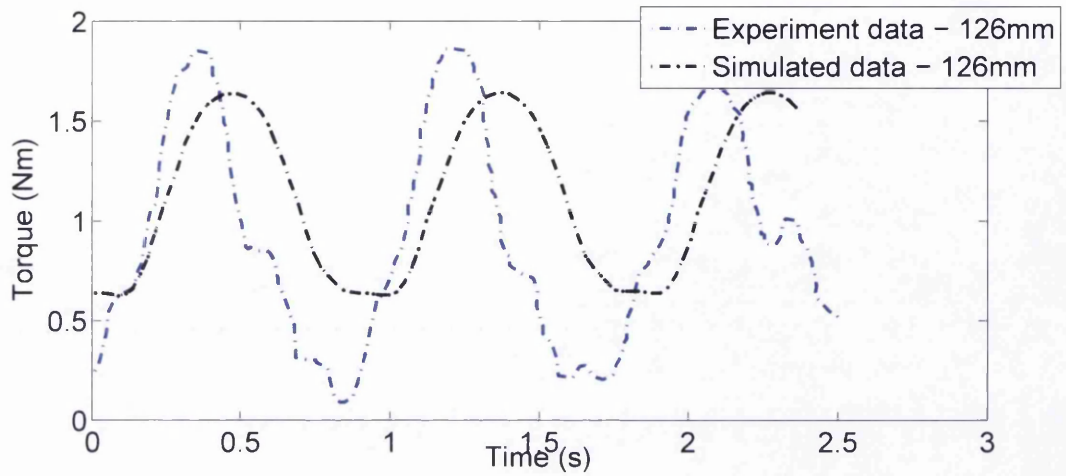

(a)

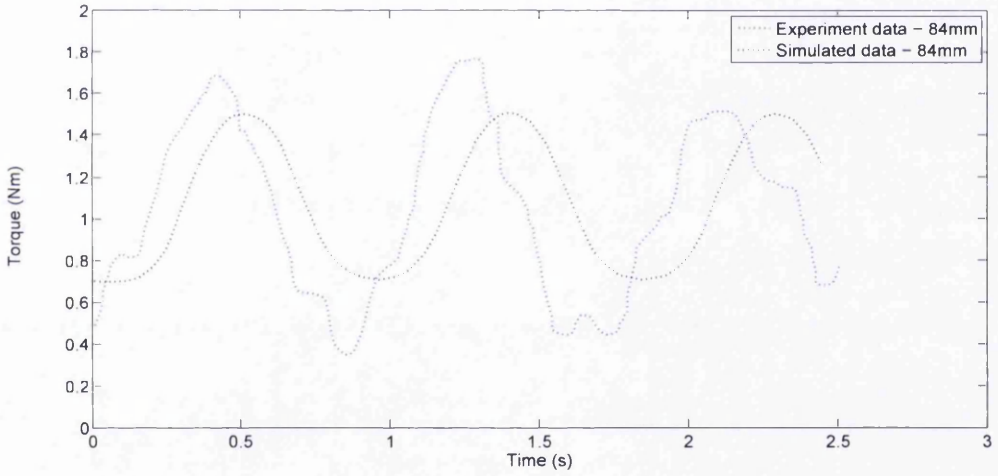

(b)

Figure 4.19: Towing tank experimental results for a turbine rotating at 90rpm compared to simulated results: Time histories of (a)Torque with 126mm wave height and (b)Toque with 84mm wave height, $0.7ms^2$ current flow, in the presence of waves with frequency 0.833Hz as presented in Barltrop *et al.* [2007].

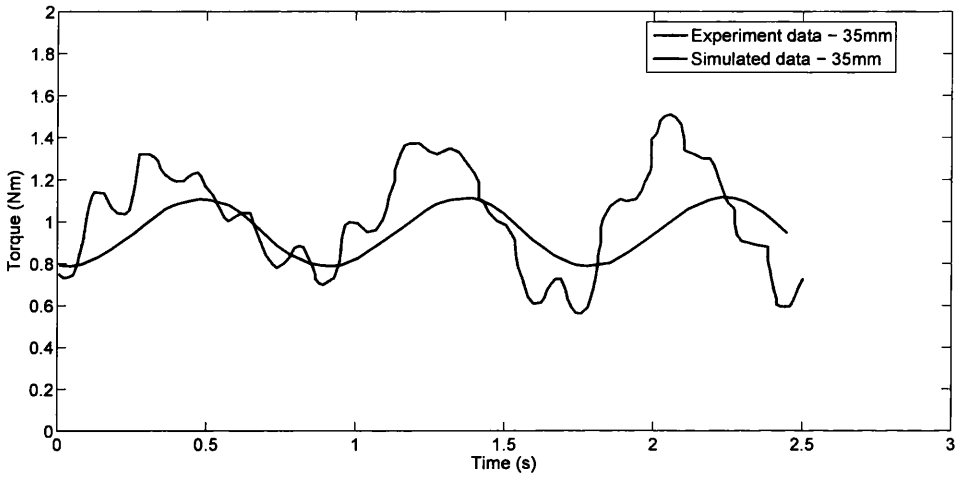

(a)

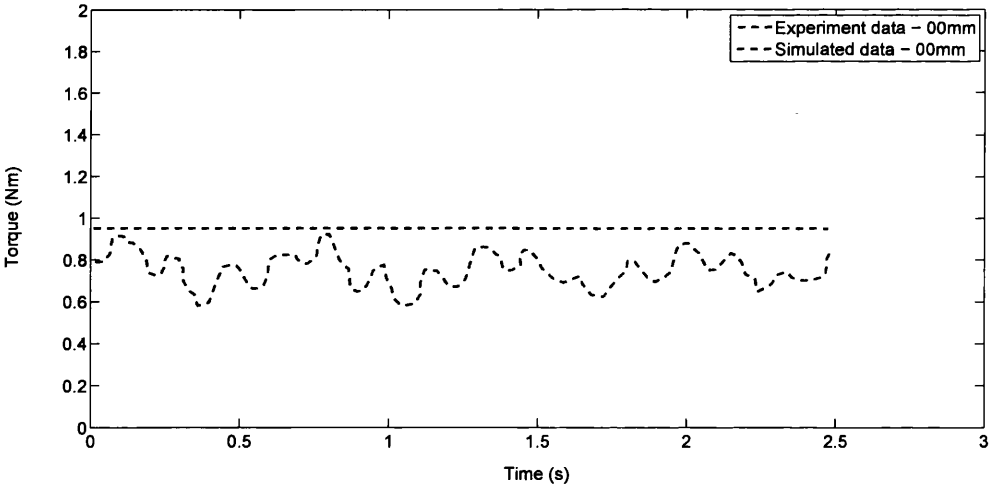

(b)

Figure 4.20: Towing tank experimental results for a turbine rotating at 90rpm compared to simulated results: Time histories of (a)Torque with 35mm wave height and (b)Toque with 0mm wave height, $0.7ms^2$ current flow, in the presence of waves with frequency 0.833Hz as presented in Barltrop *et al.* [2007].

Minimum axial force occurs at a wave crest and the gradient at a TSR below operating TSR, marked by the 00mm TSR results, is steeper and more consistent than the gradient at a TSR above the operating TSR. Therefore, the axial force result is not symmetrical.

Torque reacts to waves in a similar way, however the torque profiles either side of operating TSR are similar. Figure 4.21 shows how, in the presence of waves, the steady state performance result of the turbine circulates with time around a set, controlled, operating point. Therefore the effect of a wave velocity is unique to the turbine shape, dimensions and C_L, C_D values, and the set operating conditions.

In Barltrop *et al.* [2007] it is shown that the mean axial force and mean torque are less affected by wave height if tidal velocity is increased. Remembering that all the experiments were conducted at a constant rpm, by increasing tidal velocity, TSR is decreased towards the peak from over-speed or away from it into the stall region and therefore the axial force variation with time from the mean will be more symmetric.

4.15 Validation Study 2

4.15.1 The Self Weight and Buoyancy Term

For any horizontal axis turbine, the weight of the rotor blade and its buoyancy act in the plane of the swept area and therefore will contribute to the in-plane bending moment around the blade root. This extra torque loading on the blade root has the same frequency as the rotational frequency of the turbine and is an important consideration for turbine material composition.

For each blade element, BEMT calculates values such as torque and axial force and then sums over the blade length and number of blades. For one blade, the relation of in and out of plane bending moments around the blade root to elemental torque and axial force respectively is shown in Equations 4.26 and 4.27. The number of blade elements on one blade length is m.

The second term in Equation 4.27 is the self weight and buoyancy term and consists of the buoyancy force and blade element weight force resolved in the torque direction. The moment of these forces around the blade root is calculated by multiplying by the

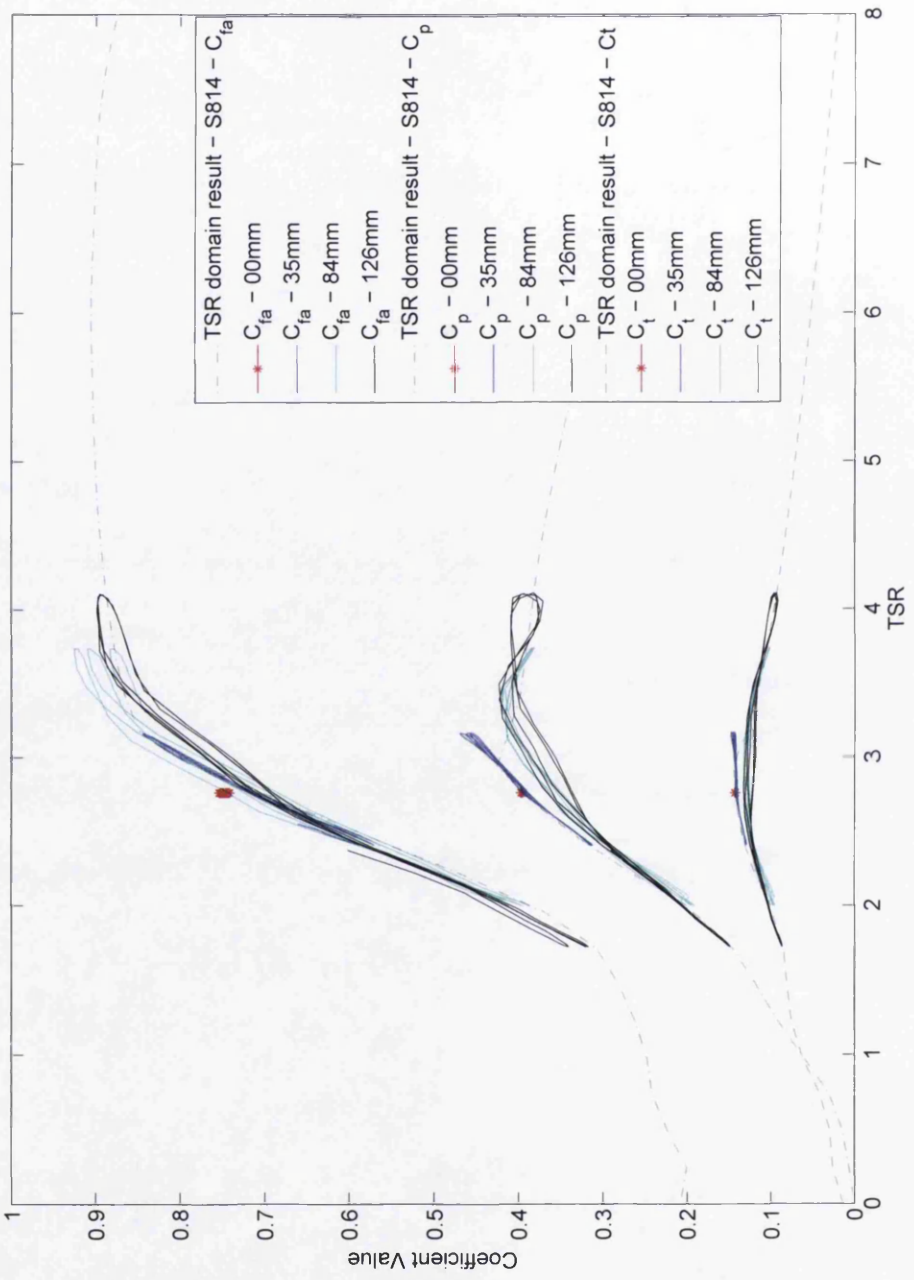

Figure 4.21: Simulated steady flow performance coefficients of C_{fa}, C_p and C_t against TSR. On the same graph, the time-dependent simulation results are presented again but now against TSR. Wave frequency 0.833Hz, differing wave heights.

distance between the blade element position $r(j)$ and the hub radius R_{hub}.

$$Mx(t) = \sum_{j=1}^{m} dFa(j,t)\,(r(j) - R_{hub}) \tag{4.26}$$

$$My(t) = \sum_{j=1}^{m} \left[\frac{dT(j,t)}{r(j)} + (A_\alpha(j)dr)\, g\,(\rho_{blade} - \rho) \sin(\gamma(t)) \right] (r(j) - R_{hub}) \tag{4.27}$$

The self weight and buoyancy term has a significant effect on the in-plane bending moment around the blade root. The effect of this term is shown by simulating the bending moments for the Barltrop test turbine, details of which can be found in Barltrop *et al.* [2006] and Section 1.6.2.

Figure 4.22(a) presents the in turbine plane bending torque, My, without this term and Figure 4.22(b) presents My with self weight and buoyancy considered.

As the rotational velocity is set to about $200rpm$, the time taken for one full revolution is $0.3s$. This is the time period of the high frequency oscillations introduced by the self weight and buoyancy term as once per revolution this term acts in the direction of torque to give the maximum and opposite direction to torque to give the minimum.

The whole turbine torque is found by summing the elemental torque over the blade length and number of blades. Although the effect of self weight and buoyancy on the in-plane bending moment of one turbine blade is shown to be significant, it has no effect on the total turbine torque assuming that the blades are equally spaced. The proof for this is given in Appendix B.

4.15.2 Results

Although the turbine rotational speed is set to 200 rpm, the towing speed varies from 0.3 to $1ms^{-1}$ giving operating TSR values of 12.22 and 3.77 respectively.

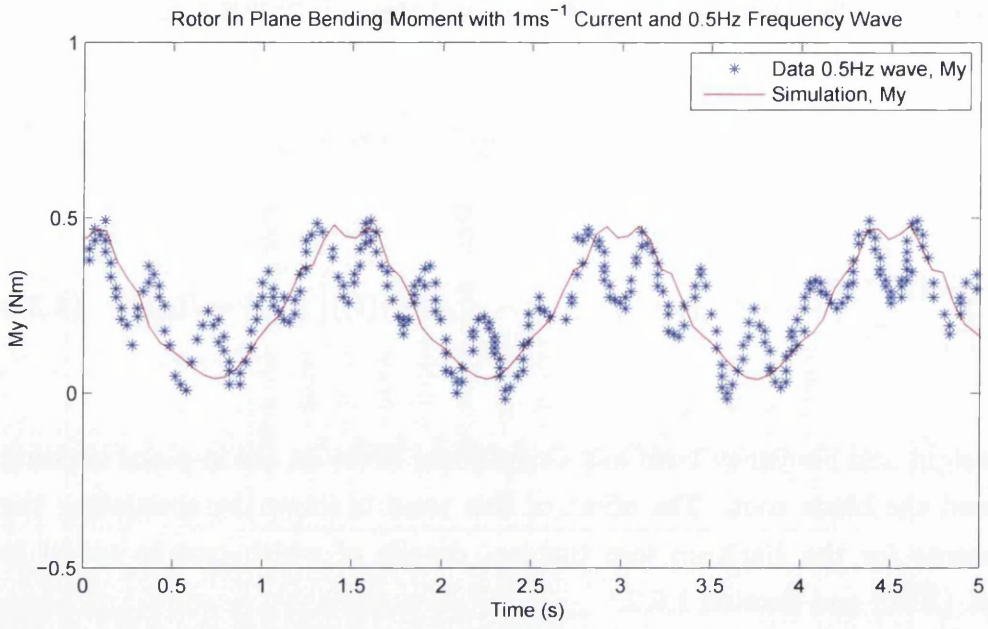

(a)

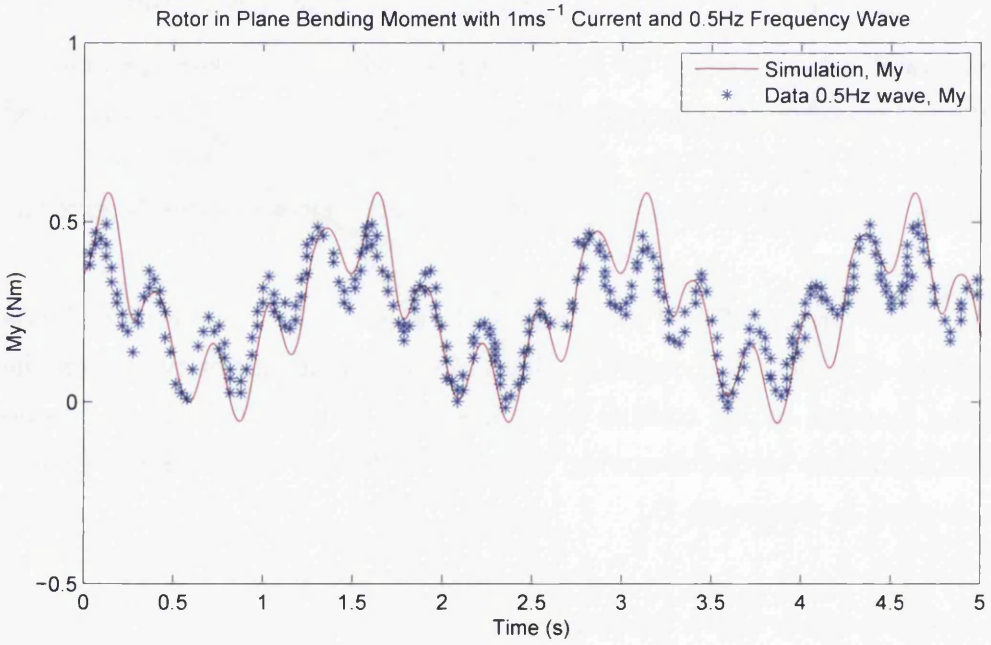

(b)

Figure 4.22: The effect of the self weight and buoyancy term on the in-plane blade torque (a) without the self weight torque and (b) with the self weight torque.

4. BEMT FOR TIME-VARYING FLOW

The commonly used Buhl [2005] high induction correction causes BEMT turbine simulation to over predict axial force, torque and power at high operating TSR, Togneri *et al.* [2011]. The same result is found with current speed $0.3ms^{-1}$ due to the high operating TSR.

The simulated bending moments for $1ms^{-1}$ current speed and steep waves of frequency $1Hz$ is compared to experimental data in Figures 4.23 and 4.24.

The variation in axial force bending moment is over-predicted by BEMT with stream function wave theory. The simulated torque bending moment agrees well with results and the effect of self weight is clearly seen in Figure 4.24 with the same frequency as the number of rotations per second.

The simulated and experimental effective wave frequencies do not agree as the simulated wave frequency is too low. As the turbine was towed to simulate current flow, there will be no effect on the waves due to current. The wave speed used in the simulation is a simple addition of current and uncoupled wave speed.

Figures 4.25 and 4.26 give the same results but with lower frequency waves resulting in less steep wave peaks. There is improved agreement between simulation and experimental results however the simulated wave frequency is now too high. The torque bending moment simulated result with self weight oscillations is particularly accurate.

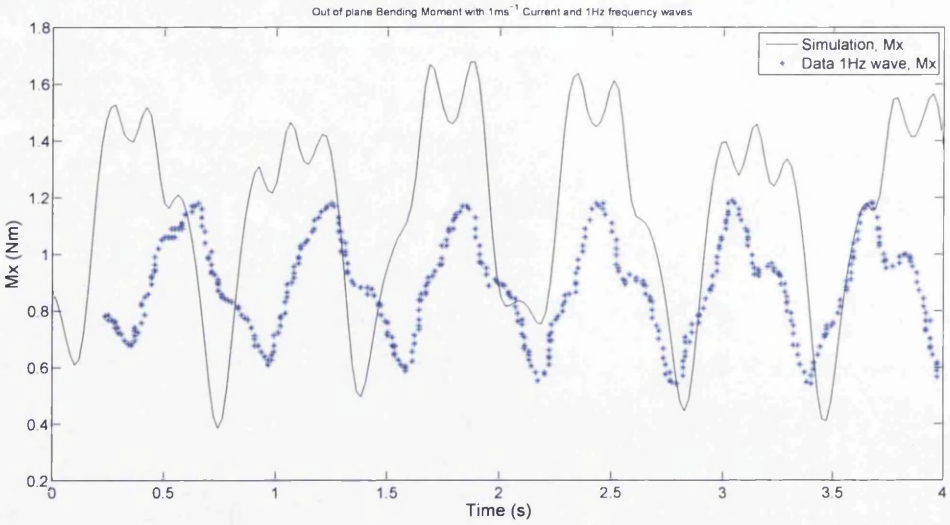

Figure 4.23: Bending moment of the axial force on the blade root with 1Hz

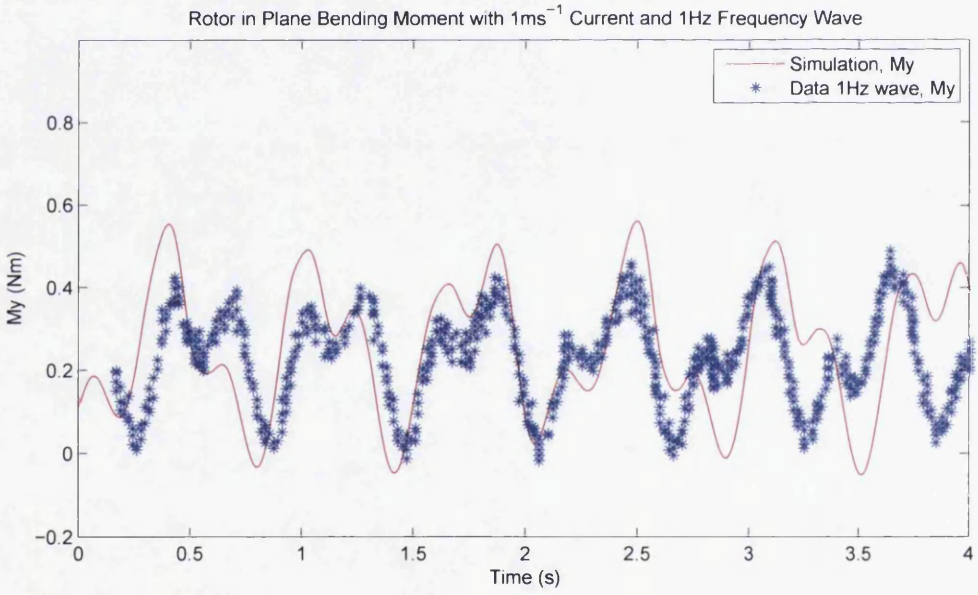

Figure 4.24: Bending moment of the in-plane torque force on the blade root with 1Hz

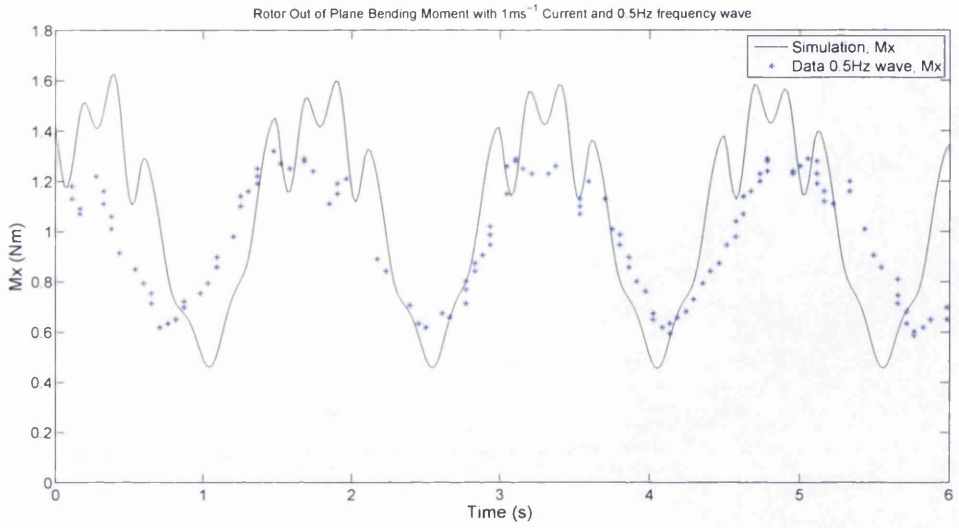

Figure 4.25: Bending moment of the out of plane torque force on the blade root with 0.5Hz

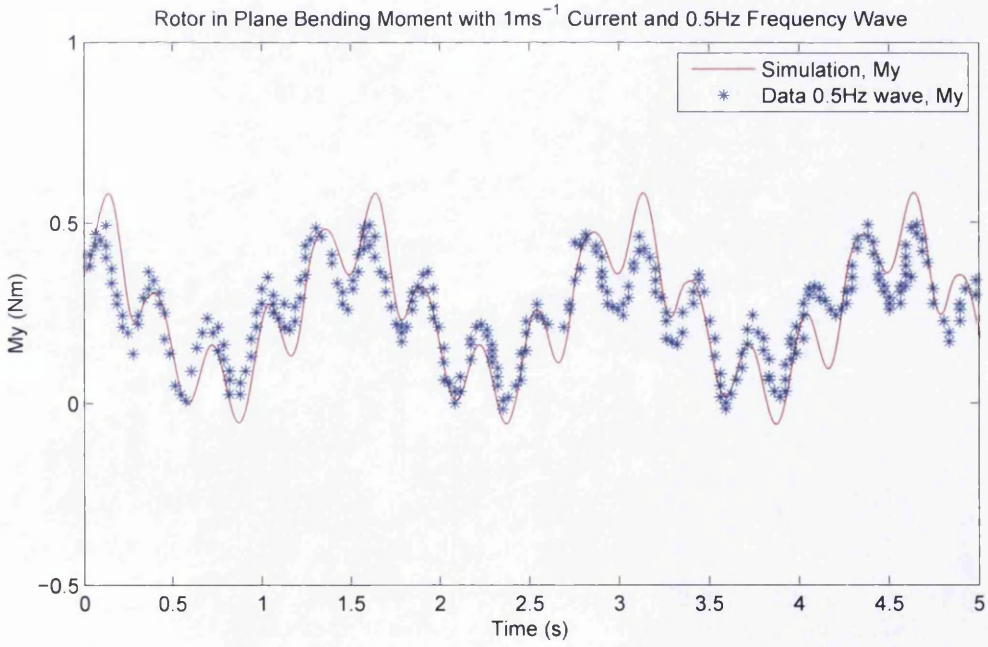

Figure 4.26: Bending moment of the in-plane torque force on the blade root with 0.5Hz

4.16 Discussion

The effect of buoyancy and self weight is significant on the blade root torque and could contribute to load fatigue at the root. A self weight and buoyancy term is introduced and discussed for the BEMT and stream function wave theory scheme.

For a horizontal axis turbine with $N_B > 1$ this torque term is proven to always cancel when the three blade torques are summed to produce total turbine torque. The Barltrop *et al.* [2006] experimental data is given in terms of axial force and torque bending moments around the blade root, therefore these terms are validated.

The simulation compares well with the experimental results and the full comparison for all data sets given in Barltrop *et al.* [2006] is given in Section 4.15.2.

The self weight effect can be coupled with BEMT to affect the torque bending moment of a blade and is shown to be accurate compared to experimental data. Further work is needed to understand the wave and current interaction. Other effects, such as tower shadow, are present in the experiment but not simulated. However, the effect on torque is expected to be significantly less than the effect of self-weight.

4.17 Conclusion and Recommendations

Blade element momentum theory with the stream function wave theory, and combined with a purposefully non-reactive coupling between waves and tides, produce a turbine performance simulation tool with dynamic inflow.

A validation study on the transient BEMT formulation is presented. A comparison is shown between the Barltrop *et al.* [2007] experimental results of a towing turbine in a wave tank and the BEMT simulation with the wave model.

The performance data of the turbine with time is compared to the simulation. A good agreement is found and presented here between the experiment data and the simulated results for axial force and torque.

The conclusion drawn from these investigations is that effect of waves on turbine performance coefficients is to create oscillations around the C_T(TSR), C_p(TSR) and C_{Fa}(TSR) curves. An increase in inflow velocity, with a fixed turbine rotational speed, will always give a decrease in TSR. Whether this decrease in TSR gives an

increase or decrease in axial force and torque depends on the background conditions and the background TSR. Therefore wave effects are dependent on the shape of the performance coefficient TSR curve, as shown in figure 4.21, around the operating condition of the turbine.

It is important that wave effects do not cause the rotor to periodically stall, as shown in this example, as this maximises the amplitude of wave effects on turbine performance coefficients.

It is also important that the turbine structure is designed to survive maximum axial force. The presented BEMT scheme coupled with stream function wave theory is proven to be a quick, simple and robust engineering tool suitable for predicting torque, axial force and performance characteristics of real tidal turbines.

This section contains validation studies for the BEMT scheme with the wave model implementation. The scheme is shown to be accurate in simulating the axial force and torque loadings on a tidal stream turbine with a dynamic inflow, as it has reproduced the unique experimental data by Barltrop *et al.* [2007], thus extending the established and widely-used BEMT model to dynamic inflow problems. This provides confirmation that BEMT is still valid for these inflow conditions. The self weight and buoyancy term is introduced and is shown to significantly effect single blade root torque. Good agreement is also found between the simulation and the two sets of experimental data, also by Barltrop *et al.* [2006]. The inflow velocity and acceleration profiles will be further developed to include turbulence, Chapman *et al.* [2012], and more complex wave climates and a reactive coupling method is discussed.

A study in Volume 2 of this thesis tests the strength of a Swanturbines scale blade over one revolution.

Finally, this section presents a real application of a BEMT coupled with a cavitation inception model. The model is a useful tool for the indication of cavitation occurrence during turbine design and gives a good indication of the extent of cavitation occurrence along the blade length. A comparison between published experimental cavitation data and the simulation results of the combined BEMT and cavitation model scheme are consistent with experimental observations. However, as these observations are limited, further quantitative validation is required as more data becomes available. The scheme has been used in turbine design to assess the inception point and extent of cavitation for a tidal stream turbine.

Chapter 5

Turbine Response

5.1 Introduction

The study presented in this section, compares the turbine response results when considering the irregular sea state simulation to the turbine response results with measured ADCP data. This will assess the difference in the turbine loadings with idealised, irregular wave representation from wave theory and measured turbulent wave inflow. Any change of lift and drag coefficients due to onset turbulence is neglected. The ADCP data used in this study is described by Chapman [2009] as site data from the European Marine Energy Centre and is irregular. From the ADCP data analysis, there is a free stream maximum flow of $U \simeq 2.1\text{ms}^{-1}$ and a large boundary layer effect, therefore x is set to 4. The apparent wave frequency is also estimated from the ADCP data as well as the wave frequency. The direction between dominant wave propagation and tidal flow is unknown, and so it is assumed here that the waves are unidirectional and the direction of propagation is aligned with the tidal flow direction. The flow is considered independent of cross-stream location.

The simulation results are produced using these input values and the water depth is set to 45m, as dictated by the ADCP data set. For this study, the full scale $10m$ diameter theoretical Swansea turbine is considered in the flow, situated half way up the water column at 25m hub height. The size of the turbine suggests a suitable angular speed is 6 revolutions per minute. This dictates the TSR operating value and for this study the performance oscillates in the stall region. Alternative rpm of 10 and

15 set the operating TSR region to peak C_p TSR and overspeed TSR respectively. This section demonstrates the ability to use the irregular sea state simulation tool to predict tidal stream turbine performance in irregular waves.

5.2 Idealised Regular Waves

In Section 4.4 the effect of U_{ref}, the velocity used to non-dimensionalise the power, torque and axial force and to calculate TSR, is explored for the TSR domain using the Bahaj *et al.* [2007] 0.8m diameter turbine with a boundary layer tidal velocity. The result using the $U_{ref} = U_{Hub}$ common approach is compared to U_{ref} = average U, where average U is defined in Equation (4.3). To consider the effect of U_{ref} with waves, the same rotor is now simulated, as in Section 4.4 but with the addition of single regular stream function wave, wave height 0.5m and frequency 0.2Hz. The result is presented for the $U_{ref} = U_{Hub}$ and the $U_{ref} = averageU$ case.

Figure 5.1 is used to illustrate how the simulation gives the same axial force and torque for both cases, therefore any difference in the performance coefficients is exclusively due to U_{ref}. These figures also show clearly the recursive effect of the wave and the irregular result during the first half wave period due to start up conditions. As expected, after this time, the non-dimensionalised performance coefficients for the two cases do not agree and C_p and C_{fa} are plotted against TSR in Figures 5.2(a) and 5.2(b) respectively.

If the hub velocity is used, the power coefficient deviates greatly from the no wave result. In Section 4.2.1 it is shown how a depth-dependent inflow velocity can cause significantly different steady state results, depending on the turbine blade positions and the maximum and minimum result limits are found. In the TSR domain, this causes recurring cyclic results, dependent on the rotational frequency of the turbine as the blade positioning changes. However, if the hub velocity is used for U_{ref}, the amplitude of the deviation from the steady state result is nonphysically large as maximum C_P reaches 0.55. Using the average U for U_{ref} results in much smaller variations from the steady state result.

A close view of C_{Fa} in Figure 5.3 illustrates how this result still cycles around the minimum and maximum, due to blade position in the depth-dependent inflow

velocity. The start up condition irregularities are shown in Figure 5.2. Figure 5.4 shows how, using U_{ref} = average U, the dynamic inflow result with a bed boundary layer and a stream function wave is still comparable to the steady state experimental results of Bahaj *et al.* [2007] and a good agreement is found between BEMT with dynamic inflow and experimental data.

5.2.1 Fixed Angular Velocity

There are two methods available in the scheme to 'fix' the rotational speed of the turbine. Firstly, the more literal approach of $\Omega = \Omega_{\text{START}}, \forall i$ can be used, where Ω_{START} is a constant input variable. Physically this assumes the turbine is under complete control. Secondly, an alternative generator model is implemented by Chapman [2009], to simulate a generator in terms of the generator torque FG, as discussed in Section 5.2.2. A target TSR is specified by the user and, with each iteration, the amount of torque necessary to operate at target TSR, FG, is calculated and acts on Ω to restore target TSR.

This section, however, considers the Bahaj *et al.* [2007] turbine with an incident wave, with wave height 0.5m, frequency 0.2Hz and 1.73ms^{-1} current flow. Figure 5.5 shows how the power, axial force and torque are effected by the waves and Figure 5.6 shows the translation of this effect into the respective coefficients.

Both are compared to U_{ref} on a second axis, which indicates the instantaneous wave phase and the x ordinate is time, normalised with respect to the the wave period.

Considering the two figures, the effect of the wave on the performance indicators of power, torque and axial force is very different to the effect of the same wave on the respective coefficients. Figure 5.5, shows how a wave crest increases the power, axial force and torque.

In Figure 5.6 although an increase is found for C_t with wave crest, C_{fa} is shown to decrease. Interestingly, C_p increases with a building wave crest but decreases at the peak of the wave crest giving a double peaked recurring result with wave period.

The reason for this difference is the translation from performance value to the non-dimensionalised performance coefficient. The performance coefficients give the amount of power, axial force and torque on the turbine considering the flow velocities.

The results in Figure 5.6 can be explained by considering the TSR domain, Figure 5.7. As found previously, Figure 5.7 also shows an unphysical result for time less than half a wave period, due to the start up conditions that does not osciallate around the TSR domain result.

The turbine rotations per minute is set to 300 resulting in an operating TSR$\simeq$ 6.5. A wave trough decreases U_{ref} from the current velocity value of 1.73ms^{-1} and therefore increases TSR. The operating TSR$\simeq$ 6.5 is less than the TSR value for peak C_{fa}, higher than the TSR value for peak C_t and similar to the TSR value at peak C_p.

Due to the positive differential with increasing TSR on the C_{fa} curve, a wave trough results in an increase in C_{fa}. Conversely, the negative differential of the C_t curve with increasing TSR causes C_t to decrease with a wave trough.

The differential of the C_p curve is both positive and negative over the operating TSR region, resulting in the double peaked C_p trace in Figure 5.6 with every wave.

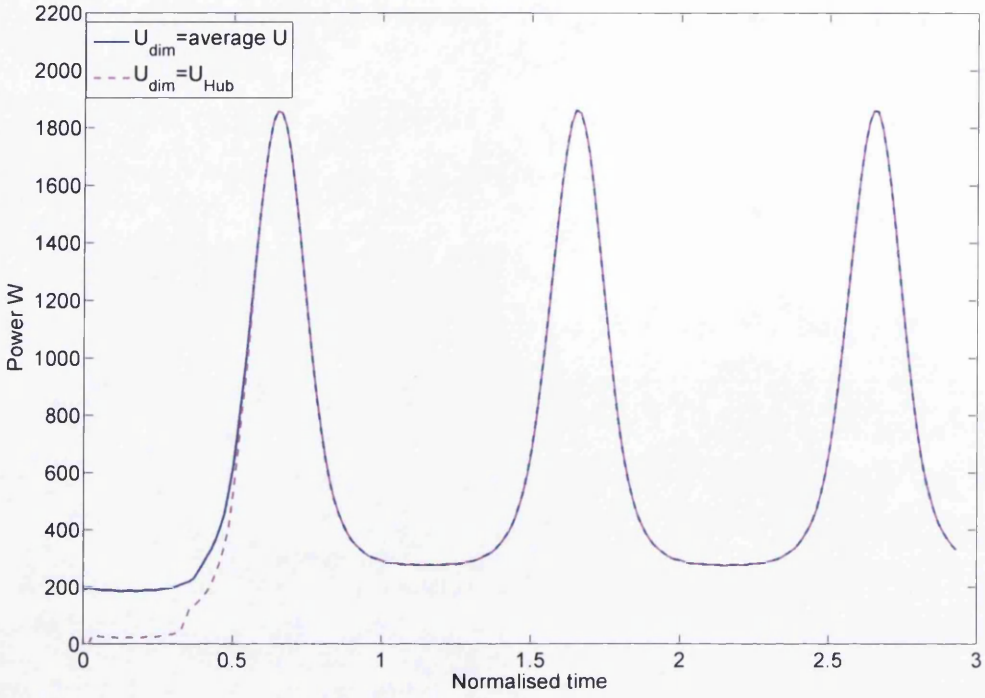

(a)

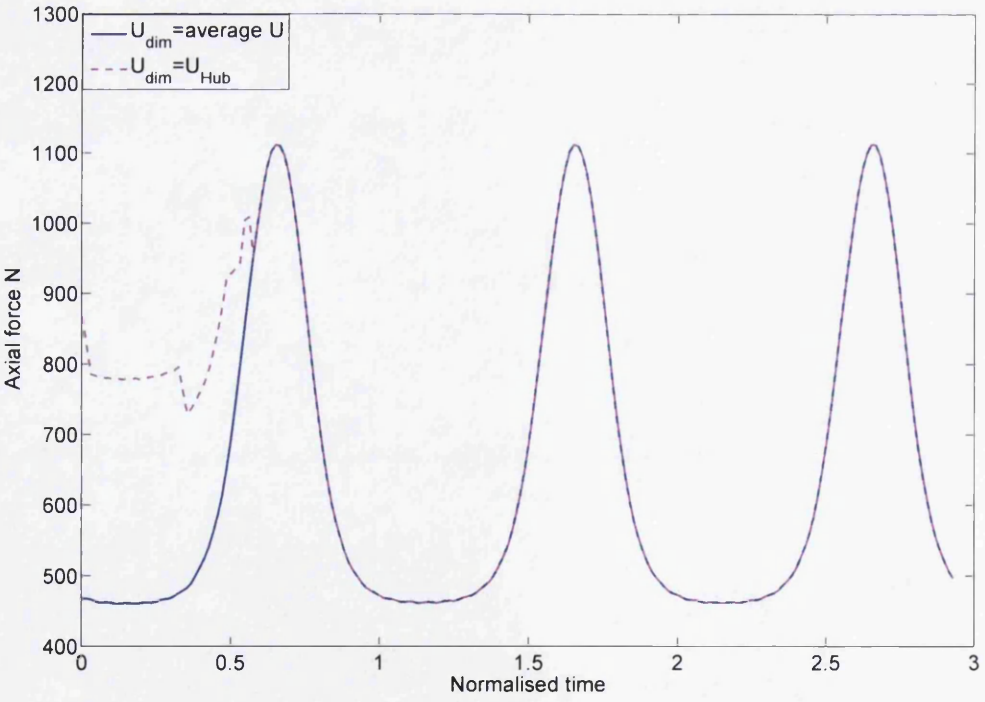

(b)

Figure 5.1: (a) Power and (b) Axial force vs. time normalised by the wave period for Bahaj *et al.* [2007] the turbine and experiment, with the addition of a stream function wave; $\lambda = 0.5$m and $f = 0.2$Hz.

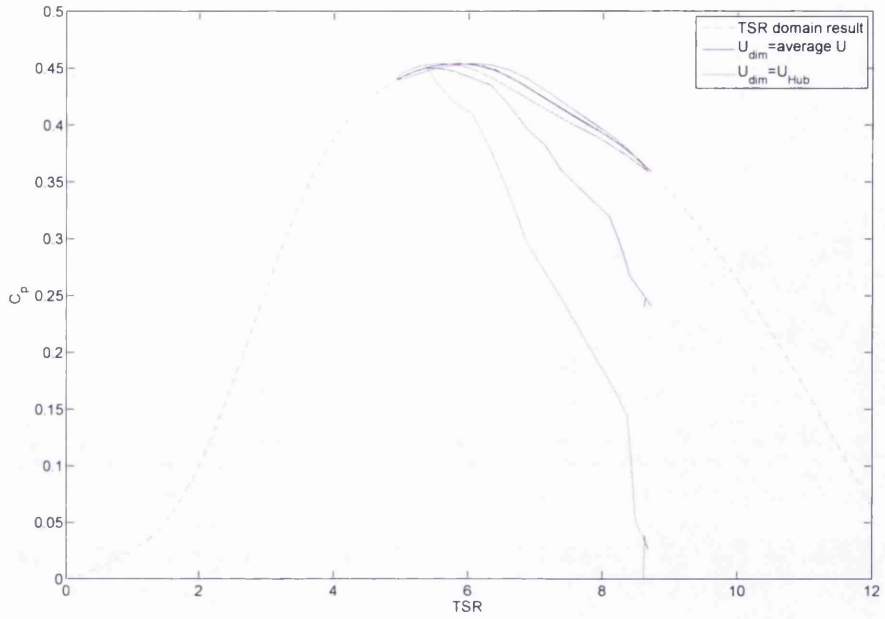

(a)

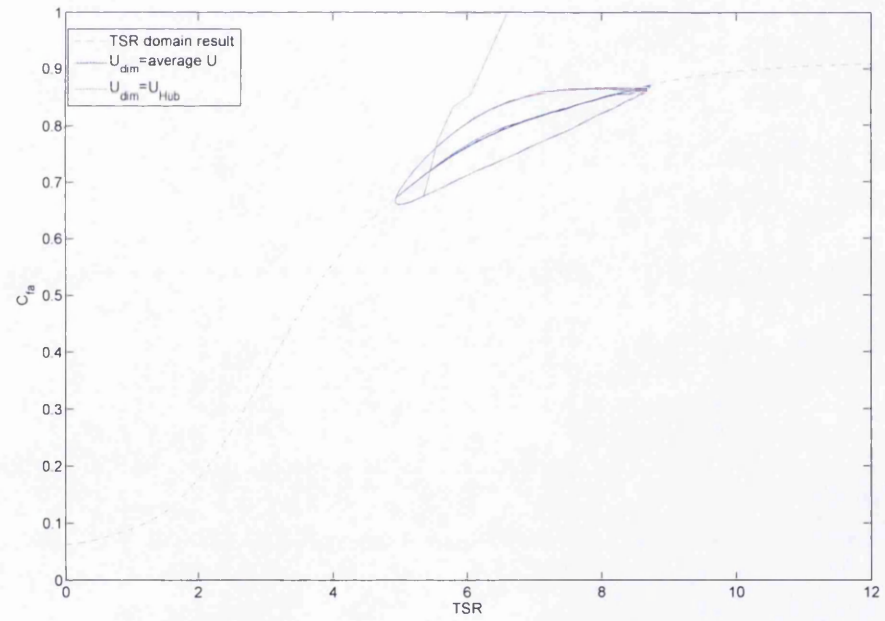

(b)

Figure 5.2: The (a) C_P and (b) C_{fa} time domain result plotted against TSR for the turbine and experiment, as described in Bahaj *et al.* [2007], with the addition of a stream function wave, wave height 0.5m and frequency 0.2Hz.

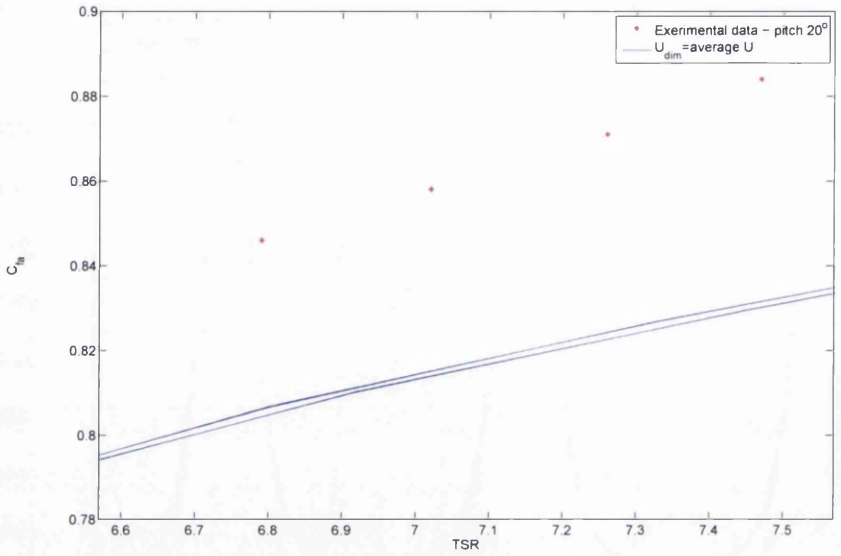

Figure 5.3: The C_{Fa} time domain result plotted against TSR for the turbine and experiment, as described in Bahaj *et al.* [2007], with the addition of a stream function wave, wave height 0.5m and frequency 0.2Hz.

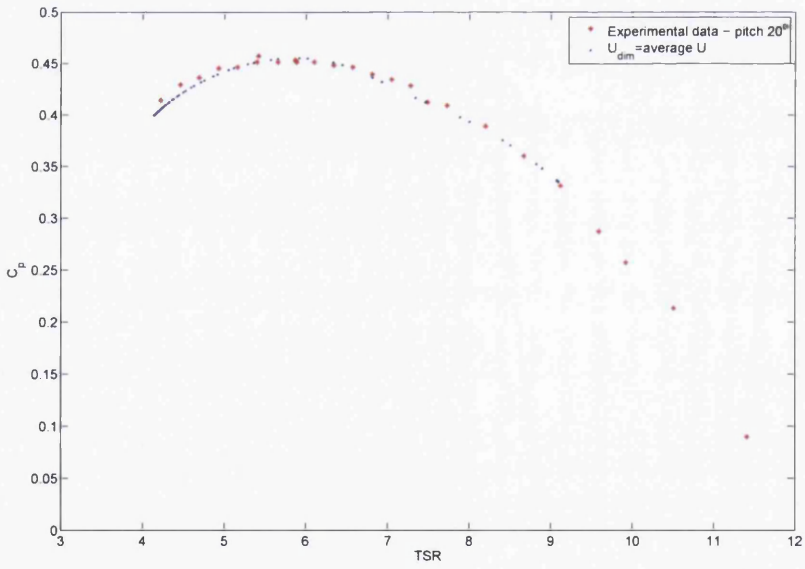

Figure 5.4: The C_P time domain result plotted against TSR for the turbine and experiment, as described in Bahaj *et al.* [2007], with the addition of a stream function wave, wave height 0.5m and frequency 0.2Hz.

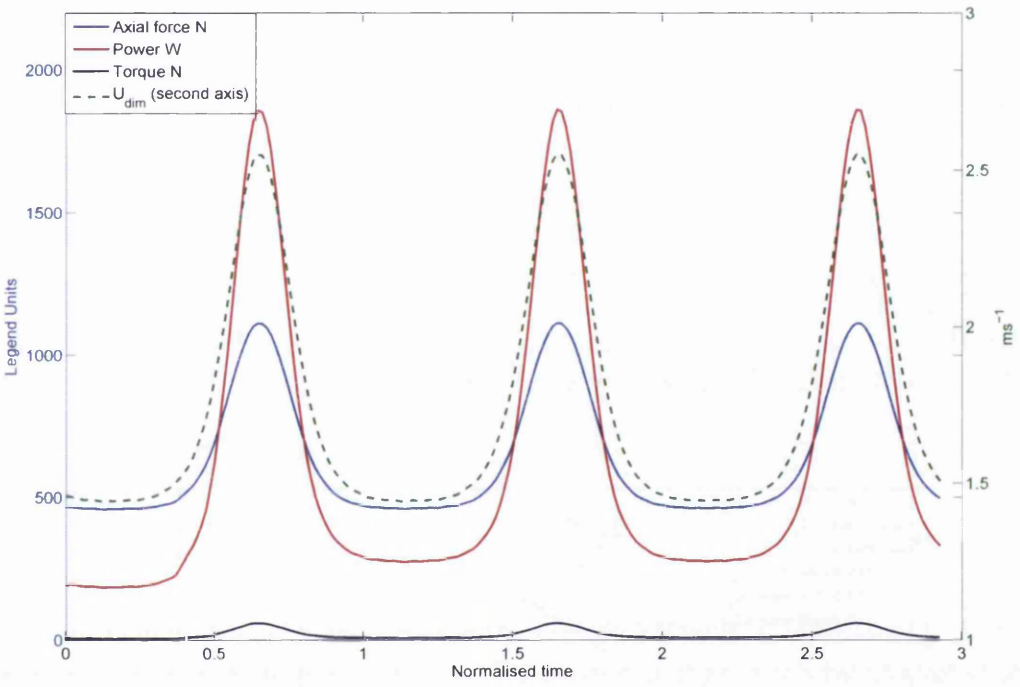

Figure 5.5: The Bahaj *et al.* [2007] turbine and experiment simulation results with the addition of a stream function wave, wave height 0.5m and frequency 0.2Hz in the time domain normalised by wave period.

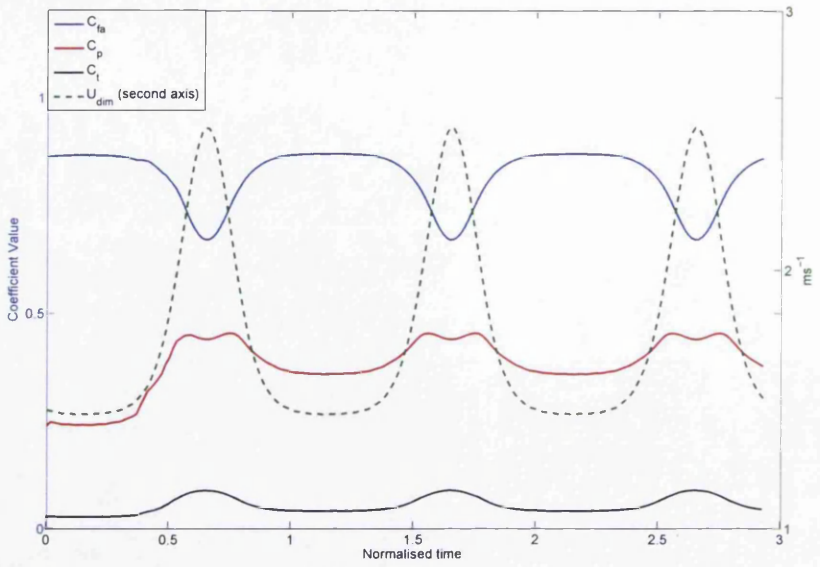

Figure 5.6: The Bahaj *et al.* [2007] turbine and experiment simulation coefficient results with the addition of a stream function wave, wave height 0.5m and frequency 0.2Hz in the time domain normalised by wave period.

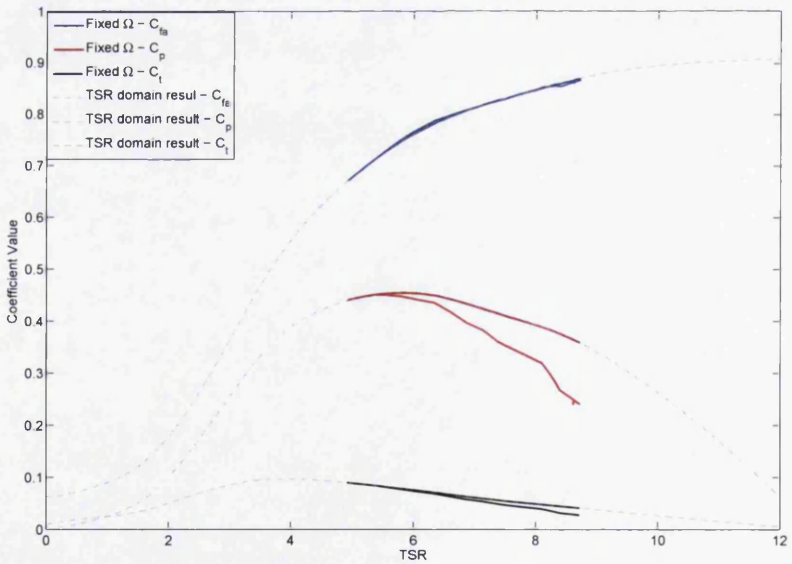

Figure 5.7: The Bahaj *et al.* [2007] turbine and experiment coefficient simulation results with the addition of a stream function wave, wave height 0.5m and frequency 0.2Hz, plotted against TSR.

5.2.2 The Stall TSR Effect

Low TSR occurs if the axial flow speed increases quickly which can cause the turbine to stall. Stall recovery is particularly important for dynamic inflow investigations as the waves can act to quickly increase U. Low TSR can also occur if the rotational velocity of the turbine reduces with a constant tidal flow, which may happen if fodder or driftwood impacted on the turbine.

If stall occurs, considering the inflow in the blade element frame of reference, the stall region is characterised by a steep gradient from a high C_p to a very low C_p with decreasing TSR. By setting the operating TSR to a small value, the stall condition is simulated. Now, the rotor attempts to increase and decrease rotational speed, tracing the wave motion.

The second method of 'fixing' the rotational speed is to allow a variable Ω and introduce a constant generator torque TG defined by Equation (5.1). TG is dependent on the target operational C_p and Ω. Both these values can be found if the operational TSR is set. In this section, operating TSR is set to 4 and the stall TSR region is $2 < \text{TSR} < 4$.

$$TG = \frac{\text{operating } C_p}{\text{operating } \Omega} \tag{5.1}$$

When modeling a turbine that has the freedom of varying Ω, the presence of waves does still affect the turbine performance, illustrated in Figure 5.8 by the axial force, power and torque results. For iteration $i+1$, the angular velocity of the turbine, Ω_{i+1} measured in $rads^{-1}$, is not fixed. The angular accelerations from the previous time step related to TG, friction torque, TF_i, and the torque, T_i of the turbine itself are considered, as in Equation (5.2).

$$\Omega_{i+1} = \Omega_i + \Delta t \left(\frac{(T_i - TG) + TF_i}{I} \right) \tag{5.2}$$

For this investigation, no friction torque is assumed and the moment of inertia of the turbine, I, is set to 68kgm^2. Comparing Figure 5.9 to 5.6, the effect of a wave crest now also decreases C_p and C_t as well as C_{fa}. This is due to the turbine specific TSR curve profile for these values at the two different operating positions; comparing

Figures 5.7 and 5.10. The large amplitudes of oscillation reducing C_p are a result of operating in the stall region and illustrate how this is an undesirable operating region for turbine performance.

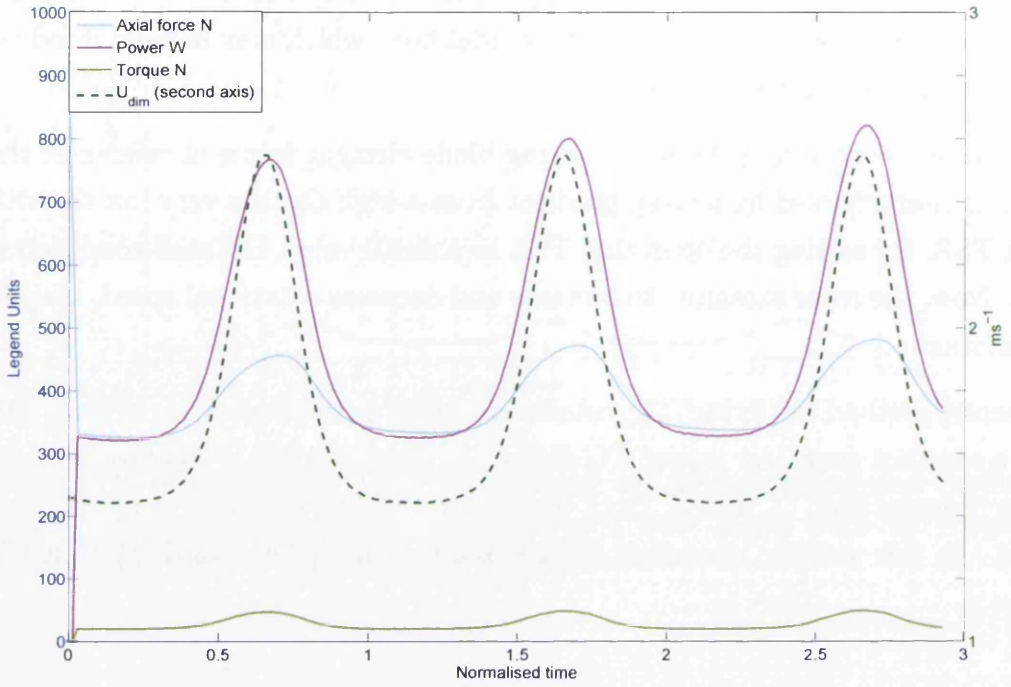

Figure 5.8: The Bahaj *et al.* [2007] turbine and experiment simulation results with the addition of a stream function wave, wave height 0.5m and frequency 0.2Hz in the time domain normalised with wave period. The turbines operation is fixed at $TSR = 4$.

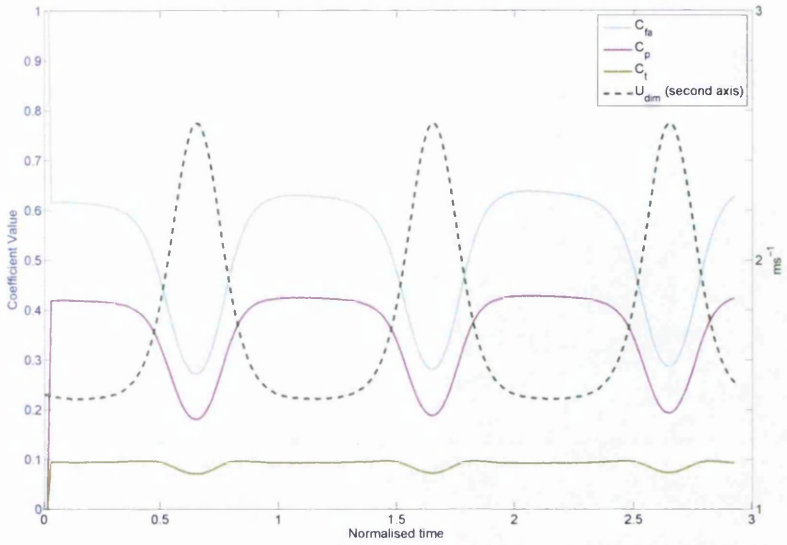

Figure 5.9: The Bahaj *et al.* [2007] turbine and experiment simulation coefficient results with the addition of a stream function wave, wave height 0.5m and frequency 0.2Hz in the time domain normalised with wave period. The turbines operation is fixed in the stall region at TSR= 4.

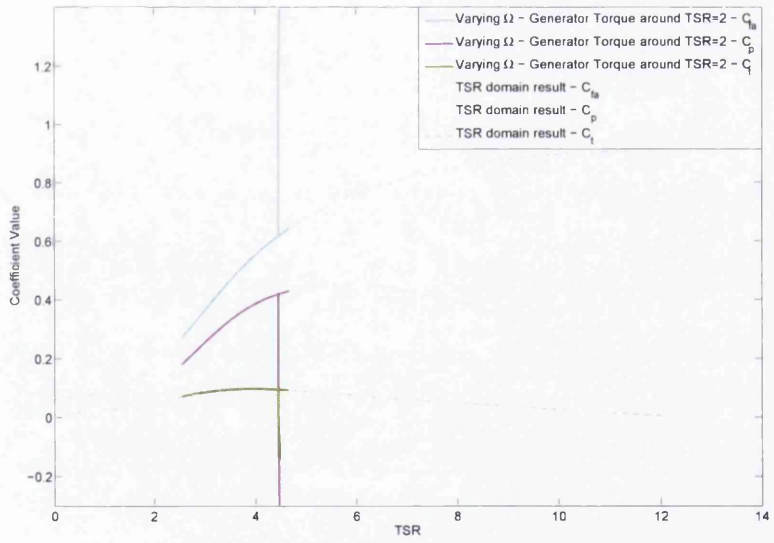

Figure 5.10: The Bahaj *et al.* [2007] turbine and experiment simulated coefficient results with the addition of a stream function wave, wave height 0.5m and frequency 0.2Hz, plotted against TSR. The turbines operation is fixed in the stall region at TSR= 4.

5.2.3 Freely rotating turbine

In this section, the same method is used but considering a freely rotating turbine, therefore the generator torque TG is 0. Equation (5.2) thus reduces to leave T_i alone to dictate the rotational acceleration to be considered in the $i+1$ iteration. Therefore Ω increases with each iteration until the torque result oscillates symmetrically about $Torque = 0$.

In addition to wave effects, Figures 5.11 and 5.12 show this progression of the performance values and coefficients with time. The performance then oscillates in a steady manner around zero torque and as the power is used to rotate the turbine, the extractable power is consistently zero with time.

The axial force and power coefficients also oscillate with torque, depending on their TSR curve shapes at the TSR value for $Torque = 0$. The amplitude and range of this oscillation is dictated by the shapes of the TSR curves, i.e. the turbine blade design, although the C_p result will similarly oscillate around the $C_p = 0$ result.

Numerically TG= 0 is effectively the same as setting operating $TSR \simeq 13$. The time period for the steady oscillations with time around $t = 0$ to be reached is determined by the moment of inertia of the system I, in Equation (5.2).

Larger I increases the transient result time, however the zero average torque state will eventually be reached, irrespective of I. The physical effect of frictional torque would be to resist the wave influence on the turbine, reducing the oscillation amplitudes for all coefficients and increasing the transient result time period.

U is maximum close to the wave crest, therefore, as TSR$\propto 1/U$, this gives minimum TSR. Conversely, the wave trough produces minimum U and maximum TSR. The operating TSR region will dictate the effect of the wave on turbine performance. In Figure 5.13 it is clear that TSR is above the TSR value at peak C_p. Therefore minimum TSR, such as at a wave crest, produces maximum C_p in this case. In the same manner, the minimum C_p is produced by the wave trough.

As the regular, non-linear Chaplin waves pass over the rotor, the power and torque coefficients trace up and down the TSR curves repeatedly with each wavelength. The coefficients have a slight circular trace around the TSR curve, which is most obvious with the axial force coefficient, due to the depth dependency of the incident flow.

5. TURBINE RESPONSE

As the turbine is rotating with time, the specific azimuthal position, and therefore the proximity to the free surface, of the three blades varies. Therefore, depending on the frequency of the waves and the rotational frequency of the turbine, for the same inflow conditions, the power, axial force and torque may be different due to the different position of the turbine blades. Even a small change in local inflow can significantly effect the result, as the lift and drag coefficients are interpolated from the blade element inflow angle.

Considering the definitions of the performance coefficients, as in Equation (2.22), the expectation is that the axial force coefficient would be less sensitive than torque and power coefficients to a depth-dependent inflow.

The blade elements close to the tip will have a larger depth position range than the elements close to the hub. The performance of these elements, which are most effected by depth-dependent inflow, is more significant when calculating torque.

Both torque and power are derived in Equation (2.17) from $C_L(\varphi)sin\phi+C_D(\varphi)cos\phi$, whereas axial force is derived from $C_L(\varphi)cos\phi - C_D(\varphi)sin\phi$. The second expression is more sensitive to altering inflow angle than the first giving the circular trace seen in axial force.

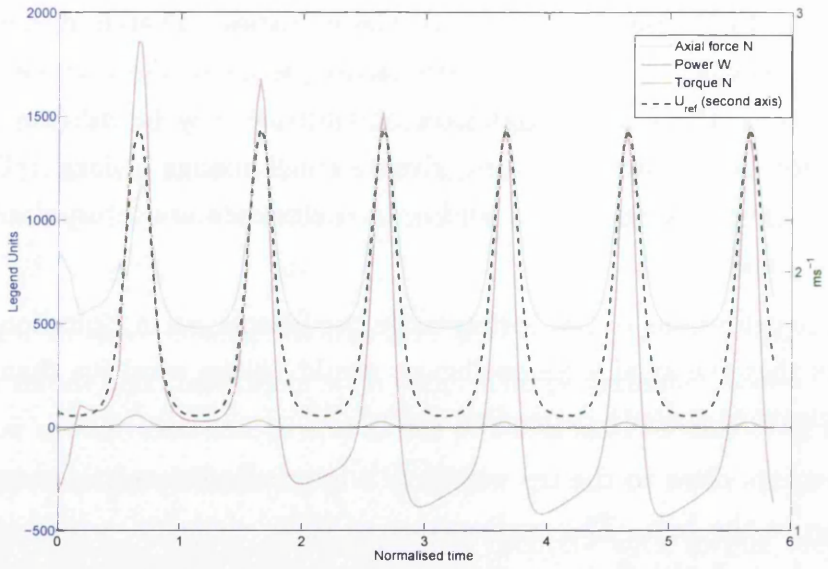

Figure 5.11: The Bahaj *et al.* [2007] turbine and experiment simulated results with the addition of a stream function wave, wave height 0.5m and frequency 0.2Hz in the time domain normalised with wave period. The turbine is freely rotating.

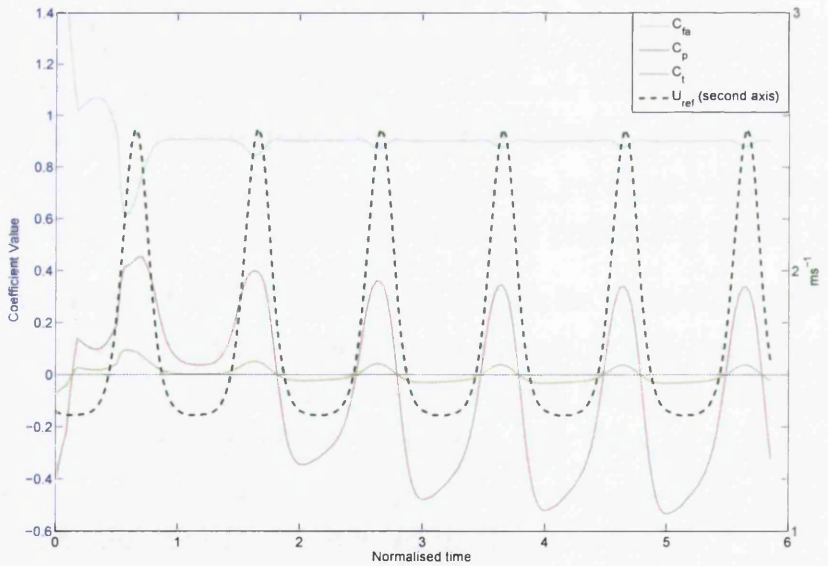

Figure 5.12: The Bahaj *et al.* [2007] turbine and experiment simulated coefficient results with the addition of a stream function wave, wave height 0.5m and frequency 0.2Hz in the time domain normalised with wave period. The turbine is freely rotating.

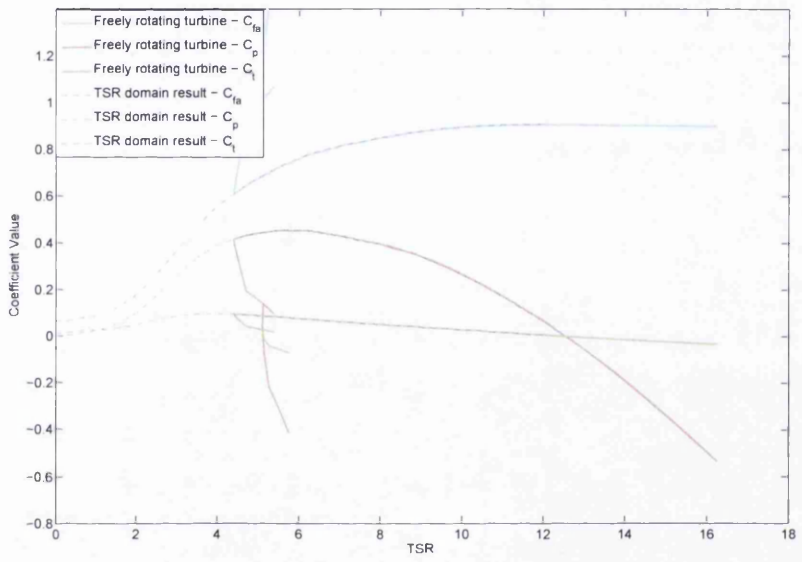

Figure 5.13: The Bahaj *et al.* [2007] turbine and experiment simulated coefficient results with the addition of a stream function wave, wave height 0.5m and frequency 0.2Hz, plotted against TSR. The turbine is freely rotating.

5.3 Discussion

The effect of the previously introduced Chaplin's stream function wave theory as dynamic incident velocity with BEMT is considered in this Chapter. The BEMT response to depth-dependent inflow is considered and the non-dimensionalisation velocity U_{ref} for the performance coefficients is evaluated for time and depth-dependent BEMT incident velocity.

The implementation of waves and currents is outlined. U_{ref} is calculated and the turbine performance result is considered and compared for three turbine operating cases.

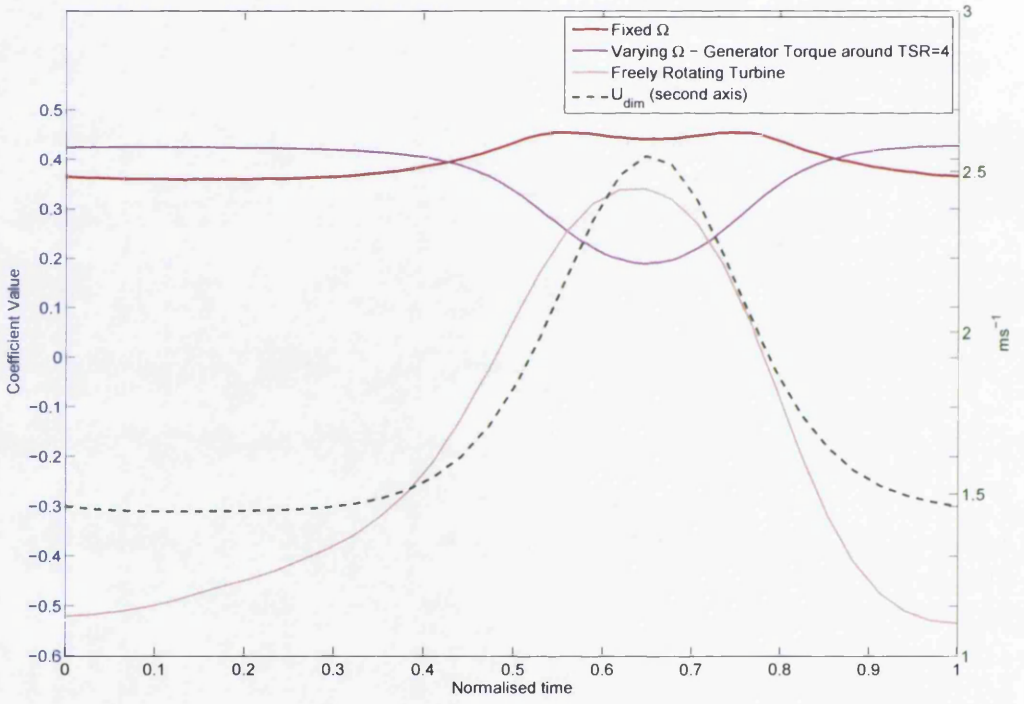

Figure 5.14: Comparison of C_p over one wave period for a fixed Ω, generator torque around $TSR = 4$ and a freely rotating turbine. Incident wave with wave height $=$ 0.5m and wave frequency $= 0.2$Hz.

In Figure 5.14 C_p for the three studies presented in this chapter are compared against U_{ref}. Fixing Ω close to peak C_p forces the power to remain high throughout the wave cycle. By setting the operational TSR to 4 the opposite effect of increasing

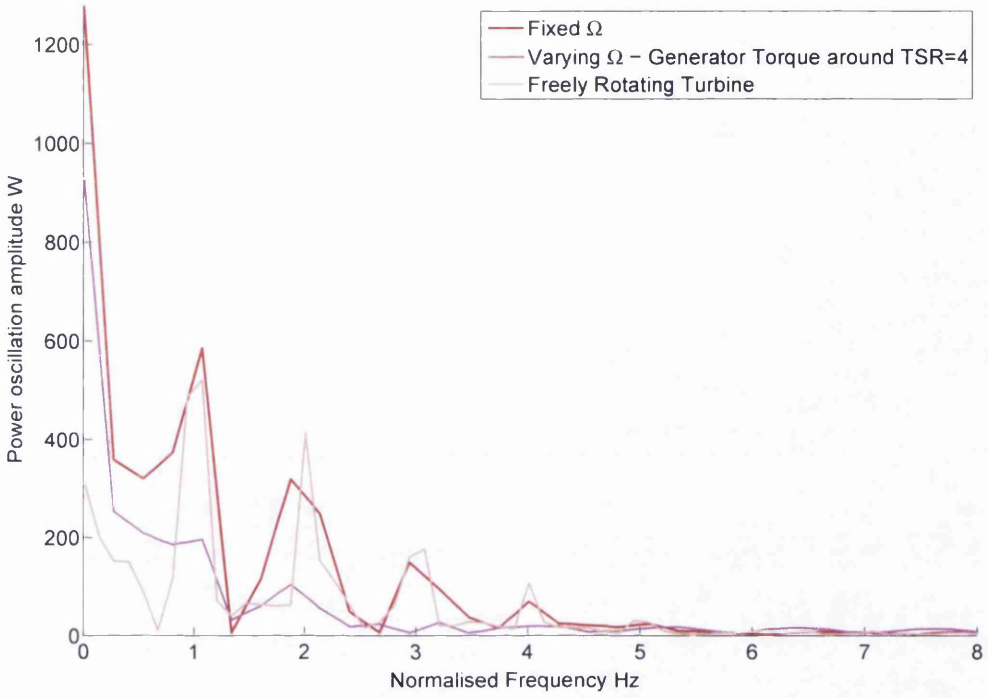

(a)

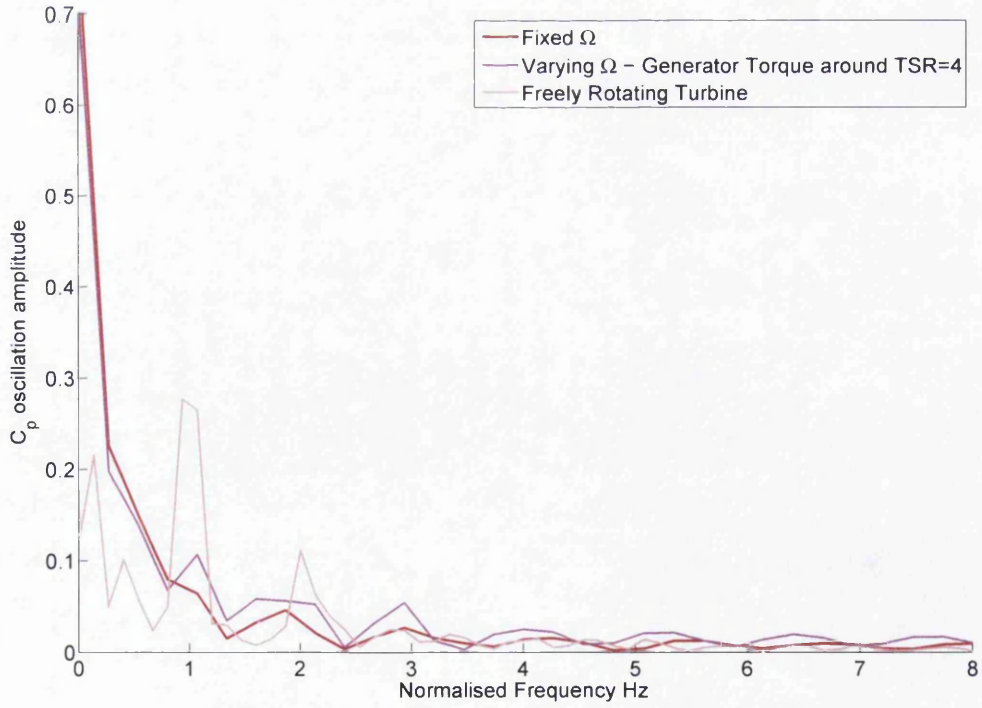

(b)

Figure 5.15: (a) Power and (b) C_p vs. frequency normalised by wave frequency. Incident wave period=5s, waveheight=0.5m.

C_p with decreasing U_{ref} is illustrated and is due to the turbine operating at a TSR value lower than the peak C_p TSR value.

Although target $TSR = 4$ is close to peak C_p TSR the effect of the wave forces the turbine to stall with each crest. The freely rotating turbine is most affected by the wave motion as the result settles in an oscillatory motion around zero torque and therefore zero C_p. This is a significant result. Physically is suggests that if an arbitrary tidal turbine is left to freely rotate zero average torque will be reached.

With wave motion the torque traces the TSR torque curve as it oscillated around 0. Turbine developers must design for and specify the turbine operation during storm conditions.

To reduce the bending moment on the blades it is suggested that a tidal turbine should be left to freely rotate with the waves in this case. Therefore the axial force oscillations around the TSR value at zero torque are the turbine design maximum axial force limit, as Figure 5.11 shows the axial force for a freely rotating turbine is in this region.

Fast Fourier Transformation can be used to evaluate the power and C_p time results in the frequency domain for all cases in this chapter, as presented in Figures 5.15(a) and 5.15(b) respectively. The magnitude of the frequency peaks corresponds to the specific amplitude of the performance value oscillations and the frequency is normalised with wave frequency. Therefore we expect the wave motion to produce frequency peaks at 1. For the fixed Ω result, a large peak at 1 is shown for power but not for C_p.

By comparing Figures 5.5 and 5.6 the wave crest has a significant effect on power but the C_p amplitude response to wave crest is suppressed by the C_p TSR curve shape and due to operating the turbine over peak C_p. For the power frequency result, the harmonic of the wave frequency produces smaller amplitude peaks at integer normalised frequencies.

The generator torque acts against the turbine response to the incident wave to remain at a target TSR. This results in low amplitude power oscillations for the generator torque case. Although the power oscillations are low compared to the fixed Ω case the C_p amplitude is higher. This is a result of the steep stall effect on C_p as TSR decreases below TSR= 4 and with each wave the turbine is stalling.

C_p oscillations have the largest amplitude for a freely rotating turbine as there is no generator torque opposing the wave motion and the C_p/TSR curve around zero torque is steep for all turbines.

Therefore an oscillating U_{ref} and TSR alters C_p over a large range. This section illustrates the capabilities of the BEMT scheme with incident waves as well as tides and considers the BEMT assumptions regarding the incident velocity profile. The relevance of U_{ref} could be further explored by considering the experimental power, torque and axial force against non-dimensionalised results with the various usual definitions of U_{ref} in the presence of waves or a power law inflow velocity profile.

5.4 Representing a Real Site

The JONSWAP spectrum, described in Section 3.3.2, is considered most suited for the site and the tide flows in the wave propagation direction. The significant wave period is taken from the oscillation period of the ADCP data. The significant wave height is difficult to obtain and $H_{1/3}$ is chosen to fit the ADCP result. A relatively low energy wave climate is estimated with $T_{1/3} = 4$ and $H_{1/3} = 0.75$. The discretised waves in this input are looped over the device position with the respective discrete wave frequency and superimposed. Figure 5.16 shows agreement between the sea spectrum and the reconstructed sea state from the simulated input suggesting the simulated flow represents the prescribed sea state as accurately as possible.

ADCP data does not usually record surface elevation which is needed to determine the sea state spectrum. Therefore, the velocity disturbance from the wave climate at 22.5m is alternatively used to compare the simulated and real sea spectra. Figure 5.17 compares the wave disturbance at the turbine location by plotting the parallel stream velocity deviation from the mean tidal velocity. In addition, Figure 5.18 compares the fast Fourier transformation of these time series. The maximum amplitude oscillations are found at similar frequencies, 0.13Hz for the ADCP data and 0.14Hz for the simulated result. However the maximum amplitude for the simulated result is nearly double that of the ADCP data. In addition, the turbulence present in the ADCP data causes low amplitude oscillations at all frequencies that are not simulated by this model.

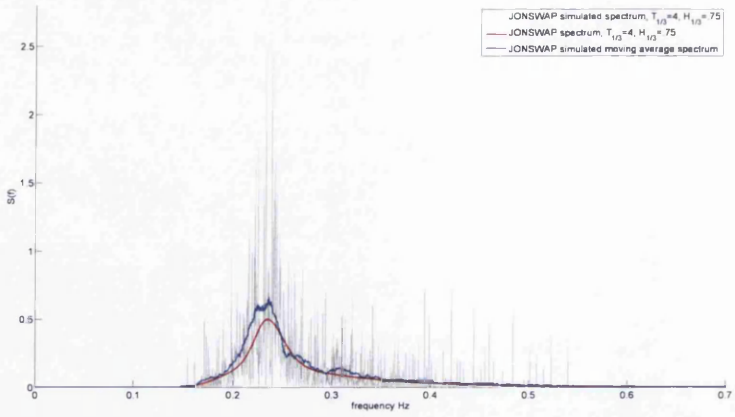

Figure 5.16: The prescribed sea spectrum, $S(f)$, against the wave frequency f and also compared to the power spectral density of the water elevation produced by the simulation.

Figure 5.19 shows the sea state evolution through the water column for the ADCP data, by comparing to arbitrary depths throughout the water column. Further studies should include studies of change in turbulence intensity and wave kinematics over the swept depth of the turbine. The wave climate is shown to become more prominent near the surface with larger velocity oscillation amplitudes over a small frequency range.

Close to the sea bed, the wave climate amplitudes are similar to the turbulence amplitudes that increase with depth. Comparing this with the results in Figure 5.18 the effect of turbulence on the sea state is to increase the amplitudes of oscillations outside the wave frequency range. Figure 5.20 presents the turbine C_p response with TSR to the ADCP and simulated irregular sea states. The turbine rotational velocity is considered fixed at three rpm of 6rpm, 10rpm and 15rpm.

The effect of turbulence in the ADCP data is more prominent when compared to the steady state result for the 10m diameter turbine shape. The simulated irregular sea state result agrees well with the steady state results for all rotational velocity cases as there is no turbulence. The same result is shown in Figure 5.21 with the addition of the C_{fa} and C_t turbine performance results for the simulated case and real ADCP data case. Similarly, the turbulence of the ADCP data also effects C_{fa} and C_t and therefore the simulated irregular sea state shows better agreement with the steady state result.

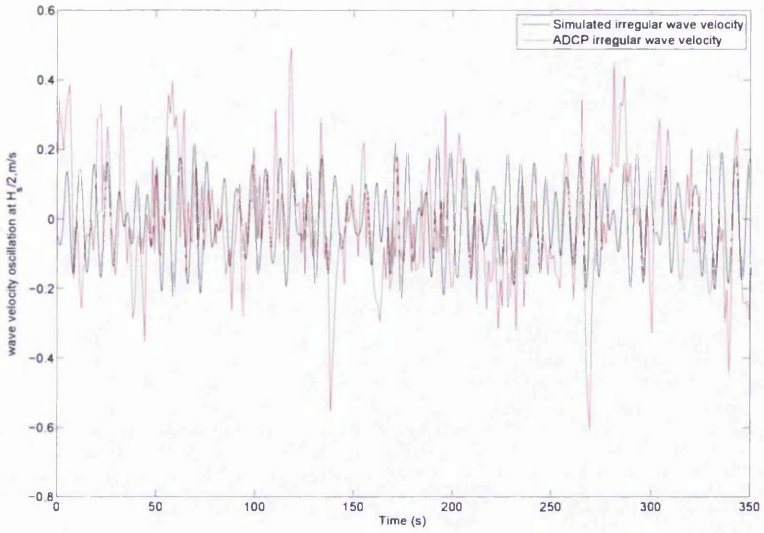

Figure 5.17: Time series for the wave oscillation velocity of the ADCP data input compared to the simulated input at half the water depth, $H_s/2$.

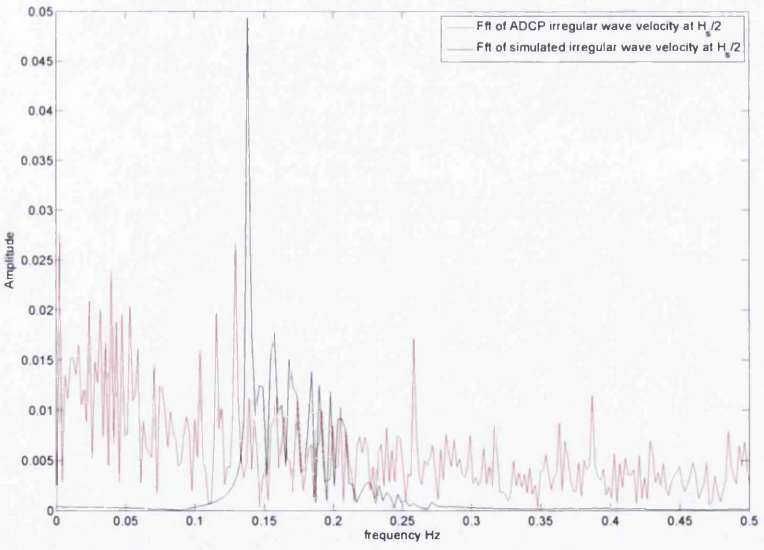

Figure 5.18: The frequency domain result for the wave oscillation velocity of the ADCP data input against simulated input at half the water depth, $H_s/2$.

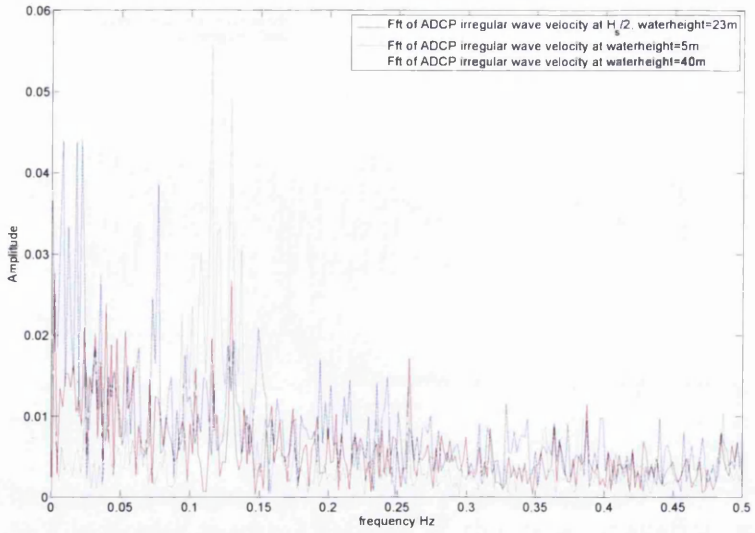

Figure 5.19: The frequency domain result for the wave oscillation velocity of the ADCP data input at half the water depth, $H_s/2$, close to the surface at $H = 40$m and close to the sea bed at $H = 5$m.

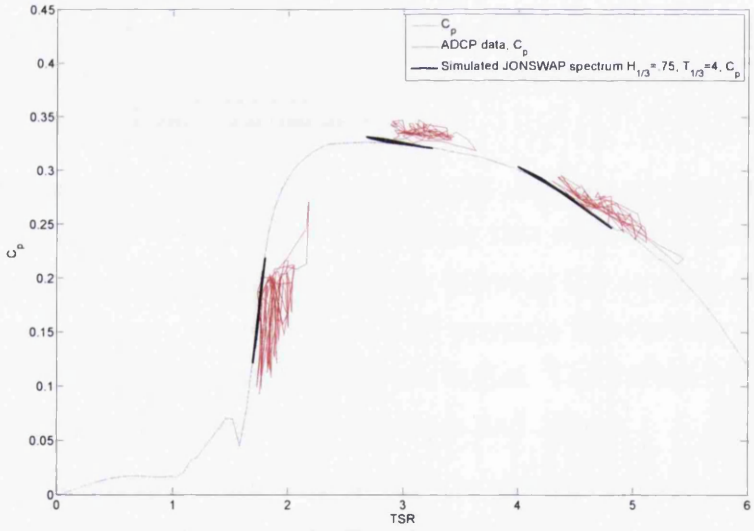

Figure 5.20: Power coefficient, C_p, of the tidal turbine against TSR with real ADCP data inflow. Compared with the simulated TSR result for C_p. $U_{average}$ is used as the non-dimentionalisation constant. Three cases of operating TSR are set by increasing turbine revolutions per minute from 6 to 10 and 15.

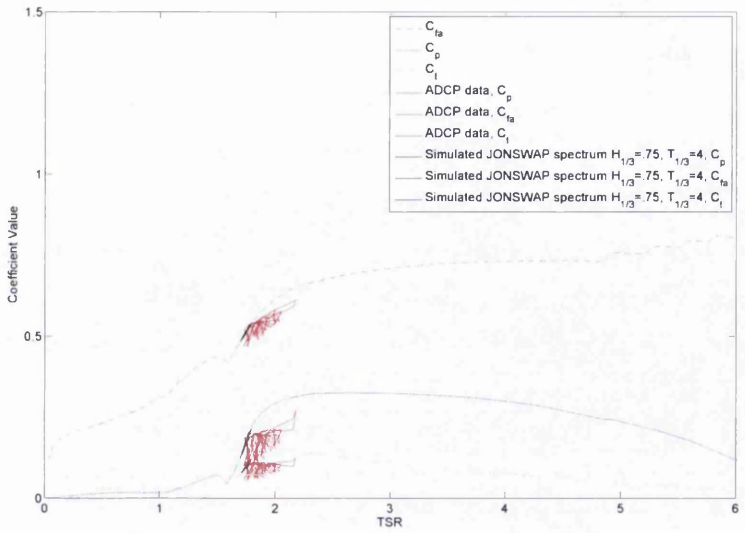

Figure 5.21: Power, axial force and torque coefficient, C_p C_{fa} C_t, of the tidal turbine against TSR with real ADCP data inflow. Compared with the simulated TSR result for all performance coefficients. $U_{average}$ is used as the non-dimentionalisation constant.

5.5 Conclusion and Recommendations

This section utilises the irregular sea state simulation to represent an example site specific irregular sea and the effect on the performance of a 10m turbine is considered. The ADCP velocity data at the turbine depth, 23m, is compared to the simulated result that does not consider turbulence in the flow. The turbulence in the ADCP data causes random large amplitude velocity oscillations during the time series. Considering the same result in the frequency domain really illustrates the effect of turbulence in the velocity data. Oscillation amplitude peaks are found over the whole frequency range and the peak amplitude is reduced. The peak amplitude frequency for the simulated velocity time series can easily be adjusted by changing $T_{1/3}$.

By considering the ADCP data only, the effect of the depth on the wave velocity time series is presented in the frequency domain. Water heights of 5m, 23m and 40m are compared. Turbulence is shown to increase towards the sea bed as the peak amplitudes are spread over a wider frequency range. The wave climate peak reduces with distance from the sea surface until wave and turbulent oscillation amplitudes

become comparable near the sea bed.

The velocity time series for ADCP and the simulation are then used as BEMT input to consider the 10m turbine performance. Good agreement is found between the simulated results and the ADCP data for the tidal turbine performance. As BEMT is an iterative method where the result at time $i+1$ is dependent on the result at time i, the turbulence in the ADCP data causes deviation of C_p from the steady state result. Most noticeably, the operating TSR for the ADCP result is higher than that for the simulated result. This implies that the non-dimensional constant, $U_{average}$, is lower for the ADCP data. This is a result of a more steep tidal velocity shear in the ADCP data compared to the simulated data.

This chapter illustrates how the irregular sea state simulation can be used to predict site specific turbine performance results if the sea state is known. However, if the sea state is not known and ADCP data is available, as is the case in the results presented here, the ADCP data can be analysed to estimate the site specific sea spectrum. This introduces uncertainties in the results and the results are not reliable if the sea state is unknown. This highlights the need for a method to calculate sea spectra from ADCP velocity measurements obtained from a turbulent flow with waves. The same result is also found by comparing the ADCP data irregular sea state and the simulated irregular sea state for the additional turbine performance coefficients C_t and C_{fa}.

Chapter 6

Conclusions and Recommendations for Further Research

This thesis combines research into BEMT as a tidal turbine application and regular linear and non-linear wave simulation as well as irregular sea state representation. In particular, an alternative BEMT tip and hub loss implementation has lead to a significant improvement of the turbine axial force prediction and understanding of the high induction region. An alternative BEMT optimisation method is proposed that improves the compatibility with transient and depth dependent inflow, as well as an improved non-dimensionalisation constant to calculate the performance coefficients. Validation studies are presented for BEMT coupled with regular, non-linear wave theory as good agreement is found with published experimental data. The turbine response to irregular wave theory is considered against the turbine response to real ADCP data and, by regenerating the sea power density spectrum in the frequency domain, the effect of tidal flow and water depth on sea spectrum is explored.

Combined wave and current flows co-exist in the tidal turbine operating environment. This document analyses power-law tidal velocity profiles, regular wave and irregular wave velocity and acceleration profiles and develops simple wave and tide relationships as well as introducing a complex and reactive coupling scheme. The analysis of the flow environment is presented in the specific context of tidal stream turbine (TST) simulations. Coupling transient and spatially variant inflow with a steady state blade element momentum theory (BEMT) based TST simulation model is discussed. The combined model is validated at stages throughout the study by

comparison between published experimental data and simulated turbine performance results with transient inflow.

Chapter 1 outlines the state of academic and industrial progress of marine renewables in both a national and global context. Successful tidal turbine developers and devices are identified as well as relevant published works. BEMT is introduced and compared with alternative tidal turbine computer simulation approaches. BEMT is useful for tidal turbine performance predictions and design of rotor geomentry as well as determining some extreme loads. Chapter 2 continues, by presenting the theoretical basis of BEMT as a robust and computationally inexpensive tidal turbine simulation tool suitable for the nascent state of the industry. To utilise BEMT to simulate TST's it is important to assess the theoretical validity of any standard corrections for this specific application, as presented in Chapter 2. In particular, tip and hub losses and high induction corrections are considered.

The application of hub loss to tidal stream turbine blades in the exact manner as wind turbine blades is questioned. As opposed to the blades of wind turbines, tidal turbine blades usually connect directly to the hub nacelle. A denser fluid increases the blade loads which dictates an increase in blade root strength. It is concluded that this renders the theoretical basis of hub loss invalid, in this case. By considering the established tower shadow model with alternative geometry, a hub shadow model is proposed to simulate the effect of the hub nacelle on the inflow velocity. This results in performance reduction for the blade elements near the hub in a similar manner to the Prandtl's hub loss formulation results and therefore is shown to also agree well with experimental scale turbine data. This considers hub shadow as a loss correction to BEMT in the case of tidal turbines, with the improvement of sound theoretical basis. However, the result of this method is dependent on four unknown input variables and further work is needed to determine these values and further validate the result. Comparison with accurate CFD results of nacelle wake would be needed to determine the reference factors of b_{ref} and x_{ref} and the variable values predicted are dependent on Reynolds number.

In the high induction region BEMT is invalid. This effect is introduced in Chapter 1 and discussed in the context of time-varying and spatially varying inflow in Chapter 2. Several published corrections are identified and shown to consistently over-predict turbine power and axial force when compared to experimental data. The development

of the most established quadratic correction is analysed and an alternative is proposed that assumes the relationship between axial induction factor and axial force coefficient to be cubic in the high induction region. The high induction correction tht has been developed is shown to significantly improve the agreement with the experimental data for the case presented in this thesis. Further comparison with other experimental data sets is needed to confirm this conclusion. These experimental data sets will be of a tidal turbine in high induction operating region, high TSR.

By analysis of the literature on the combined tip and hub loss factor, an accepted simplification is found in the implementation of the factor on BEMT. This simplification is shown to significantly alter the BEMT result. The simplification was necessary for the primitive calculation techniques available at the time of conception and in Chapter 2 the alternative method, without the simplification, is considered and easily computed.

Eliminating the simplification introduces dependency of the high induction region on the tip and hub loss factor. In this case, considering the relationship between C_{fa} and a, a spread of data is found in the high induction region. This agrees with previously published work, which also indicates a large spread of data in this region. However, a similar modern experiment is suggested as important further research to determine the high induction region.

The alternative loss implementation method proposed here is shown to consistently increase in axial force coefficient compared to the loss factor with the simplified implementation whist minimally effecting power coefficient. This is significant as, by considering the literature, BEMT commonly shows agreement with power coefficient experimental data whilst under-predicting axial force coefficient. The alternative method presented in this work aligns the turbine axial force result with the power result and give a more accurate agreement with experimental data.

The simulation outlined in this thesis has been extensively used as a design tool to maximise performance of tidal stream turbines and determine loads for survivability. It is desirable to design turbine blades that will operate without the detrimental effect of cavitation on the blade aerofoil shape. A minor change in the aerofoil shape will have a large effect on the lift and drag coefficients of the blade element and therefore greatly effect whole turbine performance. A novel BEMT turbine simulation coupled with a model to detect blade element cavitation inception is also presented in Chapter

2 and validated against published experiment data. The results are presented in terms of % of blade length and swept area cavitating and are considered conservative. Discrepancy between simulation and experiment may be due to the limitations with using the pressure coefficient to predict blade surface cavitation, which is a Reynolds number dependent value. However, good agreement is found between the simulated results and the experiment observations for the published experiment, suggesting the model can be used to design TSTs in the operating environment without cavitation.

BEMT is a steady state theory. Chapter 3 outlines and evaluates the incompatibilities between BEMT and transient or depth dependent inflow. Considering a depth dependent inflow, the steady state result is found dependent on the set azimuthal angle blade positioning. This violates the generality of the result. The factor R_T is proposed as a indicator of the depth gradient velocity change and, with a value of $R_T > 10\%$, as shown in 3, the loss of generality of the depth dependent velcoty inflow on BEMT is significant. In this case, the value of the non-dimensionalisation constant U_{ref} can produce a non physical effect on the turbine performance results when $U_{ref} = U_{hub}$, as defined in the literature. An alternative $U_{ref} = U_{average}$ where $U_{average}$ is defined in Chapter 3 is proposed. This definition creates physical steady state BEMT results in depth dependent inflow, such as the common tidal boundary layer velocity model.

Chapter 3 also proposes a novel BEMT implementation method to account for instantaneous blade position and hence enabling simulation of response due to a steady depth profile and due to a time varying depth profile such as wave induced kinematics. This has been developed and validation is presented. Rather than solving each blade element independently, the three blade elements on the same annulus of the turbine disc are solved simultaneously. The annuli are combined to solve the whole BEMT equations by comparing with the whole turbine momentum theory. This alteration is necessary and an important change as the flow over an annulus is considered homogeneous in steady state BEMT. Therefore the simultaneous axial force and torque BEMT calculations were previously deduced based on homogeneous inflow over an annulus. The method proposed here deduces different BEMT simultaneous equations that do not assume homogeneous inflow over an annulus whilst limiting the effect on CPU time. This increases the validity of BEMT for various inflow models. This implementation of BEMT gives a different turbine performance result with time-

varying inflow and the effect is more significant with turbulent inflow, as presented in Chapman *et al.* [2012].

The Regular, non-linear wave theory is discussed in Section 4.10 and Chaplin's stream function is introduced. Chapter 4 compares the model results against two experimental data sets of a tidal turbine in a test tank with regular waves.

For the first study, the axial force and torque against time are compared to the data sets. The agreement between the model and the published data in these studies validate the method. The conclusion of the validation studies show how the power curve with TSR of the turbine near operating TSR dictates the effect of the wave profile on the turbine performance. Therefore to design a powerful turbine, as well maximising operating TSR power coefficient, the curve must plateau around operating TSR. If there is a steep drop in power near operating TSR, turbulent flow can cause turbine stall and waves can cause periodic stall. In this case, the wave climate disturbance will significantly reduce mean power output.

The second validation study presents the root bending moment on a single turbine blade and the self weight and buoyancy term is introduced. Although this term cancels in whole turbine torque, the force continuously effects the individual blade bending moment and must be considered to determine root strength. Good agreement is shown between the experimental bending moment with time and the simulated bending moment, as well as the self weight and buoyancy term, is validated. The turbine is towed to simulate tidal flow. Therefore unfortunately no wave and current coupling will be present and the velocity of the tide is simply added to the wave propagation velocity to accurately effect the apparent frequency of the wave. This is not representative of the reality of wave and current coupling, as the tide will effect the non-linearity of the wave and the wave, to a lesser extent, effects the tide near the free surface. However, using the most recent published data available, this study validates transient inflow coupled with a BEMT model with accurate simulated results. In further chapters, a novel reactive wave and tide coupling is introduced. The theoretical justification of the coupling is discussed, however validation of the method can only take place after suitable experimental results are available. The extension of BEMT to simulate turbine wave loadings is presented here with limited validation against published experimental results. This validation is limited due to the limited range of wave conditions considered. Future experimental results with a

turbine in irregular sea states and multiple wave fronts will be published and will be useful in extending the validation of this simulation approach.

The tidal stream turbine simulation scheme with waves is used to consider various operating conditions and turbine settings. The significant impact of the turbine TSR performance coefficient curves on the wave effect is illustrated by comparing alternative turbine operating conditions. The oscillating result of a freely rotating turbine is also considered. In this case, it is shown how zero average torque is always eventually reached, however this is observed here for one rotor design only and does not consider the effect of turbulence. During storm conditions, the forces on the turbine can be deduced assuming the turbine is allowed to freely rotate as a conservative measure. The turbine can then be designed to survive the axial force value around zero torque as this is the maximum storm force.

This thesis extends the scheme further by proposing a novel irregular wave implementation method. The method is successfully used to simulate non-linear irregular waves and a reactive wave and tide coupling is also proposed. It is shown that the sea state can be recovered from the surface elevation of the superimposed discrete waves. The model is further developed by including a breaking limit model. This model extends the regular wave breaking limit formula to consider an irregular sea state. The breaker model is found to reduce the unphysically large wave heights. For application to BEMT, this model is preferred to other irregular sea state representations as it produces an irregular sea state grid of velocities and accelerations through the whole water column depth.

The result of this sampling scheme is a set of N wave values of wave height H and wave angular frequency ω. The wave heights satisfy the Rayleigh probability distribution and the significant wave height of the sea spectrum, $H_{1/3}$ and a breaking limit is considered. The energy contribution of each single regular wave to the irregular sea state wave front is calculated from the height and affects the angular frequency ω of the single, component wave.

In Chapter 5 the method is utilised to simulate a real ADCP data inflow velocity in water depth 45m with a 10m turbine at hub height 23m. Turbulence in the ADCP data causes random large amplitude velocity oscillations in the inflow velocity time series when compared to the simulated inflow velocity. In the frequency domain, oscillation amplitude peaks are found over the whole frequency range and the peak

amplitude is reduced for the ADCP data. This study ensures the peak amplitude frequency for the simulated velocity time series is similar to the peak frequency of the ADCP data, and this provides a basis for comparison of the turbine loadings with simulated and measured inflow.

The effect of the depth on the wave velocity time series is investigated by considering the ADCP data in the frequency domain. Water heights of 5m, 23m and 40m are compared. For this preliminary study, turbulence is shown to increase towards the sea bed as the peak amplitudes are spread over a wider frequency range. The wave climate peak reduces with distance from the sea surface until wave and turbulent oscillation amplitudes become comparable near the sea bed. Further investigations into the turbulence dependency on depth is suggested as future work.

Chapter 5 uses these velocity time series, both for ADCP and the simulation, to input into the BEMT model. The 10m turbine performance is compared for the simulated results and the ADCP data. As BEMT is an iterative method where the result at time $i+1$ is dependent on the result at time i, the turbulence in the ADCP data causes deviation of C_p from the steady state result. Most noticeably, the operating TSR for the ADCP result is higher than that for the simulated result. This implies that the non-dimensional constant, $U_{average}$, is lower for the ADCP data. This is a result of a more steep tidal velocity shear in the ADCP data compared to the simulated data.

This study illustrates how the irregular sea state simulation can be used to predict site specific turbine performance results if the sea state is known. However, if the sea state is not known and ADCP data is available, the ADCP data can be analysed to estimate the site specific sea spectrum. The estimate introduces uncertainties in the results, highlighting the need for a method to calculate sea spectra from ADCP velocity data.

The reactive coupling method is proposed as an alternative to the simple wave and tide coupling described in Section 4.11. A combined inflow is created including tidal flow effects on the the wave apparent frequency over the turbine and also the wave velocity and acceleration profile shape by changing the wave non-linearity. This extends the BEMT inflow model to simulate the physical phenomena of increased wave peakedness in opposed tidal flow and a relax of the wave peakedness with tidal flow in the wave propagation direction. In addition, the less significant effect of

the waves on the current flow is considered. Using the Stokes drift velocity, for a non-linear wave representation the tidal flow velocity on the free surface is effected by the mass transport velocity of the wave field. Chapter 5 considers the scheme by simulating real ADCP data of irregular wave and tide and comparing the tidal turbine performance coefficient results compared to those results when using the real ADCP site data. However, validation of this scheme is limited by the availability of published experiments on wave and current interactions.

This method creates realistic inflow for BEMT with a novel, coupled wave and tidal flow scheme where waves effect tides and tides effect waves until a steady coupling solution is reached. The model has been integrated into the BEMT code and used to model a full scale tidal stream turbine successfully. The result remains to be validated against experimental wave and current interactions findings as they become available.

The conclusions of this work significantly improve the BEMT model to include transient inflow, in particular a combined reactive coupling of waves and current. The compatibility of BEMT with transient inflow is also applicable for turbulent inflow implementation and analysis.

Other outcomes of this work include investigation of numerous areas of research to aid the development of tidal turbine technology, including blade design, maximum load simulations and the effect on the flow regime. Volume 2 of this thesis comprises of a collection of reports documenting my research and therefore is restricted under a confidentiality agreement. This includes a commercial report to develop a tidal basin modelling tool to be utilised as part of an Environmental Impact Assessment. Also the publication, Buckland *et al.* [2013], details the cavitation inception study.

Further research outlined in this thesis includes creating a CFD model to determine the dependence of the reference wake width and length for different turbine hub dimensions and Reynolds number of flow. Further analysis of the turbine operformance in the high-induction region is needed, particularly experimental investigations of a turbine perating in high induction, which may be used to validate the high induction correction theory presented in this work. Finally, other highlighted investigations for future work would include simulation of a turbine in truly coupled tidal and wave flows to evaluate the coupling method and experimental analysis of turbine reaction to irregular sea states.

Appdx A: Regular, Non-Linear Wave Theory

1. The Laplace equation is applicable to incompressible flow,

$$\nabla^2 \Psi = 0 \tag{1}$$

2. On the bed boundary, where there is no fluid transport, the kinematic boundary condition is applicable,

$$\frac{\partial \Psi}{\partial y} = 0 \qquad \text{on} \quad y = -d \tag{2}$$

3. Considering the uniform free surface and writing, $F(\overline{x},t) = y - \eta(x,y,t)$, this surface can be alternatively defined as when $F(\overline{x},t) = 0$ and is where the kinematic free surface condition holds,

$$\frac{DF}{Dt} = \frac{\partial F}{\partial t} + (\overline{u}.\nabla)\, F = 0 \qquad \forall \ \overline{x},t \tag{3}$$

Since the frame of reference moves with the fluid $\frac{\partial \eta}{\partial t} = 0, \ \forall t$ and as the model is 2D, $\frac{\partial \Psi}{\partial z} = 0$. Therefore, after some substitution, Equation 3 reduces to:

$$\frac{\partial \eta}{\partial x} = v/(u - C) \qquad \text{on} \quad y = \eta(x) \tag{4}$$

4. The dynamic free surface boundary condition satisfies the Bernoulli equation where the free surface pressure is assumed constant and set to 0,

$$Q = \eta(x) + \frac{v^2 + (u - C)^2}{2g} \qquad \text{on } y = \eta(x) \tag{5}$$

All conditions, apart from condition 5, can be satisfied by choosing a stream function of order N with the form:

$$\Psi(x, y) = -\frac{L}{T_w}x + \sum_{n=1}^{N} a_n \sinh \frac{2\pi n y}{L} \cos \frac{2\pi n x}{L} \tag{6}$$

The first term is the wavelength multiplied by frequency and the x position in the frame of reference. It represents the mean resultant flow and is the direct consequence of the moving frame of reference whereas the summation term represents the wave disturbance.

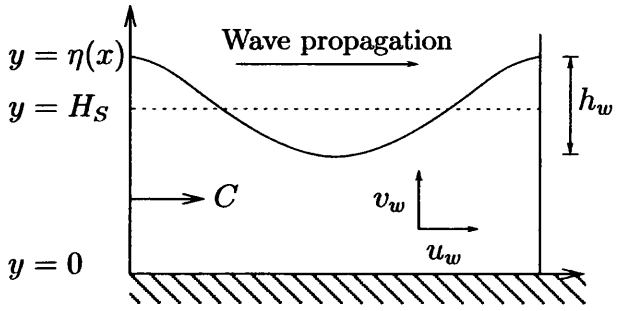

The numerical problem defined by this formulation of wave theory, is to determine the unknown values of $a_1, a_2, \ldots, a_N$ and L and $\Psi(x, \eta)$ such that Equation 5 is satisfied as closely as possible. In the formulation of stream function theory by Dean [1965], by specifying the mean water depth, total head and wave period, the parameters $a_1, a_2, \ldots, a_N$ and L are found using least squares method to minimise the errors on condition 5. The unknown parameter values are initially estimated and, from there, the solution progresses iteratively, using the modified form of the Gauss Method. The sum of squares of the boundary condition errors are minimised for a solution as in Chaplin [1979]. Total head, Q, is unknown and so is interpolated by Dean using the input parameter of wave height.

However, Chaplin [1979] shows how most integral wave properties, such as total head, peak before the maximum wave height. This fact increases with wave steepness and creates 2:1 mapping therefore Dean's solution of interpolation is increasingly inaccurate with wave steepness whereas Chaplin [1979] suggests total head should be abandoned as an input parameter and proceeds by creating a non-dimensionalised

problem, which is suitable for steeper waves.

$$\Psi = \frac{\Psi(x,y)}{\Psi(x,\eta)}, \quad X = \frac{x}{L}, \quad S = \frac{y}{L}, \quad A = \frac{a}{\Psi(x,\eta)} \tag{7}$$

The new input parameters for the numerical problem are average water height, H_S, wave period, T_w, and wave height, h_w. The independent unknowns to be found are now the surface height above the sea bed, $S_1, S_2, \ldots, S_{J-2}$ at positions along the x axis , $x, x_2, \ldots, x_{J-2}$, in the moving frame of reference, between a crest and a trough. The non-dimensionalised stream function reads,

$$\Psi = A_{N+1}X + \sum_{n=1}^{N} A_n \sinh 2\pi n S \cos 2\pi n X \tag{8}$$

The coefficients A_n cannot be derived directly by the method of Fourier analysis since the functions $A_n \sinh 2\pi n S_j \cos 2\pi n X_j$ and X_j are not orthonormal, Chaplin [1979]. They are, however, linearly independent and so, using the Schmidt process, a set of orthonormal functions can be generated.

A series of orthonormal functions $\phi_1(X_j)$, $\phi_2(X_j)$, ... , $\phi_{N+1}(X_j)$ can be defined by the matrix equation, with the dummy variable k where:

$$\zeta_{n,j} = C_{n,k}\phi_{k,j} \quad \text{where} \qquad \phi_{k,j} = \phi_k(X_j), n = 1, 2, \ldots, N+1 = 1, 2, \ldots, J \tag{9}$$

where C is a lower triangular matrix. The elements of the nth row of ϕ are then found from:

$$\phi_{n,j} = \frac{-\sum_{k=1}^{n-1} C_{n,k}\phi_{k,j} + \zeta_{n,j}}{C_{n,n}} \qquad j = 1, 2, \ldots, J \tag{10}$$

This method is repeated until all the elements of the matrices ϕ and C are known. Unfortunately, the round up error of this means that the component vectors of ϕ become progressively less orthogonal. Therefore a correction by Davies is applied in Chaplin [1979]. The problem is now a system of J non-linear equations and $J-1$ unknowns and can now be directly solved using the Gauss non-linear least squares

method. Although this method is more complex than Dean's formulation, there is no interpolation error as the total head of the wave is calculated directly from the input wave height.

The number of functions is chosen to equal J, the number of positions evaluate from crest to following trough. Therefore $N+1=J$.

Setting,

$$\zeta_{n,j} = \sinh 2\pi n S(X_j) \cos 2\pi n X_j \qquad n = 1, 2, \ldots, N \tag{11}$$

$$\zeta_{N+1,j} = X_j \tag{12}$$

Now a series of orthonormal functions $\phi_1(X_j), \phi_2(X_j), \ldots, \phi_{N+1}(X_j)$ can be defined by the matrix equation, with the dummy variable k where:

$$\zeta_{n,j} = C_{n,k}\phi_{k,j} \qquad \text{where } \phi_{k,j} = \phi_k(X_j) \qquad n = 1, 2, \ldots, N+1 = 1, 2, \ldots, J \tag{13}$$

where C is a lower triangular matrix. To define C it is necessary to define a series of weights W_j over which the numerical integration of the function can be performed, within the interval $0 \leq X \leq 1/2$. Although the solution can be obtained from a number of methods, Simpson's rule was used. The matrix C is evaluated recursively by rows and after each cycle one row of the matrix will be evaluated. For example, the first values of matrix C to be found is $C_{1,k}$ which comprises of $C_{1,1}$ only as the matrix is triangular. It is given that,

$$C_{1,1} = \sqrt{\sum_{j=1}^{J} {\zeta_{1,j}}^2 W_j} \tag{14}$$

Now by rearranging the matrix equation, the first row of ϕ follows:

$$\phi_{1,j} = \frac{\zeta_{1,j}}{C_{1,1}} \qquad j = 1, 2, \ldots, J \tag{15}$$

Thereafter the non-zero elements of the nth row of C are given by,

$$C_{n,k} = \sum_{j=1}^{J} \zeta_{n,j}\phi_{k,j}W_j \qquad k = 1, 2, \ldots, n-1 \tag{16}$$

and for the diagonal components,

$$C_{n,n} = \sqrt{\sum_{j=1}^{J} \left(-\sum_{k=1}^{n-1} C_{n,k}\phi_{k,j} + \zeta_{n,j} \right)^2 W_j} \tag{17}$$

and so the triangular matrix of C expands as,

$$nth\ row \left\{ \begin{array}{ccccccccc} C_{1,1} & 0 & & \cdots & & & & 0 \\ C_{2,1} & C_{2,2} & 0 & & & \cdots & & 0 \\ & & & & \cdot & & & \\ & & & & \cdot & & & \\ & & & & \cdot & & & \\ C_{n,1} & C_{n,2} & & \cdots & C_{n,n} & 0 & \cdots & 0 \\ & & & & \cdot & & & \\ & & & & \cdot & & & \\ & & & & \cdot & & & \\ C_{N,1} & C_{N,2} & & & \cdots & & C_{N,N} & \end{array} \right\} \tag{18}$$

$$= \left\{ \begin{array}{ccccccc} \sqrt{\sum_{j=1}^{J} {\zeta_{1,j}}^2 W_j} & , & 0 & \cdots & & & 0 \\ & & & & \cdot & & \\ & & & & \cdot & & \\ & & & & \cdot & & \\ \sum_{j=1}^{J} \zeta_{n,j}\phi_{1,j}W_j & , & \sum_{j=1}^{J} \zeta_{n,j}\phi_{2,j}W_j & , & \cdots & \sqrt{\sum_{j=1}^{J} \left(-\sum_{k=1}^{n-1} C_{n,k}\phi_{k,j} + \zeta_{n,j} \right)^2 W_j} & , \quad 0 \quad \cdots \quad 0 \\ & & & & \cdot & & \\ & & & & \cdot & & \\ & & & & \cdot & & \\ \sum_{j=1}^{J} \zeta_{N,j}\phi_{1,j}W_j & , & \sum_{j=1}^{J} \zeta_{N,j}\phi_{2,j}W_j & , & \cdots & \sqrt{\sum_{j=1}^{J} \left(-\sum_{k=1}^{N-1} C_{N,k}\phi_{k,j} + \zeta_{N,j} \right)^2 W_j} & \end{array} \right\} \tag{19}$$

. APPDX A: REGULAR, NON-LINEAR WAVE THEORY

The elements of the nth row of ϕ are then found from:

$$\phi_{n,j} = \frac{-\sum_{k=1}^{n-1} C_{n,k}\phi_{k,j} + \zeta_{n,j}}{C_{n,n}} \qquad j = 1, 2, \ldots, J \tag{20}$$

The matrix ϕ expands as,

$$\left\{ \begin{array}{cccc} \frac{\zeta_{1,1}}{C_{1,1}} & , \quad \frac{\zeta_{1,2}}{C_{1,1}} & , \quad \cdots & \frac{\zeta_{1,J}}{C_{1,1}} \\ & \vdots & & \\ \frac{-\sum_{k=1}^{n-1} C_{n,k}\phi_{k,1}+\zeta_{n,1}}{C_{n,n}}, & \frac{-\sum_{k=1}^{n-1} C_{n,k}\phi_{k,2}+\zeta_{n,2}}{C_{n,n}} & , \quad \cdots & \frac{-\sum_{k=1}^{n-1} C_{n,k}\phi_{k,J}+\zeta_{n,J}}{C_{n,n}} \\ & \vdots & & \\ \frac{-\sum_{k=1}^{N-1} C_{N,k}\phi_{k,1}+\zeta_{N,1}}{C_{N,N}}, & \frac{-\sum_{k=1}^{N-1} C_{N,k}\phi_{k,2}+\zeta_{N,2}}{C_{N,N}}, & \cdots & \frac{-\sum_{k=1}^{N-1} C_{N,k}\phi_{k,J}+\zeta_{N,J}}{C_{N,N}} \end{array} \right\} \tag{21}$$

This method is repeated until all the elements of the matrices ϕ and C are known. Unfortunately, the round up error of this means that the component vectors of ϕ become progressively less orthogonal. Therefore a correction by Davies (1962) is applied to each individual row of ϕ Chaplin [1979]. Now set $\overline{\phi}_{n,j}$ as the uncorrected solution for the nth row of matrix ϕ, the corrected solution is now:

$$\phi_{n,j} = \overline{\phi}_{n,j} - \sum_{l=1}^{n-1} \left(\sum_{m=1}^{k} W_m \phi_{l,m} \overline{\phi}_{n,m} \right) \phi_{l,j} \qquad j = 1, 2, \ldots, J \tag{22}$$

Now equation (11) may be written as,

$$1 = \sum_{n=1}^{N} B_n \phi_{n,j} \qquad j = 1, 2, \ldots, J \tag{23}$$

Where B_n are unknown coefficients.

Since ϕ are orthonormal over the interval $0 \leq X \leq 1/2$ the approximate orthonor-

mality condition holds in this region,

$$\sum_{j=1}^{J} \phi_{k,j}\phi_{i,j}W_j = \begin{cases} 0, & i \neq k \\ 1, & i = k \end{cases} \tag{24}$$

Therefore the coefficient B_n can be evaluated using the generalised Fourier procedure in order to satisfy the orthonormality condition and Equation 23,

$$B_n = \sum_{j=1}^{J} \phi_{n,j}W_j \qquad n = 1, 2, \ldots, N \tag{25}$$

And finally, the coefficients A_n can be evaluated for a particular wave profile as,

$$A = (C^{-1})^T B \tag{26}$$

Now we have found the coefficients A_n we can refer back to the original problem of the stream function

$$\Psi = A_{N+1}X + \sum_{n=1}^{N} A_n \sinh 2\pi n S \cos 2\pi n X \tag{27}$$

The contribution of the term $A_{N+1}X$ represents the dimensionless stream flow due to the choice of a moving frame of reference. Considering the non-dimensionalised stream function at the sea bed:

$$\Psi = A_{N+1}X \tag{28}$$

$$\frac{\Psi(x,y)}{\psi(x,\eta)} = A_{N+1}\frac{x}{L} \tag{29}$$

It is previously shown that on the sea bed,

$$\Psi(x,y) = -\frac{L}{T}x \tag{30}$$

Therefore by substitution,

$$\Psi(x,\eta) = -\frac{L^2}{A_{N+1}T}\frac{D^2}{D^2} \tag{31}$$

. APPDX A: REGULAR, NON-LINEAR WAVE THEORY

$$\Psi(x,\eta) = -\frac{d^2}{TD^2A_{N+1}} \tag{32}$$

The total head components, Q_j, from the dynamic free surface boundary condition that needs to be satisfied can now be expressed in non-dimensional form by normalising with respect to the mean water depth d,

$$Q_j = \frac{S_j}{D} - 1 + \frac{d/2gT^2}{D^2{A_{N+1}}^2}\left(\left(\frac{\partial\Psi}{\partial X_j}\right)^2 + \left(\frac{\partial\Psi}{\partial S_j}\right)^2\right) \qquad on \;\; y = \eta(x) \tag{33}$$

The problem is now a system of J non-linear equations and $J-1$ unknowns and a solution can now be obtained using the Gauss method.

$$F_j(S_1, S_2, \ldots, S_{J-2}, D) = Q_j - \frac{1}{J}\sum_{k=1}^{J} Q_k = 0 \qquad j = 1, 2, \ldots, J \tag{34}$$

In order to do this however, the derivatives, $\frac{\partial F_j}{\partial S_i}$ and $\frac{\partial F_j}{\partial D}$ must be derived for all $j = 1, 2, \ldots, J$ and $i = 1, 2, \ldots, J-2$. By using the chain rule this is normally straightforward but, $\frac{\partial A_j}{\partial S_i}$ must be found and the Schmidt process complicates the calculations. Setting,

$$A^{(i)} = \left\{ \begin{array}{c} \frac{\partial A_1}{\partial S_i} \\ \frac{\partial A_2}{\partial S_i} \\ \cdot \\ \cdot \\ \cdot \\ \frac{\partial A_J}{\partial S_i} \end{array} \right\} \quad \text{...etc.} \tag{35}$$

It can be found that,

$$A^{(i)} = \left(C^{-1}\right)^T \left(C^{-1}\right)\left[\zeta^{(i)}W - \left(CC^T\right)^{(i)}A\right] \tag{36}$$

Where C^{-1} is already computed by the Schmidt process and the only non-zero column of $\zeta^{(i)}$ is the i^{th}. The elements of $\left(CC^T\right)^{(i)}$ are found by noting that $C$and $C^{(i)}$ are

triangular matrices and using the relation,

$$W_i(\zeta_{k,i}\zeta_{j,i})^{(i)} = \left(\sum_{m=1}^{j} C_{k,m}C_{j,m}\right)^{(i)} \qquad j = 1, 2, \ldots, k \qquad (37)$$

As with the matrix C the elements of $C^{(i)}$ are evaluated row by row, and therefore in the order ${C^{(i)}}_{1,1}$, ${C^{(i)}}_{2,1}$, ${C^{(i)}}_{2,2}$, ${C^{(i)}}_{3,1}, \ldots$ etc.

Using the relation shown above, an explicit formula for each elements in terms of those already calculated can be written. For example;

$${C^{(i)}}_{4,2} = \frac{1}{C_{2,2}}\left[W_i\left(\zeta_{4,i}\zeta_{2,i}{}^{(i)}\zeta_{4,i}{}^{(i)}\zeta_{2,i}\right) - C_{2,1}{C^{(i)}}_{4,1} - {C^{(i)}}_{2,1}C_{4,1} - C_{4,2}{C^{(i)}}_{2,2}\right] \qquad (38)$$

Continuing in this manner will evaluate all $A^{(i)}$ and so $\frac{\partial F_j}{\partial S_i}$ can be found which are required for the Gauss non-linear least-squares method that is subsequently used.

Although this method is obviously more complex than Dean's formulation, there is no interpolation error in finding the total head of the wave as it is calculated directly from the input wave height. There is also the advantage that, as the solution is found directly, good starting values for the iterative process can be obtained from linear theory, Chaplin [1979].

. APPDX A: REGULAR, NON-LINEAR WAVE THEORY

Appdx B: Proof: The summation of the self-weight effect to give total turbine torque equal to zero.

For any given horizontal axis turbine with number of blades greater than 1, N_B, self weight torque will contribute to the in-plane bending moment of each blade.

However, when these in-plane bending moments are summed to give the total torque for the whole turbine the self weight contribution cancels with itself as long as the blades are evenly spaced. This is true for any horizontal axis turbine.

For each blade element, the elemental torque is given as,

$$dT_{tot} = dT + V_\alpha g \left(\rho_T - \rho\right) \sin\theta \tag{39}$$

Where V_α is the volume of the blade element, ρ is the density of the fluid, ρ_T the average density of the turbine blade element and θ is the azimuthal position of the turbine blade for the blade element.

Total torque is the summation over blade length and blade number,

$$T_{tot} = T + T_{SW} = \sum_{k=1}^{R}\sum_{p=1}^{N_B} dT + \sum_{k=1}^{R}\sum_{p=1}^{N_B} V_\alpha g \left(\rho_T - \rho\right) \sin\theta \tag{40}$$

When summing the self-weight torque over the blade length the blade element volume V_α and the density ρ_T will change but are constant when summing over blade number assuming all blades are identical. The variable when summing over blade number is azimuth angle θ. Therefore the summed self-weight torque can be

. APPDX B: PROOF: THE SUMMATION OF THE SELF-WEIGHT EFFECT TO GIVE TOTAL TURBINE TORQUE EQUAL TO ZERO.

rewritten as,

$$T_{SW} = \sum_{k=1}^{R} V_\alpha g \left(\rho_T - \rho\right) \sum_{p=1}^{N_B} \sin\theta = A \sum_{p=1}^{N_B} \sin\theta \tag{41}$$

As the blades are equally spaced,

$$T_{SW} = A \sum_{p=1}^{N_B} \sin\left(\theta_1 + \frac{(p-1)2\pi}{N_B}\right) \tag{42}$$

where θ_1 is the azimuthal angle of the first blade. The summation can be rewritten as,

$$T_{SW} = A \sum_{p=0}^{N_B-1} \sin\left(\theta_1 + \frac{p}{N_B}2\pi\right) \tag{43}$$

This can be expanded using trigonometric identities to give,

$$T_{SW} = A\sin\theta_1 + A\sin\theta_1 \sum_{p=1}^{N_B-1} \cos\left(\frac{p}{N_B}2\pi\right) + A\cos\theta_1 \sum_{p=1}^{N_B-1} \sin\left(\frac{p}{N_B}2\pi\right) \tag{44}$$

$\forall N_B > 1$ Equations 45 and 46 hold as shown in lemma .0.1. The expression for T_{SW} is reduced to Equation 47.

$$\sum_{p=1}^{N_B-1} \cos\left(\frac{p}{N_B}2\pi\right) = -1 \tag{45}$$

$$\sum_{p=1}^{N_B-1} \sin\left(\frac{p}{N_B}2\pi\right) = 0 \tag{46}$$

$$T_{SW} = A\sin\theta_1 - A\sin\theta_1 + 0 = 0 \tag{47}$$

Therefore, for any equally spaced $N_B > 1$, summing the torque over the number of blades reduces the self-weight torque contribution to zero.

Lemma .0.1 *Let $z_0, ..., z_{n-1}$ be the n-th roots of unity, i.e.,*

$$z_j = \cos\left(\frac{2\pi j}{n}\right) + i\sin\left(\frac{2\pi j}{n}\right) \tag{48}$$

From this definition, it is clear that $z_0 = 1$. For the n-th root of unity it is true that,

$$\begin{aligned} z^n - 1 &= 0 \\ z^n - 1 &= (z - z_0)(z - z_1)...(z - z_{n-1}) \\ z^n - 1 &= z^n - z^{n-1}(z_0 + z_1 + ... + z_{n-1}) + z^{n-2}(...) + ... \end{aligned} \tag{49}$$

By comparing the z^{n-1} term on the left and right hand-side of the equality it is true that,

$$z_0 + z_1 + ... + z_{n-1} = 0 \tag{50}$$

Therefore,

$$\begin{aligned} \Re(z_0) + \Re(z_1) + ... + \Re(z_{n-1}) &= 0 \\ \Im(z_0) + \Im(z_1) + ... + \Im(z_{n-1}) &= 0 \end{aligned} \tag{51}$$

Using $z_0 = 1$ and the definition for z_j the two equations in 51 become,

$$\begin{aligned} 1 + \cos\left(\frac{1}{n}2\pi\right) + \cos\left(\frac{2}{n}2\pi\right) ... + \cos\left(\frac{n-1}{n}2\pi\right) &= 0 \\ 0 + \sin\left(\frac{1}{n}2\pi\right) + \sin\left(\frac{2}{n}2\pi\right) ... + \sin\left(\frac{n-1}{n}2\pi\right) &= 0 \end{aligned} \tag{52}$$

$$\begin{aligned} \sum_{p=1}^{n-1} \cos\left(\frac{p}{n}2\pi\right) &= -1 \\ \sum_{p=1}^{n-1} \sin\left(\frac{p}{n}2\pi\right) &= 0 \end{aligned} \tag{53}$$

. APPDX B: PROOF: THE SUMMATION OF THE SELF-WEIGHT EFFECT TO GIVE TOTAL TURBINE TORQUE EQUAL TO ZERO.

References

I. Afgan, J. McNaughton, D. D. Apsley, S. Rolfo, and T. Stallard P. K. Stansby. Large-eddy simulation of a 3-bladed horizontal axis tidal stream turbine: comparisons to rans and experiments. *7th International Symposium on Turbulence, Heat and Mass Transfer (THMT7) (2012)*, 7, 2012. 27

ANSYS. Ansys. `www.ansys.com`, 2012. 22

E. Aulisa, S. Manservisi, and R. Scardovelli. A mixed markers and volume-of-fluid method for the reconstruction and advection of interfaces in two-phase and free-boundary flow. *Journal of Computational Physics*, 188:611–639, 2003. 25, 26

A.S. Bahaj, A.F. Molland, J.R. Chaplin, and W.M.J. Batten. Power and thrust measurements of marine current turbines under various hydrodynamic flow conditions in a cavitation tunnel and a towing tank. *Renewable Energy*, Volume 32(Issue 3): 407–426, 2007. 27, 29, 48, 49, 55, 62, 63, 64, 65, 66, 68, 69, 70, 71, 72, 73, 75, 78, 79, 80, 119, 126, 131, 132, 134, 135, 137, 138, 142, 166, 167, 169, 170, 171, 172, 173, 175, 176, 179, 180

R.K. Bansal. *Fluid Mechanics and Hydraulic Machines.* Laxmi Publications Ltd, 1998. 132

N. Barltrop, K. S. Varyani, A. Grant, D. Clelland, and X. P. Pham. Wave-current interactions in marine current turbines. *Journal of Engineering for the Maritime Environment*, 220:195–203, 2006. 16, 17, 29, 30, 31, 120, 158, 163, 164

N. Barltrop, K. S. Varyani, A. Grant, D. Clelland, and X. P. Pham. Investigation into wave-current interactions in marine current turbines. *Journal of Power and Energy*, 221:233–242, 2007. 31, 120, 147, 148, 149, 152, 153, 154, 155, 156, 163, 164

REFERENCES

W.M.J. Batten, A.S. Bahaj, A.F. Molland, and J.R. Chaplin. The prediction of the hydrodynamic performance of marine current turbines. *Renewable Energy*, Volume 33(Issue 5):1085–1096, 2008. 9, 13, 28, 29

Bisplinghoff and Ashley. *Principles of Aeroelasticity.* Dover Publications (New York), 1975. 144, 145

C L Bretschneider. Significant waves and wave spectrum. *Ocean Industry*, pages 45–50, 1968. 87, 88

H.C. Buckland, I. Masters, J.A.C. Orme, and T. Baker. Cavitation inception and simulation in bemt for modelling tidal stream turbines. *Journal of Power and Energy (2013)*, 2013. 198

M. L. Jr. Buhl. A new empirical relationship between thrust coefficient and induction factor for the turbulent windmill state. In *National Renewable Energy Laboratory*, volume Technical Report NREL/TP-500-36834, 2005. 12, 58, 59, 63, 65, 81, 160

T. Burton, D. Sharpe, N. Jenkins, and E. Bossanyi. *Wind Energy Handbook.* John Wiley and Sons Ltd, West Sussex, England, 2001. 11, 12, 36, 40, 44, 46, 50, 57, 59, 73, 81

J. R. Chaplin. Developments of stream-function wave theory. *Coastal Engineering*, 3:179–205, 1979. 18, 200, 201, 204, 207

J. C. Chapman. Tidal energy device hydrodynamics in non-uniform transient flows. *PhD Thesis, Civil and Computational Engineering, Swansea University (2009)*, 2009. 9, 10, 13, 16, 18, 34, 37, 47, 53, 63, 85, 112, 140, 141, 143, 165, 167

J.C. Chapman, I. Masters, M. Togneri, and J.A.C. Orme. The buhl correction factor applied to high induction conditions for tidal stream turbines. *Renewable Energy (submitted 2012)*, 2012. 164, 195

E. D. Christensen, L. Yde, and H. Gravesen. Wave loads on offshore wind turbine foundations in shallow water. engineering models vs. refined flow modelling. In *EOW (European Offshore Wind conference)*, Berlin, 2007. 26

G. D. Crapper, editor. *Introduction to Water Waves.* E. Horwood, 1984. 20

T. A. de Jesus Henriques, A. Botsari, S. C. Tedds, R. J. Poole, H. Najafian, and C. J. Sutcliffe. The effects of wave-current interactions on the performance of horizontal axis tidal-stream turbines. *Proceedings of the 2nd Oxford Tidal Energy Workshop*, 2:17–18, 2013. 26

R.G. Dean. Stream function representation of non-linear ocean waves. *Journal of Geophysical Research*, 70:4561–4572, 1965. 200

Department of Trade and Industry's Renewables 2010 Target Team. The world offshore renewable energy report. 2009. 1, 2

O. DeVires. Fluid dynamic aspects of wind energy conservation. *AGARD Report AG-243*, pages Chapter 4: 1–50, 1979. 12

FLOW-3D Flow Science. `http://www.flow3d.com/`, 2010. 22, 23, 24, 25, 26

FlowaveTT. `www.flowavett.co.uk`, October 2012. 4, 15

C. Freeman, A. Teixeira, F. Trarieux, and R. Ayre. Design of a gravity stabalised fixed pitch tidal turbine of 400kw. *In proc. 8th European Wave and Tidal Energy Conference*, 2009. 84

Future Energy Solutions. Dti new and renewable energy programme annual report 2005/06. 2007. 1

P. W. Galloway, L. E. Myers, and A. S. Bahaj. Studies of a scale tidal turbine in close proximity to waves. In *3rd International Conference on Ocean Energy*, 2010. 141

GL Garrad Hassan Tidal Bladed. Tidal bladed. `www.gl-garradhassan.com/en/software/GHTidalBladed.php`, 2013. 17

H. Glauert. Section l 'airplane propellers'. *Durand's 'Aerodynamic Theory'*, Volume IV:169–360, 1934. 9, 11, 12, 37, 43, 44, 45, 46, 49, 52, 58, 59, 63, 73, 75, 76, 78, 81

Y. Goda. *Random Seas and Design of Maritime Structures Third Edition.* World Scientific Publishing Co. Pte. Ltd., 2010. xvi, 16, 17, 87, 88, 90, 91, 93, 94, 98

R. T. Griffiths. Energy from the wind. 1974. 9, 40

REFERENCES

R. T. Griffiths and M. G. Woolard. Performance of the optimal wind turbine. *Applied Energy, Applied Science Publishers Ltd, Essex, England*, Volume 4:261–272, 1978. 10, 11, 37, 38

J. Groeneweg and J. Battjes. Three-dimensional wave effects on a steady current. *Journal of Fluid Mechanics*, 478:325–343, 2003. 21

Hammerfest Strom Ltd. `www.hammerfeststrom.com`, 2010. 2, 6

Garrad Hassan and Partners Ltd. Development of a design tool for axial flow tidal stream devices. *BERR Emerging Energies Technology programme, AEA Energy and Environment*, 2008. 10, 11, 17, 33, 34

K. Hasselmann, T. P. Barnett, E. Bouws, H. Carlson, D. E. Cartwright, K. Enke, J. A. Ewing, H. Gienapp, D. E. Hasselmann, P. Kruseman, A. Meerburg, P. Mï£¡ller, D. J. Olbers, K. Richter, W. Sell, and H. Walden. Measurements of wind-wave growth and swell decay during the joint north sea wave project (JONSWAP). *Deutches Hydrographisches Institut*, 1973. 89

A. Khayyer and H. Gotoh. Wave impact calculations by improved SPH methods. In *The Nineteenth (2009) International Offshore and Polar Engineering Conference*, Osaka, Japan, June 21-26 2009. ISOPE. 22, 23

R. Lanzafame and M. Messina. Fluid dynamics wind turbine design: Critical analysis, optimization and application of bem theory. *Renewable Energy*, 32:2291–2305, 2007. 9

C. N. Lock, H. Batemen, and H.C. Townsend. An extension of the vortex theory of airscrews with applications to airscrews of small pitch, including experimental results. *Aeronautical Research Committee Reports and Memoranda, London: Her Majestys Stationery Office. (1926)*, 1014, 1926. 12, 58, 61, 62, 75, 76, 77, 78, 82

X. Lv, Q. Zou, Y. Zhao, and D. Reeve. A novel coupled level set and volume of fluid method for sharp interface capturing on 3d tetrahedral grids. *Journal of Computational Physics*, 229, 2010. 25, 26

R. Malki, I. Masters, A. J. Williams, and T. N. Croft. The influence of tidal stream turbine spacing on performance. In *European Wave and Tidal Energy Conference*, 2011. 3, 14, 28

Marine Current Turbines Ltd. www.marineturbines.com, 2013. 2, 6, 7

I. Masters, J. C. Chapman, and J. A. C. Orme. A three-dimensional tidal stream turbine hydrodynamic performance model. In *Proc. World Renewable Energy Congress (WREC X)*, 2008. 141, 142

I. Masters, R. Malki, A. Williams, and N. Croft. The influence of turbulence model on wake structure of tsts when used with a coupled bem-cfd model. *Proceedings - Oxford Tidal Energy Workshop, Oxford, UK*, 2012. 14

I. Masters, J. A. C. Orme, M. Willis, and J. C. Chapman. A robust blade element momentum theory model for tidal stream turbines including tip and hub loss corrections. *Proceedings of the Institute of Marine Engineering, Science and Technology Part A, Journal of Marine Engineering and Technology*, 10:25–35, January 2011. 9, 10, 11, 37, 38, 40, 47

T. R. McCombes. *An Unsteady Hydrodynamic Model for Tidal Current Turbines.* PhD thesis, Department of Mechanical and Aerospace Engineering University of Strathclyde, 2013. 3

J. McNaughton, I. Afgan, D.D. Apsley, S. Rolfo, T. Stallard, and P.K. Stansby. CFD simulation of a 3-bladed horizontal axis tidal stream turbine using RANS and LES. *Proceedings - Oxford Tidal Energy Workshop, Oxford, UK*, 2012. 14

B. Le Mehaute. An introduction to hydrodynamics and water waves. *Springer-Verlag*, 1927. 13

W. H. Michel. Sea spectra revisited. *Marine Technology*, 36:211–227, 1999. 20, 96, 97

P. J. Moriarty and A. C. Hansen. Aerodyn theory manual. *Technical Report, U.S. National Renewable Energy Laboratory*, January 2005. 53

B. R. Munson, D. F. Young, and T. H. Okiishi. *Fundamentals of Fluid Mechanics.* John Wiley and Sons Ltd, 2006. 132

NationalGrid. www.nationalgrid.com, October 2012. 2

J. N. Newman. *Marine Hydrodynamics.* The Massachusetts Institute of Technology, 1977. 144

REFERENCES

J. A. C. Orme. Dynamic performance modelling of tidal stream turbines in ocean waves. *PhD Thesis, Civil and Computational Engineering, Swansea University (2006)*, 2006. 9, 10, 13, 141, 143, 144, 145

Parlimentary Office of Science and Technology. Electricity in the uk. Number 208, February 2007. 2

Renewables Advisory Board. Marine renewables: current status and implications for R and D funding and the marine renewables deployment fund. 2008. 2, 5

A. Roland, A. Cucco, C. Ferrarin, T. Hsu, J. Liau, S. Ou, G. Umgiesser, and U. Zanke. On the development and verification of a 2-D coupled wave-current model on unstructured meshes. *Journal of Marine Systems*, 78, 2009. 17

D. Ross. *Power from the Waves.* Oxford University Press, 1995. 4, 5, 18

H. Schlichting. Boundary-layer theory. *New York: McGraw-Hill.*, 7th ed. 1979. 13

Wen Zhong Shen, Robert Mikkelsen, Jens Norkar Sorensen, and Christian Bak. Tip loss corrections for wind turbine computations. *Wind Energy*, Volume 8(Issue 4), 2005. 11, 12, 49

H. Snel. Application of a modified theodorsen model to the estimation of aerodynamic forces and aerodynamic stability. *In proc. European Wind Energy Conference,London, 22-25 November*, 2004. 84

South Wales Ports. `www.southwalesports.co.uk`, October 2012. 2

C. Swan, I. Cummins, and R. James. An experimental study of two-dimensional surface water waves propagating on depth-varying currents. part 1. regular waves. *Journal of Fluid Mechanics*, 428:273–304, 2001. 140, 141

Swanturbines Ltd. Tidal Technology. `www.swanturbines.co.uk`, Janurary 2013. 2, 5, 7

The Carbon Trust. `www.carbontrust.co.uk`, 2010. 2, 6

The Energy Programme. Evaluation of the dti new and renewable energy programme 1994-8. 1999. 5, 6

The European Marine Energy Centre Ltd. www.emec.org.uk, 2012. 2, 4, 6

The UK HM Government. Marine energy action plan executive summary and reccomendations. 2010. 1, 3, 5

Tidal Energy Ltd. www.tidalenergyltd.com, October 2012. 8

M. Togneri, J. Orme, and I. Masters. Incorporating turbulent inflow conditions in a blade element momentum model of tidal stream turbines. In *Proceedings of the 21st International Offshore and Polar Engineering Conference,ISOPE, Hawaii, USA*, 2011. 38, 160

M. J. Tucker. Nearshore waveheight during storms. *Coastal Engineering*, 24:111–136, 1995. 93

S. R. Turnock, A. B. Phillips, J. Banks, and R. Nicholls-Lee. Modelling tidal current turbine wakes using a coupled RANS-BEMT approach as a tool for analysing power capture of arrays of turbines. *Ocean Engineering*, 38:1300–1307, 2011. 14

G. Umgiesser and L. Zampato. Hydrodynamic and salinity modeling of the venice channel network with coupled 1-d and 2-d mathematical models. *Ecological Modelling*, 138, 2001. 17, 22

USFOS Theory Manual. USFOS Theory Manual. 1993. 103

H. K. Versteeg and W. Malalasekera. *An Introduction to Computational Fluid Dynamics, The Finite Volume Method, Second Edition.* Pearson Education Ltd, 2007. 22, 23

L. A. Viterna and R. D. Corrigan. Fixed pitch rotor performance of large horizontal axis wind turbines. *DOE/NASA Workshop on Large Horizontal Axis Wind Turbines, Cleveland, Ohio,*, 1981. 28

Robin Wallace. Marine energy research and development in the uk, www.supergen-marine.org.uk. 2009. 5

WAMIT INC. MIT. Wamit inc. www.wamit.com, 2013 . 22

REFERENCES

G. D. Weymouth and D. K. P. Yue. Conservative volume-of-fluid method for free-surface smulations on cartesian-grids. *Journal of Computational Physics*, 229:2853–2865, 2010. 25, 26

J. I. Whelan. A fluid dynamic study of free-surface proximity and inertia effects on tidal turbines. *PhD Thesis, Department of Aeronautics, Imperial Collage London*, 2010. 84, 134, 144, 145

A. J. Williams, T. N. Croft, I. Masters, C. R. Bennet, S. G. Patterson, and M. R. Willis. A combined BEM-CFD model for tidal stream turbines, 2010. 26

M. Willis, I. Masters, S. Thomas, R. Gallie, J. Loman, A. Cook, R. Ahmadian, R. Falconer, B. Lin, G. Gao, M. Cross, N. Croft, A. Williams, M. Muhasilovic, I. Horsfall, R. Fidler, C. Wooldridge, I. Fryett, P. Evans, T. OḎoherty, D. OḎoherty, and A. Mason-Jones. Tidal turbine deployment in the bristol channel: a case study. *Proceedings of the ICE - Energy*, 163:93–105, 2010. 8

Willson and Lissaman. Applied aerodynamics of wind power machines. *Oregon State University Report*, 1974. 11, 59

XFOIL Subsonic Airfoil Development System. Xfoil subsonic airfoil development system by mark drela (also harold youngren). `web.mit.edu/drela/Public/web/xfoil/`. 28